THÈSE

Pour obtenir le grade de

**DOCTEUR DE L'UNIVERSITÉ GRENOBLE ALPES**

École doctorale : PHYS - Physique
Spécialité : Physique de la Matière Condensée et du Rayonnement
Unité de recherche : Institut Néel

# Excitations magnétiques dans les oxydes de pyrochlore : Bruit des monopoles et relation fluctuation-dissipation dans les glaces de spins & Impact d'un métal magnétique sur l'état dipolaire-octupolaire du Nd

# Magnetic excitations in pyrochlore oxides: Monopole noise and fluctuation-dissipation relation in spin ice & Impact of a magnetic metal on the Nd dipolar-octupolar state


Présentée par :

**Félix MORINEAU**

Direction de thèse :

**Elsa LHOTEL** — Directrice de thèse
Institut Néel, CNRS

**Mike ZHITOMIRSKY** — Co-directeur de thèse
PHELIQS IRIG, CEA GRENOBLE

Rapporteurs :

**Ludovic JAUBERT**
LOMA, CNRS, Université de Bordeaux

**Romain SIBILLE**
Laboratory for Neutron Scattering and Imaging, PSI


Thèse soutenue publiquement le **14 novembre 2025**, devant le jury composé de :

| | |
|---|---|
| **Ludovic JAUBERT,** LOMA, CNRS, Université de Bordeaux | Rapporteur |
| **Romain SIBILLE,** Laboratory for Neutron Scattering and Imaging, PSI | Rapporteur |
| **Paul MCCLARTY,** LLB, CNRS-CEA | Examinateur |
| **Claire COLIN,** Institut Néel, Université Grenoble Alpes, CNRS | Présidente du jury |
| **Steven BRAMWELL,** University College London | Examinateur |


Invités :

**Carley PAULSEN**
Institut Néel, CNRS

**Peter HOLDSWORTH**
Laboratoire de Physique, ENS de Lyon

# Remerciements

Je remercie tout d'abord l'Institut Néel et toutes les personnes que j'ai pu rencontrer de m'avoir chaleureusement accueilli durant ces trois années de thèse.

Parmi eux, je pense en premier lieu à mes encadrants qui m'ont accompagné tout au long de ces années : Elsa Lhotel et Carley Paulsen. Vous avez toujours été disponibles et bienveillants et m'avez transmis votre goût de la recherche. J'ai énormément appris à vos côtés : depuis les arcanes des magnétomètres à SQUID jusqu'aux confins du magnétisme frustré. Je ne vous remercierai jamais assez pour tout ce que vous avez fait.

Je remercie également Mike Zhitomirsky, malgré le fait que les aléas de la thèse et de la recherche n'ont pas pu nous permettre de mener les projets qu'on aurait voulu mener ensemble.

L'ensemble des travaux entrepris n'aurait jamais pu être concrétisé sans l'aide de nombreuses autres personnes à qui je dis un grand Merci. Peter Holdsworth pour les nombreuses discussions et l'aide apportée sur la compréhension de la dynamique des monopoles. Sean Giblin et ton regard neuf qui m'a aidé à prendre du recul sur les mesures de bruit et susceptibilité. Sylvain Petit pour ta gentillesse et ton accompagnement lors des mesures neutroniques ainsi que pour m'avoir initié aux méthodes numériques pour leur analyse. Virginie Simonet, la cheffe de l'équipe et du CSTD, avec qui j'ai affiné mon premier diffractogramme et qui a toujours su être curieuse et soucieuse de l'avancée de ma thèse. Julien Robert, d'avoir pris le temps de m'apprendre et m'aider à utiliser une procédure d'analyse de symétrie. Claire Colin, Jacques Ollivier et Bjorn Fak pour votre patience et les explications claires que vous avez su me fournir sur vos fantastiques instruments et l'analyse de leurs données. Anne Gérardin, Sébastien Triqueneaux, Olivier Tissot, Grégory Garde, et Gilles Pont pour votre aide technique précieuse sans laquelle la construction du nouveau magnétomètre n'aurait jamais pu avancer. Elise Pachoud, Abdel Hadj-Azzem, Geetha Balakrishnan et Kazuyuki Matsuhira, pour les jolis cristaux et échantillons sans lesquels ma thèse n'aurait pas eu lieu. Mathilde Berard, Caroline Bartoli, Élodie Ferrara et Emeline Mendez pour m'avoir aidé dans les procédures administratives et les missions qui ne sont toujours pas évidentes à comprendre.

Merci à Ludovic Jaubert, Romain Sibille, Claire Colin, Steven Bramwell et Paul McClarty d'avoir accepté de faire partie de mon jury.

Les membres de l'équipe MagSup avec qui j'ai pu partager mes repas ont grandement participé à la qualité de mon accueil et je vous en remercie. Évidemment je tiens également à remercier les non-permanents avec qui j'ai partagé mes journées durant ces années aussi bien au labo qu'en dehors. Je commencerai par Owen mon cher ex-collègue anglais qui m'a accompagné durant ces années avec qui j'ai longuement discuté, grimpé et même couru. Nathan avec qui on a partagé les mêmes manips et qui m'a initié à taper du carton. Et toutes les magnifiques personnes avec qui j'ai passé du temps de qualité, certains qui sont encore au labo et d'autres qui ont déjà volé vers de nouvelles contrées : Ilya, Flavien, Francis, Ed, Mads, Gabriele, Lorenzo, Armand, Mathilde, Antoine, Jeremy, Chafic, Rémy, Luca, Quentin, Antoine, Antoine, Grand Nathan, Sitaram, Gao, Mathias, Richard, Léna...

Et pour finir je remercie ma famille qui a toujours été là pour moi et qui a pris le temps de s'intéresser à ce que je faisais durant ma thèse.

# Contents


**1 Scientific background** **3**

1.1 Magnetic frustration . . . 4
1.1.1 Introduction to frustration . . . 4
1.1.2 Frustation on the pyrochlore lattice: the nearest-neighbor model . . . 7
1.2 Rare-earth pyrochlore oxides . . . 10
1.3 Spin ice materials . . . 13
1.3.1 Dipolar spin ice . . . 13
1.3.2 Magnetic monopoles: the dumbbell model . . . 15
1.3.3 Spin ice dynamics: equilibrium . . . 16
Spin ice dynamical regimes . . . 16
Quantum tunneling times $\tau_0$ . . . 18
1.3.4 Spin ice dynamics: out-of-equilibrium . . . 20
1.3.5 Noise and FDT for out-of-equilibrium properties . . . 21
1.4 Nd-based pyrochlores . . . 23
1.4.1 Dipolar Octupolar pyrochlores: the XYZ Hamiltonian . . . 23
1.4.2 The AIAO dipolar-octupolar order . . . 25
1.4.3 Dynamic fragmentation . . . 28
1.4.4 $Nd_2Ir_2O_7$ and $Nd_2Ru_2O_7$ . . . 30

**2 Experimental techniques** **33**

2.1 Neutron scattering and diffraction . . . 34
2.1.1 Neutron: a powerful tool for condensed matter . . . 34
2.1.2 Scattering cross section . . . 34
Nuclear scattering . . . 35
Magnetic scattering . . . 36
2.1.3 Neutron diffraction . . . 37
2.1.4 Inelastic neutron scattering . . . 38
2.1.5 Neutron instruments . . . 38
Powder diffraction : D1B-CRG@ILL . . . 38
Time of flight spectrometers : PANTHER@ILL and IN5@ILL . . . 39
2.2 Low temperature apparatus: dilution refrigerator . . . 41
2.2.1 $^4$He and $^3$He cryogenics fluids . . . 41
2.2.2 Principle of the dilution refrigerator . . . 41
2.2.3 Miniature dilution refrigerator or diluette . . . 43
2.3 Magnetometry . . . 44
2.3.1 SQUID magnetometers . . . 44

Extraction magnetometer . . . 45
Noise magnetometer . . . 46
2.3.2 Magnetization and susceptibility . . . 48
DC susceptibility . . . 49
AC susceptibility . . . 51
2.3.3 Magnetic noise . . . 52
General description . . . 52
External Noise and Cleaning Procedure . . . 54
2.3.4 Measuring the fluctuation-dissipation theorem . . . 55

**3 Spin ice dynamics** **57**
3.1 Equilibrium dynamics . . . 58
3.1.1 Experimental method . . . 58
3.1.2 Magnetic susceptibility measurements . . . 59
3.1.3 Noise measurements . . . 60
3.1.4 FDR in equilibrium . . . 61
3.1.5 Dynamics analysis using empirical models . . . 62
AC susceptibility . . . 62
Noise . . . 65
3.1.6 Results and discussion on the equilibrium dynamics . . . 66
3.2 Low temperature regime . . . 72
3.2.1 FDR violations . . . 72
3.2.2 New relaxation process at low temperature . . . 75
3.3 Conclusion about spin ice dynamics . . . 78
3.4 Demagnetization corrections . . . 80
3.4.1 The demagnetization effect . . . 80
3.4.2 The need for demagnetization corrections in noise measurements . . . 81
3.4.3 Experimental procedure . . . 82
3.4.4 Estimation of N factors in $Ho_2Ti_2O_7$ . . . 83
3.4.5 Kramers-Kronig integration for correcting the noise . . . 88
3.4.6 Behavior with N . . . 90
3.4.7 Impact of $N$ as a function of temperature . . . 94
3.5 $Dy_2Ti_2O_7$ isotopic differences . . . 96

**4 Instrumental development** **103**
4.1 Magnetic shielding . . . 104
4.2 Motivations for a new setup . . . 106
4.3 Optimization of detection . . . 107
4.4 Design realization . . . 112
4.5 Dilution refrigerator performances . . . 114

**5 Impact of a magnetic metal ion in Nd-based pyrochlores** **117**
5.1 Symmetry analysis . . . 118
5.1.1 The Nd-Nd interaction . . . 118
5.1.2 The *M*-*M* interaction . . . 119
5.1.3 The Nd-*M* interaction . . . 119

5.2 Measurement and analysis of $Nd_2Ir_2O_7$ and $Nd_2Ru_2O_7$ . . . . . 125
5.2.1 Experimental method . . . . . 125
5.2.2 Introduction to crystal electric field excitations . . . . . 126
5.2.3 $Nd_2Ir_2O_7$ . . . . . 127
CEF levels measurements . . . . . 127
Neutron diffraction and magnetic ordering . . . . . 128
Bulk magnetometry . . . . . 130
Spin wave measurements . . . . . 131
Analysis using the model Hamiltonian . . . . . 133
5.2.4 $Nd_2Ru_2O_7$ . . . . . 136
CEF levels measurements . . . . . 136
Neutron diffraction and magnetic ordering . . . . . 138
Bulk magnetometry . . . . . 142
Spin wave measurements . . . . . 145
Analysis . . . . . 147
5.3 Discussion and conclusion . . . . . 149
Atomic positions and local bases . . . . . 155

# Introduction

Rare earth pyrochlores are a family of oxide compounds that presents various forms of magnetic states of matter. They have been studied for several decades and more and more physics is still being discovered. One of the great advantage of these materials is that many compositions can be chemically stabilized just by interchanging its rare earth and metal sites, and in doing so tune coupling interactions giving rise to a rich playground of magnetic phenomena. Many of these phenomena originates from the constraints of the lattice. These constraints result in magnetic frustration where interactions between magnetic moments cannot be simultaneously satisfied and prevent the stabilization of conventional magnetic order. Frustrated states are often accompanied by intriguing dynamical properties with highly correlated spin phases, for instance giving rise to quasiparticle excitations.

In this context, we are interested in two families of rare earth pyrochlores: the spin ice materials and the Nd-based compounds. The first family presents a disordered magnetic phase which retains entropy down to the lowest temperatures. The dynamics of its low temperature phase, the spin ice state, is driven by emergent magnetic monopoles, which have been studied for fifteen years while their dynamics is far from being fully understood. In particular down to the lowest temperature where the timescales of the excitations diverge strongly and the spin system falls out of thermodynamic equilibrium. Further to extensive studies, both the experimental techniques and theoretical models became more refined, up to the point that nowadays only the high-hanging fruit remains. In the objective of seizing these sumptuous fruit, we have developed a new type of low temperature noise magnetometer, which is designed to probe both ac susceptibility and magnetic noise simultaneously to test the limits of the fluctuation dissipation theorem. In the second family of Nd-based compounds, the magnetic moment of the rare earth ion possesses unusual symmetry properties, generating both dipolar and octupolar magnetic components which can couple to each other. These couplings act as a quantum perturbation allowing the realization of new magnetic phases. In this thesis, we are interested in the interactions that can arise with this peculiar Nd magnetic moment when a magnetic metal is placed on the metal site of the pyrochlore lattice.

This manuscript is divided into five chapters. We will start by introducing all the necessary concepts required to understand the general physics of the two systems and all the studies pursued during this thesis. The second part introduces all the experimental techniques employed. The third part dives deep into all our experimental investigations on the fluctuation dissipation theorem in spin ice systems, and more technical aspects

involving the influence of demagnetization fields on the noise or isotopic effects are also covered. The fourth part regards improvements to the current noise magnetometer and the implementation of these improvements into a novel apparatus. Finally, the last part focuses on the impact of a magnetic metal on the dipolar-octupolar all-in/all-out ground state of Nd-based systems.

# Chapter 1

# Scientific background

## Contents


**1.1 Magnetic frustration . . . . . 4**
1.1.1 Introduction to frustration . . . . . 4
1.1.2 Frustation on the pyrochlore lattice: the nearest-neighbor model 7
**1.2 Rare-earth pyrochlore oxides . . . . . 10**
**1.3 Spin ice materials . . . . . 13**
1.3.1 Dipolar spin ice . . . . . 13
1.3.2 Magnetic monopoles: the dumbbell model . . . . . 15
1.3.3 Spin ice dynamics: equilibrium . . . . . 16
1.3.4 Spin ice dynamics: out-of-equilibrium . . . . . 20
1.3.5 Noise and FDT for out-of-equilibrium properties . . . . . 21
**1.4 Nd-based pyrochlores . . . . . 23**
1.4.1 Dipolar Octupolar pyrochlores: the XYZ Hamiltonian . . . . . 23
1.4.2 The AIAO dipolar-octupolar order . . . . . 25
1.4.3 Dynamic fragmentation . . . . . 28
1.4.4 $Nd_2Ir_2O_7$ and $Nd_2Ru_2O_7$ . . . . . 30

# 1.1 Magnetic frustration

## 1.1.1 Introduction to frustration

Frustrated spin systems have been studied for several decades. Early examples are systems of Ising antiferromagnetic interacting spins on the triangular lattice, studied by G. H. Wannier in 1950 [1], and on the pyrochlore lattice, studied by P. W. Anderson in 1956 [2]. The term *frustration*, as we know it today, was only introduced in 1977, almost simultaneously by G. Toulouse and J. Villain [3, 4], in the context of spin glasses. In a follow-up paper published the same year [5], J. Vannimenus and G. Toulouse already recognized that frustration was a concept of broader significance, going beyond the description of spin glass systems. They made the link between frustration and Anderson's 1956 work, and associated it to effects observed outside the field of material physics.

The concept of frustration is defined as a topological constraint that prevents neighboring spins from adopting a configuration where the energy is minimized on every bond. Because some interaction bonds remain unsatisfied, the ground state of a frustrated system can be highly degenerate, which gives rise to rich and unexpected behaviors at finite temperatures. Since then, many spin systems in condensed matter physics have been found to exhibit frustration, and numerous theories were established to interpret the associated experimental results. However, even up to now, many properties of these systems remain poorly understood and cannot be fully described even by the most advanced theoretical and numerical tools.

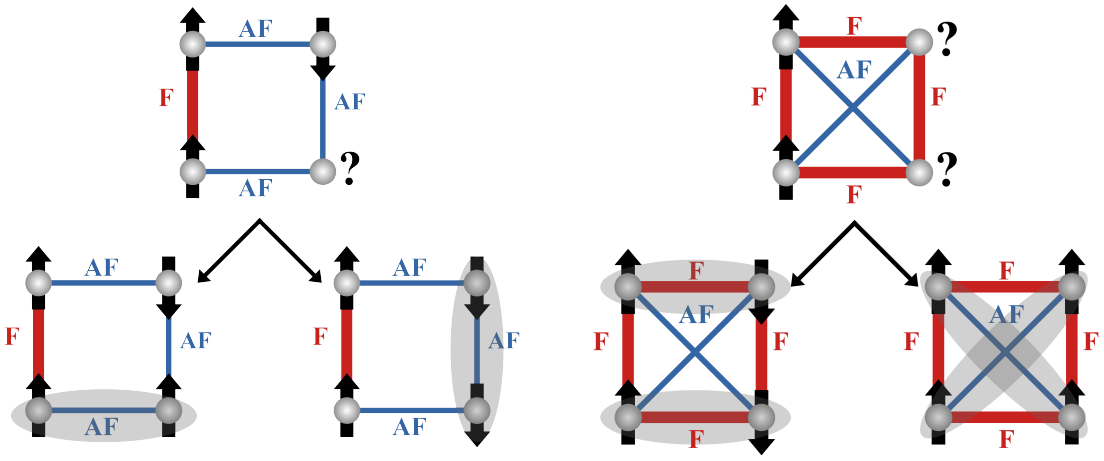


(a) (b)

Figure 1.1: Schematic of spin coupling frustration on a square for two cases. (a) Frustration due to an odd number of ferromagnetic and antiferromagnetic bonds (here 1:3 ratio), corresponding to simple spin glass models. (b) Frustration in the $J1-J2$ square model with opposite couplings. The frustrated bonds are highlighted in grey.

There can be two different origins of frustration in a magnetic system: frustration due to competing interactions, and frustration due to the lattice geometry. The first

mechanism is at the origin of the frustration observed in spin glasses. In practice, in canonical spin glass materials, frustration arises in the presence of disorder because the interactions are mediated by RKKY interactions whose sign depends on the distance between the magnetic atoms. For such systems, a simple model is to consider a fraction $x$ of the bonds to be ferromagnetic, while the remaining $(1-x)$ bonds are antiferromagnetic. These bonds are randomly distributed across the lattice, and depending on their local arrangement, some will be frustrated while others will be satisfied [3, 4].

On a square lattice, if we consider a plaquette of four bonds, if the number of ferromagnetic (or antiferromagnetic) bonds is even then all bonds are satisfied. However, if the number is odd, the plaquette will host at least one frustrated bond, leading to a two fold degenerate low-energy state, as illustrated in Figure 1.1(a). The degree of frustration depends on the number of unsatisfied interactions, which depends directly on the fraction $x$ of ferromagnetic bonds. Here, frustration is created by the random distribution of bonds in the system. If all bonds are of a single type meaning $x$ is equal to 0 or 1, then all interactions are satisfied leading to a long range ordered state, either antiferromagnetic if $x = 0$ or ferromagnetic if $x = 1$ [3].

Nonetheless, it is possible to find frustration due to competing interactions in a square lattice with periodic interactions, for example by introducing a second neighbor interaction. This leads to the $J_1 - J_2$ square lattice model, where when considering a first neighbor ferromagnetic interaction $J_1$ and a second neighbor antiferromagnetic interaction $J_2$ (along the diagonal), for $J_2/|J_1| > 0.5$, the competition between these interactions leads to a degenerate ground state [6]. Figure 1.1 (b) shows an example of frustration in the case $J_2 = -J_1$.

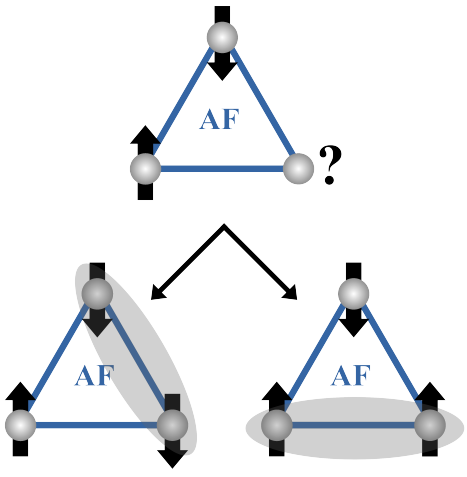


Figure 1.2: Frustration on a triangle due to antiferomagnetic exchange interactions. The frustrated bonds are highlighted in grey.

Another interesting instance where frustration arises from competing interactions is the Kitaev model. In this model, spins are arranged on a honeycomb (bipartite) lattice and interact via anisotropic bond-dependent couplings. Each spin is coupled through three different bonds: the first couples only to the $x$ component of the spin, the second

to the $y$ component, and the third to the $z$ component. As a result, the spins cannot simultaneously satisfy all three components, leading to a so-called quantum spin liquid ground state [7].

Geometrical frustration occurs when spin interactions are unsatisfied due to the combination of interaction signs and lattice connectivity, and is typically found in non-bipartite lattices. Figure 1.2 shows the most well-known example of geometrical frustration: nearest neighbor Ising spins on a triangle. If the coupling bonds are antiferromagnetic, when two spins are anti-parallel, the third spin cannot simultaneously satisfy both two bonds, ultimately resulting in one unsatisfied bond. In contrast, if the couplings are ferromagnetic, all spins can align in the same direction leading to an unfrustrated ground state. Thus, depending on the nature of the interactions, lattices prone to geometrical frustration do not always show frustrated ground states as some interactions can be trivially satisfied. The presence or absence of geometrical frustration depends on both the lattice geometry and the nature of the interactions.

To find other geometrically frustrated lattices, one must look for non-bipartite lattices. Any lattice composed of, or containing, odd-numbered plaquettes (like triangles), is non-bipartite and likely to display geometrical frustration as it is impossible to anti-align all spins on such lattices. Indeed, interesting frustrated physics has been observed in several triangle-based lattices. The best known, are shown in Figure 1.3, and include (a) the 2D triangular lattice, (b) the kagome lattice, (c) the 3D cubic face centered lattice and (d) the pyrochlore lattice.

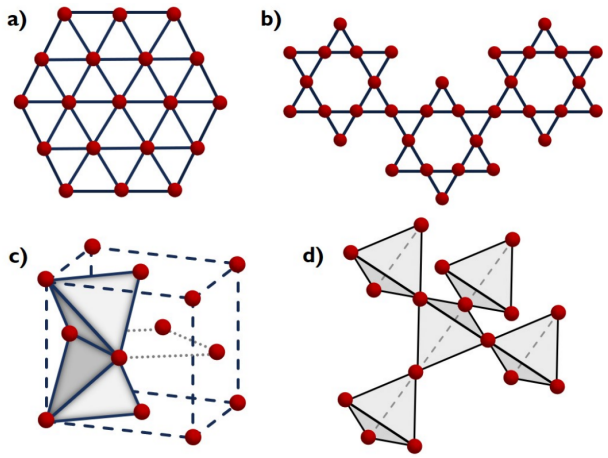


Figure 1.3: Four different lattices prone to geometric frustration: (a) the triangle lattice, (b) the kagome lattice, (c) the face centered cubic lattice and (d) the pyrochlore lattice. Figure from Ref. [8].

During my thesis, I focused on systems based on the pyrochlore lattice. This lattice exhibits a particularly rich phase diagram, with both frustrated and exotic ordered ground states. In the next subsection, we will examine frustration specifically in the nearest-neighbor Ising model on the pyrochlore lattice, which hosts the degenerate spin ice state. Following that, we will describe the general magnetic properties of the family of pyrochlore compounds. We will then discuss in more details the physics of two sub-

families of pyrochlore compounds investigated in the context of this thesis, starting with the spin ice materials and ending with the Nd-based pyrochlores.

### 1.1.2 Frustation on the pyrochlore lattice: the nearest-neighbor model

Frustration was first discovered on the pyrochlore lattice, a lattice of corner-sharing tetrahedra as shown in Figure 1.4(a), by P. W. Anderson in 1956 [2], in a model of uniaxial Ising spins coupled antiferromagnetically. Anderson recognized that this model was a direct analogue of the Pauling model for water ice introduced in 1935, where a degeneracy of the structural ice ground state was found to result in a residual entropy [9].

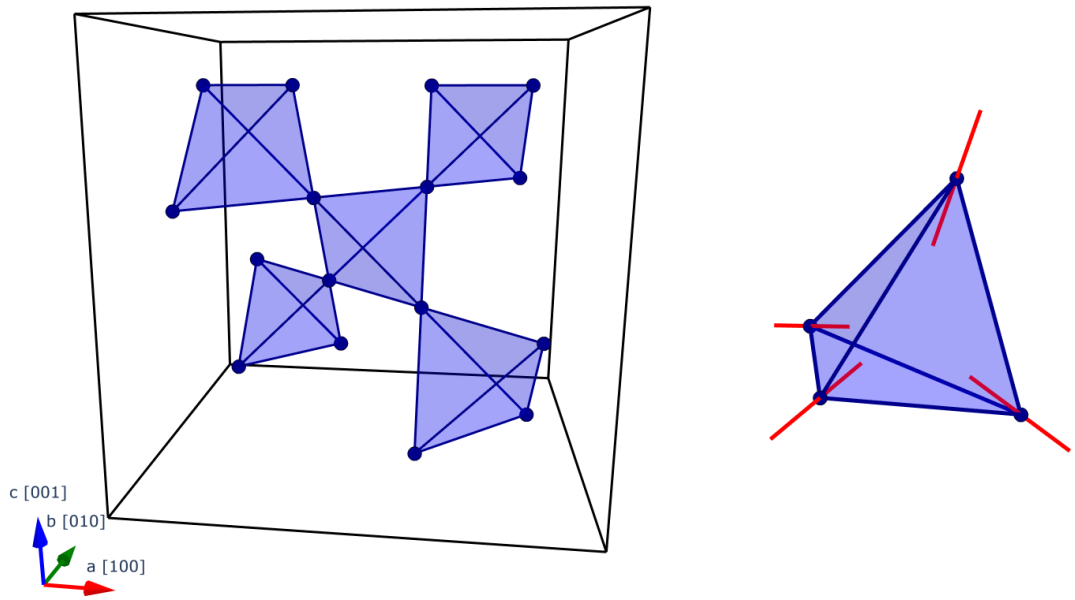


(a) (b)

Figure 1.4: (a) Corner sharing tetrahedra pyrochlore lattice in the cubic unit cell delimited by the black lines. (b) One tetrahedron with its local $z$-axes (in red) lying along the $\langle 111 \rangle$ directions.

In 1997, Harris et al. [10] measured a pyrochlore oxide compound $Ho_2Ti_2O_7$, in which Ho atoms lie on a pyrochlore lattice. They found that it exhibits similar ground state properties but surprisingly the interactions were found to be ferromagnetic. Since a uniaxial Ising spin system with purely ferromagnetic interactions cannot be frustrated, this indicated that the spins were arranged differently on the lattice. Indeed, in this case, frustration arose not from antiferromagnetic interactions between uniaxial spins, but rather from a combination of ferromagnetic coupling and strong multi-axial spin anisotropy. The spins were found to be oriented along the local axes connecting the centers of two neighboring tetrahedra, as illustrated in Figure 1.4(b), corresponding to the four $\langle 111 \rangle$ directions. The spins of a tetrahedron can be represented by four vectors, each pointing along one of the local $\langle 111 \rangle$ directions:

$$\begin{aligned} \mathbf{S}_1 &= \frac{\sigma_1}{\sqrt{3}}\begin{pmatrix}-1\\-1\\+1\end{pmatrix} \qquad \mathbf{S}_2 = \frac{\sigma_2}{\sqrt{3}}\begin{pmatrix}+1\\+1\\+1\end{pmatrix} \\ \mathbf{S}_3 &= \frac{\sigma_3}{\sqrt{3}}\begin{pmatrix}+1\\-1\\-1\end{pmatrix} \qquad \mathbf{S}_4 = \frac{\sigma_4}{\sqrt{3}}\begin{pmatrix}-1\\+1\\-1\end{pmatrix}. \end{aligned} \tag{1.1}$$

with $\sigma_i = \pm 1$ an Ising pseudospin variable. The convention gives $\sigma_i = +1$ when the spin is pointing outward from the center of a down tetrahedron. The Ising ferromagnetic model can be directly mapped on both the Anderson antiferromagnetic and the Pauling ice model, by considering the spins pointing along these local axes with the following Hamiltonian [11, 12]:

$$\mathscr{H} = -3J_{\text{eff}} \sum_{\langle i,j \rangle} \mathbf{S}_i \cdot \mathbf{S}_j = J_{\text{eff}} \sum_{\langle i,j \rangle} \sigma_i \sigma_j. \tag{1.2}$$

Here, $J_{\text{eff}}$ is the nearest neighbor effective interaction. In this nearest-neighbor spin ice (NNSI) model, frustration occurs when the coupling is ferromagnetic $J_{\text{eff}} > 0$. In contrast an antiferromagnetic coupling leads to an unfrustrated ordered ground state with alternating all-in/all-out (AIAO) configurations across adjacent tetrahedra.

When we consider $J_{\text{eff}} > 0$, the minimal energy is found when the system obeys the "ice rules". The ice rules requires that on each tetrahedron two spins point inward while the two other spins point outward. For each tetrahedron there is a total of $2^4 = 16$ spin configurations, but only $\binom{4}{2} = 6$ of them obey the 2-in/2-out ice rule. These six states constitute the ground state manifold while the remaining 10 states constitute the excited states with higher energy.

The energy of a single tetrahedron configuration can be estimated using Equation 1.1.2 by summing the energy resulting from the 6 bonds linking the 4 spins. For a 2-in/2-out tetrahedron, the calculated energy is $-2J_{\text{eff}}$. In the remaining 10 states: eight of them (3-in/1-out or 1-in/3-out configurations) have an energy of 0, and two (all-in and all-out configurations) have the highest energy of $6J_{\text{eff}}$. The different configurations and their respective energetic cost are listed in Figure 1.5.

The ground state consisting of tetrahedra obeying the 2-in/2-out ice rule has been called the "spin ice state" by Harris et al. due its analogy with the cubic water ice. When considering the whole system size, the degeneracy associated to one tetrahedron scales with the lattice size and its spin number. The resulting macroscopically degenerate ensemble of configurations are called the "Pauling states". The residual entropy per spin due to this degeneracy is given by $R/2\ln(3/2)$ [9]. Given that the total spin entropy is $R\ln(2)$, the entropy of the spin ice ground state is $R(\ln(2) - (1/2)\ln(3/2))$. This residual entropy at zero temperature was experimentally confirmed by Ramirez et al. in 1999 through specific heat measurements [14].

The 2-in/2-out ice rules impose local constraints on the Pauling states which in turns generate correlations between the spins. We can consider the magnetization of a tetrahedron on a site $M_\alpha$ defined as the sum of the four local spins $\sigma_{i\in\alpha}$ and define a coarse-grained field $\mathbf{M}(r)$ of the lattice magnetization over a large enough volume to assume $\mathbf{M}(r)$ is a smooth varying function [15, 16]. In this picture, spins corresponds to local

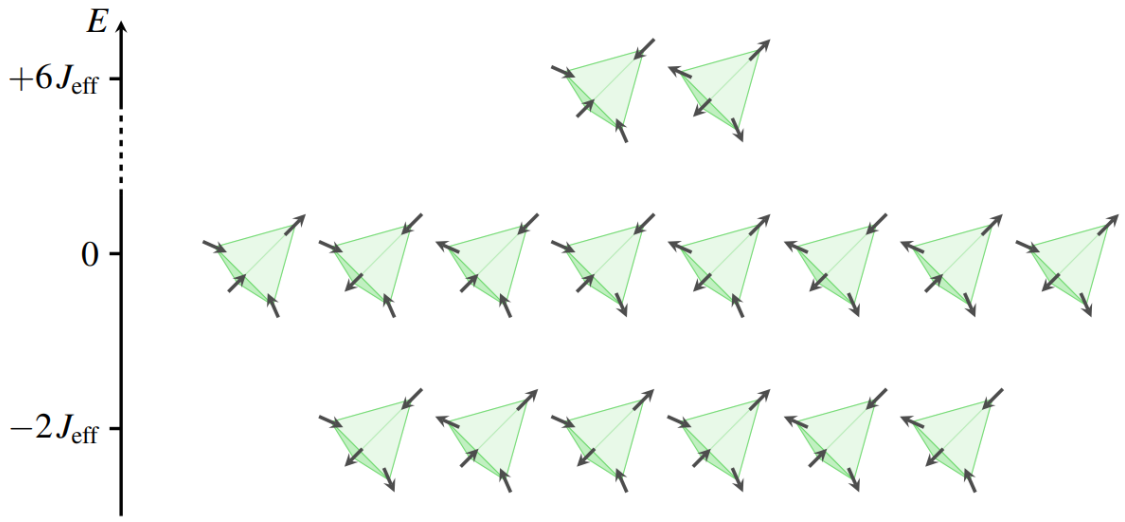


Figure 1.5: Energy of the 16 different configurations of a tetrahedron in the nearest-neighbor spin ice model. The three different energetic groups are the ice rule 2-in/2-out ground state group with $E = -2J_{\text{eff}}$, the 3-in/1-out and 1-in/3-out group with $E = 0$ and the all in- all out group with $E = 6J_{\text{eff}}$. Figure from Ref. [13].

fluxes of magnetization, and the 2-in/2-out rule implies that the net flux at the center of a tetrahedron is zero. This flux conservation is a divergence free condition of the magnetization field $\mathbf{M}(r)$, which also means that $\mathbf{M}(r)$ behaves as the curl of an emergent gauge field $\mathbf{A}$:

$$\nabla \cdot \mathbf{M}(\mathbf{r}) = 0 \iff \mathbf{k} \cdot \tilde{\mathbf{M}}(\mathbf{k}) = 0 \text{ and } \mathbf{M}(\mathbf{r}) = \nabla \times \mathbf{A} \tag{1.3}$$

Systems that exhibit such divergence-free constraints are said to host a "Coulomb phase" [17]. This divergence free condition in real space have an equivalent condition for the magnetization field $\tilde{\mathbf{M}}(\mathbf{k})$ in the reciprocal space. This condition forces the magnetization $\tilde{\mathbf{M}}(\mathbf{k})$ to be orthogonal to the wave vector $\mathbf{k}$:

$$\left\langle \tilde{M}_\mu(-\mathbf{k})\tilde{M}_\nu(\mathbf{k}) \middle| \tilde{M}_\mu(-\mathbf{k})\tilde{M}_\nu(\mathbf{k}) \right\rangle \propto \delta_{\mu\nu} - \frac{k_\mu k_\nu}{|\mathbf{k}|^2} \tag{1.4}$$

with $\mu$, $\nu$ Cartesian coordinates. This equation directly gives the shape of the magnetic correlations in the reciprocal space which can be compared to the magnetic scattering function measured with neutron scattering experiments [18], as illustrated in Figure 1.6. This description accurately predicts the appearance of "pinch points" singularities, resembling bow-ties. The form of the real space correlations are obtained by Fourier transforming the reciprocal space correlation :

$$\left\langle \tilde{M}_\mu(\mathbf{0})\tilde{M}_\nu(\mathbf{r}) \middle| \tilde{M}_\mu(\mathbf{0})\tilde{M}_\nu(\mathbf{r}) \right\rangle \propto \delta(r) + \frac{1}{r^3}\left(\delta_{\mu\nu} - \frac{3r_\mu r_\nu}{r^2}\right) \tag{1.5}$$

This expression reveals that spin correlations have a $1/r^3$ spatial dependence, like usual dipole-dipole interactions. The spatial decrease of the interactions depends, more

generally on the dimension $d$ of the Coulomb phase lattice, as $1/r^d$. For instance, a $2d$ kagome lattice that support a Coulomb phase will show a $1/r^2$ spatial dependence.

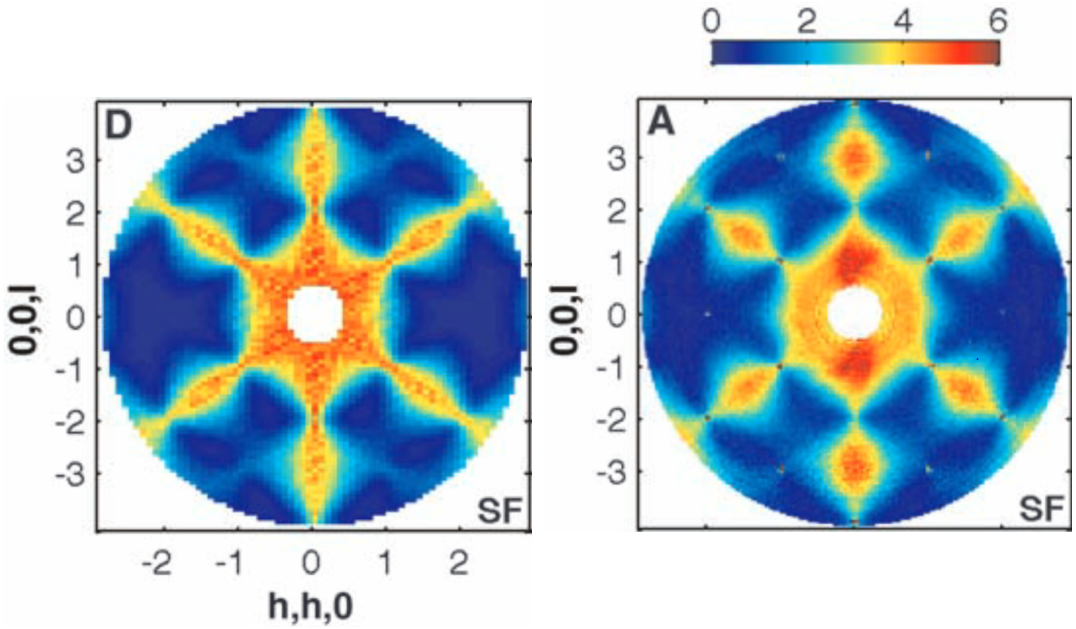


Figure 1.6: Calculated (left) and measured (right) pinch-points neutron scattering pattern, characteristic of a Coulomb phase. Figures from Ref. [18].

When the ice rules are obeyed, the system's total magnetization is constrained to be exactly zero. Dynamics and spin relaxation processes in spin ice can only be understood by considering defects that violate the ice rules. These defects occur when a spin is flipped out of the ice rule, creating a pair of neighboring excited tetrahedra: one in a 3-in/1-out configuration (positive magnetic charge) and the other in 1-in/3-out (negative magnetic charge). These defects will host magnetic local charges, which can move from site to site without the creation of new defects [19].

Such excitations, are always created in pairs for an energy cost of $4J_{\text{eff}}$, as each excited tetrahedron costs an energy of $2J_{\text{eff}}$. Higher energy configurations, like all-in/all-out tetrahedra, carry double magnetic charge forming double charge defects.

These defects can be described as magnetic quasiparticle excitations. Nevertheless, in the NNSI model, they are not "true" magnetic monopoles, because they do not interact through a Coulomb interaction but through an entropic interaction. When going beyond this model and considering the dipolar interactions it was shown that these emergent quasiparticles can be described as magnetic monopoles [20]. Some compounds of the rare-earth pyrochlore family do realize this dipolar spin ice state and host magnetic monopoles.

## 1.2 Rare-earth pyrochlore oxides

The materials studied in this thesis belongs to the pyrochlore family of rare-earth oxides of formula $R_2M_2O_7$, with $R^{3+}$ a trivalent rare-earth ion and $M^{4+}$ a tetravalent metal ion [21]. These compounds crystallize in the space group $Fd\bar{3}m$ (No. 227), where

the $R^{3+}$ and $M^{4+}$ ions are arranged on two distinct pyrochlore sublattices. These are shown in blue ($R$) and red ($M$) in Figure 1.7. The two tridimensional $R$ and $M$ sublattices, composed of corner-sharing tetrahedra, are interpenetrated and related by translational symmetry. There are two distinct oxygen sites in the structure, which influence the single-ion physics of both $R$ and $M$ atoms due to electrostatic and covalent bonding effects.

A wide variety of rare-earth and metal combinations can realize this structure. Historically, early studies focused on pyrochlores where only the rare-earth ion was magnetic. These systems already exhibited a broad range of magnetic ground states, some of which remain not fully understood until now. More recently, pyrochlore compounds in which a magnetic metal ion is included have been thoroughly studied, offering new exotic magnetic ground states to explore due to the magnetic interactions between the two sublattices [21–25]. The relative simplicity of the pyrochlore lattice allowed the scientific community to explore refined theoretical models that describe the experimental findings with success.

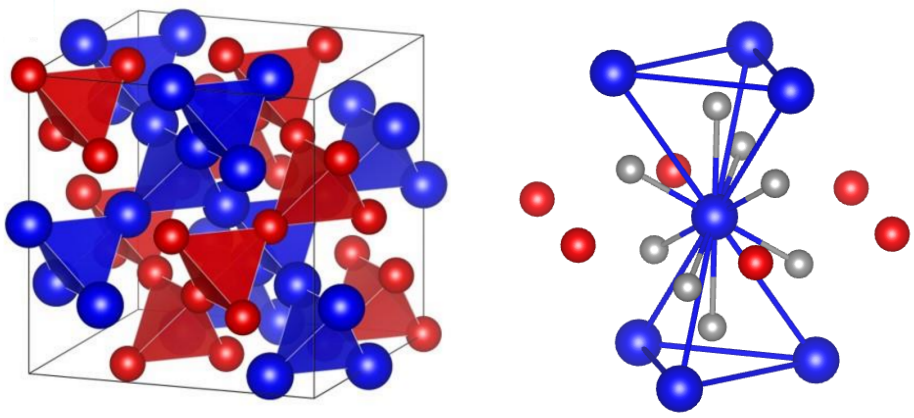

Figure 1.7: Left: The two rare-earth (blue) and metal ion (red) pyrochlore sublattices of the $Fd\bar{3}m$ pyrochlore structure. Right: Local environment of a rare-earth ion (blue) consisting of 6 first neighbor metal ions (red) and 8 oxygen ions (grey).

The different ground states observed in these systems depends on two main factors: the single-ion anisotropy and the magnetic interactions [26]. The lowest energy state of a multi-electron ion is determined when the Coulomb and spin-orbit energies are minimized according to the empirical Hund's rule [27]. In rare-earth ions, the large spin-orbit coupling makes the total angular momentum $J = L + S$ a good quantum number. The ion's ground state is typically composed of the lowest-energy multiplet $|J, m_J\rangle$, with total angular momentum $J$ and a total $(2J+1)$ degeneracy. The octahedral environment of surrounding oxygen atoms, shown in Figure 1.7, lifts the $(2J+1)$ degeneracy by inducing a local crystal electric field (CEF). For most rare-earth pyrochlore materials, the lowest energy states take the form of a doublet well separated from the higher energy excited states.

The states of the ground state doublet is a mixture of $|\pm m_J\rangle$ states, whose physics can be effectively described by a pseudospin operator $\mathbf{S}$. In pyrochlore materials, the $S^z$ pseudospin component is aligned along the local $\langle 111 \rangle$ axis connecting the center of two tetrahedra, while the $S^x$ and $S^y$ components are in the plane perpendicular to the $\langle 111 \rangle$

axis.

The symmetry properties of the $|\pm m_J\rangle$ states forming the doublet determine the anisotropic $g$-factor, which defines the magnetic moment $\mathbf{m}_i$ of the ion at position $i$ as [26]:

$$\mathbf{m}_i = -\mu_B[g_z \mathbf{z}_i S_i^z + g_\pm(\mathbf{x}_i S_i^x + \mathbf{y}_\mathbf{i} S_i^y)] \tag{1.6}$$

where $\mathbf{x}_i, \mathbf{y}_i, \mathbf{z}_i$ are unitary vectors of the local frame at a site $i$ with $\mathbf{z}_i$ aligned along $\langle 111 \rangle$.

Three different types of pseudospin anisotropies, illustrated in Figure 1.8, can be found depending on the rare-earth elements. The first one is the Heisenberg anisotropy where the spins can freely explore a sphere space of positions ($g_\pm \approx g_z$). The second one is the XY anisotropy where the spins are located entirely in the local planes perpendicular to the $z$ direction ($g_\pm \gg g_z$). Finally, the last one is the Ising anisotropy where the moment lies entirely along the local $z$ direction and can either be pointing inward or outward a tetrahedron ($g_z \gg g_\pm$).

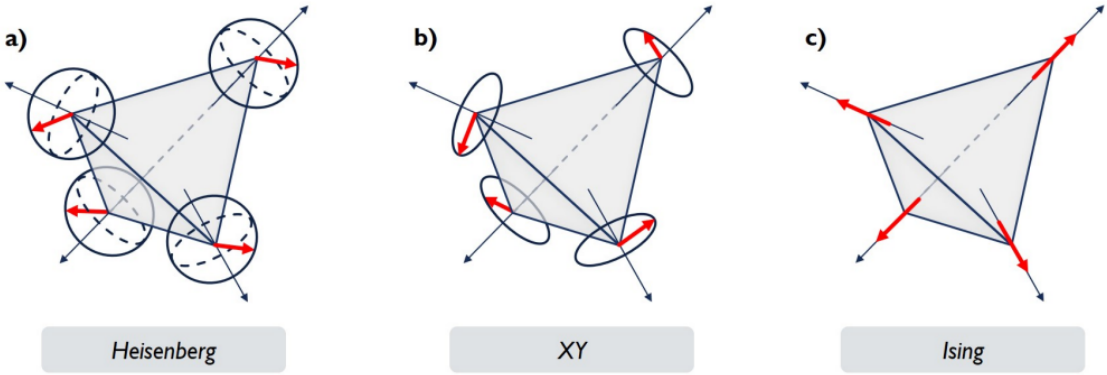


Figure 1.8: Schematic of the three spin anisotropies found in pyrochlore compounds: a) Heisenberg, b) XY and c) Ising. Figure from Ref. [8].

The two families of compounds studied in this thesis both exhibit strong rare-earth Ising spin anisotropies. However, even for the same single-ion anisotropy, the observed ground state and the associated properties are entirely different.

The first family shows an effective ferromagnetic coupling between the rare-earth ions which results in the frustrated spin ice ground state. This family includes various compounds such as $Ho_2Ti_2O_7$, $Dy_2Ti_2O_7$, $Ho_2Sn_2O_7$ and $Dy_2Sn_2O_7$ [10, 14, 28]. Our focus in this thesis is on the two most extensively studied members of this family: $Ho_2Ti_2O_7$ and $Dy_2Ti_2O_7$, which can be grown as large single crystals.

The second family is the Nd-based pyrochlores, where the magnetic interactions stabilize an unfrustrated all-in/all-out (AIAO) long range order with exotic ground state doublet symmetries. We investigate two compounds, $Nd_2Ir_2O_7$ and $Nd_2Ru_2O_7$, in which the transition metal ion is also magnetic, and is expected to disturb the ordering of the Nd sublattice.

We begin discussing the physics of the spin ice materials $Dy_2Ti_2O_7$ and $Ho_2Ti_2O_7$, introducing both experimental results and the theoretical models used to described their

physics. In this context, we then present our motivations and the experimental investigations we aimed to perform for this thesis. Afterward, we turn to the Nd-based pyrochlores, reviewing the current literature understanding and then motivating our own studies of these systems.

## 1.3 Spin ice materials

The concepts introduced in this section are the most essential and relevant for understanding the studies conducted in this PhD. An exhaustive and detailed description of spin ice physics can be found in Ref. [29].

### 1.3.1 Dipolar spin ice

The exchange coupling between rare-earth ions is very weak ($J \sim 1$ K) as the valence leaves a unfilled 4f shell that is screened by the 5s, 5p and 6s orbitals. For comparison, in transition metals ions, the exchange interaction is typically much stronger with $J \sim 10^2$ K. In the rare-earth ions $Ho^{3+}$ and $Dy^{3+}$, dipolar interactions are particularly important due to their very large magnetic moment, approximately $10\mu_B$, making these interactions non-negligible [30, 31].

The relevant Hamiltonian for spin ice materials, like $Dy_2Ti_2O_7$ and $Ho_2Ti_2O_7$, is composed by the sum of these two interactions and is called the dipolar spin ice (DSI) Hamiltonian:

$$\mathscr{H} = -J \sum_{\langle i,j \rangle} \mathbf{S}_i \cdot \mathbf{S}_j + D r_{\text{nn}}^3 \sum_{i>j} \left[ \frac{\mathbf{S}_i \cdot \mathbf{S}_j}{|\mathbf{r}_{ij}|^3} - \frac{3(\mathbf{S}_i \cdot \mathbf{r}_{ij})(\mathbf{S}_j \cdot \mathbf{r}_{ij})}{|\mathbf{r}_{ij}|^5} \right] \tag{1.7}$$

with $J$ the exchange coupling constant, $D$ the dipolar coupling constant, and $r_{nn}$ the nearest-neighbor distance between rare-earth ions. $D$ is defined by the strength of the moment $\mu$ through the standard magnetic dipole-dipole interaction:

$$D = \frac{\mu_0 \mu^2}{4\pi r_{\text{nn}}^3} \tag{1.8}$$

The only free parameter in the DSI model is $J$ which is obtained by comparison between Monte Carlo simulations and experimental observables like specific heat, neutron scattering or magnetization [32, 33].

In order to consider the combined effects of exchange and dipolar interactions, it is useful to define an effective nearest-neighbor coupling $J_{\text{eff}}$ for Ising spins $\sigma$:

$$J_{\text{eff}} = J_{\text{nn}} + D_{\text{nn}} = \frac{J + 5D}{3} \quad \text{and} \quad \mathscr{H}_{\text{nn}} = -3J_{\text{eff}} \sum_{\langle i,j \rangle} \mathbf{S}_i \cdot \mathbf{S}_j = J_{\text{eff}} \sum_{\langle i,j \rangle} \sigma_i \sigma_j \tag{1.9}$$

where $J_{\text{nn}} = J/3$ is the nearest-neighbor exchange between $\langle 111 \rangle$ Ising spins, and $D_{\text{nn}} = 5D/3$ is the dipole-dipole interaction at nearest-neighbor distance.

In $Dy_2Ti_2O_7$ and $Ho_2Ti_2O_7$, Monte-Carlo fits to specific heat measurements yield antiferromagnetic values for $J$, which would typically favor a long-range magnetic order. However, their nearest-neighbor dipole-dipole interaction $D_{\text{nn}}$ is ferromagnetic and strong

enough to counter-balance the antiferromagnetic exchange, leading to a ferromagnetic effective coupling. The coupling values for the nearest-neighbor DSI model are summarized in Table 1.1.

| | $D$ | $D_{\text{nn}}$ | $J$ | $J_{\text{nn}}$ | $J_{\text{eff}}$ |
|---|---|---|---|---|---|
| $Dy_2Ti_2O_7$ | 1.41 | 2.35 | $-3.72$ | $-1.24$ | 1.1 |
| $Ho_2Ti_2O_7$ | 1.41 | 2.35 | $-1.65$ | $-0.52$ | 1.8 |

Table 1.1: Nearest neighbor interactions deduced from the exchange and dipolar coupling constant along with the resulting nearest neighbor effective coupling in K [31, 33].

The nearest neighbor DSI model is equivalent to the NNSI model introduced earlier (Equation 1.1.2), where the effective ferromagnetic coupling gives rise to frustration, stabilizing the spin ice state in the $Dy_2Ti_2O_7$ and $Ho_2Ti_2O_7$ compounds. When long-range dipolar interactions beyond nearest-neighbors are included, one would expect the anisotropic and long-range nature of these interactions to impose energy constraints on the spin ice state which would lift the ground state degeneracies at a temperature of the order of the dipolar constant $D$. However, the degeneracy of the spin ice state is largely maintained as long-range interactions are almost perfectly screened [34, 35].

The small residual unscreened contribution of the dipolar interactions creates a really small splitting of the Pauling states resulting in a finite bandwidth of states. At sufficiently low temperatures ($\sim 180$ mK), this small energy scale becomes relevant, and a transition to a long-range ordered ground state is theoretically predicted [36].

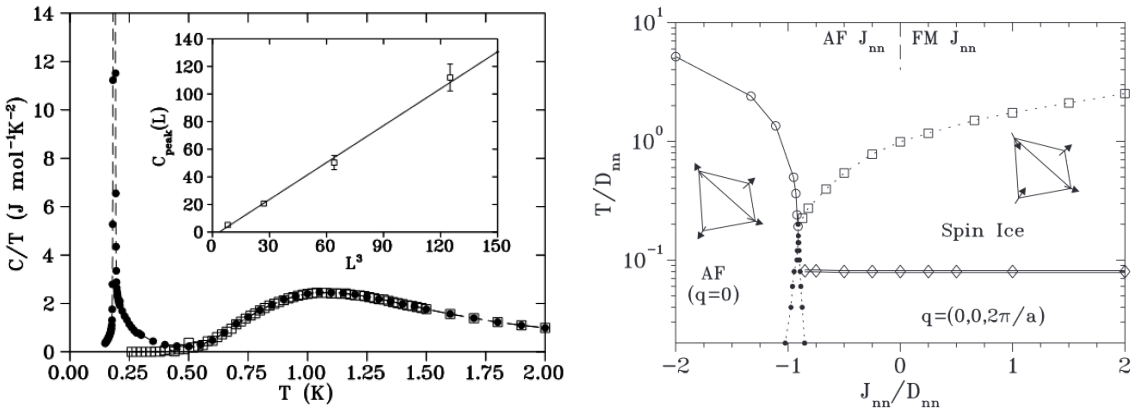


(a) (b)

Figure 1.9: (a) Specific heat data from Monte Carlo simulations of the DSI model using single spin flips (square) and single spin flips with loop moves (circles). Inset : Finite size scaling of the specific heat peak with the expected behavior for a first order phase transition. Figure from Ref. [36]. (b) Phase diagram of the DSI model in zero applied field with the antiferromagnetic AIAO ordered state, the spin ice state and the predicted $\mathbf{q} = (0,0,2\pi/a)$ ordered ground state. Figure from Ref. [32].

This predicted order was observed in DSI Monte Carlo calculations of specific heat using an algorithm that, in addition to single spin flips, includes loop moves. These

loop moves enable transitions between the different Pauling states, allowing the system to explore the degenerate spin ice manifold. Figure 1.9 (a) shows the calculated specific heat with this method, revealing a sharp transition peak at 180 mK. For comparison, the calculated curve obtained using an algorithm with only single spin flip moves is shown, in this case the order is not captured because the system remains blocked in a local minimum.

The predicted long-range ordered ground state has been investigated but not observed until one study reported its possible detection through specific-heat measurements [37]. However, these results were strongly debated, and more recent studies have shown that such order remains unobservable even after very long waiting times at low temperatures [38, 39]. The absence of measured order is due to a freezing of the dynamics which prevents the system from reaching its equilibrium state.

The zero field phase diagram of the DSI model, shown in Figure 1.9 (b), includes four different phases: a high temperature paramagnetic phase, the spin ice state, the AIAO ordered phase and the low temperature long-range ordered state characterized by $\mathbf{q} = (0,0,2\pi/a)$, which is due to the dipolar induced splitting of the Pauling states. Nowadays, to reproduce more accurately experimental results, a generalized dipolar spin ice model (g-DSM) including additional $J_2$ second-neighbor and $J_3$, $J_3'$ third-nearest-neighbor exchange couplings is commonly employed [38, 40].

### 1.3.2 Magnetic monopoles: the dumbbell model

The dynamics of spin ice are governed by the excitations of its ground state, which take the form of defects that locally violate the ice rule. When dipolar interactions are taken into account, these spin defects fractionalize into magnetic monopoles possessing the necessary long-distance interaction properties [20]. The monopole picture naturally emerges in the context of the dumbbell model, illustrated in Figure 1.10, in which each spin in the dipolar spin ice (DSI) model is represented as a pair of opposite magnetic charges forming a "dumbbell". The charge of a given tetrahedron can be defined as the sum of the charges at the extremity of each dumbbell belonging to this tetrahedron.

The lattice formed by the centers of the tetrahedra, parent to the pyrochlore lattice, is a diamond lattice and its vertices host the spins magnetic charges of magnitude $q = \pm\mu/r$, where $\mu$ is the magnetic moment and $r = \sqrt{\frac{3}{2}} r_{nn}$ is the diamond lattice bond length. Once created, 3-in/1-out and 3-out/1-in defects carry an excess of positive or negative magnetic charge $Q = \pm 2q$, while all-in and all-out defects carry twice that magnetic charge $Q = \pm 4q$. These excitations behave as quasi-particle magnetic monopoles, because they interact via a long-range Coulomb interaction and are accompanied with the creation of a magnetic field line called "Dirac string" (which is not the case for the nearest neighbor spin ice model).

The energy of a monopole configuration in the dumbbell model is calculated as a pairwise sum of monopole interactions which follows the magnetic Coulomb law on a diamond lattice [20]:

$$\mathscr{H}_{\text{Dumbbell}} = \frac{1}{2} v_0 \sum_{\alpha} Q_{\alpha}^2 + \frac{\mu_0}{4\pi} \sum_{\alpha \neq \beta} \frac{Q_{\alpha} Q_{\beta}}{|\mathbf{r}_{\alpha\beta}|} \tag{1.10}$$

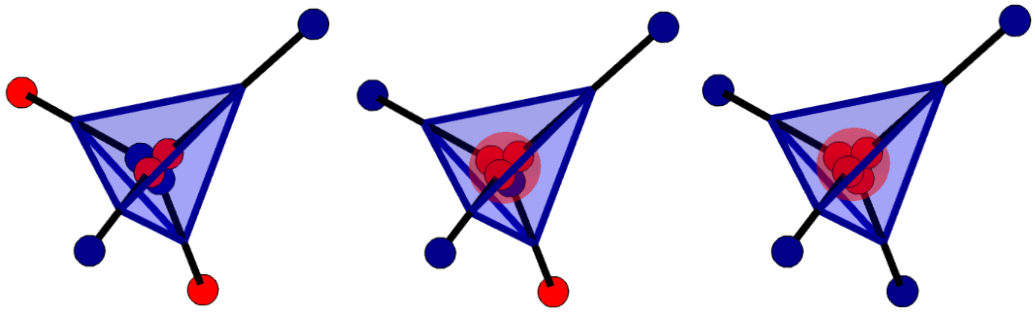

Figure 1.10: Schematic of the dumbbell model: each spin is seen as two opposite charges (a magnetic dumbbell) sitting on the vertices of the diamond lattice (dashed lines). From left to right: (i) 2-in/2-out configuration with no net magnetic charge. (ii) 1-in/3-out configuration where the ice rule is broken, the sum of magnetic charges at the center of tetrahedron is $Q = +2q$. (iii) all-out configuration, the sum of magnetic charges is doubled with $Q = +4q$.

The first term accounts for the on-site energy required to create monopoles and is necessary to reproduced correctly the nearest-neighbor interaction. It is controlled by the parameter $\nu_0$ that can be derived from the coupling constants of the DSI model:

$$\nu_0 \left(\frac{\mu}{r}\right)^2 = \frac{J}{3} + \frac{4}{3}\left[1 + \sqrt{\frac{2}{3}}\right] D \tag{1.11}$$

where $\nu_0$ is defined by the dipolar and exchange couplings along with the magnetic moment $\mu_0$ and the first neighbor distance $r$. Once created, the scale of the Coulomb interaction between monopoles is set only by $\mu$ and $r$.

These magnetic monopoles behave as a gas of charged particles on the diamond lattice, described by a statistical grand canonical ensemble. Their motion and dynamics, which can be probed using neutron scattering or bulk magnetometry, are influenced by both Coulomb correlations and local constraints imposed by the underlying spin ice rules.

Despite its elegance, the dumbbell model does not directly map onto the DSI model, since the $1/r^5$ terms of the dipolar interactions are neglected. These corrections are small and become relevant only at very low temperatures, where the dumbbell model fails to capture the ordering predicted by the DSI model. For very low temperature investigations, it is therefore preferred to use the DSI model, although the dynamics are still often discussed in terms of monopoles. Even after years of extensive studies, the correlated motion of monopoles is not entirely understood, particularly at low temperatures.

### 1.3.3 Spin ice dynamics: equilibrium

#### Spin ice dynamical regimes

The study of the dynamical properties of spin ice compounds began with magnetization and susceptibility measurements performed in the early 2000s, shortly after the discovery of the $Dy_2Ti_2O_7$ compound [41–43]. These experiments revealed a clear peak in

the dissipative part of the ac susceptibility $\chi''(f)$, characteristic of the magnetic relaxation timescale $\tau$, which is shifted toward low frequencies with decreasing temperature.

The relaxation timescale, shown in Figure 1.11 (a), displays three distinct dynamical regimes: above 15 K it follows a thermally activated Arrhenius behavior, between 15 K and 2 K it enters an intermediate regime nearly independent of temperature, and below 2 K it increases rapidly, diverging toward really long timescales.

In the high temperature Arrhenius regime, the spin flip process was immediately attributed to thermal activation over the anisotropy energy barrier, directly associated to the first excited CEF level ( $\sim$ 200-300 K). Below 15 K, the thermal energy becomes insufficient for the spins to overcome the CEF energy barrier. Instead, the spin relaxation can only occur by quantum tunneling through the energy barrier [44, 45]. The quasi-independent temperature behavior of $\tau$ in this regime supports this idea. Similar relaxation effects were found previously in molecular magnets where quantum tunneling governs spin flip processes [46].

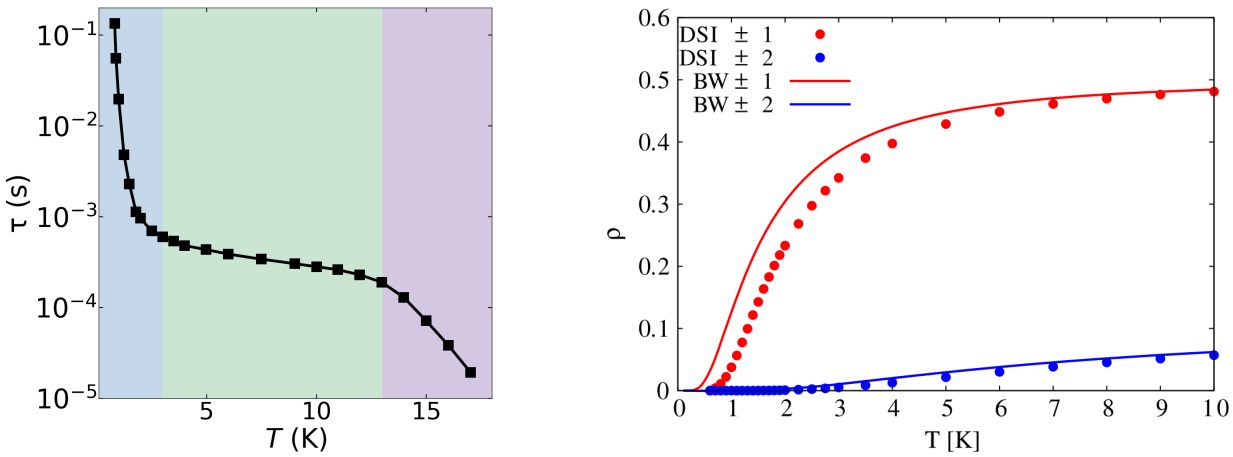


(a) (b)

Figure 1.11: (a) Measured relaxation time $\tau$ with respect to temperature in $Dy_2Ti_2O_7$. The three dynamical regimes are highlighted with different colored backgrounds: (i) thermal regime (purple), (ii) quasiplateau regime (green), (iii) low temperature $\tau$ diverging regime (blue). Figure adapted from Ref. [43]. (b) Density of monopoles $\rho$ with respect to temperature for the DSI model (circles) and the expected Boltzmann weight for the NNSI model for $Dy_2Ti_2O_7$ (line). The density of 3 in-1 out and 3 out-1 in defects are in red and the AIAO defects are in blue. Figure from Ref. [47].

In the intermediate regime, and in the absence of interactions, the system would behave as a paramagnet with a relaxation time $\tau$ that is temperature independent and equal to the intrinsic tunneling time $\tau_0$. When interactions are present, however, the relaxation time follows an Arrhenius law, $\tau = \tau_0 \exp(E/T)$, where $E$ corresponds to the energy cost of the process. In the NNSI model, as defect creation and annihilation (3-in/1-out or 1-in/3-out configurations) requires an energy cost of $4J_{\text{eff}}$ (a single spin flip creating two defects), we would expect the Arrhenius behavior to be governed by this energy barrier $E = 4J_{\text{eff}}$.

However it was found from experimental data for $Dy_2Ti_2O_7$ that, in the plateau regime, the energy cost is closer to $2J_{\text{eff}}$ [43, 48]. This discrepancy is resolved by the NNSI model when including higher energy single spin flip processes with their associated probabilities. The mean energy barrier calculated by taking into account the Boltzmann weights of each different process is $E \approx 2J_{\text{eff}}$, as expected from experiments.

In the low temperature regime, below 2-3 K, the measured divergence of the relaxation time cannot be captured by the Arrhenius law. It is because Coulomb interactions between monopoles accelerate the decrease of the monopole density compared to the NNSI model, as shown in Figure 1.11(b). The exponential fall in monopole concentration is what is driving the anomalous increase of the relaxation timescale and results in a freezing of the spins on laboratory timescales [43].

Monte Carlo simulations of the DSI or the dumbbell model are able to reproduce quantitatively the dynamics down to 1 K with only one fitting parameter: the tunneling spin flip rate or $\tau_0$ [47]. The Monte Carlo timescale is adjusted to the tunneling rate of the experimental data in the intermediate temperature regime where Coulomb interactions are negligible. These simulations agree better with experimental data than the non-interacting NNSI model, reinforcing the significance of dipolar interactions and validating the monopole picture.

Studying the relaxation time temperature behavior, the dynamics of spin ice has proven to be rich and full of subtleties. The shape of the ac susceptibility curves from which the relaxation time $\tau$ is extracted also gives valuable information on the dynamics. In both $Dy_2Ti_2O_7$ and $Ho_2Ti_2O_7$, it was found that the dissipative ac susceptibility peak exhibits an asymmetric shape, suggesting that the dynamics cannot be attributed to a single relaxation process [49, 50]. Empirical models using multiple relaxation times or distribution of times can be used to obtain a phenomenological description of the dynamics [51].

#### Quantum tunneling times $\tau_0$

The origin of the magnitude of the quantum tunneling times $\tau_0$ and its variations across different spin ice compounds is still discussed. Explaining the origin of $\tau_0$ requires going beyond the ground-state doublet approximation by accounting for higher orders of the CEF Hamiltonian. In addition to the CEF, the dipolar and exchange interactions act as local magnetic fields that disturb the single-ion behavior, increasing the energy splitting of the ground state doublet. The magnitude of this splitting is directly inversely proportional to the the characteristic timescale $\tau_0$ [52]. In the small field limit, Kramers ions ($Dy^{3+}$) and non-Kramers ions ($Ho^{3+}$) exhibit different transverse field behaviors, with $Ho^{3+}$ being more sensitive to the perturbation.

At low temperatures, the spin dynamics is governed solely by monopole hopping, as monopole creation and annihilation are suppressed. Calculations of internal field distributions can show that spins from 2-in/2-out tetrahedra experience local longitudinal fields generated by interactions with neighboring spins [54]. These local fields prevent tunneling spin flip events, effectively freezing the spins. The vast majority of spin is thus frozen and only some of the spins adjacent to a monopole experience non-longitudinal fields, allowing tunneling.

When looking at the four spins of a tetrahedron hosting a monopole in the 3-in/1-out

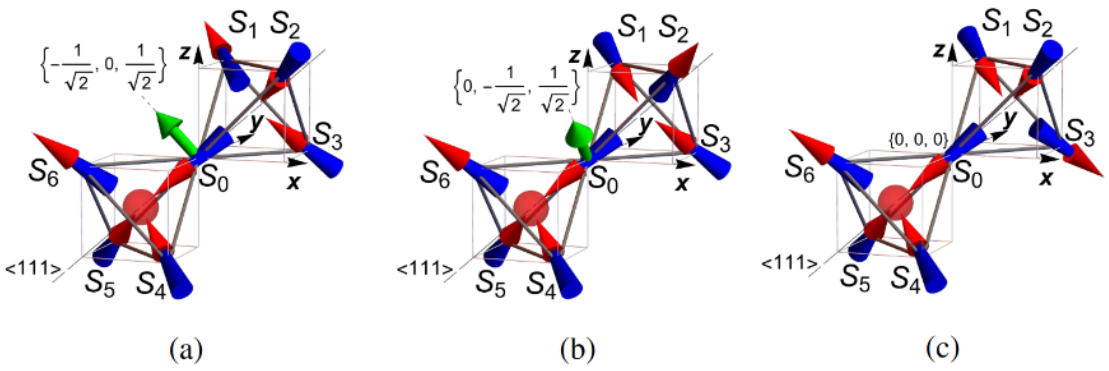


Figure 1.12: The three configurations of non-frozen spins experiencing non-longitudinal fields. In the two first configurations (a)-(b) the spin is subject to a local transverse field of 0.45 T (in green). The third configuration (c) is subject to a vanishing local transverse field of $\sim 0.03$ T. The configurations verify a bimodal distribution with 2/3 experiencing local transverse field and 1/3 the vanishing local transverse field. Figure from Ref. [53].

configuration, it appears that the "pointing out-spin" cannot be flipped as it would necessitate an energy cost (creation of a double monopole). The three other are unfrozen spins, where the local dipolar and exchange interactions create a bimodal distribution of transverse fields. Within the different configurations of unfrozen spins, shown in Figure 1.12, 1/3 of the configurations are subject to a vanishing local transverse field ($\sim 0.03$ T), while the other 2/3 feel a transverse field of the order of 0.45 T [53]. The tunneling time rate of the transverse field configurations is greatly enhanced compared to the vanishing field configurations, creating two distinct relaxation times. The magnitude of the timescales and the separation between the "slow" ($\tau_{slow}$) and "fast" ($\tau_{fast}$) processes depend on the combination of the dipolar, exchange constants and the single-ion CEF scheme.

Recent $Dy_2Ti_2O_7$ noise measurements [55] were reproduced with a modified g-DSM Monte Carlo model taking into account the bimodal separation of the tunneling times (called bSM) [56]. In that study, the slow-relaxing spins (with vanishing transverse fields) were treated as static, as their relaxation times lie beyond the experimental window. This new model gives better agreement with the experimental data than the previous models (called SM), as shown in Figure 1.13, demonstrating that the monopole dynamics is even more constrained than previously thought. From these new constraints, they proposed that monopoles behave as an interacting gas of charge particles evolving on a real space of reduced dimensionality (effective dimension $\approx 1.85$) according to a fractal pattern.

Further investigations using this model could lead to a better understanding of the spin ice dynamics and especially the one of the $Ho_2Ti_2O_7$ compound which has recently been discovered to be more complex than expected. Indeed two distinct relaxation timescales were experimentally observed in $Ho_2Ti_2O_7$ through ac susceptibility and neutron scattering data, thanks to an access to higher frequencies [57].

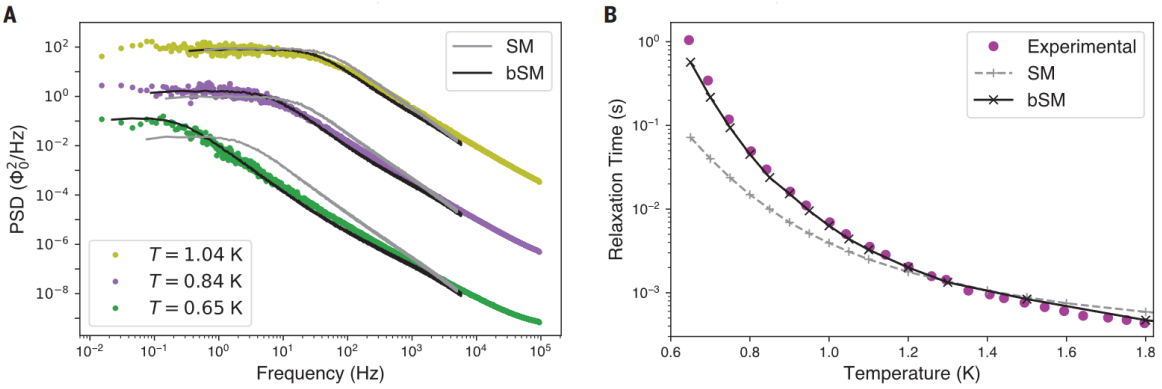


Figure 1.13: (A) Measured magnetic noise power spectral density (PSD) with respect to frequency in $Dy_2Ti_2O_7$ at three distinct temperatures measured in Ref. [55]. Monte Carlo simulation fits a g-DSM model without taking into account the bimodal distribution (SM in grey) or by taking into account the bimodal distribution (bSM in black). (B) Experimental relaxation time (purple) along with the $\tau$ extracted from the SM fits (grey) and bSM fits (black). Figures from Ref. [56].

### 1.3.4 Spin ice dynamics: out-of-equilibrium

When entering the low temperature regime of spin ice, the system freezes in a glassy state, evidenced by the splitting of Zero Field-Cooled (ZFC) Field-Cooled (FC) magnetization curves (Figure 1.14 (a)) [43]. This freezing occurs at approximately 600 mK and indicates that the dynamics enters in a non-ergodic regime, where the system falls out of equilibrium. Interestingly, the properties of the frozen spin ice state differs strongly from the properties of a spin glass system. In particular, the ac susceptibility dynamics in spin ice still shows a well-defined relaxation process, in opposition to the broad distribution of relaxation times characteristic of a spin glass near its transition. Additionally, there is no structural or interaction disorder in spin ice (at least in a first approximation), so the nature of the spin ice out-of-equilibrium regime is definitely distinct.

The properties of the spin ice state in the out-of-equilibrium regime are both difficult to probe and model. On the experimental side, the relaxation timescales become too slow for conventional ac susceptibility measurements, and the low monopole density requires highly sensitive flux detection. Theoretically, the low monopole density necessitates very large system sizes, leading to long computation times.

Nevertheless, theoretical studies reported the possibility of trapping a high density of monopoles at low temperatures using rapid thermal quenches [58]. Under such protocol, pairs of monopoles of opposite charge form non-contractible pairs, where the two monopoles are constrained by their own Coulomb interaction. Figure 1.14(b) shows the density of monopoles after a rapid quench with respect to time. It reveals that the non-contractible pair can live on longer times than free monopoles at low temperature.

Experimentally, such high-density monopole states have been created down to 60 mK using a method known as the Avalanche Quench Protocol [59]. The monopole current $J$ driven by an applied magnetic field $H$ was studied at low temperature for those high density states. $J$ showed good agreement to the expected $\sim \exp\{\sqrt{H}\}$ dependence

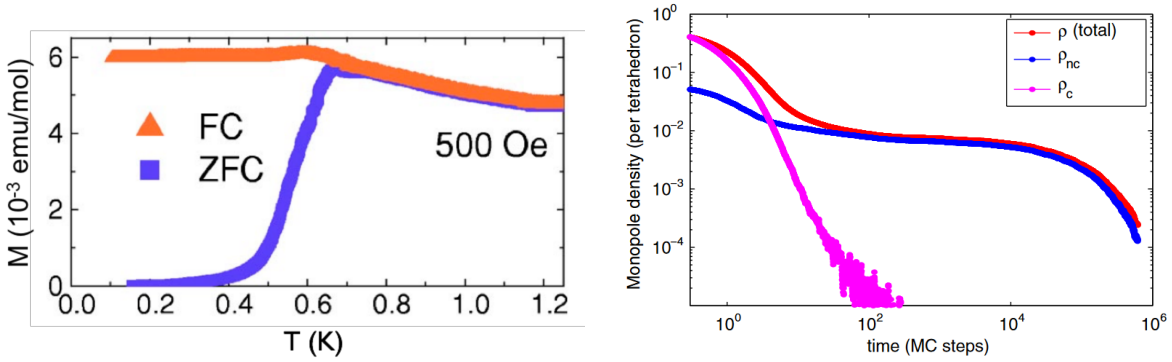


(a) (b)

Figure 1.14: (a) Zero Field-Cooled (ZFC) - Field-Cooled (FC) splitting of the measured magnetization curves in $Dy_2Ti_2O_7$ at an applied field of 500 Oe from Ref. [43]. (b) Monte Carlo simulated density of monopoles with respect to time at $T = 0.125$K after a thermal quench. The total density of monopoles $\rho$ (red curve) is the sum of the contractible monopole pair density $\rho_c$ (pink curve) and the non-contractible monopole pair density $\rho_{nc}$ (blue curve). Figure from Ref. [58].

(Figure 1.15), consistent with the unbinding of non-contractible monopole pairs under Coulomb interaction at temperatures below 300 mK [60]. At higher temperatures, the current curves exhibit a Wien effect, characteristic of the field response of a mixed population of vacuum 2-in/2-out states, bound pairs, and free monopoles [61, 62].

These studies of the out-of-equilibrium dynamics proved once again the strength of the monopole description of spin ice. However, they require applying external magnetic fields, which disturb the low-temperature spin ice state by forcing monopoles to move along specific paths. To probe the intrinsic monopole dynamics without applying an external field, one solution is to directly measure the spontaneous fluctuations of the magnetization with respect to time. This technique requires a low residual field environment and a highly sensitive detection of magnetic flux, which is made possible thanks to SQUID amplifier devices. Such techniques were first introduced to condensed matter in the study of spin glass materials [63, 64].

### 1.3.5 Noise and FDT for out-of-equilibrium properties

As briefly mentioned earlier, noise measurement techniques were recently introduced to spin ice materials to study the equilibrium spin ice regime between 4.2 K and 600 mK, giving new successful insights [56, 65]. Theoretically, noise is strictly equivalent to ac susceptibility in equilibrium and simply provides an alternative way of addressing the dynamics. However, one of the major interests in noise measurements lies in their ability to explore the out-of-equilibrium regime. A previous set of measurements investigated noise in the very low-temperature regime of spin ice, though without a quantitative understanding of the dynamics [55].

Combined with ac susceptibility measurements, noise measurements allow a direct test of the Fluctuation–Dissipation Theorem (FDT). The FDT states that, when a sys-

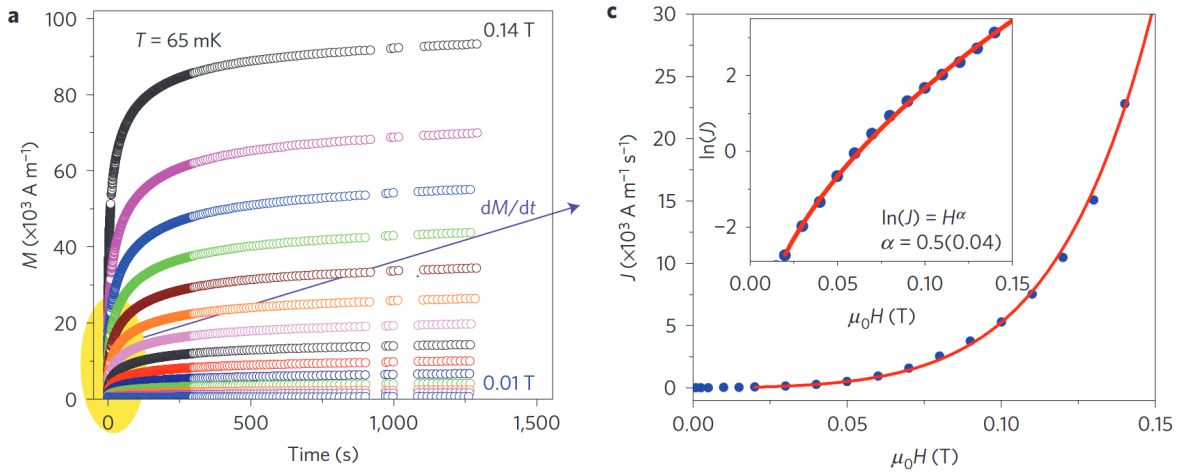


Figure 1.15: (a) Magnetization $M$ vs time $t$ at 60 mK for fields between 100 and 1400 Oe in steps of 100 Oe. (b) Monopole current $J = \partial M/\partial t$ vs field at 65 mK. The line is a fit to $J = a\exp\left\{\sqrt{\beta_C H}\right\}$ expected for unbinding of pair of particles interacting with Coulomb interaction. Figures from Ref. [60].

tem is in thermodynamic equilibrium, fluctuations (magnetic noise) are directly related to dissipation (ac susceptibility). However, when the system is out of equilibrium, deviations from the FDT can be expected. The behavior of these deviations are studied from the Fluctuation-Dissipation Relation (FDR), and can be interpreted in terms of an effective temperature, providing quantitative information about the nature of the out-of-equilibrium processes at play [66].

The FDT for non-equilibrium dynamics has been studied in a wide variety of systems including structural glasses, colloids or liquid crystals for instance [67–69]. In the context of magnetism, it has been mainly studied in spin glasses system and deviations to the FDT where successfully measured as shown in the parametric fluctuation dissipation plot in Figure 1.16(a) [70].

These properties have already been investigated theoretically in spin ice materials using the dumbbell model. It was shown that the FDT is obeyed down to 400 mK when the system is allowed to reach local equilibrium [71]. Nonetheless, using a rapid quench protocol, deviations from the FDR were observed at 100 mK (Figure 1.16(b)), associated with the dynamics of an excess of monopoles in the non-contractible pair regime.

In the dumbbell model the Pauling states are degenerate, but the results for experimental measurements may differ due to the splitting of the band of these low energy states when considering the more realistic DSI model [36]. The development of hierarchical dynamics through the existence of closed loops moving the system between Pauling states of different energies may appears around 150 mK.

These fundamental questions about the true spin ice materials ground state are still left unanswered. Low temperature noise and ac susceptibility measurements could be key to deepen our understanding of this regime. The first objective of this thesis is to improve and complete the development of an extremely sensitive noise magnetometer, started by Vadim Cathelin and Carley Paulsen [72]. This instrument will enable precise

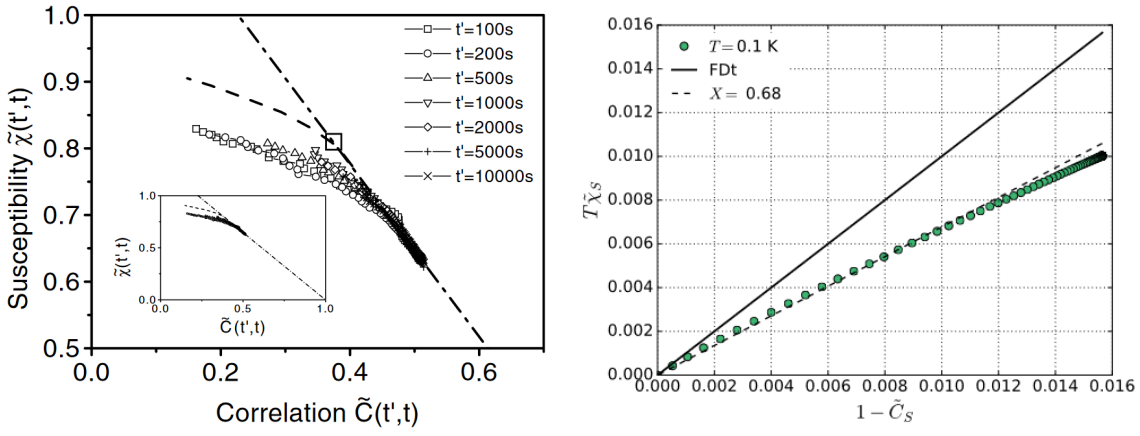


(a) (b)

Figure 1.16: (a) Fluctuation dissipation parametric plot susceptibility versus correlation, measured for different waiting times after quench passing through the glass temperature $T_g$ at $T = 0.8T_g$ in the spin glass compound $CdCr_1.7In_0.3S_4$. Departure to the FDT behavior, represented by the dot-dashed line, is observed. Figure from Ref. [70]. (b) Fluctuation dissipation plot calculated from Monte Carlo simulations of the dumbbell model for $Dy_2Ti_2O_7$ coupling parameters at $T = 100$ mK after a rapid quench. The solid black line represents the equilibrium FDT behavior. Figure from Ref. [71].

FDR measurements and allow a deeper investigation of spin ice dynamics. Both the equilibrium and out-of-equilibrium regimes will be investigated using this novel technique on the two most extensively studied spin ice compounds: $Ho_2Ti_2O_7$ and $Dy_2Ti_2O_7$.

## 1.4 Nd-based pyrochlores

For many years, the search for systems realizing a Quantum Spin Liquid (QSL) ground state has strongly driven the frustrated magnetism community [73]. The pyrochlore structure has been theoretically proposed as a host for Quantum Spin Ice (QSI) states, a specific type of QSL characterized by novel and intriguing excitations [74, 75]. These QSI states appear in systems where the rare-earth ion possesses an Ising character (as in classical spin ice), with in addition transverse quantum effects. In this context, rare-earth ions with "dipolar–octupolar" (DO) doublets have attracted great interest. The $Nd^{3+}$ ion possesses this exotic DO character, and intriguing new physics has been discovered in Nd-based pyrochlores. This section aims to present the necessary concepts for understanding the physics of this family of compounds and the work carried out on them during this PhD.

### 1.4.1 Dipolar Octupolar pyrochlores: the XYZ Hamiltonian

Nd-based pyrochlores are an intriguing family of compounds due to the unique properties of the $Nd^{3+}$ ion. As in $Dy_2Ti_2O_7$ and $Ho_2Ti_2O_7$, the ground state doublet is

well separated from the first excited state compared to the energy scale of the exchange interactions. Consequently, this doublet can be described by an effective pseudo-spin 1/2.

However, for Kramers ions with an odd number of electrons under specific CEF constraints (such as Ce, Nd, Sm, Dy), the pseudo-spin 1/2 doublet $\tau_i = (\tau_i^x; \tau_i^y, \tau_i^z)$ transforms differently under symmetry operations compared to an usual pseudo-spin described by a pseudovector [76]. Namely, the $x$ and $z$ components transform like the $z$ component of a magnetic dipole, while the $y$ component transforms like a component of a magnetic octupole tensor.

Although the $x$ component transforms like a dipole, it is actually octupolar in nature, like the $y$ component. This means that they both couple very weakly to external perturbation. For instance, they do not respond to applied magnetic field and have a low intensity neutron structure factor located at large $Q$-vector. By contrast, the $z$ component is an usual dipolar moment and responds the usual way to external perturbations. However, this $z$-dipolar component still couples to the $x$-octupolar component because they transform identically.

Since the octupolar components do not couple to external magnetic fields, the on-site magnetization of this pseudospin doublet is given by:

$$\mathbf{m}_i = g_z \mu_B \tau_i^z \hat{\mathbf{z}}_i \tag{1.12}$$

where $\hat{\mathbf{z}}_i$ is a unit vector oriented along the local $\langle 111 \rangle$ axes, and $g_z$ is the $z$ component of the local $g$-tensor. Since the transverse $g_x$ and $g_y$ components of the $g$-tensor are zero, the anisotropy of the single-ion doublet is purely Ising and aligned along the local $z$-axes of the pyrochlore lattice.

This peculiar single-ion ground state doublet has been called "dipolar-octupolar" (DO) doublet, and the corresponding compounds are named DO pyrochlores. The most general Hamiltonian allowed from the symmetry properties of such doublets is quite concise and involves only four coupling parameters: $J_x, J_y, J_z$ and $J_{xz}$ [76]:

$$\mathscr{H}_{\text{DO}} = \sum_{\langle ij \rangle} \left[ J_x \tau_i^x \tau_j^x + J_y \tau_i^y \tau_j^y + J_z \tau_i^z \tau_j^z + J_{xz} \left( \tau_i^x \tau_j^z + \tau_i^z \tau_j^x \right) \right] \tag{1.13}$$

In the case of the $Dy^{3+}$ ion, the composition of the doublet gives the $J_z$ coupling to be highly dominant leading to a system that behaves like a classical Ising dipole [77]. The additional large dipolar coupling gives rise to the well-known spin ice state discussed earlier. For the other DO ions, the dipolar interaction can be neglected in a first approximation ($\sim 70$ mK for $Nd^{3+}$). The transverse octupolar $J_x$ and $J_y$ and the dipolar-octupolar $J_{xz}$ coupling parameters can be relevant, so the model cannot be further simplified.

A more convenient form of the DO Hamiltonian (Equation 1.13) can be obtained by rotating the local axes in the $(xz)$ plane to remove the $J_{xz}$ coupling term. The rotation yields to a new basis of rotated pseudospins $\tilde{\tau}_i^{\tilde{\alpha}}$, parametrized by an angle $\vartheta$ defined from the coupling parameters:

$$\begin{aligned} \tilde{\tau}_i^{\tilde{x}} &= \cos(\vartheta)\, \tau_i^x + \sin(\vartheta)\, \tau_i^z, \quad \tilde{\tau}_i^{\tilde{y}} = \tau_i^y, \\ \tilde{\tau}_i^{\tilde{z}} &= \cos(\vartheta)\, \tau_i^z - \sin(\vartheta)\, \tau_i^x, \quad \tan(2\vartheta) = \frac{2J_{xz}}{J_x - J_z}. \end{aligned} \tag{1.14}$$

In this tilted pseudo-spin basis, the Hamiltonian corresponds to an XYZ model with three tilted coupling parameters:

$$\mathscr{H}_{\mathrm{DO}}^{\mathrm{XYZ}} = \sum_{\langle ij \rangle} \left[ \tilde{J}_x \tilde{\tau}_i^{\tilde{x}} \tilde{\tau}_j^{\tilde{x}} + \tilde{J}_y \tilde{\tau}_i^{\tilde{y}} \tilde{\tau}_j^{\tilde{y}} + \tilde{J}_z \tilde{\tau}_i^{\tilde{z}} \tilde{\tau}_j^{\tilde{z}} \right] \tag{1.15}$$

The correspondence between the two sets of coupling parameters is given by the angle $\vartheta$ using the following formulas:

$$\begin{aligned} J_x &= \tilde{J}_x \cos^2(\vartheta) + \tilde{J}_z \sin^2(\vartheta) \\ J_y &= \tilde{J}_y \\ J_z &= \tilde{J}_z \cos^2(\vartheta) + \tilde{J}_x \sin^2(\vartheta) \\ J_{xz} &= (\tilde{J}_x - \tilde{J}_z) \sin(\vartheta) \cos(\vartheta) \end{aligned}$$

The on-site magnetization in the tilted pseudospins $\tilde{\tau}_i^{\tilde{\alpha}}$ basis becomes:

$$\mathbf{m}_i = g_z \mu_B (\tilde{\tau}_i^{\tilde{z}} \cos(\vartheta) + \tilde{\tau}_i^{\tilde{x}} \sin(\vartheta)) \hat{\mathbf{z}}_i = \mathbf{m}_i^{\tilde{z}} + \mathbf{m}_i^{\tilde{x}} \tag{1.16}$$

Both $\tilde{\tau}_i^{\tilde{x}}$ and $\tilde{\tau}_i^{\tilde{z}}$ are described by a mixture of dipolar and octupolar moments and transform under symmetry operations like dipoles.

The ground state phase diagram of the XYZ Hamiltonian (Equation 1.15) is theoretically predicted to contain 6 distinct phases [78]. Four of these phases are disordered quantum spin ice phases with different octupolar or dipolar character, and the two others are magnetically ordered. For the various Ce-based compounds that have been studied, experimentally determining the ground state has proven challenging, as these systems do not exhibit magnetic order down to accessible temperatures (above 20 mK) due to low couplings. In $Ce_2Zr_2O_7$ and $Ce_2Hf_2O_7$, the ground state appears to be a quantum spin liquid phase, while the nature of the ground state in $Ce_2Sn_2O_7$ is still under debate. For this compound, sample quality seems to be play a crucial role in the observed properties and different growth methods may explain the differences between the obtained results [79].

In the large variety of Nd-based pyrochlores studied so far, they all show the same long-range ordered antiferromagnetic ground state with a transition temperature between 0.3-1.1 K [80]. This ordered ground state is antiferromagnetic showing a clear AIAO magnetic structure, confirmed by neutron diffraction. Due to the specificity of the DO doublet, the experimental observables present exotic features that are well captured by the XYZ Hamiltonian.

The first and most studied compound of this family is $Nd_2Zr_2O_7$. In the next subsection we will discuss both the experimental and theoretical properties of the DO AIAO order using $Nd_2Zr_2O_7$ as an example.

### 1.4.2 The AIAO dipolar-octupolar order

$Nd_2Zr_2O_7$ neutron diffraction measurements on powder samples have unambiguously confirmed that the $Nd^{3+}$ sublattice orders into an AIAO structure [81]. This magnetic structure can be identified by examining the magnetic intensity at the $(2,2,0)$ and $(1,1,3)$ Bragg peaks, which are characteristic of AIAO order in pyrochlore systems. Neutron

diffraction patterns measured at 150 mK and 4 K (Figure 1.17 (b)) show the emergence of magnetic intensity at these two reflections in the low temperature pattern. Additionally, no magnetic intensity appears at the $(1,1,1)$ and $(0,0,2)$ peaks, consistent with the AIAO symmetry.

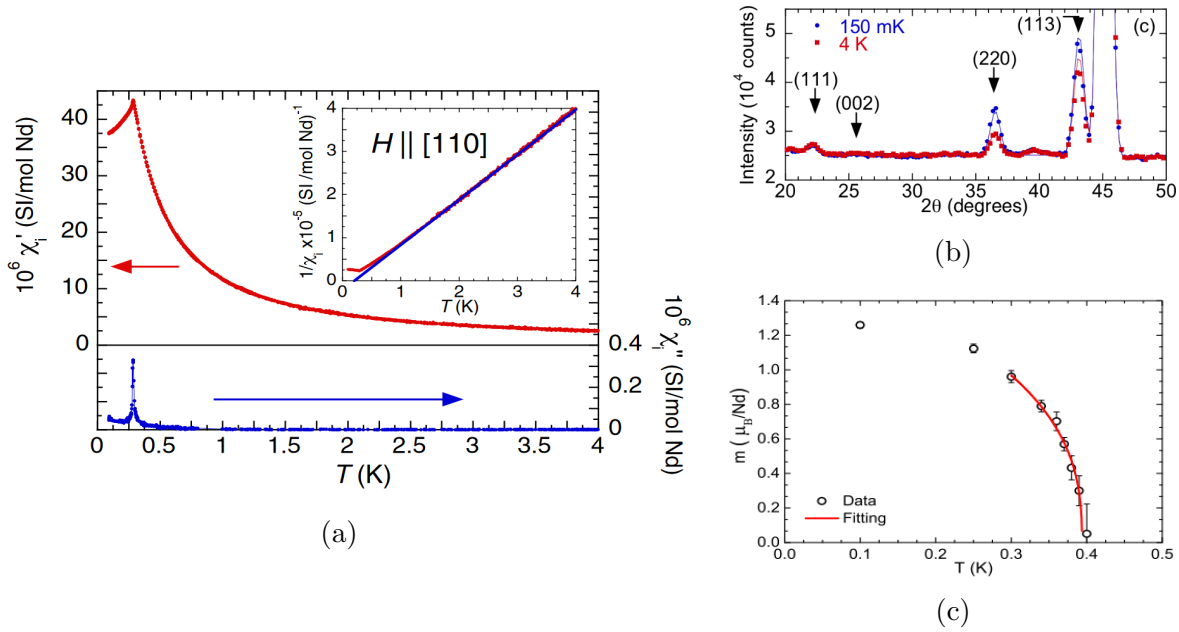


Figure 1.17: (a) ac susceptibility $\chi'$ and $\chi''$ with respect to temperature for an ac field applied along the [110] direction for a frequency of 5.7 Hz of a $Nd_2Zr_2O_7$ single crystal sample. Inset: Inverse of in-phase susceptibility $\chi'$ with respect to temperature fitted to a Curie-Weiss law (blue curve). (b) Neutron diffraction patterns of $Nd_2Zr_2O_7$ above the magnetic transition at 4 K (red) and below at 150 mK (blue). Figures (a) and (b) from Ref. [81]. (c) Temperature dependence of the refined ordered moment of Nd in powder $Nd_2Zr_2O_7$ from Rietveld fits of neutron diffraction patterns. Figure (c) from Ref. [82].

The $Nd^{3+}$ magnetic ordering at zero applied field was shown to occur at a Néel temperature of 285 mK for a single crystal from the measurement of the magnetic susceptibility along the [110] direction (Figure 1.17(a)). For powder samples, the transition temperature is higher (around 400 mK), as observed from the temperature dependence of the refined ordered moment of the AIAO structure (Figure 1.17(c)) [82].

Interestingly, a fit of the susceptibility between 1 and 4 K to the Curie-Weiss law gives $\theta_{CW} = 195$ mK, clearly indicative of effective ferromagnetic interactions despite the antiferromagnetic AIAO order at low temperature. The effective moment extracted from this fit is $\mu_{eff} = 2.45\mu_B$, in good agreement with the $2.4\mu_B$ magnetic moment of the ground state doublet determined from the analysis of the CEF scheme. The saturated magnetization of about $1.2\mu_B$ obtained with magnetization vs field measurement is also consistent with a single-ion moment of about $2.4\mu_B$, considering the multi-axial anisotropy for Ising spins on the pyrochlore lattice. However, the ordered moment obtained from the refinement of the neutron diffraction patterns is strongly reduced with a value of $\sim 1\mu_B$, much lower than the expected $2.4\mu_B$.

The positive $\theta_{CW}$ and the reduced ordered moment are two puzzling observations that seems inconsistent with an AIAO ordering and were initially unexplained. However, they

are naturally resolved within the XYZ model for DO doublets [83].

As illustrated in Figure 1.18 left panel, when $J_{xz}$ is non zero, the pseudo-spin orders can order in an AIAO structure along the tilted local axis $\tilde{z}_i$ (red) rather than the original $z$-axis (black). The ordered pseudo-spin $\tilde{\tau}_i^{\tilde{z}}$ is then a mixture of the dipolar $\tau_i^z$ and the octupolar $\tau_i^x$ components (see Figure 1.18 right panels). Since most experimental probes (neutron scattering, magnetization) are only sensitive to the dipolar $\tau_i^z$ component of $\tilde{\tau}_i^{\tilde{z}}$, the observed ordered moment is the projection of $\tilde{\tau}_i^{\tilde{z}}$ onto the $z$-axis (green), resulting in a reduced intensity by a factor $\cos(\vartheta)$. The octupolar $\tau_i^x$ component of $\tilde{\tau}_i^{\tilde{z}}$ is also ordered, but it remains unobservable to standard probes.

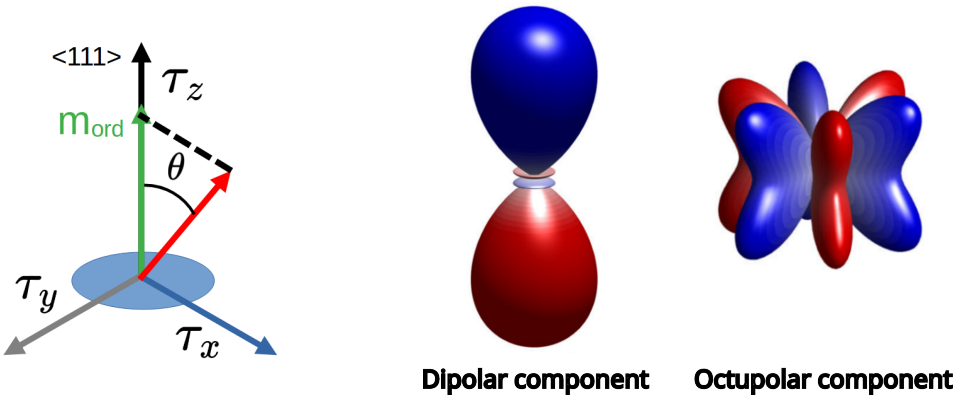


Figure 1.18: Left panel: schematic of the AIAO dipolar-octupolar order at one site. The pseudospin orders along the $\tilde{z}_i$ local axis (red) with an angle $\theta$ from the $z$-axis (local $\langle 111 \rangle$ direction). The projection of $\tilde{\tau}_i^{\tilde{z}}$ on the $z$-axis corresponds to the observed ordered moment (green). Right panels: Magnetic charge density corresponding to dipolar and octupolar components. Figure from Ref. [84].

In conventional Ising systems, transverse components are unobservable due to the anisotropy that ensure $g_x$ and $g_y$ are zero. In DO doublets systems, $g_x$ and $g_y$ are also zero, but due to the change of pseudo-spin basis, a component of the transverse term $\tilde{\tau}_i^{\tilde{x}}$ projects along the local $z$-axis (with $g_z \neq 0$). The misalignment between the local order along the $\tilde{z}$-axis and the $z$-anisotropy axis allows detection of the $\tilde{x}$-transverse term. This dipolar projection of the transverse term $\tilde{\tau}_i^{\tilde{x}}$ shows fluctuations that are measurable with inelastic neutron scattering.

Using the XYZ model and linear spin wave theory, one can estimate the fluctuations coming from the $\tilde{x}$-transverse term. Figure 1.19 shows a direct comparison of the $Nd_2Zr_2O_7$ measured inelastic spectra [85] to the calculated spin waves with the following set of parameters: $(\tilde{J}_x, \tilde{J}_y, \tilde{J}_z) = (1.2, 0, -0.55)$ K [83]. The agreement between the model and the experimental data is almost perfect.

From those parameters, the corresponding Curie-Weiss temperature for the XYZ model is estimated with:

$$\theta_{\mathrm{CW}} = \frac{1}{2k_B}\left(\tilde{J}_z \cos^2(\vartheta) + \tilde{J}_x \sin^2(\vartheta)\right) \tag{1.17}$$

When taking $\vartheta \approx 0.83$, estimated from the reduced ordered moment, this yields $\theta_{CW} \approx$ 200 mK which is very close to the experimental value [81, 82, 86]. The model explains the

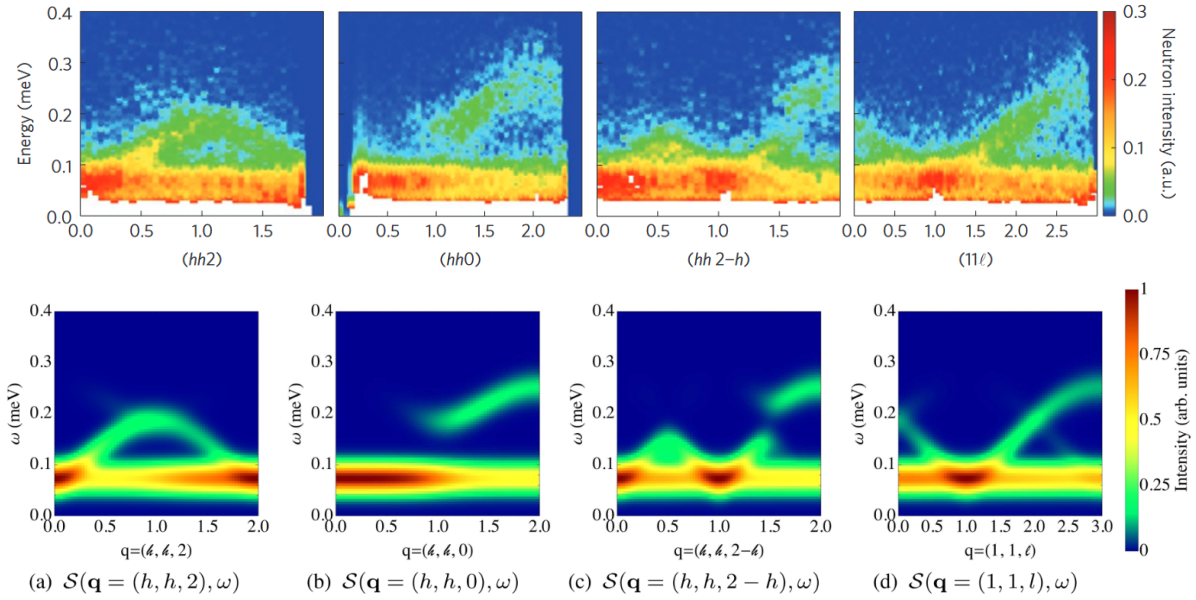


Figure 1.19: Top: Measured inelastic neutron scattering spectra for four different reciprocal directions in $Nd_2Zr_2O_7$ at 65 mK. Figure from Ref. [85]. Bottom: Best fit model for the spin wave patterns of $Nd_2Zr_2O_7$ using the XYZ dipolar-octupolar model. Figure from Ref. [83].

reduced measured ordered moment and indicates that the puzzling positive Curie-Weiss temperature is in fact compatible with an antiferromagnetic AIAO ground state.

### 1.4.3 Dynamic fragmentation

Magnetic fragmentation was initially introduced theoretically to describe the physics of a crystal of monopoles. In this state, each tetrahedron in a 3-in/1-out or 1-in/3-out configurations can be decomposed into two fragments via a Helmholtz decomposition: a divergence-full component (carrying the monopole charge) and a divergence-free component (with no monopole charge) [87].

This Helmholtz decomposition is applied on the magnetization density $\mathbf{m}$, separating it into two distinct fragments: one divergence full $\nabla\psi$ and one divergence free $\nabla \times \mathbf{A}$:

$$\mathbf{m} = \nabla\psi + \nabla \times \mathbf{A} \tag{1.18}$$

In the DO AIAO ground state, the $\tilde{\tau}_i^{\tilde{z}}$ component is fully ordered. Within the concept of fragmentation, $\mathbf{m}_i^{\tilde{z}}$ is therefore entirely divergence-full. As a result, fragmentation is not relevant for describing the ground state of Nd-based systems. However, the concept becomes meaningful when applied to the fluctuations of the $\mathbf{m}_i^{\tilde{x}}$ and $\mathbf{m}_i^{\tilde{y}}$ components.

Writing down the equations of motion for $\mathbf{m}_i^{\tilde{x}}$ and $\mathbf{m}_i^{\tilde{y}}$ and linearizing around the ground state, one obtains [83]:

$$\partial_t \mathbf{m}_i^{(\tilde{\alpha})} \approx \varepsilon_{\tilde{\alpha}'\tilde{\alpha}\tilde{z}} S \left( \tilde{J}_{\alpha'} \nabla_i (\nabla \cdot \mathbf{m}^{(\tilde{\alpha}')}) \right) + \left( 6|\tilde{J}_z| - 2\tilde{J}_{\alpha'} \right) \mathbf{m}_i^{(\tilde{\alpha}')}, \tag{1.19}$$

where $\tilde{\alpha}' = \tilde{y}$ when $\tilde{\alpha} = \tilde{x}$, and inversely and where $\varepsilon_{\tilde{x}\tilde{y}\tilde{z}} = -\varepsilon_{\tilde{y}\tilde{x}\tilde{z}} = 1$. This equation can be solved in terms of the Helmholtz decomposition, yielding:

$$\begin{aligned} \partial_t \psi^{(\tilde{\alpha})} &= \varepsilon_{\tilde{\alpha}'\tilde{\alpha}\tilde{z}} S \left( \tilde{J}_{\alpha'} \nabla^2 \psi^{(\tilde{\alpha}')} \right) + \left( 6|\tilde{J}_z| - 2\tilde{J}_{\alpha'} \right) \psi^{(\tilde{\alpha}')} \\ \partial_t \mathbf{A}^{(\tilde{\alpha})} &= \varepsilon_{\tilde{\alpha}'\tilde{\alpha}\tilde{z}} S \left( 6|\tilde{J}_z| - 2\tilde{J}_{\alpha'} \right) \mathbf{A}^{(\tilde{\alpha}')} \end{aligned} \tag{1.20}$$

The two fragments of the fluctuations $\partial_t \mathbf{m}_i^{(\tilde{\alpha})}$ are completely independent. The divergence-free component $\partial_t \mathbf{A}^{(\tilde{\alpha})}$ forms a flat band at finite energy:

$$\Delta_{\text{flat}} = \sqrt{\left( 3|\tilde{J}_z| - \tilde{J}_x \right) \left( 3|\tilde{J}_z| - \tilde{J}_y \right)} \tag{1.21}$$

while fluctuations of the divergence-full component $\psi^{(\tilde{\alpha})}$ gives rise to dispersive bands lying above the flat mode. In practice, the $\partial_t \mathbf{m}_i^{(\tilde{y})}$ component cannot be measured as it is purely octupolar and only the fluctuations of the $\tilde{\tau}_i^{\tilde{x}}$ are accessible. In Nd-pyrochlores, this phenomenon is referred to as "dynamic fragmentation", since it is the spin waves that fragment and not the ground state itself.

Because the flat band originates from a divergenceless component, it exhibits the pinch points, characteristic of the correlations of a Coulomb phase, previously observed in spin ice materials [18]. The key difference here is that this Coulomb signal arises from finite-energy excitations rather than from the ground-state correlations.

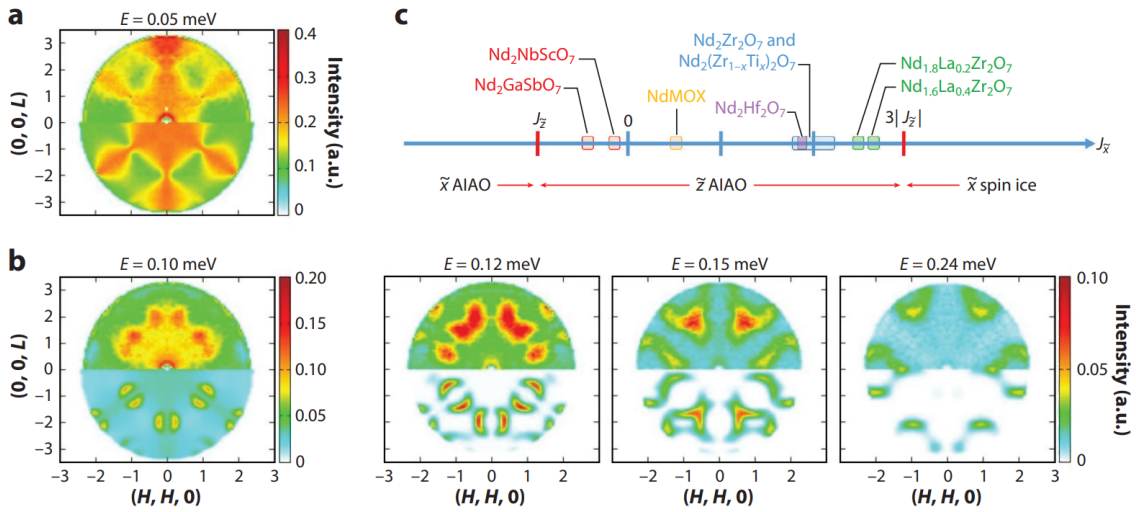


Figure 1.20: (a) and (b) Constant energy slices of neutron scattering in the $(H,H,L)$ plane of experimental (top half) and calculated data (bottom half) for $Nd_2Zr_2O_7$. (a) At $E = \Delta_{\text{flat}} = 0.05$ meV, pinch point pattern in the spectral weight is characteristic of the diffuse scattering of a Coulomb phase. (b) Higher energy slices showing the patterns of the dispersing branches situated on top of the flat band with appearances of half-moons. (c) Phase diagram of the XYZ dipole-octupole model for $\tilde{J}_z < 0$ and $\tilde{J}_y = 0$, that describes well Nd-based pyrochlores. The positions of several Nd-based compounds are included. Figures from Ref. [79].

As shown in Figure 1.20(a), the pinch points of the Coulomb fragment are clearly visible with both measured and calculated neutron scattering slices in the $(H,H,L)$ plane at the gap energy ($\sim 0.05$ meV in $Nd_2Zr_2O_7$) [79, 85]. At higher energies, Figure 1.20(b), the dispersive excitations appear as half-moon arcs of diffuse scattering signal, located around the position of the pinch points [88].

Remarkably, it was observed that these excitations persist above the AIAO transition temperature $T_N$. The temperature dependence of $Nd_2Zr_2O_7$ inelastic patterns was thoroughly investigated. It was shown that close above $T_N$, the flat mode softens and loses intensity while at the same time appears a new distinct elastic $E = 0$ Coulomb component [89, 90]. In the intermediate temperature range, the system displays coexistence between the inelastic fragmented excitations associated with the AIAO order (both dispersive and flat-band branches) together with the elastic Coulomb phase associated to the $\tilde{\tau}_i^{\tilde{x}}$ component. This elastic Coulomb phase disappears around 1 K, well above the temperature of the AIAO order.

The coexistence of these two phases is a result of the competing interactions at play within the XYZ hamiltonian approach and are captured by Monte Carlo calculations [89]. The negative $\tilde{J}_z$ coupling term favors the $\tilde{z}$-AIAO ordered phase, while the $\tilde{J}_x$ interaction favors the elastic U(1) Coulomb phase associated to $\tilde{\tau}_i^{\tilde{x}}$.

The resulting ground state depends on the ratio $\tilde{J}_x/|\tilde{J}_z|$ and the associated phase diagram is shown in Figure 1.20 (c) (assuming $\tilde{J}_z < 0$ and $J_y = 0$). All measured Nd-based compounds studied up to now have been found to stabilize the $\tilde{z}$-AIAO ground state [80]. However, a transition value exists at the ratio $\tilde{J}_x/|\tilde{J}_z| = 3$ (in the classical approach), above which the interactions would favor the $\tilde{x}$ U(1) spin liquid Coulomb phase as the ground state [83].

### 1.4.4 $Nd_2Ir_2O_7$ and $Nd_2Ru_2O_7$

The proximity of Nd-based compounds to an $U(1)$ spin liquid has motivated extensive investigations into new compounds of this family. However the $Nd^{3+}$ DO AIAO order appears remarkably robust to different CEF environments. New ways to disturb the ground state are needed to understand the origin of this stability and gain insight into its microscopic origin.

An approach is to introduce a magnetic metallic ion on the second pyrochlore sublattice. This approach has been shown to stabilize new types of magnetic order for the rare-earth ion. For instance, in $Dy_2Ir_2O_7$ and $Ho_2Ir_2O_7$ a fragmented state was discovered, stabilized by the molecular field induced by the antiferromagnetic ordering of the $Ir^{4+}$ sublattice [23, 24]. Recent studies on $Ho_2Ru_2O_7$ show that substituting the metal site with $Ru^{4+}$ similarly induces a fragmented state [91].

In this context, probing the low temperature and low energy magnetic properties of the $Nd^{3+}$ sublattice in $Nd_2Ir_2O_7$ and $Nd_2Ru_2O_7$, that are expected to combine both the DO physics and metal-rare earth interactions, offers complementary ways to understand the physics of the Nd ground state.

In both materials, the $Nd^{3+}$ sublattice exhibits an AIAO ordering with a reduced ordered moment, reminiscent of the DO AIAO order in $Nd_2Zr_2O_7$ [22, 25]. The metal ion orders into two different magnetic structures in both compounds (AIAO in $Nd_2Ir_2O_7$ and easy-plane antiferromagnetic $\Gamma_5$ in $Nd_2Ru_2O_7$ [92]) at two different temperature scales

(35 K and 150 K respectively). Due to these two different metal site orderings, the $Nd^{3+}$ ions are expected to experience distinct inter-sublattice couplings, leading to potentially different low-temperature behaviors.

Despite their interest, the low-temperature magnetic properties of these compounds have not yet been extensively explored. The magnetic orderings were identified but no systematic studies of the temperature dependence of the ordered moment or the neutron inelastic pattern was done.

In $Nd_2Ir_2O_7$, research was mainly focused on the metal-insulator transition associated with the $Ir^{4+}$ ordering [93]. Nonetheless, a spin wave flat mode was observed using neutron scattering in this compound by Tomiyasu et al. [94] in 2012 but it has not been analyzed using the XYZ model as it was not formulated yet.

In $Nd_2Ru_2O_7$, in addition to a diffraction study, a correlation bump of the $Nd^{3+}$ sublattice was measured around 2 K in specific heat measurements but the spin wave excitations were not investigated [92].

The purpose of the study on these two compounds of the Nd-based family is to characterize the low temperature dependence by combining the bulk magnetic response, the neutron static magnetic order with neutron diffraction, and the magnetic fluctuations with inelastic scattering. The careful determination of these observables will be used to deduce a new Hamiltonian model based on the XYZ model that accounts for coupling between the rare-earth and metal sublattices. The symmetry investigation of the allowed magnetic couplings between the rare-earth and metal sublattice will give a minimal Hamiltonian model to which the parameters will be fitted to the measured experimental data.

# Chapter 2

# Experimental techniques

## Contents


**2.1 Neutron scattering and diffraction . . . . . 34**
2.1.1 Neutron: a powerful tool for condensed matter . . . . . 34
2.1.2 Scattering cross section . . . . . 34
2.1.3 Neutron diffraction . . . . . 37
2.1.4 Inelastic neutron scattering . . . . . 38
2.1.5 Neutron instruments . . . . . 38
**2.2 Low temperature apparatus: dilution refrigerator . . . . . 41**
2.2.1 $^4$He and $^3$He cryogenics fluids . . . . . 41
2.2.2 Principle of the dilution refrigerator . . . . . 41
2.2.3 Miniature dilution refrigerator or diluette . . . . . 43
**2.3 Magnetometry . . . . . 44**
2.3.1 SQUID magnetometers . . . . . 44
2.3.2 Magnetization and susceptibility . . . . . 48
2.3.3 Magnetic noise . . . . . 52
2.3.4 Measuring the fluctuation-dissipation theorem . . . . . 55

## 2.1 Neutron scattering and diffraction

The concepts introduced in this section are the most essential and relevant for understanding the studies conducted in this PhD. An exhaustive and detailed description of neutron scattering techniques can be found in Ref. [95].

### 2.1.1 Neutron: a powerful tool for condensed matter

The neutron is a subatomic particle with no electric charge (hence its name), a mass slightly greater than that of a proton ($m_n \approx 1.67 \times 10^{-27}$ kg), and a nuclear spin of 1/2. Neutrons interact with matter through the short-range strong force with atomic nuclei, which underlies many of their experimental advantages. In particular, neutrons possess a high penetration depth in matter, making them well-suited for probing bulk properties. They are also sensitive to light elements like hydrogen or oxygen, which are difficult to detect using X-rays. Furthermore, neutrons are also sensitive to magnetism at the microscopic scale because they carry a spin 1/2, allowing them to interact with the moment carried by magnetic atoms.

The energy of a neutron can be defined from its mass:

$$E = \frac{h^2}{2m_n}\frac{1}{\lambda^2} = k_B T \tag{2.1}$$

where $h$ is the Planck constant, $k_B$ is the Boltzmann constant and $\lambda$ is the neutron wavelength. In condensed matter, the energy of neutrons is usually expressed in milli-electron volts (meV) or kelvins (K). Indeed, the energy required to probe interatomic distances on the order of 1.8 Å is about 25 meV (corresponding to 300 K). Neutrons with energies in the range 10 meV $< E <$ 130 meV are called thermal neutrons, as their energy is close to room temperature and they are produced via thermalization with a room temperature moderator.

Different moderators allow production of neutrons across different energy ranges: high-temperature moderators produce hot neutrons with an energy range 60 meV $< E <$ 500 meV, while low-temperature moderators generate cold neutrons with an energy $E <$ 20 meV. Having neutrons over a broad energy band is crucial for probing various processes in condensed matter systems that span over a wide spectrum of energy scales.

Currently, two main types of neutron sources are used to generate neutrons. First nuclear reactors, where neutrons are produced as fission products from fuel elements such as enriched uranium. Secondly spallation sources, based on nuclear spallation effect, where proton pulses are accelerated then released onto a target (like mercury) to generate pulses of neutrons. The actual working European neutron source, the Institut Laue-Langevin (ILL) is a neutron source that works using nuclear fission, while the upcoming European Spallation Source (ESS) will use the spallation method.

### 2.1.2 Scattering cross section

The scattering amplitude of a neutron beam is directly proportional to the neutron flux (determined by the source performance) and to the scattering cross section. During a scattering event (Figure 2.1), an incident neutron in an initial state $\lambda_i$, defined by its

wavevector, energy and spin $(\mathbf{k}_\mathrm{i}, E_\mathrm{i}, \sigma_i)$, is scattered by the sample into a final state $\lambda_\mathrm{f}$ defined with $(\mathbf{k}_\mathrm{f}, E_\mathrm{f}, \sigma_\mathrm{f})$ within a small solid angle $d\Omega$. During this event, the neutron transfers momentum and energy to the sample, defined as:

$$\mathbf{Q} = \mathbf{k}_\mathrm{i} - \mathbf{k}_\mathrm{f} \quad \text{and} \quad \hbar\omega = E_\mathrm{i} - E_\mathrm{f} \tag{2.2}$$

The final intensity of the scattered neutron beam, characterized by the number of neutrons scattered into $d\Omega$ with energy between $E_\mathrm{f}$ and $E_\mathrm{f} + dE$, is proportional to the partial differential scattering cross section, obtained from the Fermi's golden rule:

$$\left(\frac{d^2\sigma}{d\Omega\, dE}\right)_{\lambda_\mathrm{i}\to\lambda_\mathrm{f},} = \frac{k_\mathrm{f}}{k_\mathrm{i}}\left(\frac{m_n}{2\pi\hbar^2}\right)^2 |\langle\lambda_\mathrm{f}, \mathbf{k}_\mathrm{f}, \sigma_\mathrm{f}|V|\lambda_\mathrm{i}, \mathbf{k}_\mathrm{i}, \sigma_\mathrm{i}\rangle|^2\, \delta(E_\mathrm{i} - E_\mathrm{f} - \hbar\omega) \tag{2.3}$$

where $V$ is the total scattering potential. This potential describes the nature of the neutron-matter interactions and is the sum of two main contributions: the nuclear $V_N$ and the magnetic $V_M$ contributions.

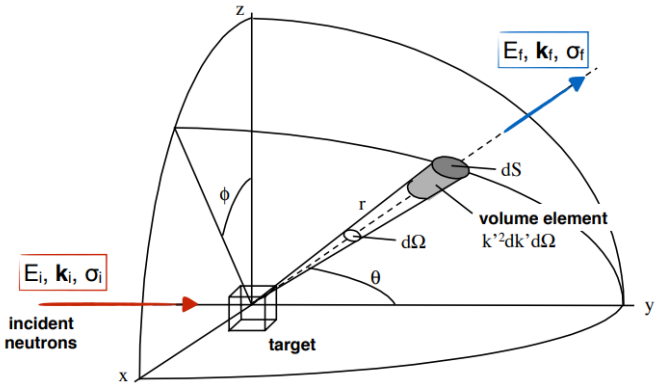


Figure 2.1: Schematic of a scattering process on a target sample. Figure from Ref. [96].

### Nuclear scattering

The nuclear interaction potential originates from the strong force between the neutron and the atomic nuclei of the scattered sample. For a scattering event at site $j$, it is described by the Fermi pseudo-potential:

$$V_{Nj}(\mathbf{r}) = \frac{2\pi\hbar^2}{m_n} b_j \delta(\mathbf{r} - \mathbf{R}_j), \tag{2.4}$$

where $\mathbf{r}$ is the neutron position, $\mathbf{R}_j$ is the position of the scattered nucleus, and $b_j$ its scattering length. The scattering length is a parameter that depends on the nucleus spin state, the element and the isotope considered. It is tabulated for all elements of the periodic table [97]. Because $b_j$ varies among spin states and isotopes, for one element, the total scattering length is not uniform and can be decomposed into two components. The first one is the coherent scattering length, which represents the average scattering

length. The second one is the incoherent scattering length, which is associated to the deviations of scattering length from the average.

The total scattering cross section $\left(\frac{d^2\sigma}{d\Omega\, dE}\right)$ can be written as the sum of a coherent and a incoherent cross section contributions. The coherent cross section is related to the spatial correlations between atoms and gives information on the crystal structure or collective excitations. The incoherent cross section is sensitive to self-correlations and yields information about single particle dynamics or localized vibrational modes for instance. In the neutron measurements made during this thesis, we focused exclusively on coherent processes, so the following discussions will assume that only the coherent component is relevant.

Substituting $V_{Nj}$ in Equation 2.1.2, the nuclear scattering cross section becomes:

$$\left(\frac{d^2\sigma}{d\Omega\, dE}\right)_N = \frac{k_\mathrm{f}}{k_\mathrm{i}} \frac{1}{2\pi\hbar} \int_{-\infty}^{\infty} \langle N^\dagger(\mathbf{Q},0) \cdot N(\mathbf{Q},t) \rangle_\omega \exp^{-i\omega t}\, dt \tag{2.5}$$

where $^\dagger$ denotes the complex conjugate and $N(\mathbf{Q},t)$ is the nuclear structure factor, expressed as follows:

$$N(\mathbf{Q},t) = \sum_j b_j e^{i\mathbf{Q}\cdot\mathbf{R}_j(t)} \tag{2.6}$$

$N(\mathbf{Q},t)$ describe the scattering amplitude of a neutron wave by the nucleus of an atom. As the interaction is localized, the scattering length $b_j$ is constant thus the amplitude decay in $\mathbf{Q}$ depends only on the exponential term.

### Magnetic scattering

The same methodology can be applied to the magnetic scattering cross section using the magnetic scattering potential $V_M$. It arises from the interaction between the neutron magnetic moment and the magnetic field produced by unpaired electron spins in a material and is written as:

$$V_M = -\mu_n \cdot \mathbf{B}_e \tag{2.7}$$

where, $\mu_n = \gamma \mu_N \sigma$ is the neutron magnetic moment with $\mu_N$ the nuclear magneton and $\gamma$ the gyromagnetic factor. The magnetic field created by the electrons is $\mathbf{B}_e$.

Similarly to the nuclear part, by substituting $V_M$ in the scattering cross section, the magnetic scattering cross section is expressed as:

$$\left(\frac{d^2\sigma}{d\Omega\, dE}\right)_M = \frac{k_\mathrm{f}}{k_\mathrm{i}} \frac{1}{2\pi\hbar} \int_{-\infty}^{\infty} \langle \mathbf{M}_\perp^\dagger(\mathbf{Q},0) \cdot \mathbf{M}_\perp(\mathbf{Q},t) \rangle_\omega \exp^{-i\omega t}\, dt \tag{2.8}$$

with $\mathbf{M}_\perp(\mathbf{Q},t)$, the projection of the magnetic structure factor $\mathbf{M}(\mathbf{Q},t)$ on the plane perpendicular to the scattering vector. It is written:

$$\mathbf{M}_\perp(\mathbf{Q},t) = \sum_j f_j(\mathbf{Q}) \mathbf{S}_\perp^j e^{i\mathbf{Q}\cdot\mathbf{R}_j(t)} \tag{2.9}$$

$\mathbf{S}_{\perp}^{j}$ is the component perpendicular to the scattering vector of the magnetic dipole moment at site $j$. It indicates that neutrons only see the component of magnetization that is perpendicular to their scattering vector.

$f_j(\mathbf{Q})$ is the magnetic form factor and takes into account the spatial dependence of the electron density which cannot be considered as a delta function. $f_j(\mathbf{Q})$ decreases for large $\mathbf{Q}$ and adds up on the exponential decay, meaning that magnetic properties are better measured for small scattering vectors.

### 2.1.3 Neutron diffraction

Neutron diffraction is an experimental technique that uses elastic neutron scattering on a crystalline sample to extract information about both the nuclear and magnetic structures. In elastic scattering, the incident neutron does not transfer energy to the lattice, implying that $\hbar\omega = E_{\mathrm{i}} - E_{\mathrm{f}} = 0$.

Under this condition, the nuclear and magnetic scattering cross sections are significantly simplified:

$$\left(\frac{d^2\sigma}{d\Omega\, dE}\right)_N = \frac{(2\pi)^3}{V} N_{\mathrm{cell}} \sum_{\mathbf{H}} |\mathbf{N}(\mathbf{Q})|^2 \delta(\mathbf{Q}-\mathbf{H}) \tag{2.10}$$

$$\left(\frac{d^2\sigma}{d\Omega\, dE}\right)_M = \frac{(2\pi)^3}{V} N_{\mathrm{cell}} \sum_{\mathbf{H}} \sum_{q} |\mathbf{M}_{\perp}(\mathbf{Q})|^2 \delta(\mathbf{Q}-\mathbf{H}-q) \tag{2.11}$$

Here, $\frac{(2\pi)^3}{V}$ is the reciprocal unit cell volume, $N_{cell}$ is the number of unit cells in the crystal, $\mathbf{H} = h\mathbf{a}^{\star} + k\mathbf{b}^{\star} + l\mathbf{c}^{\star}$ denotes the reciprocal lattice vectors, and $q$ is the propagation vector of the magnetic order. The Dirac delta functions correspond to the positions where the Bragg conditions are fulfilled, and where constructive interferences will generate intense peaks denoted as the Bragg peaks.

The Bragg conditions for the nuclear and magnetic cross sections are not necessarily the same, due to the presence of $q$, which describes the periodicity of the magnetic structure, that can be distinct from the the crystallographic phase. As a result, the magnetic Bragg peaks are shifted from the nuclear Bragg peak positions and are found at $\mathbf{H} \pm q$.

The corresponding nuclear and magnetic structure factors for elastic scattering are given by:

$$\mathbf{N}(\mathbf{Q}) = \sum_{\nu} b_{\nu} e^{i\mathbf{Q}\cdot\mathbf{r}_{\nu}} e^{-W_{\nu}} \tag{2.12}$$

$$\mathbf{M}(\mathbf{Q}) = \sum_{\nu} f_{\nu}(\mathbf{Q}) \mathbf{S}_{q}^{\nu} e^{i\mathbf{Q}\cdot\mathbf{r}_{\nu}} e^{-W_{\nu}} \tag{2.13}$$

where $\mathbf{r}_{\nu}$ is the position of atom $\nu$, $W_{\nu}$ is the Debye-Waller factor accounting for thermal motion.

### 2.1.4 Inelastic neutron scattering

In inelastic neutron scattering, the measurements focus about the energy transfer between the incident neutrons and the sample. Inelastic scattering provides insight into the creation and annihilation of excitations within the system. The quantitative evaluation of the inelastic cross section is complex so it will not be addressed here. We just discuss below the two main types of inelastic signals we have observed in our study.

Lattice excitations includes phonons, which can stem from the nuclear Bragg peaks (acoustic modes) or appear at finite energy (optical modes). As they are bosonic excitations, their thermal population follows Bose-Einstein statistics. One of the key feature of inelastic scattering associated to phonons is that its intensity is proportional to the square of the wavevector: $I \propto (\mathbf{Q} \cdot \mathbf{e}_s)^2$. The phonon polarization vector $\mathbf{e}_s$ implies the measured intensity is maximal when $\mathbf{Q} || \mathbf{e}_s$.

Magnetic excitations include spin waves as well as single-ion CEF excitations. Depending on the nature of the spin interaction, spin waves may exhibit both acoustic and optical branches. CEF excitations are associated to the magnetism of localized single-ion and manifest as dispersionless flat modes in $\mathbf{Q}$-vector. The $\mathbf{Q}$-dependent intensity of magnetic excitations is different from the one of phonons. It scales with the magnetic form factor as $I \propto |f(\mathbf{Q})|^2$, and since $f(\mathbf{Q})$ decreases with increasing $|\mathbf{Q}|$, magnetic excitations are typically detected at low wavevector.

Thanks to the different $\mathbf{Q}$-dependencies, by looking at the intensity $\mathbf{Q}$-profile it is possible to identify the nature of the measured excitation.

### 2.1.5 Neutron instruments

In this thesis, we have used neutron instruments from the European neutron source: the Institut-Laue-Langevin (ILL). Experiments were performed using a powder diffractometer and time-of-flight (TOF) spectrometers. This section presents the principles of these two techniques, emphasizing on the specificity of each of the three instruments used to perform experiments.

#### Powder diffraction : D1B-CRG@ILL

D1B-CRG@ILL is a 2 axis powder diffractometer used to determine both crystallographic and magnetic structures of a sample. This type of experiments is only focused on the elastic part of the scattering cross section. However, actually there is no analysis of the neutron energy so all scattered neutrons are taken into account. Thus the signal is integrated over all transferred energy, but the elastic contribution usually strongly dominates the inelastic signal.

The diffraction condition is satisfied at the Bragg peak positions and is expressed by the Bragg's law:

$$2d \sin\theta = \lambda_i \quad \text{or} \quad Q = 2k_i \sin\theta \tag{2.14}$$

where $d = \frac{2\pi}{Q}$ is the interplanar spacing, $\lambda_i = \frac{2\pi}{k_i}$ is the incident neutron wavelength, and $2\theta$ is the scattering angle satisfying the Bragg's condition.

For a powder diffractometer instrument like D1B-CRG@ILL, there is no specific orientation of the sample as all crystallographic orientations are statistically represented.

Thus all the families of planes are scattered and averaged over all orientations according to the Bragg conditions, resulting in Debye-Scherrer cones at each $2\theta$ satisfying the Bragg's law.

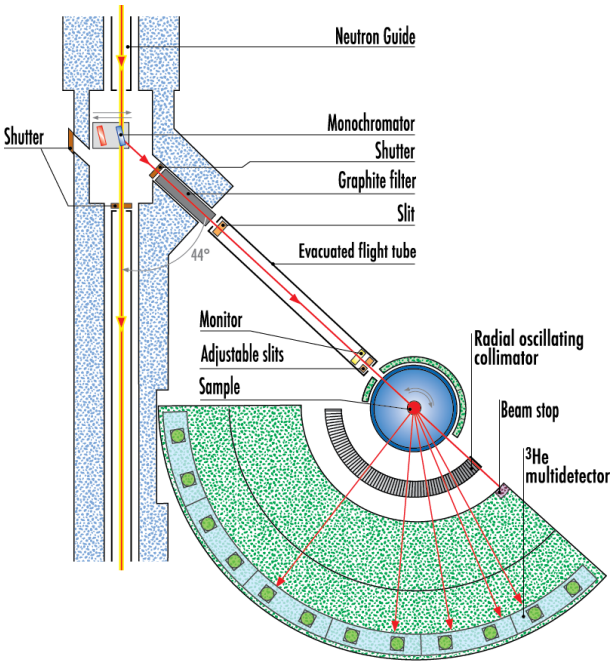


Figure 2.2: Schematic of the D1B-CRG@ILL powder diffractometer. Image from the ILL website [98].

There are two ways to detect these cones and deduce the $Q$-dependence of the diffraction pattern: either the spectrometer operates at fixed $Q$ with varying $\lambda_i$ or at fixed $\lambda_i$ with varying $Q$. In the case of D1B-CRG@ILL, the incident wavelength is fixed around $\lambda_i = 2.48$ Å, corresponding to thermal neutrons, so it is well suited for atomic scale structure measurements.

Using this $\lambda_i$-fixed mode, the whole $2\theta$-dependency is detected in one go using an half cylinder chamber of $^3$He multidetectors (Figure 2.2). Neutron detection is based on the $^3$He gas absorption reaction, producing a triton and a charged proton that can be collected using a space sensitive electronic detector. The angular range covered by the detector is from 0.8 to 128.8°. This space sensitive configuration of detectors allows for fast data collection and makes the instrument highly efficient.

**Time of flight spectrometers : PANTHER@ILL and IN5@ILL**

The time-of-flight (TOF) spectrometers are designed specifically to measure inelastic neutron scattering. They can detect simultaneously a range of scattering vectors $\mathbf{Q}$ and energies $\hbar\omega$. In TOF spectrometers, the method relies on deducing the energy difference of a scattering neutron by looking at its velocity. As it is a time resolved technique, the incident beam of neutrons must be at a well-defined velocity $v_i$. This is achieved using a series of rotating choppers, which select by rotating phase delay, neutrons of a desired velocity creating a monochromatic beam.

The final neutron velocity $v_f$ is determined from the time delay $\tau$ (or time-of-flight) between the sample and the detector over a known distance $d$. The energy transfer is then given by:

$$\hbar\omega = E_\mathrm{i} - E_\mathrm{f} = \frac{1}{2} m_n (v_\mathrm{i}^2 - v_\mathrm{f}^2) \tag{2.15}$$

Similarly to diffractometers, TOF spectrometers record simultaneously a large $2\theta$ range thanks to position sensitive detectors. To change the energy range investigated by the spectrometer, the initial velocity can be adapted by changing the chopper phase shift. However, the total energy range covered by the instrument is still limited by the initial energy of the neutron beam before it is chopped.

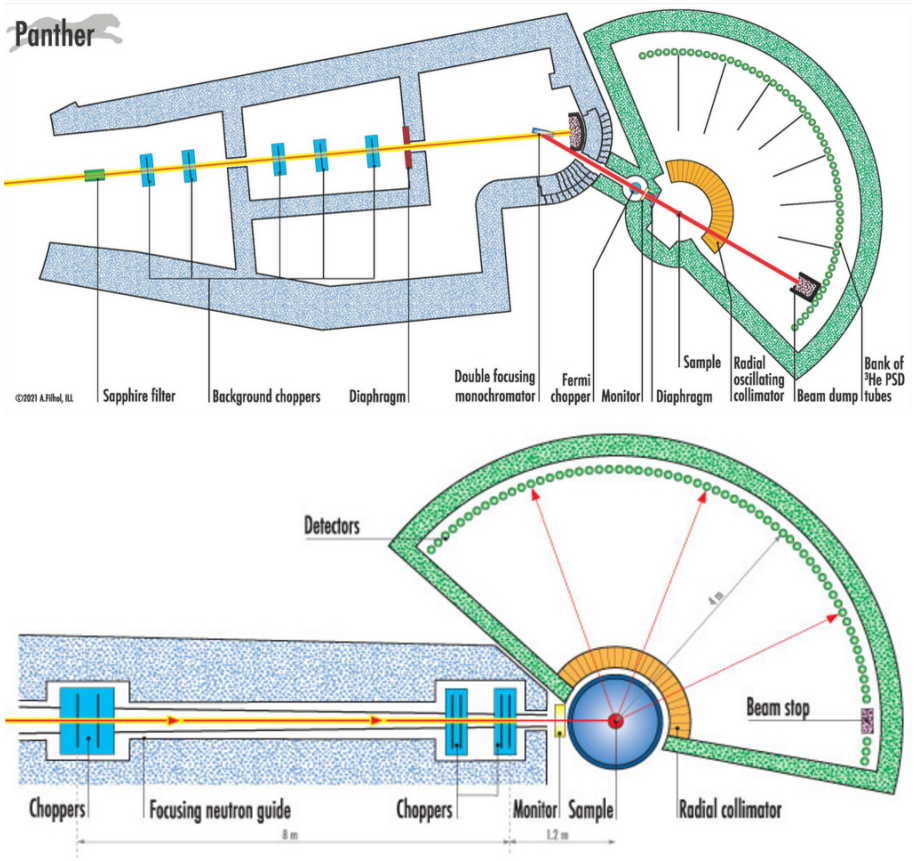


Figure 2.3: Schematics of the PANTHER@ILL (left) and IN5@ILL (right) time of flight spectrometers. Figures from the ILL website [98].

PANTHER@ILL (Figure 2.3), located close to the reactor, uses a thermal neutron beam, optimized for energy ranges from 2 meV to 150 meV. In our studies, this instrument was primarily used for the observation of CEF excitations, as the low exchange interactions in our compounds results in spins waves located at energies lower than the accessible range.

To look for these low energy spin waves, it is necessary to use an incident cold neutron beam. IN5@ILL (Figure 2.3), uses a cold neutron source and offers a extremely high resolution at low energies. Nonetheless, the energy range covered is very large and goes

from 10 $\mu$eV to 50 meV. It is one of the few instruments capable of detecting excitations below the meV range.

## 2.2 Low temperature apparatus: dilution refrigerator

The concepts introduced in this section are the most essential and relevant for understanding the studies conducted in this PhD. An exhaustive and detailed description of low temperature techniques can be found in Ref. [99].

### 2.2.1 $^4$He and $^3$He cryogenics fluids

The interesting properties of rare-earth magnetic pyrochlores usually occur at low temperatures, ranging from a few milliKelvins to a few Kelvins, due to weak effective interactions. To cool down the samples and perform measurements at such low temperatures, it is necessary to use specific cryogenic techniques. In this thesis, experiments were conducted using a $^3$He–$^4$He dilution refrigerator, which enables access to temperatures well below those achievable with conventional cryogenic fluids.

The cryogenic fluid with the lowest boiling point is $^4$He, which boils at 4.2 K at ambient pressure. Using specific cryostats equipped with thermal shielding, it is possible to limit the evaporation of this type of fluid due to ambient thermal energy. Such cryostats can be used to perform experiments down to 4.2 K and also serve as thermal shields or pre-cooling stages for experiments requiring even lower temperatures. Because the cost of $^4$He has increased significantly, helium vapor from cryostats is typically recovered and recondensed in dedicated liquefaction facilities.

To access temperatures below 4.2 K, like for all fluids, it is possible to lower the $^4$He boiling temperature by reducing the pressure. Exploiting this property, pumped-$^4$He systems reach temperatures around 1 K, depending on the quality of the pumping system, the cross-section of the pumped volume and the thermal losses. These cryostat systems have the advantage of being straightforward to operate, but they cannot reach sub-Kelvin temperatures.

For lower temperatures, it is possible to use a different isotope of helium: $^3$He. This lighter isotope boils at 3.2 K at ambient pressure and can reach temperatures down to 300 mK using pumped refrigerator. To achieve such low temperatures, it is common to use a 4.2 K liquid $^4$He bath as a thermal shield. A 1 K pot, a small volume of pumped $^4$He maintained around $\sim 1.2$ K, is also required to serve as a pre-cooling stage before the $^3$He chamber. In some systems with small volumes, the 1 K pot can be replaced by a Joule–Thomson impedance. This configuration is known as a $^3$He refrigerator and offers the advantage of reaching very low temperatures while remaining relatively easy to operate.

### 2.2.2 Principle of the dilution refrigerator

The $^3$He-$^4$He dilution refrigerator, the system used during this thesis, employs both helium isotopes to achieve even lower temperatures. It can reach temperatures around 2 mK in the most refined, high-performance designs. The mixture typically contains about 20 % of $^3$He and 80 % of $^4$He, although this ratio can be adjusted slightly to optimize

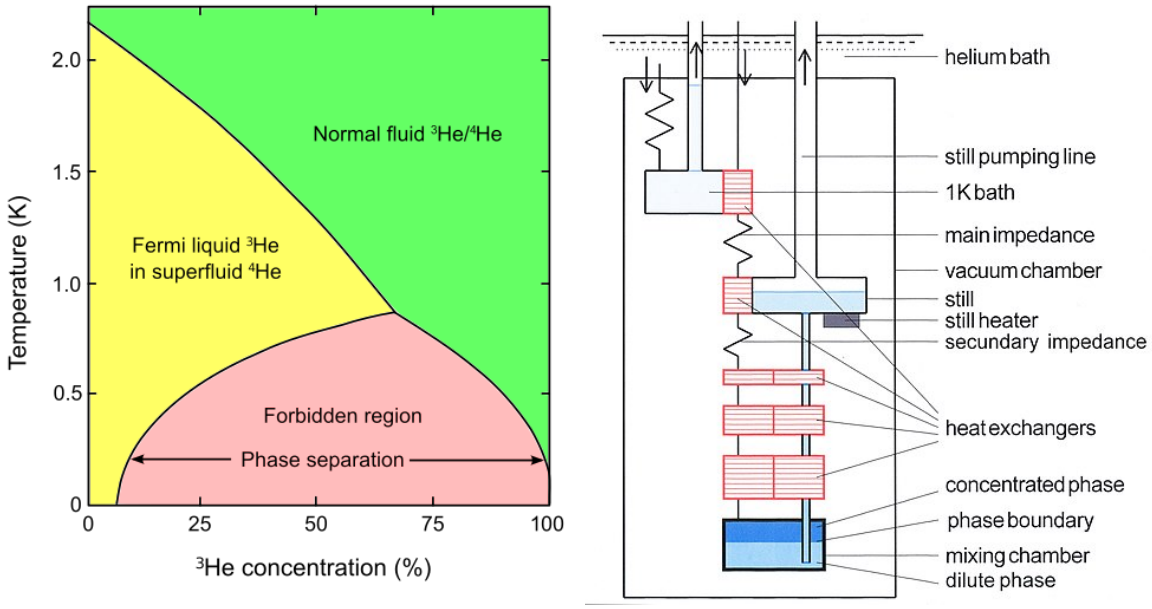


Figure 2.4: (a) Phase diagram of the $^3$He-$^4$He mixture. (b) Schematic of a conventional dilution refrigerator. Figures from Wikipedia [100].

cooling power. The cooling principle relies on the $^3$He-$^4$He mixture, which separates into two phases below 0.87 K (see Figures 2.4 (a)): a lighter, $^3$He-rich concentrated phase that floats above a denser, dilute phase with a lower $^3$He concentration ($\sim 6.6\%$). Within this mixture, an endothermic reaction will absorb heat providing refrigeration, when an atom of $^3$He moves from the concentrated phase into the dilute phase.

The concept of the dilution refrigerator (Figure 2.4(b)) is to take advantage of this reaction by mechanically pumping on the dilute phase, removing $^3$He atoms from it. To maintain the equilibrium $^3$He concentration in the dilute phase, atoms of the $^3$He-rich phase migrates into the dilute phase, triggering the endothermic reaction. The extracted $^3$He atoms become gaseous and are continuously circulated in a closed loop, re-injected into the system after being recondensed.

Several components in the circuit ensure that this process operates correctly. At startup, the dilution refrigerator is immersed in a 4.2 K liquid helium ($^4$He) bath, which cools dwon all components through a $^4$He exchange gas introduced into the calorimeter. Once cooled, the gas is removed from the calorimeter, which is a vacuum chamber, thermally decoupling the dilution from the 4.2 K bath. The $^3$He-$^4$He mixture is then injected via a capillary tube into the dilution and cooled down to 4.2 K by the time it enters the calorimeter. From there, the mixture is further cooled using a 1 K pot and Joule–Thomson impedances, after which it passes through the still and several heat exchangers before reaching the bottom of the cryostat, the mixing chamber.

In the mixing chamber, the phase separation occurs with the concentrated $^3$He phase forming on top of the dilute phase. The dilute phase fills the system up to the still. The still, connected to the pumping line, is at a temperature around 600-800 mK. The still is crucial as it enables the $^3$He evaporation for circulation and also pre-cools the injection capillary that passes through it before reaching the mixing chamber. In some cases, it is

possible to heat slightly the still at a warmer temperature to increase the $^3$He evaporation and optimize the flux of concentrated phase $\dot{n}_3$ circulating.

The pumping triggers the endothermic dilution reaction and the extracted $^3$He gas is then recondensed at room temperature and re-injected through the same capillary, maintaining a continuous flow. This flow of the concentrated phase throughout the circuit will continuously generate the cooling power necessary to maintain the experiment at low temperature.

The role of the heat exchangers located between the still and the mixing chamber is crucial. They cool down the injected $^3$He phase using the cold returning flow that is pumped from the mixing chamber. The cold power of a dilution refrigerator is directly dependent on the initial temperature $T_i$ of the pre-cooled incoming $^3$He phase. The total cooling power $\dot{Q}$ of the dilution circuit can be expressed as:

$$\dot{Q} \approx \dot{n}_3(95T_m^2 - 11T_i^2) \tag{2.16}$$

where $T_m$ is the temperature of the mixing chamber. This formula clearly shows that the two most important parameters for optimal performances are the $^3$He flux $\dot{n}_3$ and the temperature $T_i$ of the concentrated phase entering the mixing chamber.

The primary limitation on the lowest achievable temperature in this setup comes from the initial temperature of the $^3$He phase. Indeed, $T_i$ is fundamentally limited by Kapitza resistance between the helium phase and the heat exchangers. This can be mitigated by maximizing the surface area but cannot be cheated. Different stages and types of heat exchangers can be used: conventional continuous cylindrical heat exchangers allows to go down to temperature between 30-50 mK, while more expensive discrete silver powder heat exchangers can reach temperatures of a few milliKelvins.

To ensure the best possible cooling power $\dot{Q}$, one must maximize the flux. This can be achieved by scaling up the volume of the dilution refrigerator, but beyond a certain point, this would require extremely large and expensive equipments. In practical laboratory conditions, the performance of the dilution refrigerator is also reduced by thermal leaks between the cooling device and external heat sources.

### 2.2.3 Miniature dilution refrigerator or diluette

The dilution refrigerators used in this thesis are of a specific kind, known as miniature dilution refrigerators or "diluettes". These small-scale designs do not have a 1 K pot, replacing it with an additional Joule–Thomson impedance for pre-cooling. These compact designs offer some advantages but also come with drawbacks.

The main advantages arise from their size, which makes them movable during experiments. This allows them to be attached to a mechanical extraction system that enables measurement of the magnetic response in absolute units. They can also be cooled down and warmed up more quickly than conventional refrigerators due to their lower thermal mass. Another notable advantage of these apparatus is their lower construction cost and reduced $^3$He volume requirement (which is hard to find and very expensive).

However, the drawbacks of such systems also stem from their compact design. Indeed, the cooling power of this type of apparatus is limited: $\sim 20$ $\mu$W at 100 mK compared 100-500 $\mu$W at the same temperature for conventional setups. The low power of these

miniature systems makes any thermal leak dramatically impacting their performances. Furthermore, due to limited space, fitting all necessary measurement components can be challenging.

## 2.3 Magnetometry

The concepts introduced in this section are adapted from Ref. [101], where an exhaustive and detailed description of SQUID magnetometer devices can be found.

### 2.3.1 SQUID magnetometers

Superconducting QUantum Interference Device (SQUID) magnetometers are highly sensitive apparatus used to measure extremely weak magnetic fields. A SQUID consists of a superconducting loop containing one (RF-SQUID) or two (DC-SQUID) Josephson junctions. Nowadays, most magnetometers are equipped with DC-SQUIDs because the electronics is simpler. The superconducting material used for these devices is often niobium, which becomes superconducting below 9.2 K. In order to work properly, SQUIDs must be operated at low temperatures, typically around 4.2 K, the temperature of the liquid $^4$He bath.

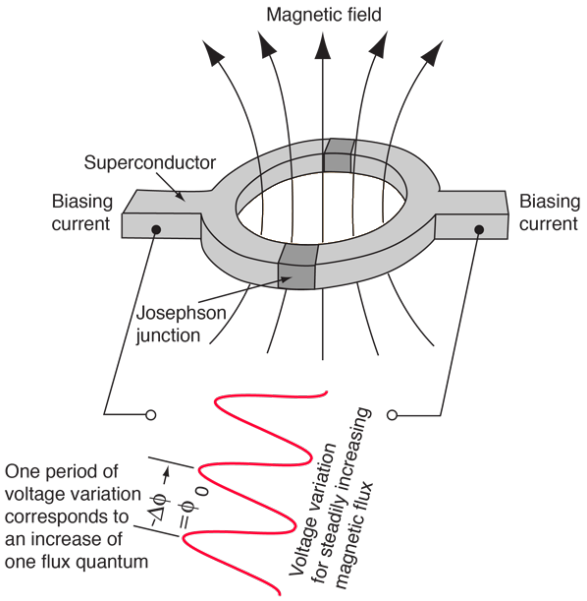


Figure 2.5: Schematic of a SQUID loop operating with a bias current, allowing magnetic flux detection via measured voltage variations. Figure from the website Hyperphysics [102].

The rough working principle of a SQUID is that a current can flow in a superconducting loop without acquiring any voltage as the material is not resistive. However, due to the loop geometry, the current splits into two currents as there are two paths, one on each side of the loop. These currents acquire different phase shifts across the Josephson

junctions when a magnetic flux enters the loop. The resulting phase difference creates quantum interferences, which modulate the total current through the SQUID.

This effect is quantified and creates a periodical current response of the SQUID to external magnetic flux. By applying an appropriate bias current to the SQUID loop, small changes in magnetic flux going through the loop result in a measurable voltage signal (Figure 2.5). Nowadays, modern SQUID designs are more complex but still rely on this fundamental principle. The most sensitive designs use arrays of successive SQUIDs acting as low-noise amplifiers which deliver performances allowing the detection of flux noise down to $\sim 1\mu\Phi_0/\sqrt{\text{Hz}}$ [103].

In magnetic measurements, the periodical voltage response is maintained around a working point using a feedback loop, which enhances greatly the sensitivity of the SQUID. However, this working point can "jump" if the magnetic flux passing through the SQUID device is too high for the sensitivity gain used. By adjusting the resistance of the feedback circuit, the sensitivity gain can be adapted to the magnitude of the expected flux to avoid this issue.

When measuring, the magnetic sample is typically not placed directly on top of the SQUID loop. This is because the measured samples can be large and would saturate the SQUID. Instead, it is better to use a gradiometer or pick-up coil, which inductively detects the sample's magnetic flux and transmits it to the SQUID via another inductive coupling. The geometry and the total induction of the gradiometer affect significantly the quality factor of the transmitted signal.

In our experiments, we used first-order superconducting gradiometers, which consist of two identical coils wound in opposite directions. The sample is placed in the center of one of the coils, enabling measurement of the magnetic flux contribution from the sample only. Indeed, this first-order geometry cancels out the residual static magnetic field. Although more complex higher-order gradiometers exist to cancel higher-order field gradients, our experience and tests showed that they offer little improvement relative to the difficulty of achieving proper coil balancing.

Two main types of SQUID magnetometers were used for the experiments performed in this thesis: extraction magnetometer and noise magnetometer. The specificity and applications of each of these magnetometers will be briefly discussed in the following paragraphs.

#### Extraction magnetometer

In the extraction magnetometer (Figure 2.6), the sample is fixed between two long and thin copper plates which are attached to the mixing chamber of a miniature dilution refrigerator, described in the previous section. These copper plates ensures good thermalization of the sample and Kapton is added to minimize eddy current effects. The base temperature ranges from 50 mK to 100 mK, depending on how optimal the conditions are. The superconducting gradiometer is not in the dilution refrigerator, but instead is mounted in the cryostat and shielded by a cylindrical superconducting shield.

The entire dilution refrigerator is mounted on a mechanical extraction system that moves the sample within the gradiometer. The resulting magnetic flux profile of the sample in the gradiometer is inductively detected by the SQUID device and integrated to yield the absolute magnetic moment. An external superconductive magnetic coil applies

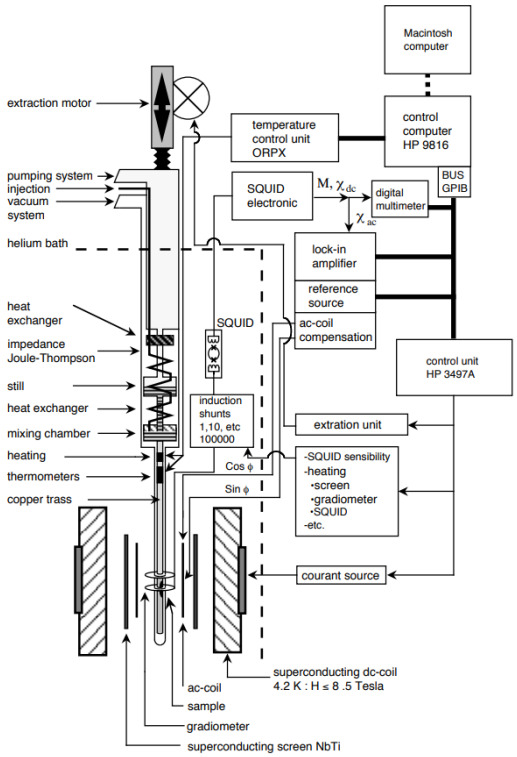


Figure 2.6: Complete schematic of the extraction magnetometers developed by Carley Paulsen at Institut Néel. Figure from Ref. [101].

the magnetic field to the sample.

Two extraction magnetometer setups are in use at Institut Néel, developed by Carley Paulsen [101]. One possesses a superconductive magnet capable of generating fields up to 8 T. The other has a maximum field of 0.4 T but is more sensitive, has less residual magnetic field and a larger frequency bandwidth for ac susceptibility measurements. These two systems are complementary and enable sensitive detection of exotic magnetic phenomena down to very low temperatures and up to relatively high magnetic fields.

### Noise magnetometer

The other existing setup, and the one I worked with the most, is the noise magnetometer. This instrument is still under continuous development and improvement. It was originally designed by Vadim Cathelin and Carley Paulsen a few years before I began my thesis work [72]. One of my objectives was to develop, from scratch, a new noise magnetometer using a spare miniature dilution fridge, capable of reaching lower temperatures and offering better sensitivity. However, numerous technical issues (primarily helium superfluid leaks) delayed construction and testing. After a year of troubleshooting, we decided to postpone development and instead focus on physical measurements using the existing setup.

I will present here the working principle of the current noise setup. In a later section, I will discuss more about the work done for the development of the "not yet" working

setup. Nonetheless, some findings about gradiometer performance and optimization were done thanks to this new development that could already be applied to the existing setup. For now, let's just focus on the concept of the noise magnetometer.

The working concept of a noise magnetometer (Figure 2.7) is really simple but the realization of the apparatus is much more complicated. Indeed, the idea is just to measure time series of spontaneous magnetization fluctuations originating from the spin dynamics in the sample. In practice, this weak noise signal requires an extremely sensitive SQUID and, more importantly, a sample environment with minimal residual magnetic fields.

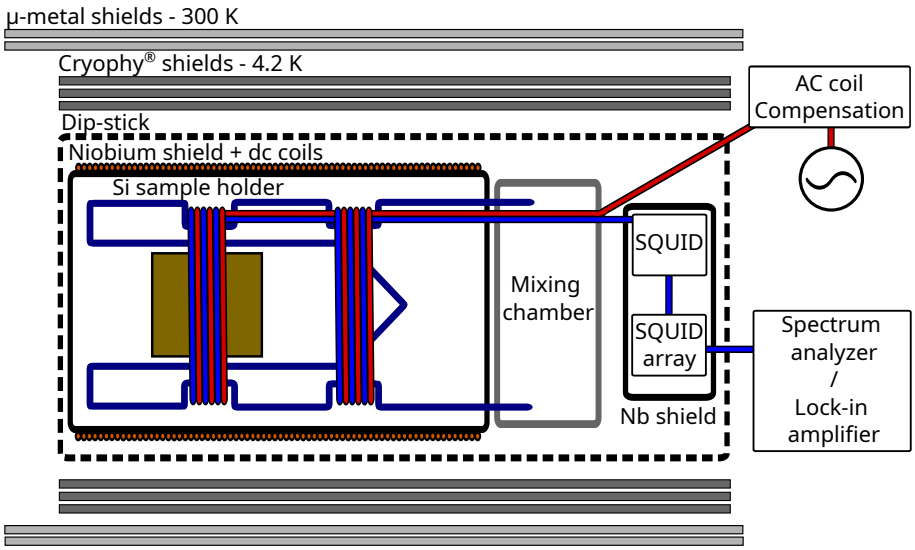


Figure 2.7: Schematic of the experimental setup used to measure both magnetic noise fluctuations and the ac susceptibility. The gradiometer is represented in blue coils, and the excitation coils are represented in red. The sample is represented by a brown square inserted in the silicon sample holder.

To ensure minimal external residual magnetic flux in the sample area, we use several layers of magnetic shielding. Outside the cryostat at room temperature two $\mu$-metal shields are used, and inside the helium bath, three Cryophy® (a Ni-Fe-Mo alloy treated for low temperature performance) shields are inserted leading to a residual magnetic field of the order 50 nT in the bath. More information about the optimization of the residual magnetic field can be found in Chapter 4.1.

The probe is connected to the mixing chamber of a miniature dilution refrigerator which is inserted into the shielded environment. The probe itself is shielded by a Niobium superconducting shield, and consists of a superconducting pick-up coil wrapped around a cylindrical single crystal silicon sample holder attached to the mixing chamber, which ensures a good thermal contact and a low magnetic noise contribution.

If an external field is present in the sample environment, a dc Magnetization vs Temperature (MvsT) response will be measurable. The greater the external field the greater the MvsT response, which will be a source of spurious low frequency noise if the temperature is not perfectly stable. Thus in order to further reduce the residual magnetic field a dc coil was wrapped around the Niobium shield for additional field cancellation. Before the start of an experimental run, measurements of MvsT in the residual field are made.

Then by heating the shield above its superconducting critical point with a small field in the dc coil, and then cooling the shield, the residual field can be reduced. By repeating this protocol the field can usually be adjusted so that the MvsT response of the sample is nearly zero. The final fields were typically less than 5 nT in the sample area.

The gradiometer is connected via mutual induction to the input coil of a Magnicon SQUID with a SQUID array preamplifier, which acts as a very low noise amplifier, measuring spontaneous magnetic fluctuations down to 1.6 $\mu\Phi_0/\sqrt{\text{Hz}}$ [103]. The SQUID is thermalized at liquid helium temperature and is attached to the dilution refrigerator, ensuring that its setup point remains stable throughout the entire measurement.

One of the main distinctive characterisitc of our setup is that in addition to the noise, we can also measure the ac susceptibility to a low applied ac field. It is thanks to two excitation coils wrapped in series which apply small ac magnetic fields (typically 50 $\mu$Oe peak to peak) to the sample. The sample response is then detected by the pick-up coil and processed with a lock-in amplifier, giving the ac susceptibility $\chi = \chi' - i\chi''$, where $\chi'$ is the in-phase response and $\chi''$ the out-of-phase response of the sample. In the case of $Dy_2Ti_2O_7$ and $Ho_2Ti_2O_7$ samples, when cooled down to low temperature (typically under 500 mK), the ac susceptibility signal becomes really weak. It is thus necessary to use an adjustable current divider put between the two excitation coils to minimize any offset in $\chi'$ in order to reach the required sensitivity.

In this setup, the sample is positioned within the gradiometer and cannot be moved in situ. Calibration of the signal in absolute values is not straightforward. Indeed, we tried calibrating the magnetometer by measuring the ac susceptibility of Pb spheres resulting in a calibration factor $k_{\text{Pb}}$, expressed in emu/$\Phi_0$. However the calibration factor is sensitive to the sample position when it is not perfectly centered in the lower detection coil. In addition, when the sample size is comparable to or greater than the geometry of the pick-up coil, the effective measured volume of the sample is smaller than the actual sample volume which in turn affects the calibration.

In order to alleviate these problems, for each sample, the ac susceptibility measured in the noise set-up (in $\Phi_0$) was scaled to the one measured in the extraction SQUID magnetometer presented above. As these magnetometers provide absolute values of the magnetization or susceptibility in emu, the scaling was typically made at 4.2 K and 800 mK in order to get accurate values of the real and imaginary parts of the susceptibility. A scaling factor $k$, expressed in emu/$\Phi_0$, is obtained and is in the range of $k_{Pb}$.

The noise (in $\Phi_0^2$/Hz) is then scaled using the same $k$ factor with the following expression $S((\text{emu/cm}^3)^2/\text{Hz}) = k^2/V^2 S(\Phi_0^2/\text{Hz})$, with $V$ the sample volume. The calibration is checked using the fluctuation-dissipation relation in the thermodynamic equilibrium regime from 4.2 K to 700 mK. For small samples we found that the relation is obeyed with no free parameters over the entire span. However for large samples a mismatch between the noise and susceptibility part was observed, and was corrected with an additional $k'$ factor, which provides information about the effective volume of the sample which is measured.

### 2.3.2 Magnetization and susceptibility

The magnetization $M$ of a material is defined as the total sum of all its internal magnetic moments per unit of volume. Magnetization can provide insights into the nature,

the anisotropy and coupling of the internal magnetic moment within the material. Magnetization is typically studied under high applied magnetic fields, for instance, in the context of magnetic saturation or metastable field-induced phases.

In most cases, we are also interested in the magnetic susceptibility $\chi$ of a material. This quantity represents the magnetic response of the material to an applied field, quantifying how much the material becomes magnetized in an applied field $H$. $\chi$ is defined as the partial derivative of the magnetization $M$ with respect to the applied field:

$$\chi = \left(\frac{dM}{dH}\right)_H \tag{2.17}$$

In practice, when the applied field is small enough for the magnetization to remain linear with the field, we assume that the susceptibility is simply the ratio between $M$ and $H$ giving M=$\chi$H. When performing susceptibility measurements, the applied field can either be static (giving the dc susceptibility $\chi_{dc}$) or time varying (giving the ac susceptibility $\chi_{ac}$). These two types of susceptibility provide complementary insights on the magnetic behavior of a material.

**DC susceptibility**

DC susceptibility is usually studied as a function of temperature and gives a first information about the effective nature of the spin interactions. At sufficiently high temperatures, magnetic materials are generally in a paramagnetic state where the internal magnetic moments do not interact with each other but align weakly with an external field, resulting in a positive magnetization along the direction of that field.

The temperature dependence of the susceptibility $\chi$ in this regime follows the Curie-Weiss law:

$$\chi = \frac{C}{T - \Theta} \tag{2.18}$$

Here, $C$ is the Curie constant of the material and $\Theta$ is the Curie-Weiss temperature. The Curie constant can be expressed for a spin system as:

$$C = \frac{\mu_0 \mu_{eff}^2}{3k_B} N \tag{2.19}$$

where $N$ is the number of atoms, $\mu_0$ is the vacuum permeability, and $\mu_{eff}$ is the effective magnetic moment which depends on the nature of the spin. Thus, the Curie constant $C$ provides information into the magnitude and the nature of the magnetic moments in the material, while $\Theta$ gives insight into the energy scale of the spin interactions. The sign of $\Theta$ indicates whether dominant interactions are ferromagnetic ($\Theta > 0$) or antiferromagnetic ($\Theta < 0$), and in non frustrated systems, $\Theta$ is close to the magnetic transition temperature.

In a perfectly paramagnetic system, $\Theta = 0$ and no long range order is present (though in reality, most systems eventually order at low enough temperature). For ferromagnetic systems ($\Theta > 0$), all moments align spontaneously along the same direction below a transition temperature $T_c$, which is approximately equal to $\Theta$. On the contrary, for

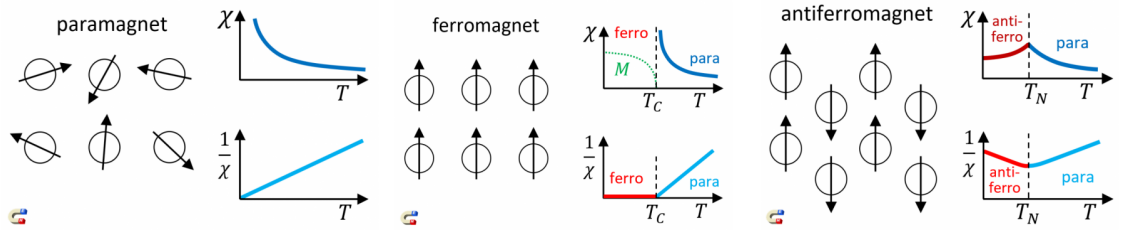


Figure 2.8: Schematic of the spin arrangement and the associated dc susceptibility $\chi$ and its Curie-Weiss behavior $1/\chi$ for three usual magnetic systems. From left to right, the magnetic systems are: the paramagnet, the ferromagnet and the antiferromagnet. Figure from Encyclopedia Magnetica [104].

antiferromagnetic systems ($\Theta < 0$), the moments anti-align spontaneously below a transition temperature, known as the Néel temperature $T_N$, which is roughly $-\Theta$. A schematic of these three different states and their susceptibility temperature behaviors is given in Figure 2.8.

In frustrated magnets, the competition of interactions or the geometry constraints result in a macroscopically degenerate ground state that resists long-range ordering. In practice, frustration degeneracy is often lifted by various mechanisms, leading to a long-range order at a lower temperature than the one expected from the interaction scale. In such cases, a mismatch between the Curie–Weiss temperature and the actual ordering temperature $T_{\text{ord}}$ is observed. The ratio between those two quantities is defined as a frustration coefficient $f$ that estimates how frustrated the system is:

$$f = \frac{|\Theta|}{T_{\text{ord}}} \tag{2.20}$$

For an ideal frustrated ground state, this ratio diverges as no ordering temperature is expected.

Further insights into spin dynamics can be obtained by comparing dc magnetization measurements using two different cooling protocols: Zero Field Cooled (ZFC) and Field Cooled (FC) measurements. In the ZFC procedure, the sample is first cooled in zero magnetic field, and the field is applied only at base temperature before measuring the magnetization upon warming. In the FC procedure, the field is first applied at high temperature and the sample is cooled under this applied field. Then the magnetization is measured while warming, similarly to the ZFC measurement.

If there are slow relaxing magnetic degrees of freedom in the material, the FC measures a state where those degrees are being polarized while the ZFC measures a state with no net initial magnetization. A split of the FC-ZFC curves indicates magnetic relaxation processes with timescales slower than the measurement time. If the dynamic is way faster than the temperature sweeping rate, both protocols will yield close results as the ZFC state will have relaxed towards equilibrium (FC state) during the time of experiment. Since temperature scans often take minutes or hours, this technique is sensitive only to very slow relaxation or spin freezing, such as that arising from domain formation, spin-glass aging, or monopole dynamics [43].

Additionally, even for slow processes, such technique usually does not give access to the characteristic relaxation times of the processes occurring unless a precise tuning of the measurement is made.

### AC susceptibility

Alternatively, the material's dynamic magnetic response to a sinusoidal ac field $H_{ac} = H_{amp}\cos(\omega t)$ can be studied. The resulting magnetization $M_{ac}(t)$ is processed using a lock-in amplifier, giving acces to the complex ac susceptibility $\chi_{ac} = \chi' - i\chi''$, where $\chi'$ is the in-phase (reactive) component and $\chi''$ the out-of-phase (dissipative) component.

This response $\chi_{ac}$ can be studied at fixed frequency during a temperature scan or at fixed temperature with varying frequency. These two measurement modes yield the same information but are chosen depending on the characteristic of the dynamics we focus on. Temperature-dependent measurements are more commonly used to study magnetic transitions and their associated dynamics, while frequency-dependent measurements offer direct insight into magnetic relaxation dynamics. In this thesis, we performed mainly frequency-dependent measurements as the goal was to study the spin ice dynamics.

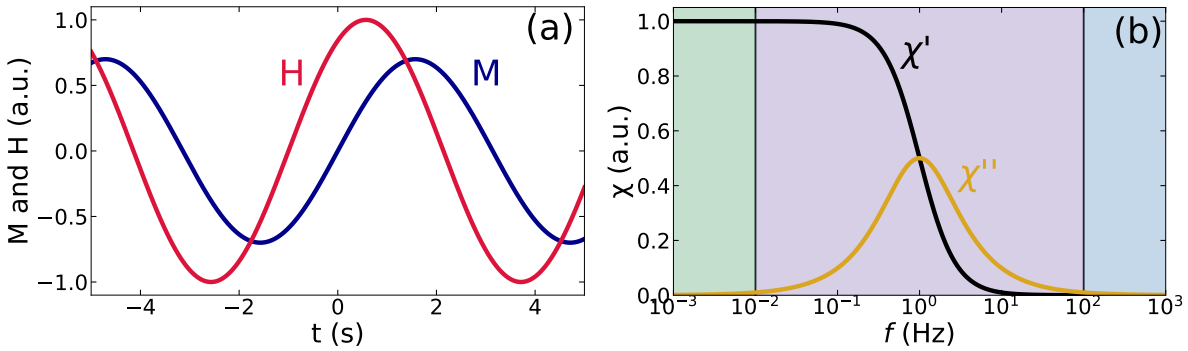


Figure 2.9: (a) Schematic of the typical magnetic response $M(t)$ to an applied ac field for a system presenting a slow magnetic dynamics. (b) Schematic of the susceptibility $\chi'$ and $\chi''$ obtained at a fixed temperature across a large frequency range. The three regimes are highlighted: in green for (i), in purple for (iii) and in blue for (ii).

In frequency measurements, the susceptibility (Figure 2.9(b)) presents, in the presence of a single relaxation time, three characteristic regimes [51]:

(i) $\omega \ll 1/\tau$: This first regime corresponds to the dc limit, where the ac and dc susceptibility are equal. The response is fully in phase with the field and $\chi''$ is equal to 0. The susceptibility in this regime is known as the isothermal susceptibility $\chi_T$.

(ii) $\omega \gg 1/\tau$: This regime is the high frequency limit, where the field oscillates too quickly for the spins to respond accordingly. The measured susceptibility in this regime is known as the adiabatic susceptibility $\chi_S$, which is usually close to 0.

(iii) $\omega \approx 1/\tau$: The intermediate regime, where the drive frequency matches the system's relaxation timescale. This manifests as a resonance peak in $\chi''$, while $\chi'$ shows a step-like transition between the other two regimes.

The frequency at which $\chi''$ peaks corresponds to the characteristic relaxation rate $\tau$ of the system. Following this peak and the shapes of $\chi'$ and $\chi''$ over temperature provides

detailed information on the system dynamics.

The typical frequency bandwidth of commercial set-ups is 0.1 Hz to $10^4$ Hz. In our noise setup, thanks to extremely high stability and to the large frequency bandwidth of the SQUID, we are able to extend this range from 0.001 Hz up to $10^5$ Hz. The high-frequency cutoff arises from the SQUID baseline itself, while the low-frequency cutoff is due to the limitations of the lock-in amplifier.

One issue in high-frequency ac susceptibility measurements is electronic dephasing. Parasitic resistance and capacitance in the measurement electronics can induce a phase shift in the recorded signal. This phase rotation $\theta$ can be quantified by measuring the response in conditions where the sample exhibits no signal or a known signal, usually at low or high temperature. Under such conditions, $\theta$ is estimated as:

$$\theta(f) = \arctan\big(\chi''(f)/\chi'(f)\big) \tag{2.21}$$

Using $\theta(f)$ we can correct our susceptibility data for all temperatures by performing a rotation of phase $\theta$ of both $\chi'$ and $\chi''$. In the noise magnetometer, this correction is sufficient, while in the extraction magnetometers an additional frequency dependent background is found due to eddy currents appearing in the copper sample holder. In that case this background can be evaluated at high temperature and is then subtracted.

For the noise setup, as a consistency check, we compare the corrected ac susceptibility with the measured noise via the fluctuation–dissipation relation, confirming agreement in the high-frequency regime.

### 2.3.3 Magnetic noise

#### General description

In spin ice, magnetic monopoles are deconfined quasi-particles that can move almost freely along the diamond lattice defined by the centers of the tetrahedra in the pyrochlore lattice. If interactions between monopoles are neglected, their motion resembles a three-dimensional random walk, a discrete analogue of the known Brownian motion. In such stochastic processes, the path of the particle gives rise to spatial and temporal noise, and analyzing the characteristics of this noise provides direct insight into the nature of the underlying dynamics.

In our case, the creation, annihilation and motion of monopoles results from spin-flip events that will produce spontaneous fluctuations in the magnetization $M(t)$, even in the absence of an external field. These fluctuations constitute the intrinsic or "internal" magnetic noise of the system. To measure it, we use the highly sensitive noise magnetometer (see Section 2.3.1 for technical details). The measured noise is a bulk quantity as it reflects a spatial average over all dynamical processes occurring throughout the sample volume. While more spatial sensitive noise measurements could in principle be realized using small SQUIDs, such experiments require significantly more complex instrumentation.

Rather than analyzing the raw time trace $M(t)$, which typically appears disordered, we examine its autocorrelation function:

$$C(t) = \langle M(0)M(t)\rangle \tag{2.22}$$

The form of the decay of the autocorrelation function $C(t)$ characterizes the system dynamical processes. The autocorrelation function can also be studied in the frequency domain by taking its Fourier Transform. By doing so we obtain a new quantity which is the Power Spectral Density (PSD) of the magnetic noise:

$$S(f) = \mathscr{F}[\langle M(0)M(t)\rangle] \tag{2.23}$$

In this thesis we studied the frequency form of the noise $S(f)$ rather than $C(t)$ as it compares more naturally to the frequency-dependent ac susceptibility measurements.

To get a better understanding of noise dynamics, we can look at three well-known processes [105]. Figure 2.10 illustrates time series and PSDs for these three cases:

- White noise (blue): Noise generated from uncorrelated random variables with zero mean value and finite variance. The intensity is constant for all frequencies so its PSD is flat.

- Brownian noise (gold): Noise generated from a Wiener process, showing a $1/f^2$ dependence in the PSD. It is a non-stationary process with a variance that scales linearly with time, hence diverging. It is not suitable to describe physical systems like spin ice, as the magnetization should not diverge over time.

- Ornstein-Uhlenbeck (OU) noise (purple): Noise generated from a modified Brownian process with added friction which results in a mean-reverting motion (mean value of the noise is constant). It exhibits a characteristic timescale $\tau$, corresponding to the typical time for the system to relax back to equilibrium.

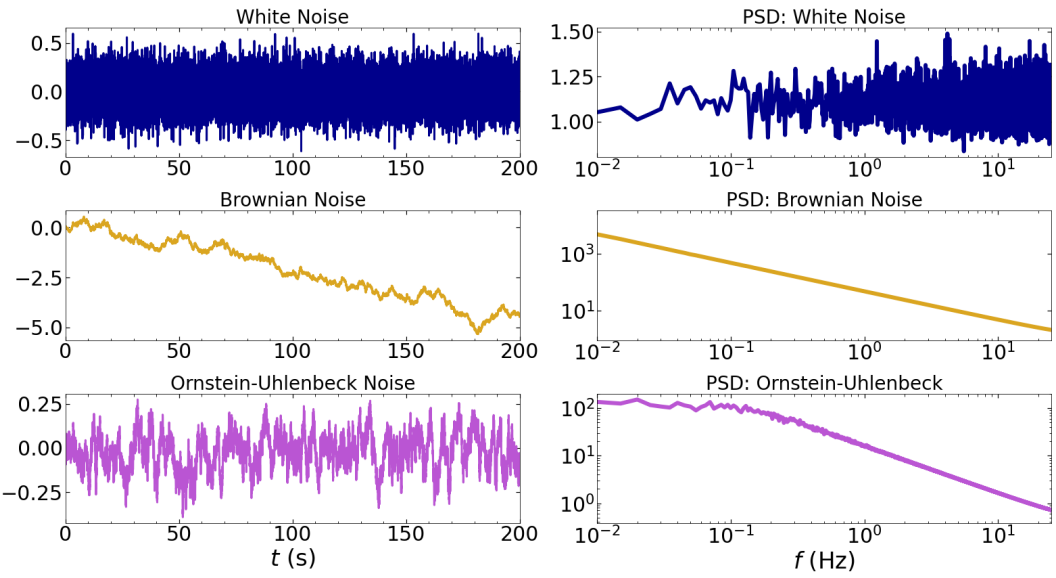


Figure 2.10: Illustration of three different types of noise: white noise (in blue), Brownian noise (in gold) and Ornstein-Uhlenbeck noise (in purple) and their corresponding Power Spectral Density (PSD). The noise and PSD are expressed in arbitrary units.

The OU process, is a process that describes a single relaxation timescale. As for ac susceptibility we find for this noise process three characteristic frequency regimes. The PSD of the OU process can be analytically calculated giving:

$$S(f) = \frac{S_0}{1 + (2\pi f \tau)^2} \tag{2.24}$$

with $S_0$ the intensity of the low frequency plateau. The low frequency regime, characterized by a flat PSD is reminiscent of the white noise, while the higher frequency power law slope is reminiscent of the PSD of a Brownian motion. The intermediate regime, with a shoulder shape, corresponds to the crossover between the white and Brownian noise behavior. The inflection point corresponds to the timescale $\tau$ of the process. We see here that noise and ac susceptibility curve carries a similar information about the dynamics of a system, which is expected from the FDT for equilibrium states.

However, as we will see in detail later, the OU process fails to fully describe spin ice dynamics. In spin ice, the high frequency power low exponent varies with temperature between 1 and 2, while it is constant and equal to 2 in the OU process. This behavior is referred to as a subdiffusive process and reflects constrained dynamics that cannot be easily captured by a single theoretical process. Later in this thesis, we will use empirical models (Section 3.1.5) to extract relevant dynamic parameters that characterize the measured noise.

#### External Noise and Cleaning Procedure

In experiments, the magnetic noise coming from the sample, that we can call "internal" noise, is inevitably superimposed with various sources of "external" parasitic noise. These includes SQUID noise (intrinsic to the device), and environmental noise such as mechanical vibrations, 50 Hz noise, or harmonics from the pumping system of the dilution (like turbo pumps).

To ensure that the sample signal dominates, one must confirm that external contributions remain well below the measured internal noise. For that we need to understand the frequency behavior of the different "external sources" the setup measures.

The SQUID noise is directly a function of its sensitivity and can be characterized with empty noise measurements. Figure 2.11(a) shows the noise PSD of the SQUID alone (in grey) and attached to the empty gradiometer (in blue). This PSD consists of a flat spectrum with a 1/f slope below a corner frequency (around 4 Hz for our Magnicon SQUID array [103]). This spectrum defines a baseline of the measurement below which fluctuations from the sample will not be detected. Our choice of the SQUID device was dictated by the quality of this baseline.

Environmental noise that happens at fixed time period appears as peaks well defined in the frequency domain. The intensity of such events varies on how well they are coupled to the setup. They create a "forest" of peaks of different intensities and can be removed easily when they are well defined in frequency and not too numerous. However, poor setup conditions (like bad magnetic shielding) can cause so many parasitic contributions that the sample noise becomes completely masked.

Other environmental noise that are randomly distributed in time also occurs and are detected by the system. This type of noise will introduce a low frequency $1/f$, similar in

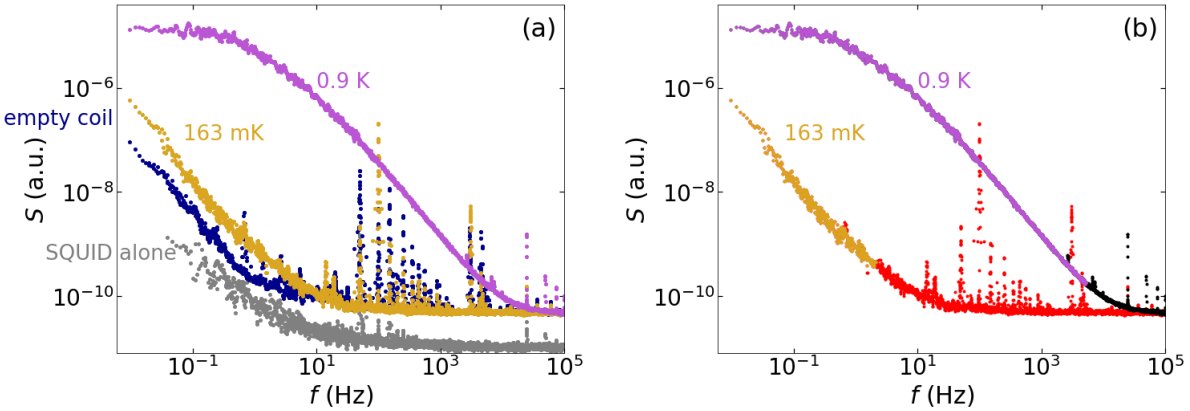


Figure 2.11: (a) Magnetic PSD measured for the SQUID when it is not connected (SQUID alone: grey), the SQUID connected to an empty gradiometer (empty coil) and the raw 0.9 K and 163 mK curves of $Ho_2Ti_2O_7$ (purple and gold respectively). (b) Magnetic PSD of the cleaned 0.9 K and 163 mK $Ho_2Ti_2O_7$ curves using the same color as in plot (a). The discarded points are shown in red for 163 mK and black for 0.9 K.

shape to the SQUID's own baseline. If those events are sufficiently shielded they should not be observed as their intensity will be lower than the SQUID low frequency baseline.

We perform a systematic cleaning procedure on the measured noise curves to remove the "external" noise contributions. The well defined peaks are removed manually and the crossover region between the sample signal and SQUID baseline together with the SQUID baseline are discarded.

Figure 2.11(a) shows raw PSD measurements at 0.9 K and 163 mK for $Ho_2Ti_2O_7$, compared to empty coil and SQUID-alone spectra. Figure 2.11(b) presents the cleaned data, with discarded points indicated.

### 2.3.4 Measuring the fluctuation-dissipation theorem

The fluctuation-dissipation theorem (FDT) relates the equilibrium fluctuations of an observable $M$ to its linear response to an applied field $h$, which is conjugate to $M$ [106]. The Hamiltonian in the presence of this field is given by $H(h) = H(0) - hM$. The response function $\chi_M$ of $M$ at time $t$ (with $t > t'$) to a perturbation of the applied field $h$ at time $t'$ is given by:

$$\chi_M(t,t') = \frac{\delta\langle M(t)\rangle}{\delta h(t')} \tag{2.25}$$

with $\langle ...\rangle$ standing for an ensemble average. The fluctuations of the observable $M$ are quantified through its autocorrelation function:

$$C_M(t,t') = \langle M(t)M(t')\rangle - \langle M(t)\rangle\langle M(t')\rangle \tag{2.26}$$

The FDT then connects these two quantities through the relation:

$$\chi_M(t,t') = \frac{1}{2k_BT}\frac{d}{dt'}C_M(t,t') \tag{2.27}$$

This expression can be passed in the frequency domain:

$$\mathrm{Im}[\chi_M(\omega)] = \frac{\omega}{2k_BT} S_M(\omega) \tag{2.28}$$

where $S_M(\omega)$ is the power spectral density of $M(t)$. The above expression represents the FDT in the classical limit $\hbar\omega \ll k_BT$, where quantum fluctuations are negligible.

In the case where the observable $M$ corresponds to magnetization and the conjugate field $h$ is the applied magnetic field, the FDT can be rewritten in CGS units with the following form [107]:

$$S(f) = D(f) \quad \text{with} \quad S(f) = \overline{M^2(f)} \quad \text{and} \quad D(f) = \frac{2k_\mathrm{B}T}{\pi V} \frac{\chi''(f)}{f} \tag{2.29}$$

Here, $V$ is the sample volume, $D(f)$ is the dissipative component defined from $\chi''$ the out-of-phase component of the ac susceptibility, and $S$ represents the power spectral density of the spontaneous fluctuations of magnetization. This equation is the magnetic fluctuation-dissipation relation (FDR), derived from the FDT.

A distinction is made between the FDT, which is a theorem valid only in equilibrium, and the FDR, which is an extended relation that can be disobeyed and used for out-of-equilibrium system. When performing measurements, we test the FDT by comparing the measured FDR to the expected theoretical behavior. If deviations are observed, we say that the FDT is "violated", not in the sense of being broken but rather that it is not applicable, as the system is not in equilibrium. Such deviations are a strict confirmation of the existence of non-equilibrium dynamics.

To quantify deviations from the FDT using the FDR, an effective temperature $T_{eff}$ can be defined via the fluctuation-dissipation ratio [66]:

$$T_{eff}(f) = T \frac{S(f)}{D(f)} \tag{2.30}$$

When $T_{eff} = T$, the system is under equilibrium conditions and the FDR becomes the FDT. The effective temperature is frequency-dependent. Thus, in systems with a separation of timescales, the FDT may hold within a certain frequency range ($T_{eff} = T$), while deviations can appear at low frequencies ($T_{eff} > T$).

This implies that a system may appear to be in equilibrium over experimentally accessible timescales, while actually being out of equilibrium on much longer ones. Therefore, the absence of FDT violations is not a definitive proof of equilibrium.

In the presence of an out-of-equilibrium system, like in spin ice below the freezing temperature [43], knowing the respective behavior of the noise and the ac susceptibility enables a deeper understanding of the underlying non-equilibrium state.

The following chapter presents the results of our measurements of ac susceptibility and noise of $Dy_2Ti_2O_7$ and $Ho_2Ti_2O_7$ spin ice compounds, across both equilibrium and freezing dynamical regimes. The analysis of noise and ac susceptibility is carried out using specific empirical models previously established in the literature [51, 65]. The fluctuation-dissipation relation (FDR) is systematically tested over the entire temperature range accessible with our noise magnetometer (150 mK to 4.2 K), revealing intriguing deviations from equilibrium behavior at low temperatures.

# Chapter 3

# Spin ice dynamics

## Contents


**3.1 Equilibrium dynamics . . . . . 58**
3.1.1 Experimental method . . . . . 58
3.1.2 Magnetic susceptibility measurements . . . . . 59
3.1.3 Noise measurements . . . . . 60
3.1.4 FDR in equilibrium . . . . . 61
3.1.5 Dynamics analysis using empirical models . . . . . 62
3.1.6 Results and discussion on the equilibrium dynamics . . . . . 66
**3.2 Low temperature regime . . . . . 72**
3.2.1 FDR violations . . . . . 72
3.2.2 New relaxation process at low temperature . . . . . 75
**3.3 Conclusion about spin ice dynamics . . . . . 78**
**3.4 Demagnetization corrections . . . . . 80**
3.4.1 The demagnetization effect . . . . . 80
3.4.2 The need for demagnetization corrections in noise measurements 81
3.4.3 Experimental procedure . . . . . 82
3.4.4 Estimation of N factors in $Ho_2Ti_2O_7$ . . . . . 83
3.4.5 Kramers-Kronig integration for correcting the noise . . . . . 88
3.4.6 Behavior with N . . . . . 90
3.4.7 Impact of $N$ as a function of temperature . . . . . 94
**3.5 $Dy_2Ti_2O_7$ isotopic differences . . . . . 96**

This chapter is devoted to unraveling the physics of dynamical processes in classical spin ice, focusing on the two emblematic compounds $Dy_2Ti_2O_7$ and $Ho_2Ti_2O_7$. The aim is to shed light on the nature of monopole dynamics across different regimes, from equilibrium to freezing, and to compare experimental observations with theoretical expectations. The chapter is structured into four parts.

Section 3.1 introduces the correlated dynamics of monopoles in the equilibrium regime, introducing the central concepts and empirical models that provide physical interpretation of the data. Building on these results, Section 3.2 explores how the dynamics evolve below the freezing transition, where the FDR becomes a powerful probe to distinguish equilibrium from out-of-equilibrium processes. The work presented in these first two sections contains the first noise measurements ever performed on the $Ho_2Ti_2O_7$ compound, along with a precise evaluation of the FDR over a large frequency and temperature range. These results have been recently published in Ref. [108].

Section 3.4 discusses a more technical but crucial point: the puzzling role of demagnetization effects in noise measurements, which raises questions about how the intrinsic dynamics can be extracted from experiments. Finally, Section 3.5 considers the potential influence of rare-earth isotopes on spin ice dynamics in $Dy_2Ti_2O_7$, highlighting how subtle parameters may play a decisive role in shaping the observed quantitative behavior.

Altogether, this chapter emphasizes the richness and complexity of spin ice dynamics and the variety of factors (microscopic, collective, and experimental) that must be accounted for to reach a consistent understanding.

## 3.1 Equilibrium dynamics

Noise and ac susceptibility provide the same information on the magnetic dynamical processes in a system at equilibrium. The primary interest for studying the FDR is to uncover the properties of out-of-equilibrium regimes, which, in the spin ice case, are expected to appear below 600 mK [43]. Nevertheless, even the equilibrium dynamics of spin ice materials are not yet fully understood. It is therefore essential to first investigate what information each technique provides about the equilibrium dynamics of spin ices and how this relates to the FDR within the expected equilibrium regime.

As discussed in more detail in Section 1.3, spin ice dynamics can be understood as the motion of interacting quasi-particles called magnetic monopoles. The relaxation times measured in this section using ac susceptibility and noise correspond to the characteristic timescales of monopole dynamics. In the equilibrium regime investigated here, we expect monopole dynamics driven by creation, recombination, and hopping processes above the spin ice transition around 2 K. Below this temperature, monopole creation is no longer entropically favorable, and the dynamics are governed solely by monopole hopping and recombination, while the monopole density strongly decreases when lowering the temperature.

### 3.1.1 Experimental method

In this study, we present data collected for the two most widely studied spin ice materials: $Dy_2Ti_2O_7$ and $Ho_2Ti_2O_7$. During my PhD thesis, we measured both the

magnetic noise and ac susceptibility in six different configurations: two for $Dy_2Ti_2O_7$ and four for $Ho_2Ti_2O_7$. The magnitude and quality of the noise data are strongly dependent on the sample's filling factor in the gradiometer. Therefore, we present in this section the data obtained from the samples with the optimal filling factor for each material: a parallelepiped sample of $^{162}Dy_2Ti_2O_7$ measuring $3.7 \times 5.1 \times 14$ mm$^3$ (with zero Dy nuclear moment) [38, 109], and a nearly cylindrical $Ho_2Ti_2O_7$ sample of 4.8 mm diameter and 8.9 mm length (see Figure 3.1).

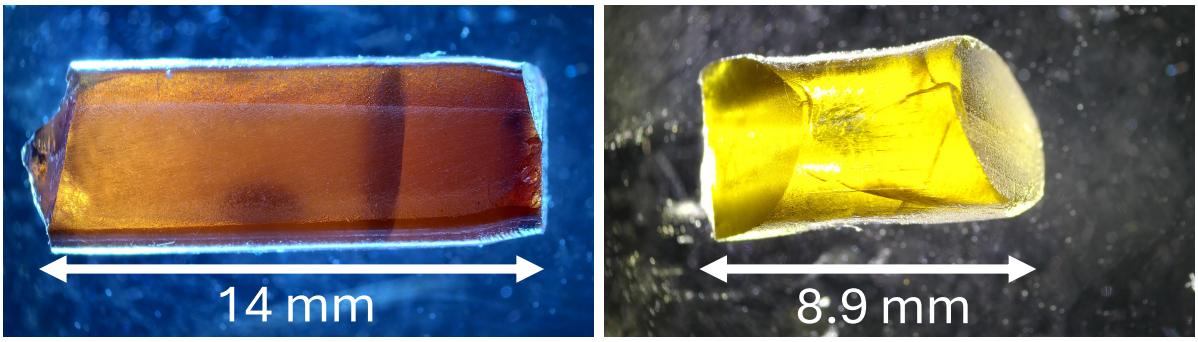


Figure 3.1: Left photo: $Dy_2Ti_2O_7$ sample. Right photo: $Ho_2Ti_2O_7$ sample.

The samples were cooled down to base temperature in a minimal external field environment, using the procedure described in Section 2.3.1. As this section focuses on equilibrium properties, we present the ac susceptibility and noise curves for temperature above 600 mK. Analysis and measurements for temperatures below 600 mK are discussed in Section 3.2.1. Both quantities were measured successively at fixed temperature, from 600 mK to 1.5 K in 100 mK steps, and then up to 4.2 K in 500 mK steps. A full frequency scan ($10^{-3}$-$10^5$ Hz) typically takes about 3 hours 30 minutes for noise measurements, and 2 hours for ac susceptibility. Above 800 mK, to reduce acquisition time, we narrow the frequency range by omitting frequencies below 0.1 Hz, where the behavior of the noise and ac susceptibility both show frequency independent behavior. For the noise measurements, the final data were obtained from the average of at least three scans to reduce standard deviation. In this temperature regime, neither the susceptibility nor the noise show time dependence behavior as thermalization of the sample is fast, hence no special care is needed.

### 3.1.2 Magnetic susceptibility measurements

Figure 3.2(a) show the ac susceptibility measured for the $Dy_2Ti_2O_7$ sample in the equilibrium regime. The curves show the expected behavior, with a peak in $\chi''(f)$ corresponding to the intermediate regime in $\chi'$, lying between the isothermal susceptibility $\chi'_T$ and the adiabatic susceptibility $\chi'_S$ [51]. From 4.2 K down to approximately 2 K, changes in dynamical properties are small, as the system remains in the plateau regime. Below 2 K, the dynamics start slowing down exponentially, causing a big shift of the $\chi''$ peak

toward lower frequencies. At 600 mK, the $\chi'$ plateau and the end of the peak of $\chi''$ are still within the frequency bandwidth of the setup.

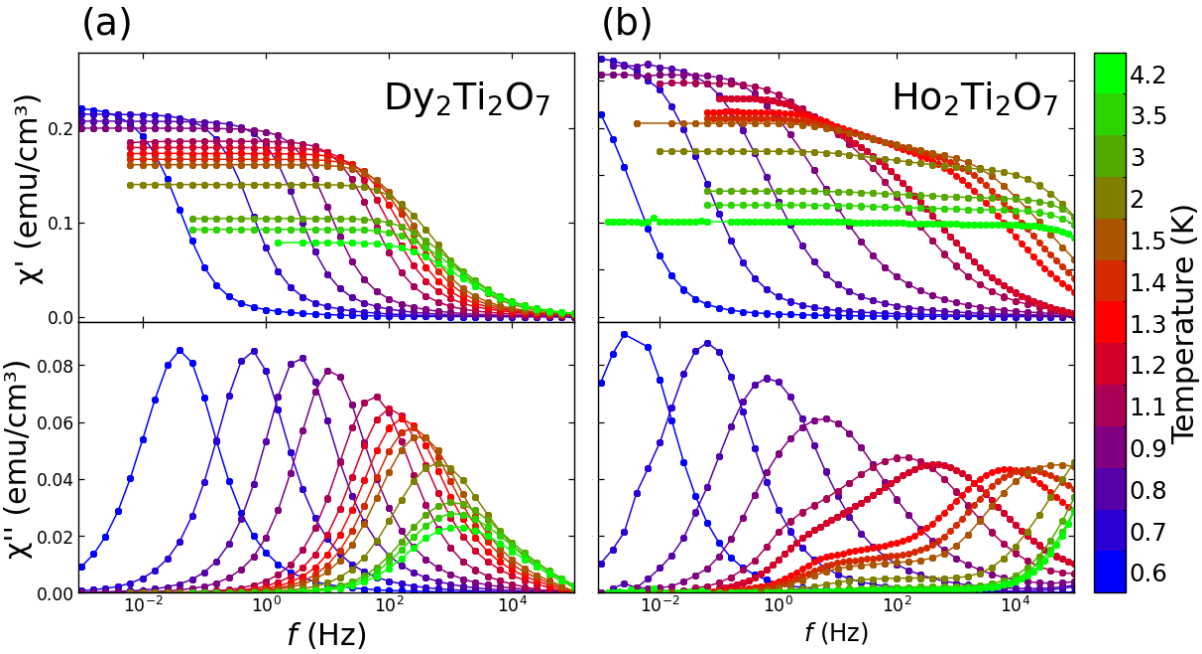


Figure 3.2: (a) $Dy_2Ti_2O_7$ and (b) $Ho_2Ti_2O_7$ ac susceptibility $\chi'$ (top panel) and $\chi''$ (bottom panel) vs $f$ for different temperatures. Lines are guides to the eye.

Figure 3.2(b) shows the ac susceptibility of $Ho_2Ti_2O_7$. The ac susceptibility behavior of $Ho_2Ti_2O_7$ is more complicated than the $Dy_2Ti_2O_7$ one, because of the presence of not only one but two distinct peaks in $\chi''$ indicating two characteristic dynamical timescales (previously observed in Ref. [57]). These two peaks are well separated above 900 mK and gradually merge into a broad peak when relaxation times start diverging at lower temperatures. It is interesting to notice that the overall dynamics of $Ho_2Ti_2O_7$ occur at higher frequencies than the one of $Dy_2Ti_2O_7$ for similar temperatures, with the high frequency relaxation time for $Ho_2Ti_2O_7$ exceeding our measurement limit ($10^5$ Hz) above 2 K.

### 3.1.3 Noise measurements

Figures 3.3(a) and (b) display the magnetic noise power spectral density (PSD) $S(f)$, for $Dy_2Ti_2O_7$ and $Ho_2Ti_2O_7$ respectively , across the same temperature range as the ac susceptibility shown above. The $Dy_2Ti_2O_7$ noise spectra exhibit a low frequency plateau, an intermediate region presenting a shoulder located at the relaxation resonance, and a high frequency power law decay. As temperature decreases, the shoulder shifts to lower frequencies as the relaxation is slowing down, and the low-frequency plateau increases in magnitude. The $Ho_2Ti_2O_7$ spectra follow the same tendency, but with two distinct intermediate regimes, consistent with the presence of two separate relaxation times.

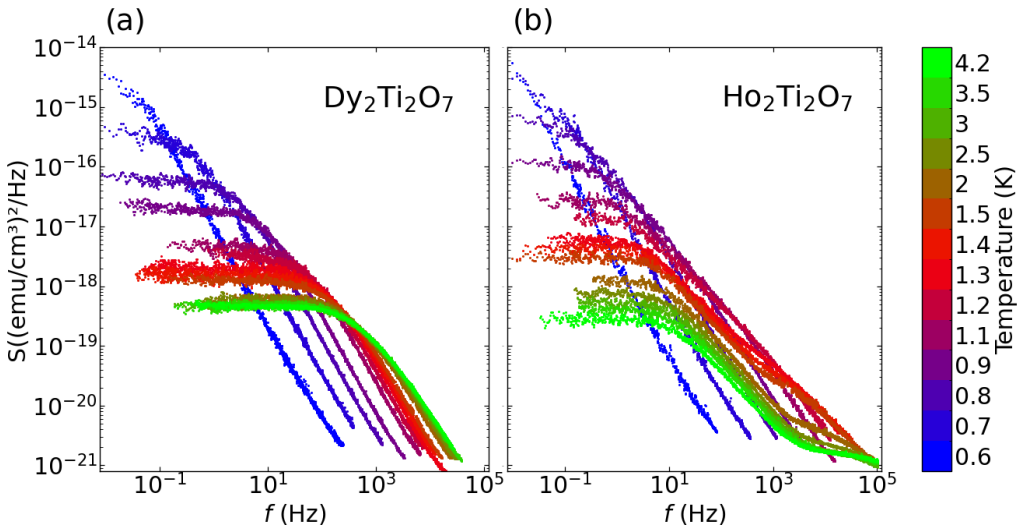


Figure 3.3: Power spectral density of noise $S(f)$ measured for (a) $Dy_2Ti_2O_7$ and (b) $Ho_2Ti_2O_7$ on a logarithmic scale measured between 4.2 K and 600 mK.

### 3.1.4 FDR in equilibrium

Just by taking a quick look at the data, we see that the noise and ac susceptibility measurements show the same overall behavior with respect to both temperature and frequency. Using the FDR (Equation 2.3.4), we can transform the measured out-of-phase susceptibility $\chi''(f)$ into its noise analog $D(f)$, allowing a direct and quantitative test of the FDT. Figure 3.4 shows $D(f)$ for both materials (following the calibration method described in Section 2.3.1) for the corresponding $\chi''(f)$ shown in Figure 3.2.

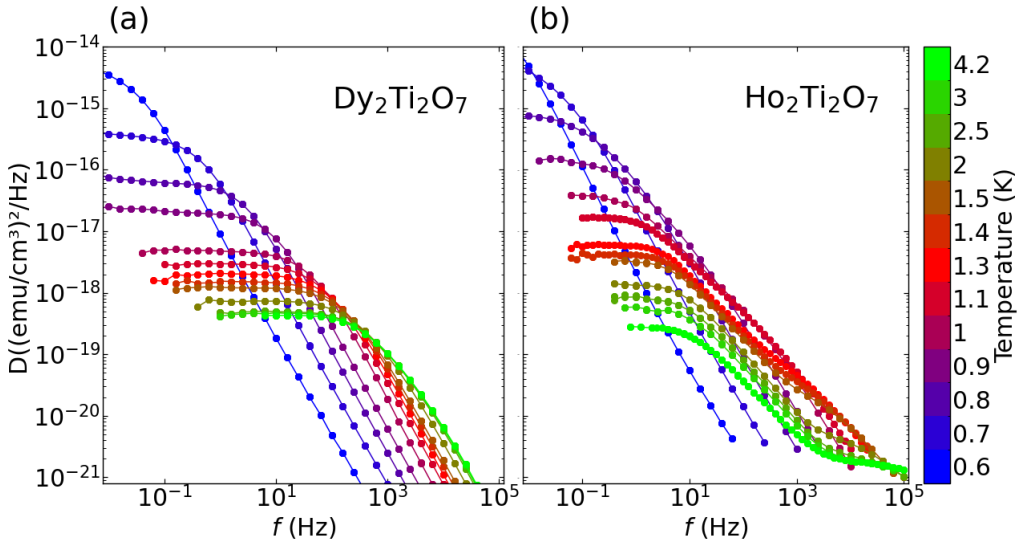


Figure 3.4: $D(f)$ obtained from the measured magnetic susceptibility $\chi''(f)$ for (a) $Dy_2Ti_2O_7$ and (b) $Ho_2Ti_2O_7$ on a logarithmic scale measured between 4.2 K and 600 mK. Lines are guides to the eye.

We can now plot $D(f)$ and $S(f)$ together to check if they indeed match at all temperatures and frequencies, as predicted from the FDT in this temperature regime. Figure 3.5 shows these two quantities for selected temperatures between 4.2 K and 600 mK for $Dy_2Ti_2O_7$ (a) and $Ho_2Ti_2O_7$ (b). Although only a few temperature points are shown in Figure 3.5 for clarity, the FDR holds for all the temperatures in this range. This result was expected, but is of crucial importance as it validates all our experimental procedure, especially our calibration method introduced in Section 2.3.1.

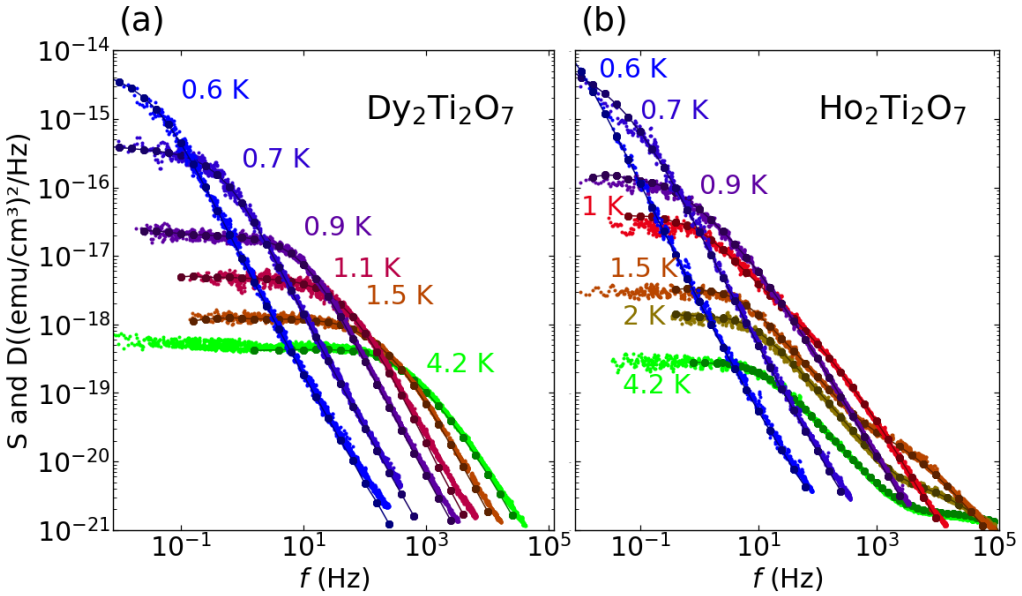


Figure 3.5: FDR plot for (a) $Dy_2Ti_2O_7$ and (b) $Ho_2Ti_2O_7$ on a logarithmic scale: $S(f)$ (small dots) and $D(f)$ (big dots) measured between 4.2 K and 600 mK. Lines are guides to the eye.

The analysis presented here gives a good first idea about the key interest in the dynamics of the spin ice materials $Dy_2Ti_2O_7$ and $Ho_2Ti_2O_7$ in the equilibrium regime. It is possible to extend this analysis by introducing empirical fitting models to extract detailed informations about the dynamics. In the following section, we will introduce such models and discuss the insights they offer into the dynamical properties of these systems. This FDR analysis in the equilibrium regime opens naturally an interest in the behavior of such relation in the low temperature regime. We will explore in details the low temperature properties of the FDR and the dynamics in a later section (Section 3.2.1).

### 3.1.5 Dynamics analysis using empirical models

#### AC susceptibility

Magnetic ac susceptibilities have been studied extensively across a wide range of systems. Many different empirical response functions were introduced to catch the main characteristics of the dynamics of those different systems [51]. These models arise from linear response theory and are usually analog to the models introduced earlier for dielectric

relaxation. The most straightforward response function one can use is introduced in the Debye model [110] (Figure 3.6, green curves):

$$\chi(f) = \chi_S + \frac{\chi_T - \chi_S}{1 + i2\pi f\tau} \tag{3.1}$$

This expression describes phenomena that relax with a single time scale. However spin ice is a strongly correlated state in which this picture of a single characteristic time scale is insufficient. In this case, it is necessary to introduce a distribution of relaxation times around a characteristic time scale $\tau$. The distributions can be parameterized by a single exponent parameter, and three different models can be derived from the Debye model this way. We will not discuss the Havriliak-Negami model [111] which introduces not only one but two new exponent parameters, resulting in possible over-parameterization of the fits.

The first model, with a symmetric $\tau$ distribution can be obtained by introducing a new exponent parameter $\gamma$, giving the generalized Debye model (Figure 3.6(a), gold curves):

$$\chi(f) = \chi_S + \frac{\chi_T - \chi_S}{1 + (i2\pi f\tau)^\gamma} \tag{3.2}$$

The second empirical model, the Cole-Davidson model (Figure 3.6(a), red curves) possesses an asymmetric $\tau$ distribution and is expressed as:

$$\chi(f) = \chi_S + \frac{\chi_T - \chi_S}{(1 + i2\pi f\tau)^\beta} \tag{3.3}$$

In the generalized Debye model, decreasing the exponent $\gamma$ from 1 to 0 symmetrically broadens the distribution around the $\tau$ value. It introduces a factor $(\omega\tau)^\gamma$ in the numerator of the $\chi''$ expression, resulting in a finite slope behavior at low frequencies when considering its noise analog $D(f)$ (see top panel, Figure 3.6). This is incompatible with our noise measurements, which show a flat "white noise" behavior in the low frequency limit.

For the Cole-Davidson model, varying $\beta$ from 1 to 0 results in a strong asymmetric broadening for time scales shorter than $\tau$ due to a cutoff in the distribution of relaxation times. This cutoff results in a flat shape at low frequencies of the associated noise, which agrees with the noise measurements. Due to this compatibility with the noise behavior, the Cole-Davidson model is chosen for the fitting procedure of the ac susceptibility curves.

The Cole-Davidson model fit is applied to both $Dy_2Ti_2O_7$ and $Ho_2Ti_2O_7$. For $Ho_2Ti_2O_7$, since there are two well separated timescales visible in the data, the fitting function is the sum of two Cole-Davidson functions. $\chi'$ and $\chi''$ are fitted simultaneously to ensure that one set of parameters reproduces both quantities and is consistent to Kramers-Kronig relations. This analysis accurately describes the $Dy_2Ti_2O_7$ data (Figure 3.6(b)) across the entire temperature range.

In the case of $Ho_2Ti_2O_7$, the fits are of poorer quality in the intermediate temperature range (between 1 and 1.5 K), where the two time scales are well separated (Figure 3.6(b)). This discrepancy is explained by the asymmetric nature of the model, which induces a non vanishing high frequency contribution for a given broadness. Thus, the low frequency peak in the fit possesses a significant intensity at higher frequencies, which affects the fitting of the higher frequency peak. The fits then need to find an optimum between

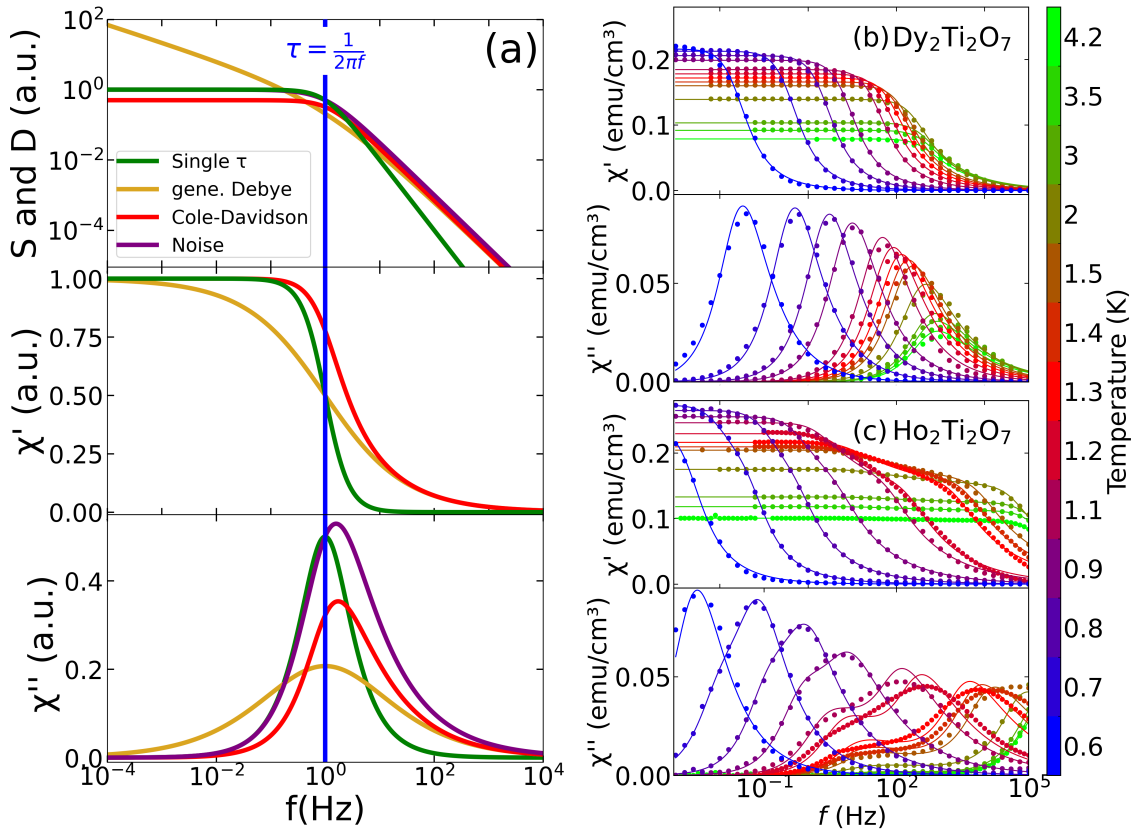


Figure 3.6: (a) Response functions as a function of frequency for the Debye model (single $\tau$), the generalized Debye, the Cole-Davidson and the noise and in green, gold, red and purple respectively. $D(f)$ and $S(f)$ (top panel), real part $\chi'$ (middle panel) and imaginary part $\chi''$ (bottom panel) of the ac susceptibility. Parameters are: $\chi_S$=0, $\chi_T$=1, $\tau$=$\frac{1}{2\pi}$ (represented by the blue line) and $\beta$=$\gamma$=0.5. (b) $Dy_2Ti_2O_7$ and (c) $Ho_2Ti_2O_7$ ac susceptibility $\chi'$ (top panel) and $\chi''$ (bottom panel) vs $f$ for different temperatures. Dots represent measured data and lines represent the Cole-Davidson fits.

matching the broadness and the intensities. For the specific case of $T = 1.1$ K, Figure 3.7 shows that the generalized Debye model does not have this issue. However, for the reasons explained above, this generalized Debye model is incompatible with the noise measurements.

These results show the complexity of spin ice dynamics, which cannot be reproduced by any of the empirical models introduced in the literature. Nonetheless, these models provide valuable information on the characteristic timescales and their associated distributions. The low-frequency behavior of the noise indicates a cut-off in the dynamics at low frequency, consistent with the Cole–Davidson model. However, the strong asymmetry of this model distribution fails to capture the shape of the susceptibility, suggesting instead a more symmetric distribution, closer to the generalized Debye model.

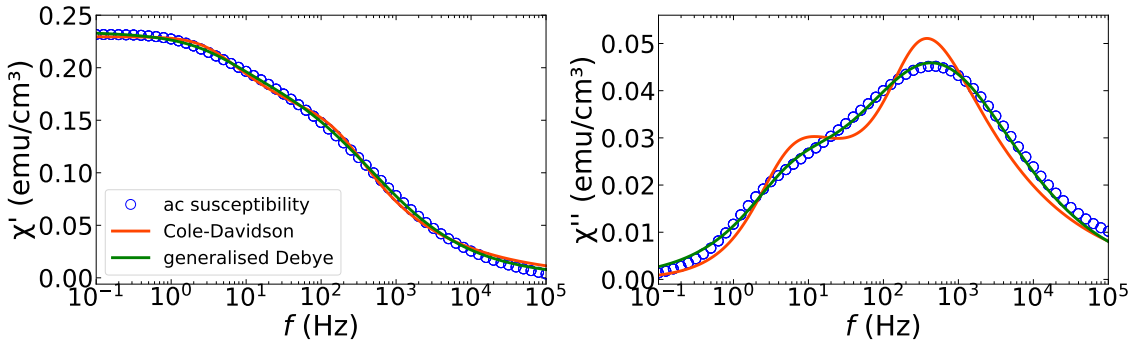


Figure 3.7: Real part $\chi'$ (top panel) and imaginary part $\chi''$ (bottom panel) of the measured ac susceptibility in $Ho_2Ti_2O_7$ at 1.1 K (blue dots) compared to Cole-Davidson (orange) and generalized Debye (green) fits.

### Noise

On the other hand, for the noise, the analog of the Debye ac susceptibility model is derived from the Fourier Transform of the Langevin equation describing fluctuations due to generation-recombination processes of monopoles pairs of charges $\pm m$ [112]. This model predicts a PSD proportional to the Ornstein-Uhlenbeck process (seen in Section 2.3.3) with:

$$S(f) = \frac{4\sigma_N^2 \tau}{1 + (2\pi f \tau)^2} \tag{3.4}$$

Here, $\sigma_N^2$ is the variance in the number of monopoles pairs, $N$, in the system. This model considers a low concentration of monopoles and treats them as non-interacting quasi-particles neglecting any correlations between them.

This model is similar to the Debye model for the ac susceptibility, and cannot reproduce well the data for the same reasons. The first empirical noise fit model used to reproduce $Dy_2Ti_2O_7$ magnetization noise spectra was introduced by Dusad et al. [65] by modifying the case of non-interacting monopoles:

$$S(f) = \frac{S_0}{1 + (2\pi f \tau)^\alpha} \tag{3.5}$$

This model is built from Equation 3.4 by adding an exponent parameter $\alpha$ in the numerator, in the same way as the Cole-Davidson model is constructed from the Debye model. Three free parameters are extracted from the fit: $S_0$ the noise at zero frequency (noise plateau value), $\tau$ the characteristic relaxation time of the system, and the power law exponent $\alpha$. It is interesting to notice that while the Cole-Davidson expression for $\chi''$ is not strictly identical to the equation used for the noise measurements, they both share similar qualitative features (see Figure 3.6(a), purple for the noise model and red for the $D(f)$ from the Cole-Davidson model).

The $Dy_2Ti_2O_7$ noise data is fitted using a least square cost function to this model and shows good agreement across the whole frequency range (see Figure 3.8(a)).

For $Ho_2Ti_2O_7$ as discussed earlier for the susceptibility, the noise spectra are fitted to the sum of two functions $S_1(f)$ and $S_2(f)$ using two sets of three free parameters

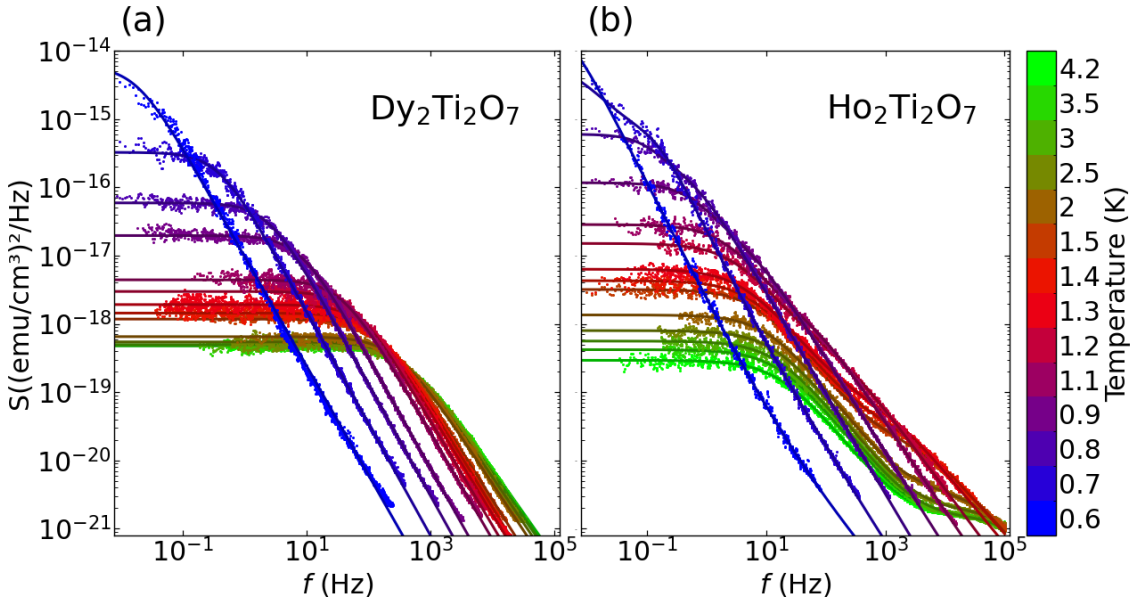


Figure 3.8: (a) and (b) $Dy_2Ti_2O_7$ and $Ho_2Ti_2O_7$ noise spectral density on a logarithmic scale. Small dots represent measured data and solid lines represent the fits according to Equation (3.5) for $Dy_2Ti_2O_7$ and Equation (3.6) for $Ho_2Ti_2O_7$.

(Figure 3.8(b)) :

$$S(f) = \frac{S_{01}}{1+(2\pi f\tau_1)^{\alpha_1}} + \frac{S_{02}}{1+(2\pi f\tau_2)^{\alpha_2}} \tag{3.6}$$

Like in the $Dy_2Ti_2O_7$case, the $Ho_2Ti_2O_7$ fluctuations are well reproduced by the noise model. While the noise fits appear better than the susceptibility fits, this perception is partly due to the noise thickness and the logarithmic scale used in the plots. These results show that the empirical models of both noise and ac susceptibility give a good global description of the data and the underlying dynamics even if they cannot fully describe the complexity of the dynamics of spin ice in the whole temperature and frequency range.

### 3.1.6 Results and discussion on the equilibrium dynamics

The noise and ac susceptibility fit models should provide a similar description, as they essentially model the same physical effect. However, they give complementary information since each measurement emphasizes on different aspects of the dynamics. The power spectral density noise function $S(f)$ or $D(f)$, enhances the sensitivity in the low-frequency regime, particularly on the plateau regime characterized by $S_0$, since it is proportional to $\chi''(f)/f$. It also provides a natural description of the exponent parameter $\alpha$, as it is directly related to the slope in the high-frequency regime. On the other hand, the ac susceptibility captures best the intermediate regime centered around the characteristic timescale of the dynamics, where the peak in the out-of-phase component $\chi''(f)$ is observed. It is also more sensitive at large frequency compared to the noise since the latter is proportional to the inverse of frequency.

One strong disadvantage of the noise measurements alone is the lack of access to the

in-phase susceptibility $\chi'$, which is essential for two reasons. First, it constrains more the fit and guarantee the Kramers-Kronig theorem is obeyed; the extracted parameters are then "physical". It is possible to obtain good quality fits for $\chi''(f)$ that give strongly overvalued or undervalued $\chi'(f)$. Second, if demagnetization corrections are necessary, they cannot be performed in a straightforward way on noise measurements (see Section 3.4). Using Equation 3.5 of the noise model, we have deduced $\chi''(f)$ and attempted an analytical Kramers–Kronig integration in order to derive the corresponding $\chi'(f)$, both to verify that the noise model parameters are physically meaningful and to enable demagnetization corrections. However, this approach was not successful.

Using the fitting procedures described above, we extract the temperature dependence of the fit parameters for the two spin ice materials. For both compounds $S$ and $\tau$ parameters were extracted from 4.2 K down to 600 mK. Below 600 mK, the noise plateau is not accessible within the measurement frequency bandwidth, so only the high frequency slope is fitted with a power law giving an estimation of the $\alpha$ parameters. Consequently, $\alpha$ parameters are determined down to 300 mK, and will be shown down to that temperature, deep in the spin freezing regime.

For $Dy_2Ti_2O_7$, three parameters are obtained, while in $Ho_2Ti_2O_7$ due to the two distinct relaxation times [57], twice a many parameters are required in the fitting procedure. From a technical perspective, this case is more complex but also particularly intriguing, as the two timescales strongly echo the concept developed by Tomasello et al. [53]. For clarity, we will refer to the two processes in $Ho_2Ti_2O_7$ as the slow process (lower frequency) and the fast process (higher frequency). We will discuss the behavior of the different parameters of both compounds in parallel, starting with the plateau $S_0$, then the relaxation times $\tau$, and finally the exponents $\alpha$.

Figure 3.9 shows the temperature dependence of $S_0$ for $Dy_2Ti_2O_7$ (a) and $S_{0fast}$ and $S_{0slow}$ for $Ho_2Ti_2O_7$ (b). In both materials, the magnitude of the plateau increases when going to lower temperature. In the specific case of $Ho_2Ti_2O_7$ the plateau $S_{0slow}$ associated with the slower timescale is easily extracted since it corresponds to the value of the noise at low frequency. However, the plateau of the high frequency mode is extracted in overlapping frequency ranges, where the low frequency timescale power law slope is mixing with the low and intermediate regions of the high frequency process. This overlap makes it difficult to determine precisely $S_{0fast}$.

The increase of the plateau should be similar to the dependence showed in relaxation times $\tau$, when considering a simple creation-recombination process, since it follows that $S_0(T)$ should be proportionate to $\tau(T)$ (Equation 3.4) [65, 112]. However, as shown in Figure 3.9 (c-d) the relationship between $S_0$ and $\tau$ is not linear. For $Dy_2Ti_2O_7$ it follows a power law behavior with an exponent 0.94, and for $Ho_2Ti_2O_7$ both fast and slow process do not follow neither a power law or linear behavior. These deviations likely reflect the influence of monopole density and correlations, since the simple model assumes a constant variance of the monopole number ($\sigma_N^2$). In $Ho_2Ti_2O_7$, additional discrepancies may arise from the difficulty of properly disentangling the different contributions.

Figure 3.10 shows the relaxation times $\tau$ of both compounds extracted between 4.2 K and 600 mK. For $Dy_2Ti_2O_7$ (Figure 3.10(a)), the timescale $\tau$ diverges below 1 K, consistently with previous measurements using noise, ac susceptibility, and magnetic re-

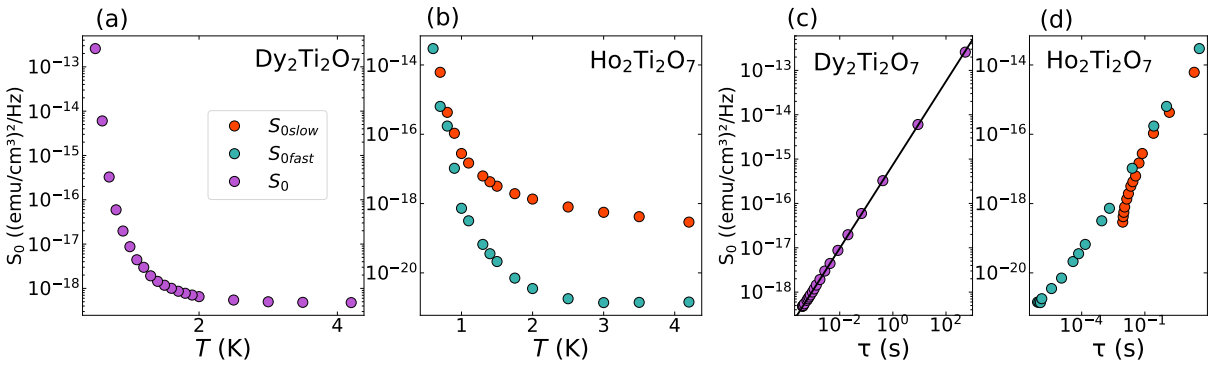


Figure 3.9: Plateau noise $S_0$ of (a) $Dy_2Ti_2O_7$ and $S_{0slow}$ and $S_{0fast}$ of (b) $Ho_2Ti_2O_7$ obtained from the fit with respect to temperature. (c) $Dy_2Ti_2O_7$ and (d) $Ho_2Ti_2O_7$ noise at zero frequency $S_0$ as a function of $\tau$. The solid black line in (c) is a fit to a power law with an exponent equal to 0.94.

laxation techniques (see Section 1.3.3) [49, 55, 65]. In $Ho_2Ti_2O_7$ the two $\tau$ parameters are well resolved, especially in the temperature regime where they are well separated. Figure 3.10(b) shows that both slow and fast relaxation times $\tau$ exhibit the same temperature dependence as $Dy_2Ti_2O_7$, with the expected plateau regime above 1 K and a sharp increase at lower temperatures. Wang et al.[57] proposed that below 0.9 K the dynamics could be described by a single relaxation time, assuming that the high frequency process disappears. In contrast, combining our two sets of measurements, we find that the two relaxation times remain close but clearly distinct down to at least 600 mK. Below this temperature the relaxation times become located outside our accessible frequency range, yet the high-frequency slope strongly suggests that both processes remain separated.

The temperature dependence of the relaxation times does not follows a simple Arrhenius thermally activated process, as the dynamics is slowing down faster than exponentially due to the fast decrease of the monopole density [47]. However, it is possible to fit independently the quasi-plateau (temperatures above 2 K) and the low temperature (below 1 K) regions. This approach allows us to characterize and quantify the relevant dynamical scales, even though these two Arrhenius fits do not correspond to well defined microscopic entities.

Above 2 K, we estimate the tunneling time of the plateau regime assuming a temperature independent time. Below 1 K, we extract an effective energy barrier of the low temperature regime using an Arrhenius law fit $\tau_0 \exp(E/T)$ with $E$ the energy barrier and $\tau_0$ an arbitrary relaxation time for scaling. In a semilogarithmic plot $\tau$ vs $T^{-1}$ (Figure 3.11 (a-b)), the Arrhenius law corresponds to straight lines where the slope is governed by the energy barrier $E$ and the intercept by $\tau_0$.

For $Dy_2Ti_2O_7$ (Figure 3.11(a)) we find the tunneling time of the plateau regime to be $\tau = 3 \cdot 10^{-4}$ s (dashed line) and an energy barrier $E = 12$ K (full line). For $Ho_2Ti_2O_7$ (Figure 3.11(b)) the tunneling times obtained in the plateau regime are $\tau_{slow} = 8 \cdot 10^{-3}$ s and $\tau_{fast} = 6 \cdot 10^{-7}$ s both with the same energy barrier of $E = 14$ K.

These two times in $Ho_2Ti_2O_7$ with a similar energy barrier can be attributed to the two different local transverse field environments influencing the quantum tunneling rates

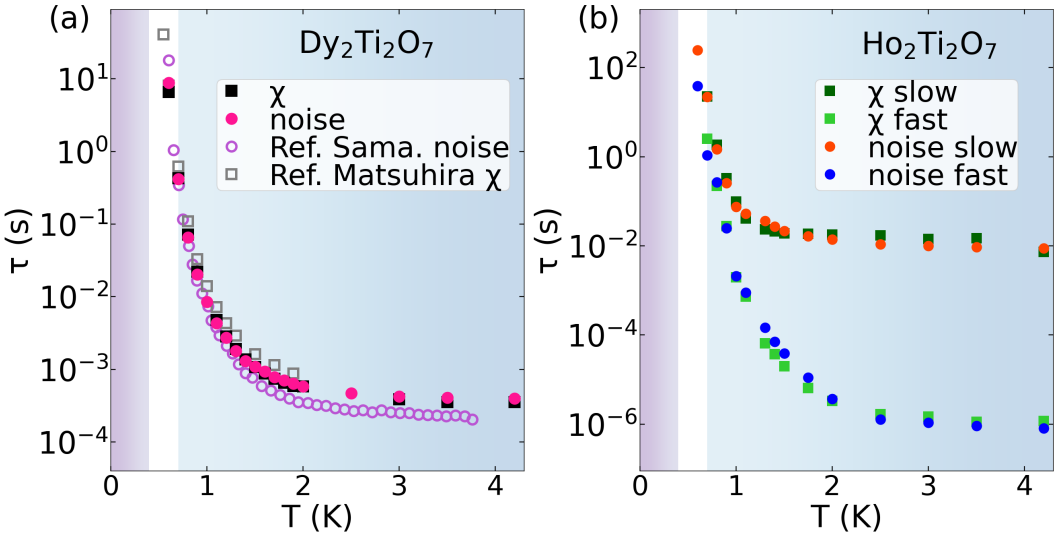


Figure 3.10: (a) Relaxation time $\tau$ (top panel) in $Dy_2Ti_2O_7$ obtained from the fits of the noise data using Equation 3.5, together with the $\tau$ obtained from the fits of $\chi(f)$ with Equation (3.3) and the results from Refs. [49, 55]. (b) Relaxation times $\tau_{slow}$ and $\tau_{fast}$ in $Ho_2Ti_2O_7$ obtained from noise measurements. The relaxation times obtained from ac susceptibility are also shown. The shaded backgrounds indicate the three temperature regimes: (i) equilibrium (blue), (ii) local equilibrium (white) and (iii) out of equilibrium (purple).

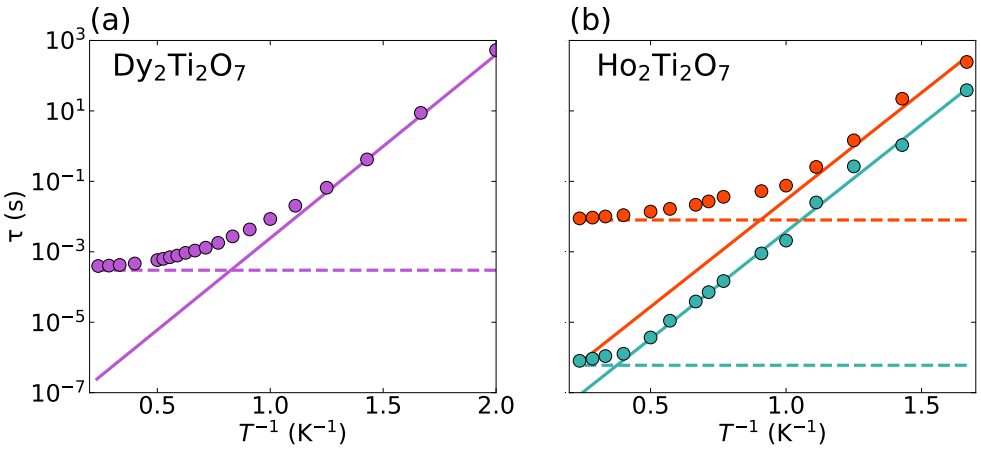


Figure 3.11: (a) $\tau$ and vs $1/T$ in $Dy_2Ti_2O_7$. Dashed lines represent the tunneling times $\tau_t$ obtained in the plateau region above 2 K, $\tau_t = 3\times10^{-4}$ s. Solid lines are Arrhenius law $\tau_0 \exp(E/T)$ with $\tau_0 = 1.5\times10^{-8}$ s with an energy barrier $E = 12$ K. (b) $\tau_{slow}$ and $\tau_{fast}$ vs $1/T$ in $Ho_2Ti_2O_7$. Dashed lines represent the tunneling times $\tau_t$ obtained in the plateau region above 2 K, $\tau_{tslow} = 8\times10^{-3}$ s and $\tau_{tfast} = 6\times10^{-7}$ s. Solid lines are Arrhenius laws $\tau_0 \exp(E/T)$ with $\tau_{0slow} = 2.5\times10^{-8}$ s, $\tau_{0fast} = 3.1\times10^{-9}$ s and the same energy barrier $E = 14$ K for both.

(see Section 1.3.3). In this picture, the energy barrier of the two processes is expected to be the same. The predicted times by Ref. [53] for $Ho_2Ti_2O_7$ are $\tau_{slow} = 2 \cdot 10^{-4}$ s and $\tau_{fast} = 7.4 \cdot 10^{-7}$ s in the plateau region, which is in good agreement to our experimental findings. For $Dy_2Ti_2O_7$, the two times proposed are $\tau_{slow} = 4.4 \cdot 10^{-2}$ s and $\tau_{fast} = 1.5 \cdot 10^{-6}$ s. The ratio between those times is about $3 \cdot 10^4$ which is much larger than in the $Ho_2Ti_2O_7$ case (ratio of 300). Consequently, we can expect a separation of times to be so large that one of the two times is located beyond our frequency window.

Figure 3.12 shows the $\alpha$ parameters of both compounds extracted between 4.2 K and 300 mK. For $Dy_2Ti_2O_7$ the $\alpha$ parameter obtained from the noise behavior (Figure 3.12(a)) agrees qualitatively with earlier work, except above 2 K, where we observe a value of approximately 1.35 versus 1.2 in Refs. [55, 65]. Three dynamical regimes can be deduced from the $\alpha$ temperature dependence: above 2 K, when the system is not yet spin ice, $\alpha$ is almost constant with a value of 1.35 below the expected value of 2 (characteristic of a random walk process with a single relaxation time). Between 2 K and 700 mK, upon entering in the spin ice regime, $\alpha$ increases to a maximum of 1.6. Below 700 mK, when entering deep in the freezing regime, $\alpha$ decreases strongly to 1.3 at 0.3 K. These findings suggest that monopole dynamics remain constrained and correlated above the spin ice regime and down to the lowest temperatures. Around 700 mK, the sharp decrease in $\alpha$ may indicate the onset of the freezing regime, where the monopole density strongly diminishes. This temperature dependence shows how complex the dynamics of the spin ice state is which explains why it is not fully understood yet.

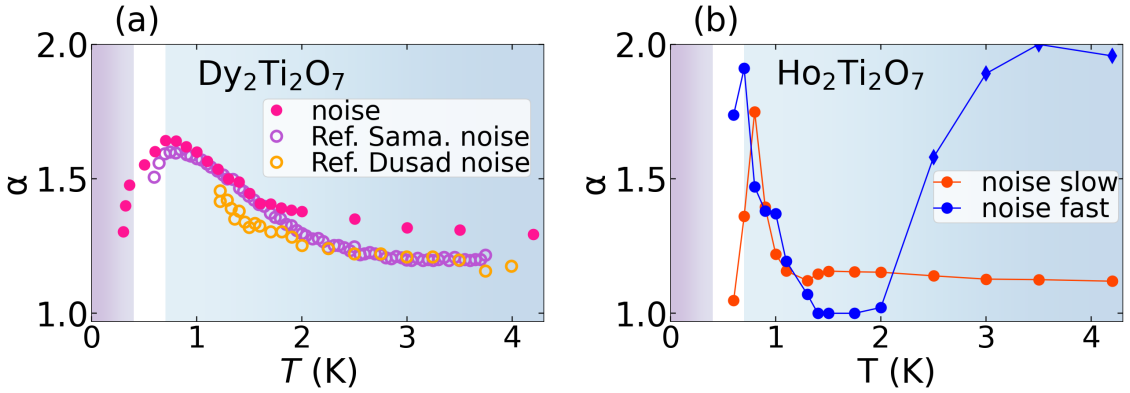


Figure 3.12: (a) Exponent $\alpha$ in $Dy_2Ti_2O_7$ obtained from the fits of the noise data using Equation 3.5, the results from Refs. [55, 65]. Below 600 mK, it is not possible to fit the noise and ac susceptibility due to the absence of shoulder in the noise and of maxima in $\chi''$. The $\alpha$ parameter can nevertheless be obtained from the slope of the noise. (b) Exponents $\alpha_{\text{fast}}$ and $\alpha_{\text{slow}}$ in $Ho_2Ti_2O_7$ obtained from noise measurements. Above 2 K, $\alpha_{\text{fast}}$ is obtained with a high uncertainty because the power law slope of the mode is at the limit of the frequency window (diamond symbols). The shaded backgrounds indicate the three temperature regimes: (i) equilibrium (blue), (ii) local equilibrium (white) and (iii) out of equilibrium (purple).

The latest spin ice Monte Carlo model [56], known as the bSM model, is based on the existence of two distincts relaxation times arising from a bimodal distribution of

transverse fields [53]. The bSM model for $Dy_2Ti_2O_7$ authorizes only the "fast" relaxation time configurations, assuming the "slow" ones would take an infinite amount of time and are thus negligible (Section 1.3.3).

Althought the model reproduces a subdiffusive monopole motion ($\alpha < 2$) and provides a reasonably good agreement with experimental observations (especially in capturing the anomalously fast divergence of time), the study did not account for the temperature dependence of $\alpha$. In the bSM model, a fraction of the monopole paths are "cut", resulting in a highly constrained motion in which the monopoles are confined to a fractal dimension. On average, a monopole moves along a random one-dimensional path embedded within the three-dimensional diamond lattice. If the monopole is assumed to follow a random walk, its dynamics become subdiffusive, producing a PSD with an exponent $\alpha = 1.5$ [56].

Following this reasoning, the path constraints are not expected to vary with temperature, leaving $\alpha$ constant. This picture describes the dynamics of a single monopole, but in a realistic spin ice system, the finite monopole density must also be considered, as correlation effects are expected (for instance, due to self avoidance). Since this density evolves with temperature, monopole path constraints should also vary with temperature, leading to a temperature-dependent $\alpha$. This expectation is supported by studies using the g-DSM model, which show that monopole dynamics become increasingly constrained upon cooling due to emerging short-range correlations [39]. These correlations confine monopole motion into clusters below ∼600 mK, before dynamics become completely frozen once the density nearly vanishes around 200 mK.

The microscopic origin of monopole dynamics is therefore likely governed by a combination of local fields and correlation induced constraints. Further studies of spin ice dynamics below 600 mK using the bSM model could provide a more complete picture, although such calculations are challenging due to the extremely low monopole density. Additional effects, such as dead ends or branching points, have also been proposed to impose further constraints on monopole motion and may be worth considering in future work.

In the case of $Ho_2Ti_2O_7$ (Figure 3.12(b)), the exponent parameters $\alpha_{fast}$ and $\alpha_{slow}$ also display a behavior similar to the one of $Dy_2Ti_2O_7$, rising around 700 mK to values of 1.6–1.8 and dropping sharply below this temperature. Above 2 K, $\alpha_{fast}$ has high uncertainty due to limitations in our frequency window which does not capture the power law slope that explains the high obtained values. Even if the analysis is less straightforward for $Ho_2Ti_2O_7$ due to the additional timescale, it seems clear that the monopole dynamics is at least as strongly correlated and constrained than the one of $Dy_2Ti_2O_7$.

In summary, noise and ac susceptibility analysis gives consistent results in the equilibrium regime, as expected from the fluctuation-dissipation theorem. They reveal that the dynamics is constrained and correlated even above the spin ice crossover with a non trivial temperature dependence. The most advanced current model [56], developed for $Dy_2Ti_2O_7$ cannot fully capture the features of the experimental results. The story seems to be even more complicated in $Ho_2Ti_2O_7$ as two relaxation times are evidenced and where no theoretical models are proposed yet to reproduce the experimental data. Nonetheless, both materials exhibit qualitative similarities in the temperature dependence of the parameters. In particular, when going toward the low frequency regime, we were able to evidence an abrupt change in the $\alpha$ parameter going toward a value of 1 for both materi-

als. This abrupt change may indicate a crossover between two distinct dynamical regime as the system enters in the spin freezing region. The next section will emphasize on the results found in this low temperature region, using the FDR as a probe.

## 3.2 Low temperature regime

### 3.2.1 FDR violations

When going below 600 mK, it becomes hard to extract quantitative information on the relaxation time from the ac susceptibility or noise analysis. However, the FDR approach which consists in comparing the noise and ac susceptibility is particularly interesting since spin ice systems enter deeply an out-of-equilibrium state [43, 113]. In this temperature regime, once the dilution refrigerator has cooled down to base temperature, noise measurements are performed on the full frequency range accessible with the set-up. At each temperature, we took care to check the absence of time dependence before averaging the successive noise scans. A minimum of three full scan averages were used to obtain enhanced noise resolution. Similarly, for ac susceptibility measurements, the frequency was swept over the entire frequency range at each temperature. In this low temperature regime, the measured ac susceptibility shows time dependence if the system comes from an higher or lower temperature state. Only the data obtained after the system is fully relaxed are used for FDR comparison with noise.

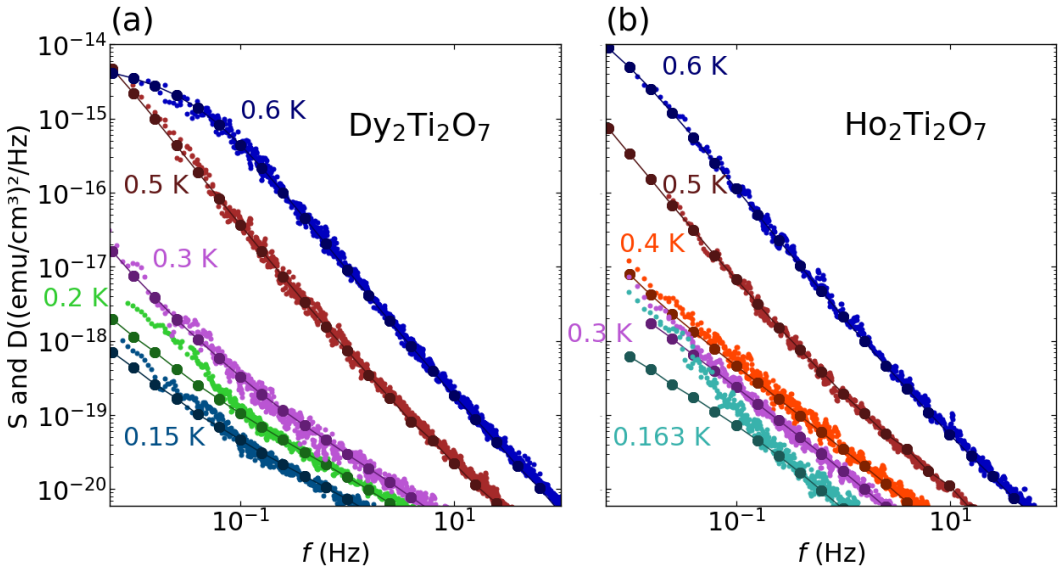


Figure 3.13: FDR plot for (a) $Dy_2Ti_2O_7$ and (b) $Ho_2Ti_2O_7$ on a logarithmic scale: $S(f)$ (small dots) and $D(f)$ (big dots) measured between 600 mK and base temperature. Lines are guides to the eye.

Figure 3.13 shows the FDR plot between base temperature and 600 mK for $Dy_2Ti_2O_7$ and $Ho_2Ti_2O_7$. Interestingly, we observe that the FDR holds at all frequencies down to 300 mK for $Dy_2Ti_2O_7$ and 500 mK for $Ho_2Ti_2O_7$. This results implies that even at those temperatures below the ZFC-FC splitting observed in the magnetization curves

[43, 113], the monopole dynamics appears to be in equilibrium. This indicates that the system is able to reach local equilibrium despite being in a non-ergodic regime, where it fails to find its equilibrium state when applying a magnetic field or lowering the temperature. These observations are in agreement with numerical simulations using stochastic dynamics, where it was found that the FDR is obeyed down to 400 mK [71]. In these calculations, it is only when the system is quenched far from equilibrium with a high density of monopoles that deviations are observed.

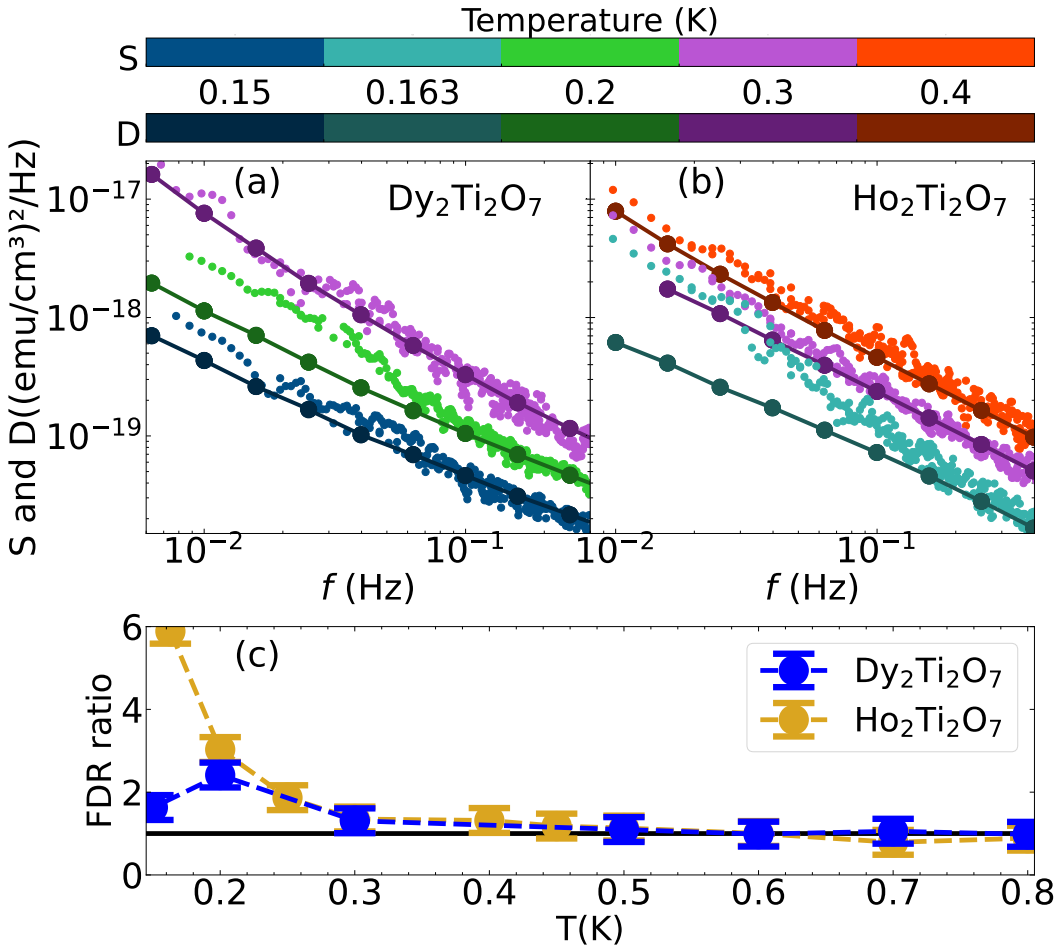


Figure 3.14: FDR plot for (a) $Dy_2Ti_2O_7$ and (b) $Ho_2Ti_2O_7$ a logarithmic scale at low temperature and low frequency: $S(f)$ (small dots) and $D(f)$ (big dots). (c) FDR ratio $S(f)/D(f)$ calculated below 0.016 Hz for $Dy_2Ti_2O_7$ (blue) and $Ho_2Ti_2O_7$ (gold) from base temperature to 800 mK. The solid black line corresponds to a FDR ratio equal to 1 which is expected when the FDT is obeyed.

Below these temperatures and only at low frequencies, typically below 0.1 Hz, we observe deviations to the FDR, due to an excess of noise compared to the measured ac susceptibility. This excess indicates that there is additional spontaneous spin fluctuations compared to the what is expected entropically. Moreover, it is especially important to state that the deviation is only observed for low enough frequencies which means that the measured dynamics involves at least two timescales exhibiting distinct thermodynamic

behaviors. This separation of timescales occurs when the "fast" processes have taken place (they have fully relaxed), while the "slow" processes are still relaxing [114]. Note that here, the two families of fast and slow processes are not related at all to the two dynamical timescales of $Ho_2Ti_2O_7$.

To better illustrate this low temperature and low frequency regime, Figures 3.14(a) and (b) provide a zoom in the temperature regime where deviations to the FDR are observed. To quantitatively characterize these deviations, we compute the ratio of the fluctuating and dissipative component of the FDR $S(f)/D(f)$ (Figure 3.14(c)). This ratio is directly related to the effective temperature (equal to the ratio times the bath temperature), which describes the energy scale of the dynamics compared to the thermal bath [66, 115]. This fluctuation-dissipation ratio is calculated for frequencies below 0.016 Hz, for temperature from 800 mK to base temperature. At lower temperature, it reaches nearly 2 in $Dy_2Ti_2O_7$ and 6 in $Ho_2Ti_2O_7$ corresponding to an effective temperature of approximately 300 mK and 1 K respectively. This result implies that, although the absolute energy scales differ, if these systems were at equilibrium they would need to be at a temperature comparable to their effective temperature in order to reach this ratio.

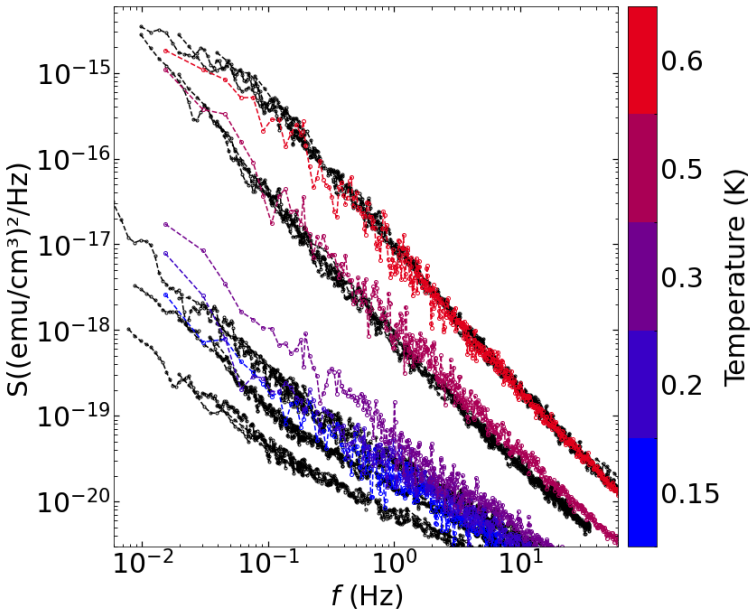


Figure 3.15: Spectral noise density $S(f)$ of Ref. [55] (color dots) compared to our data (corresponding black curves) between 600 and 150 mK. The data from Ref. [55] are converted in absolute units by scaling the 600 mK curve to our data.

Noise data measured in this low temperature regime were reported by Samarakoon et al. for $Dy_2Ti_2O_7$ [55]. In this study, the sample was a pure isotopic $^{162}Dy_2Ti_2O_7$ compound, similarly to our experiment. It is thus of strong interest to compare their data to our results. Figure 3.15 shows the noise data from this previous study (color dots) alongside our data (black dots) at the same temperatures. In Ref. [55], the data are plotted in arbitrary units. They were thus scaled to our data so that the curves matches for all frequencies at 600 mK. At low temperature, between 150 mK and 300 mK, both datasets show a similar change of slope at low frequency, which was associated in our

work to the violations to the FDR. However the curves do not quantitatively match at those temperatures, the noise from Ref. [55] being larger than in our study.

It is important to note that the purpose of this paper was not to study the low frequency, low temperature regime. The measurement protocol was not ideally adapted to obtain accurate measurements in this regime. The authors mention that the sample was slowly warmed while noise data were acquired over a 24 hours period of time and that the PSD noise curves were averaged over different time spans when taking the FFT. In the low frequency regime, a long time span is needed, and it is thus possible that the temperature was not constant during the whole measuring time, which can impact the result since noise varies significantly with temperature. Additionally, only a single averaging was performed in this low frequency regime.

### 3.2.2 New relaxation process at low temperature

In the standard representation of ac susceptibility, through $\chi'$ and $\chi''$ (and not in its noise-derived form, $D(f)$), we noticed two small intensity peaks in $\chi''$ for both compounds $Dy_2Ti_2O_7$ and $Ho_2Ti_2O_7$ (Figure 3.16). These peaks appears at low temperatures, below 400 mK, when the relaxation processes of the monopole motion (discussed in Section 3.1.5) move outside of the frequency window. These peaks then becomes better defined as the temperature is lowered and have a weak frequency dependence. A first low-frequency peak is observed just above 0.001 Hz in both compounds, while the second peak appears at intermediate frequencies, centered around 4 Hz in $Dy_2Ti_2O_7$ and 0.16 Hz in $Ho_2Ti_2O_7$.

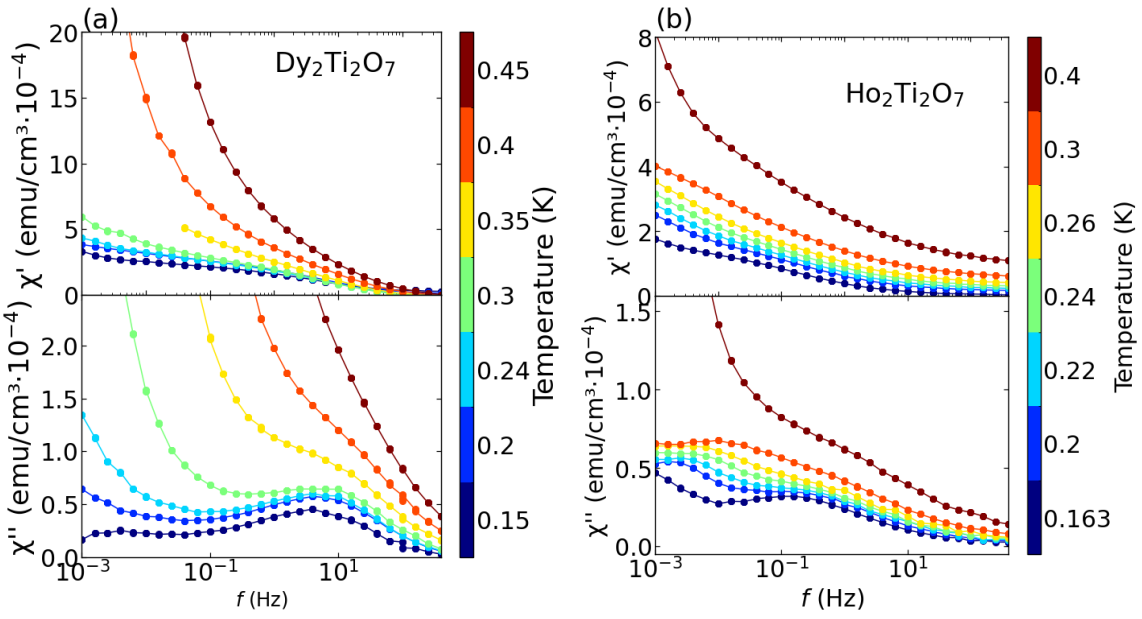


Figure 3.16: ac susceptibility $\chi'$ (top panel) and $\chi''$ (bottom panel) vs $f$ for different temperatures below 450 mK in (a) $Dy_2Ti_2O_7$ and (b) $Ho_2Ti_2O_7$.

This newly detected relaxation processes have very low intensities, about $\sim 10^{-3}$ smaller than the monopole dynamics around 1 K. Initially, they could not be resolved

from the measurement background, but after optimizing the ac susceptibility sensitivity (originally for testing the FDR), we were able to detect these new unexpected peaks.

These peaks clearly correspond to new relaxation mechanisms, since the characteristic monopole timescale diverges toward longer values at these temperatures. Interestingly, we observe these processes in the temperature range where deviations from the FDR were identified (see Section 3.2.1). The appearance of these peaks coincides with the separation of the dynamics into distinct timescales: some processes remain in quasi-equilibrium (below the freezing temperature but satisfying the FDR), while others are clearly out-of-equilibrium, as evidenced by the measured deviations of the FDR.

These observations may be due to the splitting of the degeneracy of the spin ice Pauling states induced by the long range dipolar interactions in this temperature range [32, 35]. The intermediate frequency process could corresponds to the flipping of short spin loops between different Pauling states while the slow relaxation could be linked to a deconfinement time of those monopoles.

As previously stated, in this temperature regime, the ac susceptibility exhibits time dependent properties, which we attribute to an aging effect arising from the slow relaxation of the magnetic state as the temperature of the thermal bath changes. Such behavior is expected and typical in systems relaxing toward equilibrium from an out-of-equilibrium regimes.

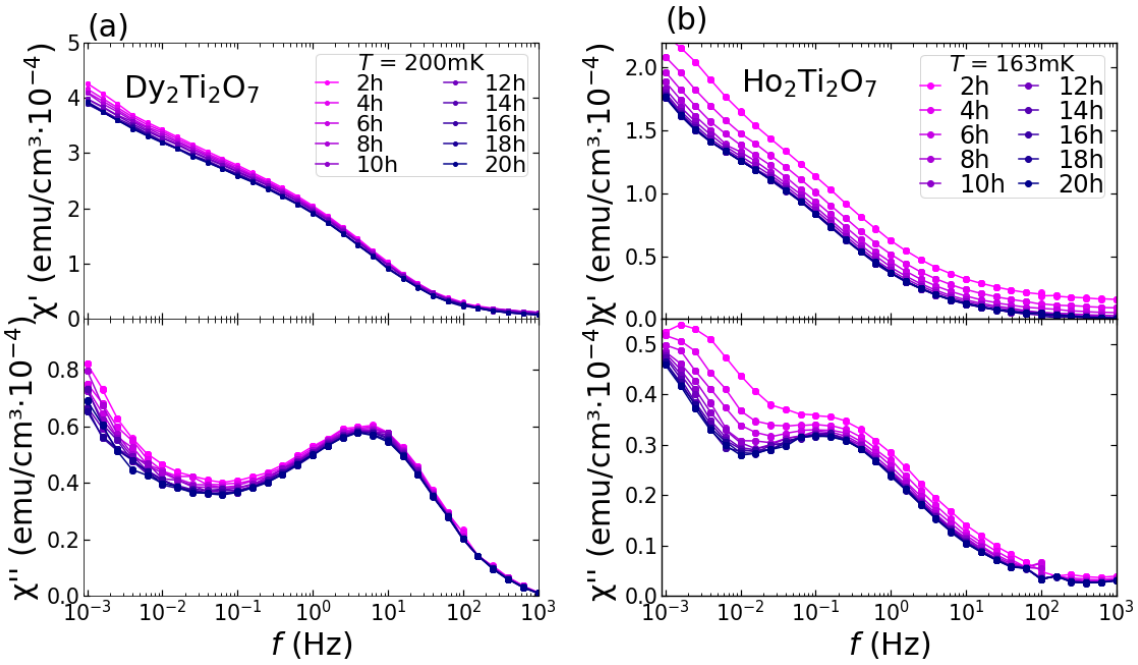


Figure 3.17: ac susceptibility measured after different waiting times at (a) 200 mK for $Dy_2Ti_2O_7$ and at (b) 163 mK for $Ho_2Ti_2O_7$ after waiting 30 s at 800 mK.

The duration of this aging effect of the susceptibility depends on temperature, both the initial and the target ones. We investigated this effect by warming up the sample to an initial temperature of 800 mK for 30 seconds, then letting it cool down to the target

temperature while acquiring the ac susceptibility data. With this protocol, the sample reaches 350 mK within 2 minutes, however it takes almost an hour to cool down to base temperature. This happens because warming the sample up to 800 mK also warms up the cold point of the dilution refrigerator, which no longer act as a thermal bath, so that time is needed to recondense the $^3$He-$^4$He mixture. The observed time dependence of the magnetic signal upon cooling cannot be explained by a problem of thermalization, since the magnetic relaxation occurs over a much longer timescale than the sample cooling time. We define the time required for the observed susceptibility to reach a stable value as the "stabilization" time.

As shown in Figure 3.17, the stabilization time is about 14 hours in $Ho_2Ti_2O_7$ at 163 mK, and 10 hours in $Dy_2Ti_2O_7$ at 200 mK (the lowest temperature for which we performed the test in both compounds). The magnitude of the new relaxation process is greater in $Dy_2Ti_2O_7$ ($6 \cdot 10^{-5}$emu/cm$^3$ at 3.8 Hz ) than in $Ho_2Ti_2O_7$ ($3.2 \cdot 10^{-5}$emu/cm$^3$ at 0.16 Hz), while the relative magnetic aging effects are stronger in $Ho_2Ti_2O_7$ (a 25 % decrease in peak amplitude from the initial to relaxed scan in $Ho_2Ti_2O_7$, versus 11 % for $Dy_2Ti_2O_7$). When performing this test at higher temperatures, the stabilization time decreases: for a target temperature of 300 mK it takes 9 hours for $Ho_2Ti_2O_7$ and 8 hours for $Dy_2Ti_2O_7$ of stabilization time, whereas at 400 mK, in both compounds the aging effect is much smaller. The first scan after 2 hours after cooling is slightly more intense but then the other scans perfectly overlaps.

For the $Ho_2Ti_2O_7$ compound, we also investigated this time dependent effect during warming, starting from base temperature and increasing successively by steps of 50 mK up to 450 mK. We found that it takes about 8 hours to reach stable ac susceptibility between 163 mK and 200 mK, 6 hours between 200 and 250 mK, 4 hours between 250 and 300 mK, 2 hours between 300 and 350 mK, and less than 2 hours for the final steps. This supports the idea that the magnetic relaxation of the state at such temperatures is much slower than the thermal relaxation itself, leading to a decoupling between thermal and magnetic equilibration.

In neither $Ho_2Ti_2O_7$ nor $Dy_2Ti_2O_7$ we were able to observe a reliable long time dependence in the noise measurements. This may seem surprising in the frequency regime where both match through the FDR, as there is no obvious reason why the magnetic response measured through the ac susceptibility would differ from the one seen in the noise. However, the origin of this discrepancy can be easily understood when comparing the corresponding $D(f)$ of the ac susceptibility for the different waiting times to the noise function $S(f)$ at the lowest measured temperature. This is shown in Figure 3.18 for $Ho_2Ti_2O_7$ at 163 mK. Above $f = 0.1$ Hz (where the FDR holds) the change of $D(f)$ with time stays within the resolution of the corresponding noise. This indicates that even if the noise would exhibit the same aging properties as the ac susceptibility, we would lack the sensitivity to detect them. At lower frequencies, where the FDR is violated, the relationship between $S(f)$ and $D(f)$ no longer holds, and it is unclear whether noise should reflect the same aging behavior. It is worth noting that the difference between $S(f)$ and $D(f)$ in this low frequency regime is much larger than the amplitude of the aging effects, thus confirming the violation of the FDR.

In FDR measurements of spin glass systems [70], aging behavior was observed in the autocorrelation function of the magnetization, which corresponds to the fluctuations and, consequently, to the noise. In their study, the authors were able to perform well-

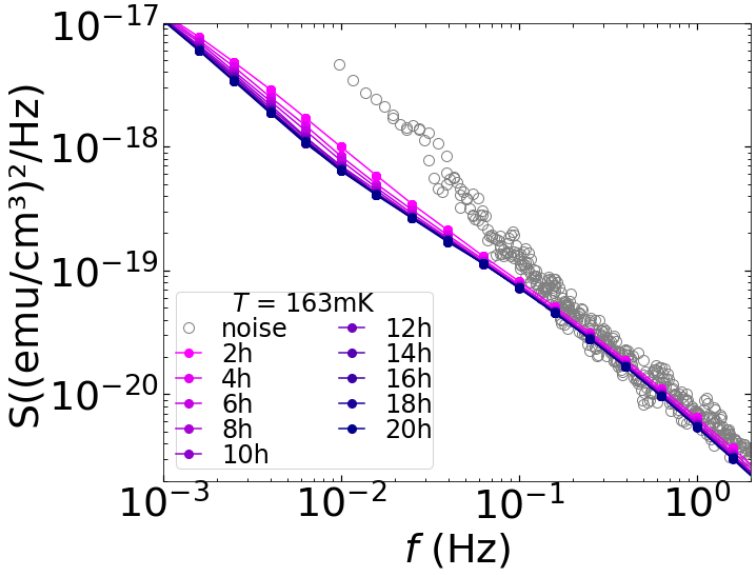


Figure 3.18: Spectral noise density $S(f)$ (grey dots) compared to $D(f)$ at different waiting times in $Ho_2Ti_2O_7$ at 163 mK. The solid line in $D(f)$ is a guide to the eye.

controlled quenches through the spin glass transition. This allowed them to precisely tune the waiting time parameter. By acquiring a sufficient number of runs for each waiting time, they achieved the sensitivity required to measure aging of the noise.

Unfortunately, our analysis of this aging effect in both the noise and the ac susceptibility is poorly quantitative as we did not have time to adapt the setup in order to have a precise control of the temperature ramping. Indeed, because of the thermal inertia of the dilution refrigerator, we were unable to produce well controlled and perfectly reproducible thermal quenches or cooling procedures. To explore this further, we need to be able to thermally decouple the sample from the bath on request or to implement avalanche quench protocols [59]. This method would help us enhance the density of monopoles in the low temperature state, potentially amplifying FDR violations or aging effects in both ac susceptibility and noise measurements.

## 3.3 Conclusion about spin ice dynamics

Our investigation of the magnetic noise spectra and the ac susceptibility in the two spin ice materials $Ho_2Ti_2O_7$ and $Dy_2Ti_2O_7$ shows that the dynamical processes taking place in those materials respects the FDR down to 400 mK over all the measured frequency range ($10^{-3}$-$10^{5}$ Hz). This result was expected for temperatures above 600 mK, spin ice materials being in thermodynamic equilibrium down to this temperature [43]. The respect of the FDR is more surprising between 600 and 400 mK, since the freezing is already observed in the magnetization in this temperature range. The validity of the FDR indicates that the dynamical processes behave as if they were in equilibrium, despite the ergodicity breaking observed in the magnetization. These processes can therefore be regarded as being in quasi-equilibrium.

Going to lower temperature (below 400 mK), we observed an excess of noise in the FDR, but only below a frequency threshold of about 0.1 Hz [108]. This indicates the separation of the dynamics into at least two distinct timescales: above this frequency threshold, local equilibrium is achieved over short time and length scales, while below it, the non-ergodicity of the system manifests over mesoscopic time and length scales, resulting in the breakdown of the FDR.

From these observations, we can define 3 characteristic regions: (i) the high temperature region, where the system is trivially in equilibrium, and the FDR is obeyed, as expected; (ii) the intermediate region, where ergodicity breaking is observed in the magnetization, but where we find that the FDR remains obeyed indicating that local equilibrium is preserved; (iii) the low temperature region, where the FDR is violated at low frequency, typically below 0.1 Hz, indicating that the system enters an out-of-equilibrium state.

In the region (iii), we also observe a new low intensity relaxation process that exhibits aging properties. Emergent short timescale processes appear in the temperature range where deviations of the FDR are reported and may corresponds to monopoles confined in short loops, while long timescales may correspond to the monopole deconfinement time. In this temperature range, it is possible that spin ice materials become sensitive to the degeneracy lifting of the Pauling states induced by dipolar interactions [32, 35]. The separation of scales could then be explained by the finite bandwidth of energy barriers between the Pauling state induced [39], which would also lead to a rough free energy surface driving the FDR violations.

Throughout the procedure described above, we studied the ac susceptibility without considering demagnetization effects. It is however known that in spin ice materials, due to the large magnetization induced by effective ferromagnetic interactions, these effects can significantly change the observed dynamics, compared to the "intrinsic" one [116]. The reason why we have not performed any corrections is that only the measured ac susceptibility matches with the corresponding measured noise. As soon as corrections are performed on $\chi''$, $D(f)$ obtained after correction and $S(f)$ have different shapes, so that the FDR cannot be obeyed, even in the high temperature regime.

At first sight, it seems surprising, as it implies that the measured noise must also be corrected, even if it is a quantity measured in a zero field environment, while the demagnetization effect is a concept initially defined for finite magnetization. However, when measuring the fluctuations of the magnetization, even if the time average magnetization is zero, a small but finite magnetization is present at all times, which is the quantity we measure. This magnetization must induce demagnetization effects. Our study shows that these effects have to be taken into account even when considering the correlations of the magnetization. Thus we must find a way to estimate and correct the noise spectra from this demagnetization.

The magnitude of demagnetization depends directly on the size of the in-phase susceptibility $\chi'$, and is typically negligible for temperature below 500 mK in spin ice materials. It does not affect any of our conclusions and analysis in the low temperature regime but it is expected to influence the dynamics in the equilibrium regime. In the next section, we will discuss in details the role of demagnetization in the noise, using the ac susceptibility as a guide.

## 3.4 Demagnetization corrections

### 3.4.1 The demagnetization effect

When measuring a sample in an applied external field $\mathbf{H}_{ext}$, any magnetized sample will possess a demagnetization field $\mathbf{H}_d$, proportional to the sample's magnetization $\mathbf{M}$, with $H_{d,i} = -N_{ij}M_j$ $(i,j = x,y,z)$. Here, $N_{ij}$ are the components of the demagnetization tensor $\mathbf{N}$, represented as a symmetric 3×3 matrix. The resulting internal field acting on the sample in a given direction is the sum of the applied and demagnetization fields in that direction:

$$H_{int,i} = H_{ext,i} + H_{d,,i} = H_{ext,i} - N_{ij}M_j \tag{3.7}$$

In the specific case of a ellipsoid sample, the internal demagnetization field $\mathbf{H}_d$ is uniform and can be analytically calculated using the $\mathbf{N}$ tensor [117]. Along the principal axes of the ellipsoid, $\mathbf{N}$ is diagonal with three components: $N_x$, $N_y$ and $N_z$, known as the demagnetization factors. The sum of those three factors (i.e., trace of the tensor) is always 1 (or $4\pi$ in cgs units). In the following, we will only consider the $N$ factor corresponding to the direction in which the sample is measured.

For non-ellipsoidal samples, the internal demagnetization field is not uniform, making the determination of $N$ impossible in most cases (except for certain geometries such as long needles, thin films and torus). Therefore $N$ is commonly estimated from approximations giving an effective demagnetization factor, with the mostly used approximation being that for parallelipiped samples [118].

From this $N$ factor, the intrinsic magnetic susceptibility of the material, $\chi_{int}$ (a shape independent quantity), can be deduced from the measured susceptibility $\chi_{mes}$ using:

$$\chi_{int} = \frac{\chi_{mes}}{1 - N\chi_{mes}} \tag{3.8}$$

Since $\chi_{mes} = \chi'_{mes} - i\chi''_{mes}$ is defined by the sum of a real and imaginary component, the demagnetization effect can be expressed separately for the in-phase and out-of-phase components:

$$\begin{aligned} \chi'_{int} &= \frac{\chi'_{mes} - N(\chi'^2_{mes} + \chi''^2_{mes})}{(1 - N\chi'_{mes})^2 + (N\chi''_{mes})^2} \\ \chi''_{int} &= \frac{\chi''_{mes}}{(1 - N\chi'_{mes})^2 + (N\chi''_{mes})^2} \end{aligned} \tag{3.9}$$

With these formula, the determination of the intrinsic susceptibility is straightforward. However, it is important to note that calculating $\chi'_{int}$ and $\chi''_{int}$ requires the knowledge of both $\chi'_{mes}$ and $\chi''_{mes}$. This means that the measured noise $S_{mes}(f)$, which is linked only to $\chi''_{mes}$, cannot be corrected on its own.

To bypass this issue, one possible solution is to derive $\chi'_{mes}$ from $\chi''_{mes}$ using Kramers-Kronig (KK) theorem. This requires integrating $\chi''_{mes}$ over the entire frequency range where $\chi''_{mes}$ is non-zero, which can be difficult given the frequency bandwidth limitations of the set-up. Another approach to observe and quantify the effect of $N$ on the noise is to use the ac susceptibility by investigating the effect on the corresponding $D(f)$, which can be easily corrected using the above equation.

In the following, we will first briefly confirm that the measured noise $S_{mes}(f)$ requires demagnetization corrections by using two illustrative examples. After describing these examples, we detail our approach to experimentally characterize the effect of the $N$ factor on the noise using the associated $D(f)$ at a fixed temperature in Subsections 3.4.2 and 3.4.3. Our attempts to correct the noise using KK integration are discussed later in Subsection 3.4.5. In Subsection 3.4.6, we explore the influence of $N$ on the dynamical parameters of the noise using the empirical fit models introduced earlier. Finally, in the last Subsection.3.4.7 we estimate how these dynamical parameters vary with temperature for a fixed demagnetization factor.

### 3.4.2 The need for demagnetization corrections in noise measurements

We noticed quite early during our analysis that demagnetization corrections have to be performed on the noise, thanks to our measurements of the FDR. This effect is shown in Figure 3.19(a) for the $Dy_2Ti_2O_7$ and $Ho_2Ti_2O_7$ samples discussed in the previous section, at 900 mK. The measured noise $S_{mes}(f)$ initially overlaps perfectly with the corresponding $D_{mes}(f)$ (dots). However, after applying demagnetization correction from Equation 3.9 to $D_{mes}(f)$ (squares), the noise and corrected $D_{int}(f)$ no longer match as it should be due to the FDT. These results show that the noise is indeed subject to the effect of demagnetization, as at this temperature, the FDR must strictly be obeyed since the system is known to be at thermodynamic equilibrium. The $N$ factors were estimated using Aharoni's formula [118]: $N = 0.131 \times 4\pi$ for $Dy_2Ti_2O_7$ and $N = 0.18 \times 4\pi$ for $Ho_2Ti_2O_7$. We use cgs units for the ac susceptibility and noise data, however $N$ is more naturally expressed in SI units, where the sum over all directions equals 1. To make the conversion explicit, we write the $4\pi$ factor when reporting values in cgs units.

Further evidence of the effect on the noise itself comes from comparing our $Dy_2Ti_2O_7$ noise data with that of Ref. [55]. This comparison was made previously in the low temperature regime below 600 mK in Section 3.2.1, where we scaled the 600 mK curve from Ref. [55] to our data. We chose this temperature because at 600 mK $\chi'(f)$ is almost zero across the whole frequency range (due to the large relaxation time at this temperature). Indeed, as shown by Equation 3.9, when $\chi'(f) \ll 1$ ($\chi''(f)$ being usually much smaller than $\chi'(f)$), the demagnetization effect can be neglected. This the case for all temperatures below 600 mK.

At higher temperatures, the limit where $\chi' \approx 0$ gradually shifts towards the high frequencies, so that demagnetization effects become non negligible for low and intermediate frequencies. Figure 3.19(b) shows the comparison between our measurements and the ones from Ref. [55] in the 700 mK - 1.5 K temperature range. At 700 mK, both datasets agree over the full frequency range, while at higher temperatures, they overlap only at high frequencies when the $\chi'(f) \to 0$ limit is satisfied. These observations support the idea that the demagnetization field is responsible for the differences in this temperature range.

Moreover, the gradiometer and sample geometry used for the measurement of Samarakoon et al. is favorable to strong demagnetization effects. Their sample is nearly flat, with its two long axes perpendicular to the gradiometer flux axis, resulting in a higher $N$ factor compared to the one obtained in our setup where the sample's long axis was aligned with the flux axis. A higher $N$ coefficient results in a smaller value of the noise

plateau, which is consistent with the observed differences between the two datasets.

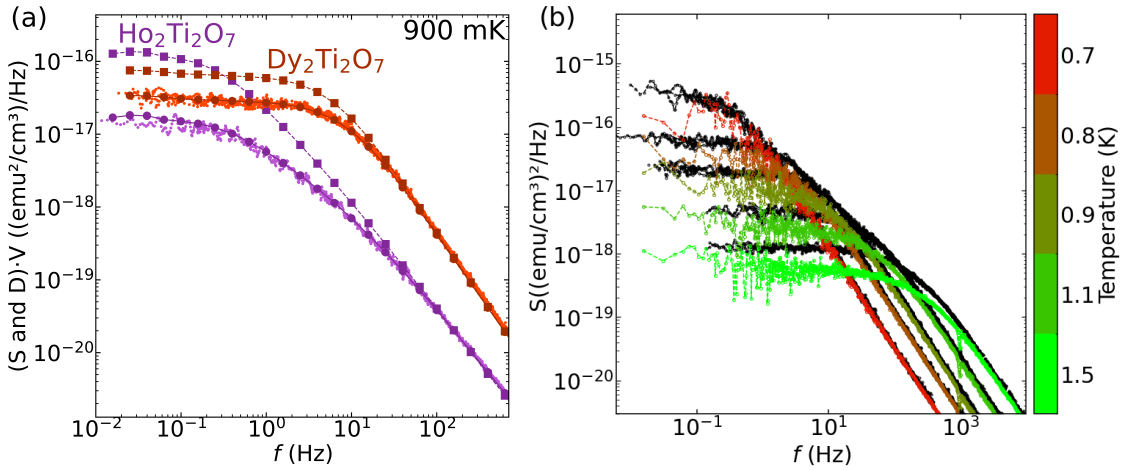


Figure 3.19: (a) $S(f)\cdot V$ vs $f$ (small dots) and $D(f)\cdot V$ measured (circles) and intrinsic (squares) for $Ho_2Ti_2O_7$ (purple) and $Dy_2Ti_2O_7$ (orange) at 900 mK (b) Spectral noise density $S(f)$ of $Dy_2Ti_2O_7$ from Ref. [55] (color) compared to our data (black curves) between 1.5 K and 700 mK. The data from Ref. [55] and were scaled to our data at 600 mK (Figure 3.15).

These two quick checks demonstrate that the measured noise spectra are indeed subject to demagnetization effects, just like the magnetic susceptibility. Differences in the $\tau$ and $\alpha$ extracted from the fit of noise curves were found and discussed in the literature [119]. Those discrepancies may arise from the role of the demagnetization field for noise measurements, which was overlooked until now. It is therefore crucial to understand and quantify the influence of demagnetization on magnetic noise curves in order to enable comparison between results from different experiments and research groups as well as comparison with the calculations.

In the following, we try to quantify this effect in the specific case of spin ice materials, although some conclusions are broadly applicable to magnetic noise measurements in any type of magnetic material using noise magnetometry.

### 3.4.3 Experimental procedure

The demagnetization field is a sample dependent effect that arises from the geometry of the sample itself. One of the primary challenges in addressing the demagnetization effect is the accurate determination of the demagnetization factor $N$ for different sample shapes. While $N$ is known for the case of ellipsoidal samples [117] (with the well known case of the sphere where $N_{sphere} = \frac{1}{3}\times 4\pi$), the situation becomes complex for non-ellipsoidal samples. In these cases, the internal demagnetization field $\mathbf{H}_d$ is not uniform, so an average over that field $\mathbf{H}_d$ is necessary to define a effective constant $N$.

Aharoni [118] provided an approximated analytical expression for $N$ for rectangular prisms in the limit $\chi_{int} \to 0$, which remains commonly used nowadays. More recently, Twengström et al. [116, 120], showed that $N$ can depends significantly on the intrinsic

susceptibility $\chi_{int}$, resulting in a temperature-dependent $N$ for non-ellipsoidal shapes. They used $Dy_2Ti_2O_7$ and $LiHoF_4$ as model systems, both exhibiting high values of $\chi_{int}$.

In Ref. [116], two primary methods are proposed to overcome this issue. The first approach consists in performing computational simulations in order to extract $N(T)$, the temperature dependence of the demagnetization factor. However, this technique is time-consuming and specific to the sample geometry. The second approach is experimental and requires a spherical sample. For this specific sample geometry, $N$ is temperature-independent and equal to $1/3 \times 4\pi$, which enables a precise determination of the intrinsic susceptibility $\chi_{int}$. Once $\chi_{int}$ is known, it can be used to deduce the effective $N$ for the other, more complex geometries.

In this work, we choose to adopt the second method. We measured three different $Ho_2Ti_2O_7$ samples: one spherical sample with a diameter of 4 mm [121], a parallepiped sample with dimensions $2.07 \times 2.41 \times 0.57$ mm$^3$, and a nearly cylindrical sample with of 4 mm diameter and 8.9 mm length [108]. The rectangular sample was measured along two different directions, one aligned with its longest side of the sample and another with its shortest side. The cylinder was measured along its length.

For $Dy_2Ti_2O_7$ we unfortunately did not have access to a spherical sample so we could not to use this method to determine $N$. Instead, we studied the sample of $^{162}Dy_2Ti_2O_7$ introduced for the noise measurement earlier in this manuscript using $N = 0.13 \times 4\pi$ obtained from Arahoni's formula. This value provides a first approximation and allowed us to explore the temperature dependence of demagnetization effects for a fixed $N$.

We will come back later to the detailed study of the temperature dependence of the demagnetization effects for fixed $N$. For now, we focus on the $Ho_2Ti_2O_7$ samples and the experimental determination of $N$ for the different sample configurations.

### 3.4.4 Estimation of N factors in $Ho_2Ti_2O_7$

In order to estimate the $N$ values using the spherical sample, we first examine how demagnetization correction affects the susceptibilities at a fixed temperature. Figure 3.20 shows both the real and imaginary parts of the susceptibility for the four different sample configurations of $Ho_2Ti_2O_7$ measured at 900 mK along with their associated corrected intrinsic susceptibility $\chi'_{int}$ and $\chi''_{int}$.

The demagnetization factor used for the sphere is $N_{sphere} = 1/3 \times 4\pi$, while the other sample configurations are corrected using values of $N$ that give the best overlap with the intrinsic susceptibility obtained from the sphere sample. We found experimental demagnetization factors of $N_\perp = 0.544 \times 4\pi$, $N_\parallel = 0.1 \times 4\pi$ for the parallepiped sample in the two short and long directions respectively, and $N_{cylinder} = 0.18 \times 4\pi$ for the cylinder. By using these values, we can achieve a relatively good overlap between the four corrected susceptibilities. This indicates that they share the same dynamical properties, the differences in the measured susceptibilities mainly coming from demagnetization effects. Further evidence for this conclusion is found by observing the high-frequency regime (above $10^2$ Hz), where the in-phase susceptibility tends to zero and the demagnetization correction becomes negligible. In this limit, all the susceptibilities naturally overlap, independently of the sample geometry.

For comparison, the values of $N$ calculated using Arahoni's method for rectangular prisms are $N_\perp = 0.646 \times 4\pi$, $N_\parallel = 0.163 \times 4\pi$, and $N_{cylinder} = 0.18 \times 4\pi$. While the cylinder

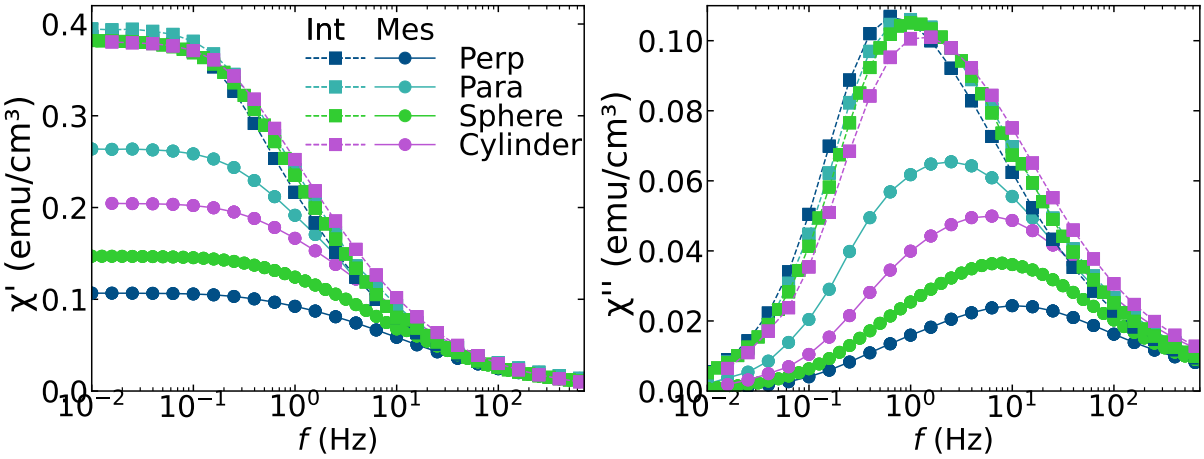


Figure 3.20: Ac susceptibility $\chi'$ and $\chi''$ vs $f$ measured at 900 mK for four different $Ho_2Ti_2O_7$ sample configurations. The dots symbols show the measured susceptibility and the square symbols the susceptibility corrected from demagnetization factor $N$ (intrinsic susceptibility). The $N$ factors are : $N_\perp = 0.544 \times 4\pi$, $N_\parallel = 0.1 \times 4\pi$, $N_{sphere} = 1/3 \times 4\pi$ and $N_{cylinder} = 0.18 \times 4\pi$. Lines are guides to the eye.

shows good agreement between the two methods, there is a noticeable difference for the case of the parallepiped. The discrepancy found for the case where the long side of the parallelepiped sample was aligned parallel to the coil is puzzling. Indeed, the sample shape is well defined, and any misalignment of the sample with respect to the coil axis should rather increase $N$ and not decrease it. The perpendicular cubic configuration corresponds to the highest expected $N$, so it seems more likely to expect some deviations between the two methods as it will be more sensitive to shape or alignment imperfections.

It is worth noting that, for large $N$, a small change in the measured susceptibility due to calibration errors will result in highly enhanced errors. This is especially relevant for a spin ice material like $Ho_2Ti_2O_7$ as it possesses strong ferromagnetic interactions with large values of $\chi'$. Among the four configurations we have measured, the parallepiped in the perpendicular case and the sphere geometries both have relatively large values of $N$. Errors in their calibration will change the calculated effective $N$ factors. The two other low $N$ configurations will also be affected as we have scaled the data on the sphere intrinsic susceptibility.

To illustrate the sensitivity of the demagnetization correction to calibration error, Figure 3.21 shows, for the configuration with $N_\perp = 0.54 \times 4\pi$, how introducing artificial errors of 1%, 5%, 10% and 20% in the measured susceptibility (pink) dramatically impacts the corrected corresponding intrinsic susceptibility (orange). The initial measured and intrinsic susceptibilities with no artificial errors are shown in blue (they almost overlap with the 1% curve). We observe with this test that the error is greatly enhanced by the $N$ factor correction. We estimate the strength of this effect by looking at the magnitude of the $\chi'_{int}(f \to 0)$ after correction. An initial error of 1% leads to a final error of 4.2%, 5% leads to 20%, 10% to 49% and finally 20% to 152%.

A similar test for the sphere configuration is shown in Figure 3.22. We find final errors of 3.2%, 14.5%, 32% and 77% after demagnetization with an initial artificial error of 1%,

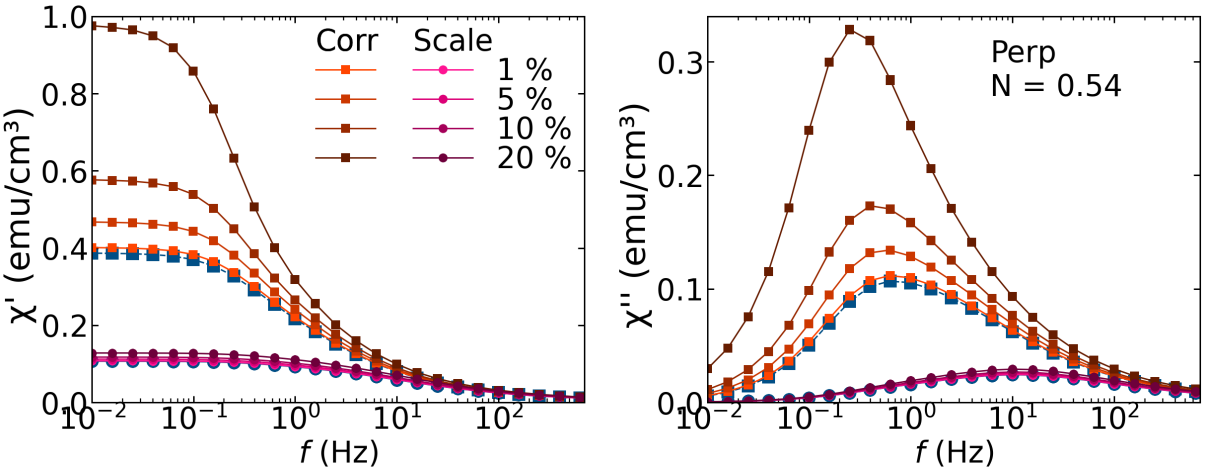


Figure 3.21: Ac susceptibility $\chi'$ and $\chi''$ vs $f$ measured at 900 mK for the parallepiped $Ho_2Ti_2O_7$ sample in the perpendicular configuration with estimated $N_\perp = 0.544 \times 4\pi$. The dots symbols show the measured susceptibility and the square symbols the susceptibility corrected from demagnetization factor $N_\perp$ (intrinsic susceptibility). The initial measured and intrinsic susceptibilities are shown in blue. In shades of pink are shown the susceptibility values obtained after adding an error of 1%, 5%, 10% and 20% on the initial measured susceptibility. In shades of orange are shown the intrinsic susceptibilities that would correspond to these modified measured susceptibilities.

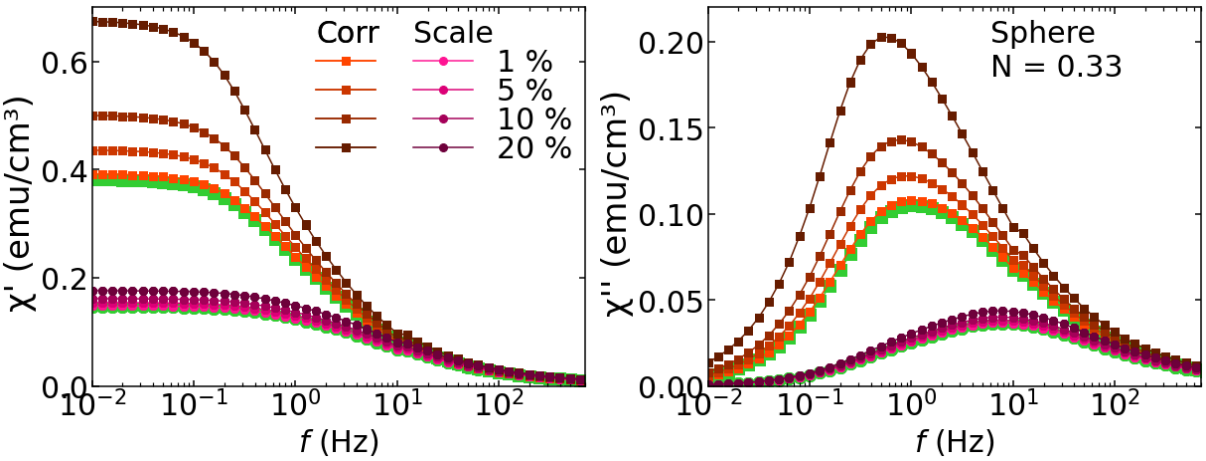


Figure 3.22: Ac susceptibility $\chi'$ and $\chi''$ vs $f$ measured at 900m K for the sphere $Ho_2Ti_2O_7$ sample with estimated $N_{sphere} = 1/3 \times 4\pi$. The dots symbols show the measured susceptibility and the square symbols the susceptibility corrected from demagnetization factor $N_{sphere}$ (intrinsic susceptibility). The initial measured and intrinsic susceptibilities are shown in green. In shades of pink are shown the susceptibility values obtained after adding an error of 1%, 5%, 10% and 20% on the initial measured susceptibility. In shades of orange are shown the intrinsic susceptibilities that would correspond to these modified measured susceptibilities.

5%, 10% and 20% respectively. The scaling error causes less dramatic effect compared to the parallepiped perpendicular geometry as $N$ is smaller. Nonetheless $N_{sphere} = 1/3 \times 4\pi$ is still a high demagnetization factor and we see that a precise calibration remains very important.

Calibration errors can originate from different sources and can be hard to deal with. One source of error is linked to the respective size of the sample comparatively to the gradiometer. Ideally, for accurate absolute susceptibility measurements, the sample needs to be in a configuration where it can be considered point like with regards to the coil. However, in noise measurements we need large samples that maximize the filling factor of the gradiometer to optimize the noise over baseline ratio. In the magnetometer used for the calibration of our data, the parallepiped and sphere samples can be assumed to satisfy this approximation but this is not clearly the case for the cylinder. Hopefully, the sphere which is our control sample should not be affected by this effect but it makes the comparison with all the different sample configurations complicated.

To summarize this study, the sphere should provide an ideal method for extracting intrinsic susceptibility due to its well-defined temperature independent $N$. However, due to its relatively large $N$ value, small calibration errors can significantly affect the final $\chi_{int}$. We thus suggest that a sample with a shape which gives the smallest $N$ factor, like a flat ellipsoid, is the best way to access the intrinsic susceptibility. Even if $N$ cannot be 0, the smaller $N$ is, the less errors are propagated through demagnetization corrections. Unfortunately, such samples can be difficult to make and are suboptimal for noise detection due to their low filling factor.

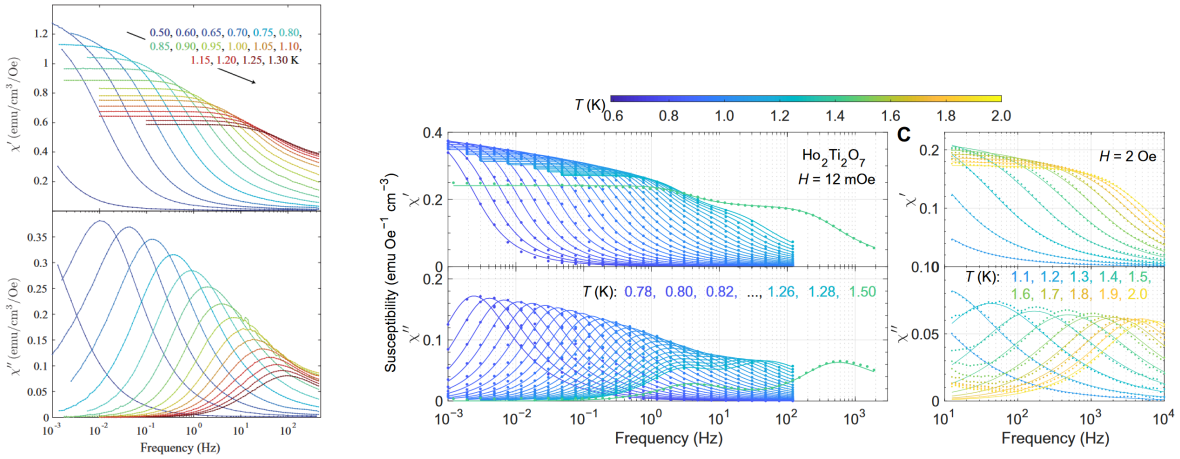


Figure 3.23: Ac susceptibility $\chi'$ and $\chi''$ vs $f$ for different temperature obtained for $Ho_2Ti_2O_7$ by (a) Ref. [50] and (b) Ref. [57].

To emphasize on this point, Figure 3.23 shows literature data on the obtained intrinsic susceptibility of $Ho_2Ti_2O_7$ from Wang et al. [57] and Quilliam et al. [50]. A big difference in the intrinsic susceptibilities values were found with $\chi'_{int}(f \to 0) = 0.37$ emu/cm$^3$ for Wang et al. and $\chi'_{int}(f \to 0) = 0.88$ emu/cm$^3$ for Quilliam et al. at 900 mK. The two measurements display more than a factor 2 in difference. In our study we find a value of $\chi'_{int}(f \to 0) = 0.4$ emu/cm$^3$, which is closer to the Wang et al. paper. Although these

different values could be due to sample dependence, we believe that it is more likely that these strong differences are due to the effect of demagnetization corrections.

In the end, the procedure we used with a sphere as a control sample gives an estimate of the intrinsic susceptibility with a precision of a few percents. We assume the $N$ values derived for the different $Ho_2Ti_2O_7$ sample configurations using this method are reliable and we proceed to estimate their impact on the noise measurements.

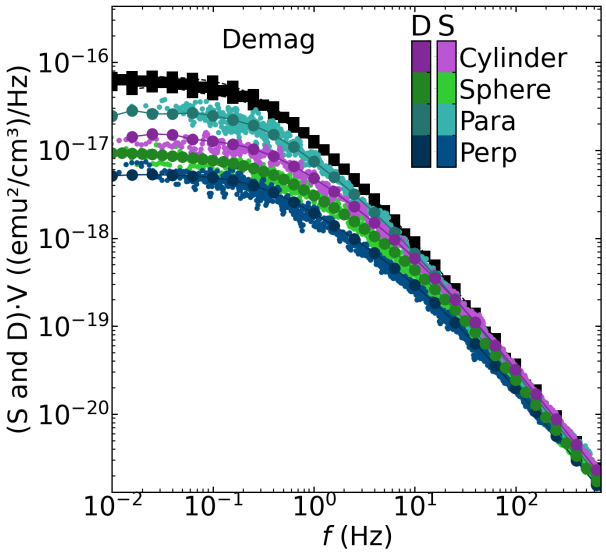


Figure 3.24: FDR plot multiplied by volume for four different sample configurations of $Ho_2Ti_2O_7$ on a logarithmic scale: $S(f)\cdot V$ (small dots) and $D(f)\cdot V$ measured at 900 mK. The square black dots represent the data corrected from demagnetization factor $D(f)\cdot V$. The $N$ factors used are : $N_\perp = 0.544\times 4\pi$, $N_\parallel = 0.1\times 4\pi$, $N_{sphere} = 1/3\times 4\pi$ and $N_{cylinder} = 0.18\times 4\pi$. Lines are guides to the eye.

Figure 3.24 shows the noise spectra $S_{mes}(f)$ of the four $Ho_2Ti_2O_7$ sample configurations measured at 900 mK. These noise spectra overlap perfectly with their susceptibility analog $D_{mes}(f)$ obtained using the FDR. To make easier the comparison between the different configurations, the plotted quantities $S(f)$ and $D(f)$, which are proportional to $\chi''(f)/f$, are multiplied by the sample volume $V$. This is done since the susceptibilities $\chi''$ are in units per volume while the FDR (Equation 2.3.4) introduces a $1/V$ factor when transforming into noise units. The noise is indeed an extensive quantity which depends on the volume so that the spectra are shifted toward higher magnitudes for samples of small volume.

Similarly to the susceptibility, the noise is clearly sample dependent with a significant change in the low frequency noise plateau $S_{0mes}$, showing a factor of nearly an order of magnitude between the parallel and perpendicular configuration. The correction of the measured $D_{mes}(f)$ gives an estimate of the intrinsic noise $S_{int}$ we should measure, this correction is shown in black for all four configurations. The corrected noise spectrum $D_{int}(f)$ shows a plateau value at $6\cdot 10^{-17}$ $((\text{emu/cm}^3)^2/\text{Hz}\cdot\text{V})$ which is one order of magnitude larger than the plateau value measured in the perpendicular configuration with

$N = 0.544 \times 4\pi$. This highlights the importance of the sample shape in quantitatively accessing the intensity of the dynamics. Indeed, theoretical models are usually performed in periodic boundary conditions that do not capture this kind of shape effects.

These results confirm that the noise is intrinsically shape dependent and that this dependence originates directly from demagnetization effects. Instead of having to rely on the susceptibility to correct this effect on the noise, ideally one would like to correct the noise spectra directly from the measured quantity $S_{mes}(f)$. The next section explores this possibility using Kramers-Kronig relation to deduce the in-phase susceptibility component from the noise itself to then be able to perform the corrections properly.

### 3.4.5 Kramers-Kronig integration for correcting the noise

When measuring magnetic noise $S(f)$, we directly access the dissipative part of the susceptibility $\chi''$, through the FDR when the system is in thermal equilibrium, similarly to the determination of $D(f)$ from $\chi''$. However, correcting from demagnetization requires knowledge of both $\chi'_{mes}$ and $\chi''_{mes}$, since the intrinsic imaginary susceptibility $\chi''_{int}$ is a mix of these two components. In physical systems such as ours, the real and imaginary parts of response functions (like the complex magnetic susceptibility $\chi$), are connected through the Kramers-Kronig (KK) relation [122]:

$$\chi'(\omega) = \frac{1}{\pi}\mathscr{P}\int_{-\infty}^{\infty}\frac{\chi''(\omega')}{\omega'-\omega}d\omega' \qquad \chi''(\omega) = -\frac{1}{\pi}\mathscr{P}\int_{-\infty}^{\infty}\frac{\chi'(\omega')}{\omega'-\omega}d\omega' \tag{3.10}$$

where $\mathscr{P}$ is the Cauchy principal value. In theory, one can use this relation to compute the $\chi'(f)$ associated to the noise by converting it into $\chi''(f)$, and then perform demagnetization corrections. This approach has been proven successful in other types of measurements such as optical conductivity and dielectric permittivity where the KK integration is used numerically directly onto the experimental data [123]. However, in practice, applying this technique in the context of our measurements is complicated.

Figure 3.25 (left panels) shows the susceptibility $\chi''_{noise}$ extracted from noise measurement at $T = 800$ mK, along with the $\chi'_{noise}$ obtained via KK numerical integration (green lines). The numerical integration was performed on Python using the pykk library. These are compared to ac susceptibility measurements $\chi_{mes}$ (green dots). As expected from the FDR, $\chi''_{noise}$ and $\chi''_{mes}$ are in perfect agreement. However, the KK integration derived $\chi'_{noise}$ is slightly underestimated compared to the direct susceptibility measurement $\chi'_{mes}$. This loss in the noise derived $\chi'_{noise}$ is a result of the limited frequency range of our measurements which does not covers fully the spectral weight of $\chi''_{noise}$. At this temperature, the missing spectral weight is located at low frequencies.

When we apply the demagnetization correction using this KK-derived $\chi'_{noise}$ along with its corresponding noise transformed $\chi''_{noise}$, we find that both the $\chi'_{int}$ and $\chi''_{int}$ (purple lines) are now underestimated compared to the intrinsic susceptibility obtained directly from ac susceptibility (purple dots). This result is expected, as the loss in the KK $\chi'_{noise}$ is amplified by demagnetization corrections. Nonetheless because the loss is small, Figure 3.25 (right panel) shows that the overall intrinsic noise spectrum $S_{int}(f)$ obtained through this method remains close to the expected curve at 800 mK.

This KK correction protocol works reasonably well when the full relaxation process is contained within the experimental frequency window. However its limitations become

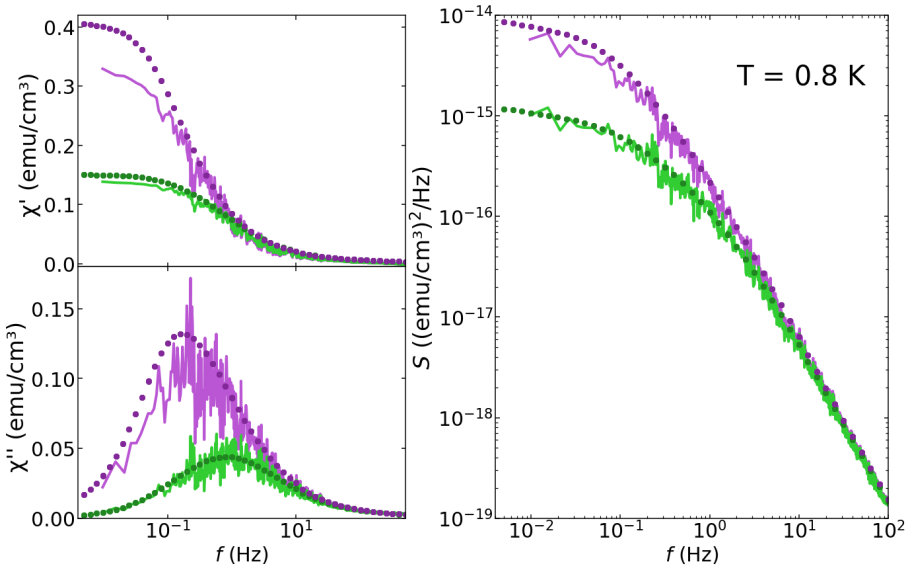


Figure 3.25: Left panel: Measured (green) and intrinsic (purple) ac susceptibility $\chi'$ and $\chi''$ vs $f$ at 800 mK for the sphere sample of $Ho_2Ti_2O_7$ (dots). $\chi''$ noise lines corresponds to the susceptibility obtained from the noise through FDR, the corresponding noise $\chi'$ is obtained with Kramers-Kronig integration. The demagnetization correction of the noise curve is realized with the measured $\chi''$ and the deduced Kramers-Kronig $\chi'$. Right panel: Measured (green) and intrinsic (purple) noise PSD $S(f)$ with the associated $D(f)$ susceptibility (dots).

evident as soon as the temperature changes and the relaxation process is not centered within our frequency range. To illustrate this, we can look at Figure 3.26 which shows the same quantities as Figure 3.25 but for $T = 1.1$ K. At this temperature, the relaxation response shifts to higher frequencies and the noise reaches the SQUID baseline at around $f = 3.2$ kHz. Beyond this frequency, the signal is no longer accessible, and as these frequencies carry a consequent part of the spectral weight, it results in a more pronounced loss of intensity in $\chi'_{noise}$ upon performing the KK integration. This loss propagates through the demagnetization correction and leads to further underestimation of both $\chi'_{int}$ and $\chi''_{int}$.

As the relaxation times in spin ice evolve on several timescales with respect to temperature [43], we usually do not cover the total spectral response for a given temperature. While the KK-based method can work, it requires full spectral coverage, which our experiments usually do not provide. One solution to overcome such issue, would be to extend the behavior of the curves beyond the measured frequency ranges using fits model or spline methods, to then perform the correction protocol. Using the empirical fit model for the noise (Equation 3.5), the KK procedure can be performed to estimate the associated $\chi'$. If there is access to the measured susceptibility, a second possibility would be to fit the Cole-Davidson (Equation 3.3), from which the intrinsic noise can be obtained by performing the usual demagnetization correction. These two methods are almost equivalent as the Cole-Davidson model and the noise fit model give close results (Figure 3.6).

Although using the fits for that purpose is a good way to understand how the curves

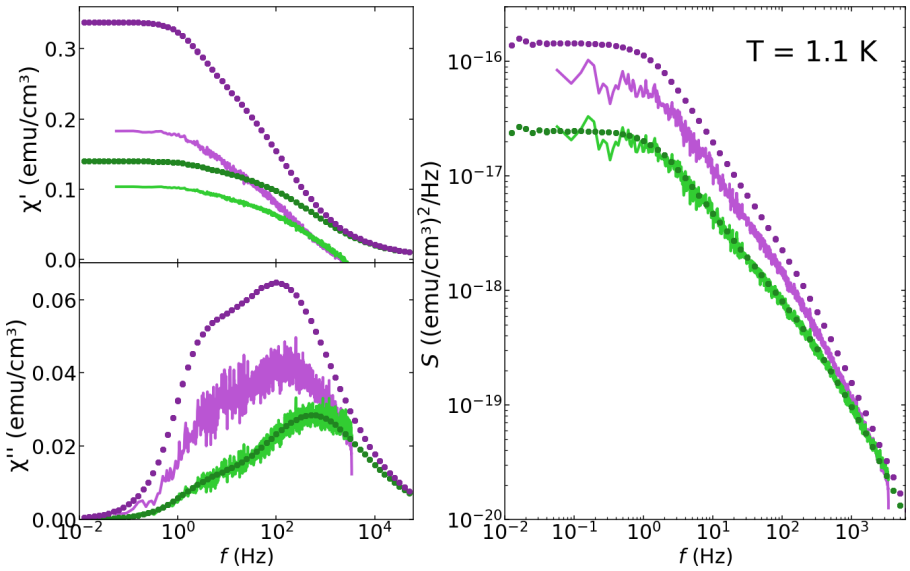


Figure 3.26: Left panel: Measured (green) and intrinsic (purple) ac susceptibility $\chi'$ and $\chi''$ vs $f$ at 1.1 K for the sphere sample of $Ho_2Ti_2O_7$ (dots). $\chi''$ noise lines corresponds to the susceptibility obtained from the noise through FDR, the corresponding noise $\chi'$ is obtained with Kramers-Kronig integration. The demagnetization correction of the noise curve is realized with the measured $\chi''$ and the deduced Kramers-Kronig $\chi'$. Right panel: Measured (green) and intrinsic (purple) noise PSD $S(f)$ with the associated $D(f)$ susceptibility (dots).

change when $N$ is evolving, we saw in Section 3.1.5 that they remain empirical models that cannot capture perfectly the whole physics of the system. We also saw that small errors (a few percents) on the measured susceptibility can strongly affect the intrinsic curves deduced, making such extrapolation methods unreliable for precise correction of the noise.

In summary, aside from the KK integration method, which we have shown not to be appropriate in our case, we do not know any protocol for correcting noise measurements using noise alone. If ac susceptibility is available, it can be used in combination with the noise data to estimate the intrinsic noise. In a recent study [124], some insights into the origin of demagnetization effects in noise spectra were provided along with the estimation of the parameters which describe the noise behavior. This paper motivated us to use the different susceptibility fit models on the noise, to estimate the evolution of noise parameters with $N$, and how well they compare to theoretical predictions from Ref. [124].

### 3.4.6 Behavior with N

When we first observed experimentally that the spontaneous fluctuations of magnetization are affected by the sample shape due to demagnetization effect, we did not understand its origin as the noise is a quantity measured at zero field. Recently, Bramwell [124] explained the microscopic origin of this effect and provided theoretical predictions regard-

ing how the noise parameters are modified by the effect of the demagnetization field.

Bramwell pointed out that the fluctuations of magnetization cost a different amount of energy depending on the canonical average $\langle ... \rangle$ considered, which itself is influenced by the sample shape. Since the shape of the noise spectra is directly derived from the fluctuations of the magnetization through the relation $S(f) = FT[\langle M(0)M(t)\rangle]$, it follows that $S(f)$ should also depend on the canonical average and therefore on the sample geometry.

Bramwell went further, discussing how the noise autocorrelation function can be analytically corrected for demagnetization in two specific relaxation scenarios: exponential relaxation (Debye model, exponent equal to 2) and pink noise relaxation (exponent equal to 3/2). Unfortunately, spin ice materials do not fall into either category. As seen previously in Section 3.1.6, the dynamics of $Dy_2Ti_2O_7$ and $Ho_2Ti_2O_7$ depends respectively on one or two relaxation times with associated anomalous exponents [39, 56, 57, 65, 108] that vary with temperature. The PSD of the corresponding noise associated to that dynamics follows the model:

$$S(f) = \frac{S_0}{1 + (2\pi f \tau)^{\alpha}} \tag{3.11}$$

So the spin ice case cannot be treated analytically for demagnetization as Bramwell shows that the measured noise $S_{mes}$ cannot be related to the intrinsic noise $S_{int}$ in the general case for monotonic relaxation. Nonetheless, ratios between the intrinsic and measured parameters of $S_0$ and $\tau$ were derived for this general case in order to estimate the effect of $N$.

The behavior of the ratio of the low frequency noise plateau is shown to follow:

$$\frac{S_{0mes}}{S_{0int}} = \frac{1}{(1 + N \cdot \chi'_{0int})^2} \tag{3.12}$$

which can also be derived directly from the demagnetization equation (Equation 3.9) since this ratio corresponds to:

$$\frac{S_{0mes}}{S_{0int}} = \frac{\chi''_{mes}(f \to 0)}{\chi''_{int}(f \to 0)} \tag{3.13}$$

This expression holds for any kind of magnetic system as long as the FDR is satisfied. The second proposed behavior concerns the characteristic times, for which the ratio $\tau_{mes}/\tau_{int}$ is proposed to vary as $(1 - N\chi'_{0mes})$ (with $\chi'_{0mes} = \chi'_{mes}(f \to 0)$).

The objective here is to quantify the effect of $N$ on the different parameters of the dynamics and to compare them with the behavior proposed by Bramwell. Since experimentally accessing any arbitrary sample shape is impractical, we estimate the $S$ and $\tau$ behavior using fitted susceptibility models. We first considered the case of a single relaxation time process, using the Debye relaxation model for simplicity.

A single relaxation process corresponds to the case of the $Dy_2Ti_2O_7$ compound, so the model is taken for values of $S_{0mes}$, $\tau_{mes}$ which correspond to the closest Debye fit to our experimental data at 900 mK. The fit model $D_{mes}(f)$ is corrected from demagnetization using the estimated value $N = 0.13 \times 4\pi$ for this sample geometry. The intrinsic spectrum obtained is then "re-demagnetized" by varying $N$ back from 0 to 1 to simulate different

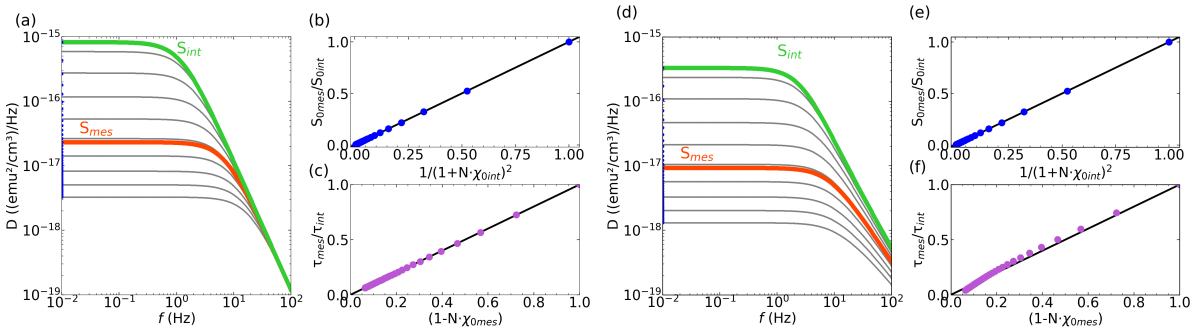


Figure 3.27: (a)(d) $D$ vs $f$ for different $N$ values between 0 and $1\times4\pi$ at 900 mK obtained with (a) the Debye model and (d) the Cole-Davidson model. The orange curve $S_{mes}$ is a fit using the parameters $\tau = 0.022$ s, $\chi_T = 0.2$ emu.cm$^{-3}$, $\beta = 1$ for (a) and $\beta = 0.4$ for (d). The grey curves correspond to the expected measured susceptibilities $S_{mes}$ for different values of $N$. (b)(e) Ratio between the measured magnetic noise plateau $S_{mes}(f=0)$ and the intrinsic $S_{int}(f=0)$ for (b) the Debye model and (e) the Cole-Davidson model as function of $1/(1+N\chi'_{0int})^2$. The solid black line corresponds to a linear curve. (c) Debye model and (f) Davidson-Cole relaxation time ratio as function of $1-N\chi'_{0mes}$. The solid black line corresponds to a linear curve.

geometries with different effective $N$. There is no need to use KK integration for demagnetization as we know both $\chi'_{mes}$ and $\chi''_{mes}$ when using the Debye model (Equation 3.1).

Figure 3.27 (left panels (a), (b) and (c)) shows several frequency spectra $D(f)$ (gray curves) for different $N$ values ranging from 0 to $4\pi$. The initial fit of the measured $D_{mes}(f)$ is highlighted in orange, and the intrinsic corrected $D_{int}(f)$ is highlighted in green. This example demonstrates that the demagnetization factor $N$ can dramatically affect the measured $D(f)$ curves, with variations up to two orders of magnitude between $N=0$ and $N=1$. The values of the parameters $S_{0mes}$, $S_{0int}$, $\chi'_{0mes}$ and $\chi'_{0int}$, needed to estimate the ratios, are extracted from the curves in the low frequency limit. The $\tau$ value is estimated from the maxima of the peak in the dissipative part $\chi''$. From those parameters we can estimate the $S$ and $\tau$ ratio behaviors with $N$. They obey the relations expected from the model, as shown by the $S_0$ and $\tau$ ratio plots as a function of $1/(1+N\chi'_{0int})^2$ and $1-N\chi'_{0mes}$ on panels (b) and (c) respectively.

Using the more realistic Cole-Davidson model (Equation 3.3), we observed that while the $S$ ratio still obeys the expected trend, the $\tau$ ratio deviates (Figure 3.27 right panels (d), (e) and (f)). This deviation of the $\tau$ ratio arises directly from the asymmetry of the relaxation time distribution of the Davidson-Cole function, which shifts the $\chi''$ peak maximum away from the $(1/2\pi)\tau$. This deviation is enhanced when the $N$ factor is large.

Similarly, we repeated this procedure for the case of a double Cole-Davidson model for $Ho_2Ti_2O_7$, using a sum of two Equations 3.3. We take the fit corresponding to the $Ho_2Ti_2O_7$ sphere sample at 900 mK, and we use $N_{sphere} = 1/3\times4\pi$ to obtain the intrinsic spectrum which we "re-demagnetized" for other $N$ values. The results are shown in Figure 3.28.

For the case of a double relaxation process, if the two timescales are well separated, the $S_0$ ratio relation is defined with the noise plateau of the low frequency process that

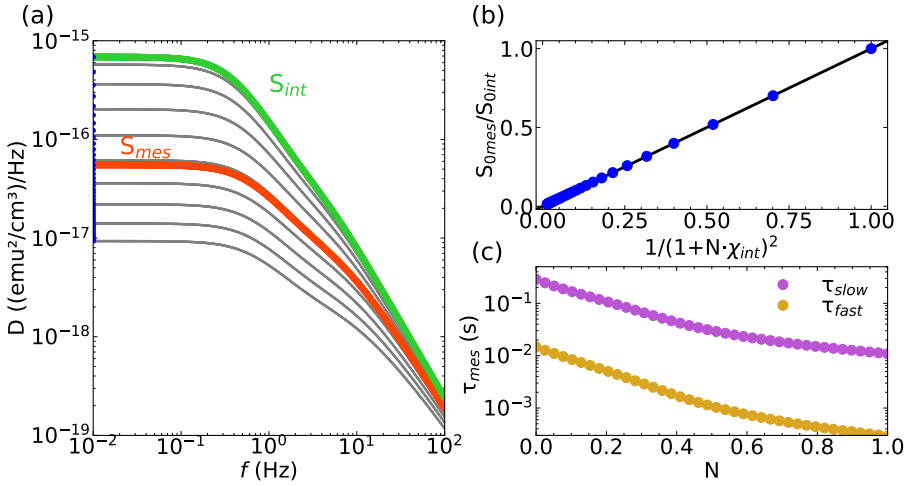


Figure 3.28: (a) $D$ vs $f$ for different $N$ values between 0 and $1\times4\pi$ at 900 mK. The orange curve $S_{mes}$ is a fit using a sum of two Cole-Davidson equations of the measured sphere sample susceptibility with $\tau_1 = 0.294$ s, $\beta_1 = 0.4$, $\chi_{T1} = 0.081$ emu.cm$^{-3}$, $\tau_2 = 0.026$ s, $\beta_2 = 0.43$, $\chi_{T2} = 0.0904$ emu.cm$^{-3}$ and $\chi_{S1} = \chi_{S2} = 0$. The green curve $S_{int}$ is obtained by correcting the orange curve using $N_{sphere} = 1/3\times4\pi$ and corresponds to the intrinsic susceptibility ($N = 0$). The grey curves corresponds to the expected measured susceptibilities $S_{mes}$ for different values of $N$. (b) Measured magnetic noise plateau $S_{mes}(f = 0)$ normalized by the intrinsic magnetic noise plateau $S_{int}(f = 0)$ varying with $1/(1+N\chi'_{0int})^2$. The solid black line corresponds to a linear curve. (c) The two relaxation times $\tau_{slow}$ (in purple) and $\tau_{fast}$ (in gold) vs the demagnetization factor $N$.

dominates at low frequencies. When the two relaxation times overlap in frequency, it becomes necessary to write the relation using their sum instead. In our example the two times are sufficiently well separated so the ratio relation is well reproduced when taking only the value of the dominating low frequency process. As in the single Cole-Davidson case, the $\tau$ ratios for both processes deviate from the expected $(1-N\chi'_{0mes})$ scaling due to the asymmetry in the peak positions. Nevertheless, we can see that the two measured relaxation times are independently both reduced with $N$ but have a different dependence.

These tests confirm that the behavior of the noise curves and the associated fit parameters depend strongly on the $N$ factor. This effect is particularly strong for the magnitude of the noise plateau $S_{0mes}$, which follows the expected $(1+N\chi'_{0int})^{-2}$ dependence. Unfortunately, to estimate this behavior it is required to know the intrinsic value of the susceptibility at low frequency $\chi_{int}(f\to0)$. This means that an extra measurement of the dc susceptibility is needed to make the demagnetization correction and estimate the intrinsic value of the noise on the low frequency plateau. As shown above, another alternative would be to model the ac susceptibility, obtained from a fit of the noise, and then to reconstruct the demagnetization behavior of the noise plateau without accessing the experimental value of $\chi_{int}(f\to0)$.

The $\tau$ parameter in contrast does not follow the behavior derived in Ref. [124] with models with an asymmetric distribution of relaxation times. This shift due to the asymmetry is not dramatic but shows how the choice of empirical fitting model affects the

extracted $\tau$.

Finally, we have not discussed the dependence of the $\alpha$ exponent on the $N$ factor. Indeed, theoretically, corrections for demagnetization field should not affect its value since it is a quantity defined in the high frequency limit where demagnetization corrections vanish. However in practice, when looking at Figure 3.28 it is clear that for $Ho_2Ti_2O_7$ we are not evaluating the noise up to this high frequency limit. As a consequence the observed slopes in the noise, and so the exponents, depend strongly on $N$. This conclusion applies also to $Dy_2Ti_2O_7$ depending on the frequency range of measurement accessible.

To summarize, we have seen that by fitting the data with phenomenological models we are able to estimate how the $S$ and $\tau$ parameters depend on the factor $N$ without needing measurements with several sample geometries. The $S$ ratio extracted from fits follows the expected scaling [124], while for the $\tau$ ratio it depends on the model. In the case of $\alpha$, it is not expected to depend on $N$. Nevertheless, one has to be careful when estimating $\alpha$ from the models or high-frequency power-law fittings. Because measurements are made up to finite frequency, if the highest frequency is not large enough, the observed slope can be modified so that $N$ will impact on the $\alpha$ determination. In the next section, we will explore how these parameters evolve with temperature for a fixed sample geometry.

### 3.4.7 Impact of $N$ as a function of temperature

In experiments, we typically study one single sample geometry over a range of temperatures, rather than fixing $T$ and varying $N$. It is therefore interesting to estimate the impact of demagnetization across the entire temperature range. We explore this effect for one sample of each spin ice material: $Dy_2Ti_2O_7$ and $Ho_2Ti_2O_7$. The spherical geometry is well suited for this analysis, as the demagnetization factor $N_{sphere}$ is temperature independent. We performed this analysis on the sphere sample for $Ho_2Ti_2O_7$. As we did not have access to a spherical $Dy_2Ti_2O_7$ sample, we conducted the analysis on the cylindrical $Dy_2Ti_2O_7$ sample, for which we used the factor $N_{cylinder} = 0.13 \times 4\pi$ estimated from Aharoni's method [118]. Note that for this geometry, $N$ varies slightly with temperature (see Section 3.4.3). However we treat it as a constant parameter for simplicity. This analysis aims at estimating the strength of the demagnetization effect and does not pretend to give the exact corrected values of the parameters.

For both materials, we corrected the noise spectra $D_{mes}(f)$ from the susceptibility to obtain the intrinsic spectra $D_{int}$ which we then fit with Equation 3.3. For $Dy_2Ti_2O_7$, which displays a single relaxation process, we used a single timescale model, whereas for $Ho_2Ti_2O_7$, we employed a two timescale model (sum of two Davidson-Cole equations). The corrected spectra $D_{int}$ were fitted across the whole temperature range from 500 mK to 4.2 K. To describe the effect of the correction, we compute the temperature dependence of the ratios $S_{0int}/S_{0mes}$ and $\tau_{int}/\tau_{mes}$. We also compare the behavior of the $\alpha$ parameter before and after correction.

Figure 3.29 shows the evolution of the parameters for the two samples. The demagnetization effect, in both compounds, induces a small increase in both $\tau$ and $S_0$ ratios when $T$ decrease from 4 to 2 K. When the temperature decreases further the effect is stronger reaching a maximum around 800 mK, followed with a sharp decrease at lower temperatures. This temperature dependence can be understood as the magnitude of the demagnetization effect is directly linked to the magnitude of the real part of the ac sus-

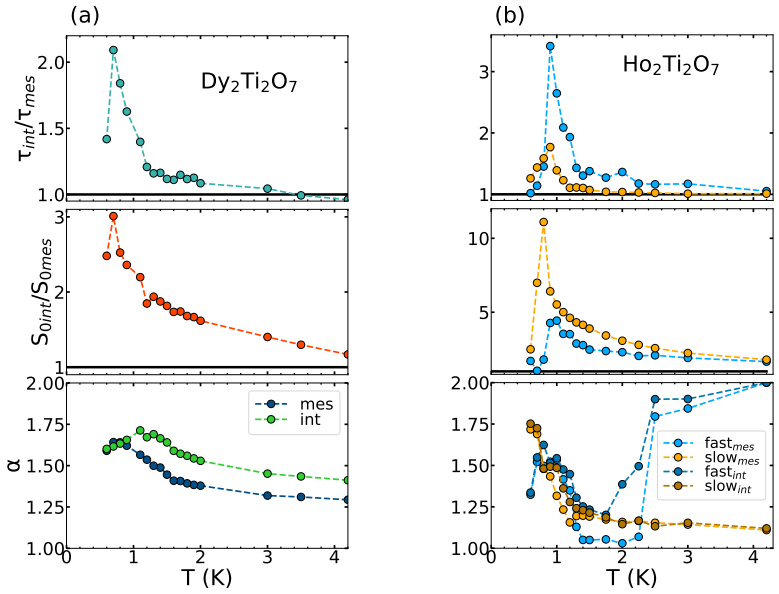


Figure 3.29: Relaxation time ratio $\tau_{int}/\tau_{mes}$ (top), noise at zero frequency ratio $S_{0int}/S_{0mes}$ (middle), $\alpha_{int}$ and $\alpha_{mes}$ (bottom) for (a) $Dy_2Ti_2O_7$ obtained from the fits of $D_{int}(f)$ and $D_{mes}(f)$ with Equation 3.3 for a cylinder sample with $N_{cylinder} = 0.13 \times 4\pi$ and for (b) the fast and slow processes in $Ho_2Ti_2O_7$ obtained from the fits of $D_{int}(f)$ and $D_{mes}(f)$ with Equation 3.3 for the sphere sample with $N_{sphere} = 1/3 \times 4\pi$.

ceptibility. When going to lower temperature (typically below 700 mK), the dynamical modes have characteristic frequencies lower than the measurement bandwidth so almost only the power law slope in the noise is measured. In that region $\chi'_{mes}(f)$ is small so the corrected $\chi'_{int}(f)$ appears less affected by the correction resulting in a smaller effect.

As expected, since $N_{sphere}$ for $Ho_2Ti_2O_7$ is more than twice the value $N_{cylinder}$ for $Dy_2Ti_2O_7$ the resulting strength of the demagnetization effect is stronger for $Ho_2Ti_2O_7$ in our example. The $\tau_{int}/\tau_{mes}$ ratio reaches about 2.25 for $Dy_2Ti_2O_7$ whereas it approaches 3.5 for $Ho_2Ti_2O_7$. The difference is even more pronounced for the $S_{0int}/S_{0mes}$ ratio, which reaches 12 for $Ho_2Ti_2O_7$ compared to 3 in $Dy_2Ti_2O_7$.

The fitted $\alpha$ parameter is also clearly affected by the demagnetization corrections both in $Dy_2Ti_2O_7$ and $Ho_2Ti_2O_7$. Since the demagnetization effects become small below 700 mK, $\alpha$ is unchanged for these low temperatures. However, in the intermediate temperature range where the correction is significant, the extracted $\alpha$ from measured noise spectra tends to be underestimated. This arises due to the frequency range of our measurements which limits the observation of the asymptotic slope at high frequency. In addition, the noise baseline can affect this asymptotic slope, and further decreases the apparent $\alpha$ exponent. As a result, the fitted $\alpha$ is extracted in a transitional regime where the low-frequency plateau or the noise baseline still influences the slope. After performing the demagnetization corrections on the noise curve, $\alpha$ increases as the plateau is enhanced and the characteristic time $\tau$ reduced. In the case of $Ho_2Ti_2O_7$, we can notice the effect on $\alpha_{slow}$ is weak compared to $\alpha_{fast}$ or the exponent of $Dy_2Ti_2O_7$.

Interestingly, for $Dy_2Ti_2O_7$, our demagnetized corrected fits yields $\alpha$ values closer to those reported by Billington et al. [119], where they used ac susceptibilities in the 2 - 30 K

range of $Dy_2Ti_2O_7$. This result resolves the discrepancies found between the $\alpha$ obtained in ac susceptibility and the anomalously low $\alpha$ values reported in noise measurements (Refs. [55, 65]). Those measurements were not corrected from demagnetization effects since this effect was never considered to play a role for magnetic noise. But as shown above, fittings of noise measurements tend to underestimate $\alpha$ compared to the intrinsic susceptibility results. Even when correcting the ac susceptibility from demagnetization it is possible that differences are found in the $\alpha$ values for different samples and measurement environments as estimating $N$ accurately is challenging.

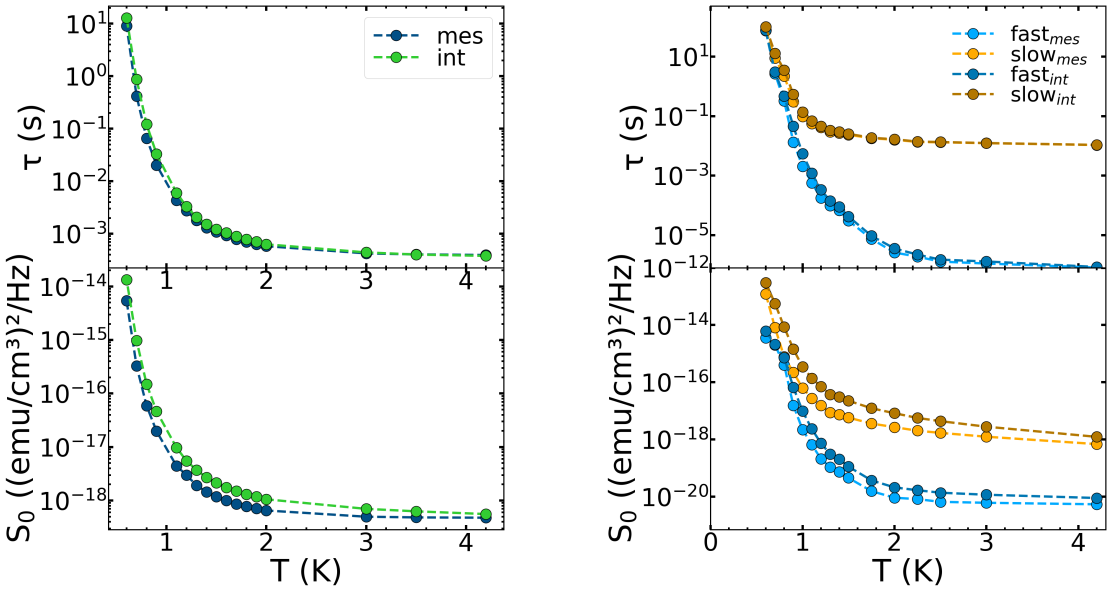


Figure 3.30: Relaxation times $\tau_{int}$ and $\tau_{mes}$ and noise at zero frequency ratio $S_{0int}$ and $S_{0mes}$ for $Dy_2Ti_2O_7$ (left panel) obtained from the fits of $D_{int}(f)$ and $D_{mes}(f)$ with Equation 3.3 for a cylinder sample with $N_{cylinder} = 0.13 \times 4\pi$ and for the fast and slow processes in $Ho_2Ti_2O_7$ (right panel) obtained from the fits of $D_{int}(f)$ and $D_{mes}(f)$ with Equation 3.3 for the sphere sample with $N_{sphere} = 1/3 \times 4\pi$.

Even though these corrections result in strong quantitative differences, the overall spin ice dynamics remains unchanged (Figure 3.30). Parameters like $\tau$ and $S_0$ naturally span over several orders of magnitude over the measurement temperature range. Even if the relative corrections can be significant, the overall changes are not dramatic when considering the differences that were found between different samples or measurements in the literature. The demagnetization effect is most critical for extracting accurately the $\alpha$ parameter that can easily be underestimated. To this respect, it is important since $\alpha$ is a key parameter to understand how correlations and constraints build up in the materials and is directly connected to the nature of the monopole dynamics [56].

## 3.5 $Dy_2Ti_2O_7$ isotopic differences

During my PhD project, we measured two types of $Dy_2Ti_2O_7$ samples: one isotopically enriched with $^{162}$Dy, and another with a natural mixture of Dy isotopes. Among the

naturally occurring isotopes, $^{161}$Dy and $^{163}$Dy have a nuclear spin $I = 5/2$, while the other isotopes, including $^{162}$Dy, do not have a nuclear spin. In the natural sample, the isotope distribution gives 19% of $^{161}$Dy, 25% of $^{163}$Dy and the 66% remaining are non nuclear spin isotopes.

In the previous sections, we focused on the results from the $^{162}Dy_2Ti_2O_7$ sample for two main reasons. First, it gives a better signal in the noise experiment because it is a large sample. Second, its dynamics is located at higher frequencies making it better suited to study the low temperature behavior despite our low frequency limit of 0.001 Hz. The origin of the faster dynamics in the $^{162}Dy_2Ti_2O_7$ compound remains unclear, especially as it was evidenced that the hyperfine interactions enhance the dynamics of quenched monopoles in the frozen regime of spin ices [125].

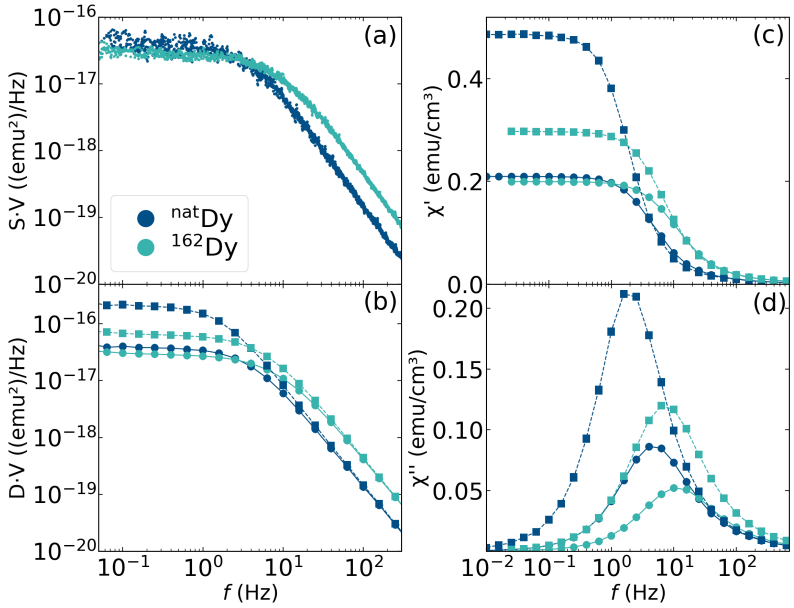


Figure 3.31: (a) $S_{mes} \cdot V$ vs $f$ and (b) $D_{mes} \cdot V$ and $D_{int} \cdot V$ vs $f$ measured for the two different isotopes $^{162}Dy_2Ti_2O_7$ and $^{nat}Dy_2Ti_2O_7$. Measured (dots) and intrinsic (squares) ac susceptibility (c) $\chi'$ and (d) $\chi''$ for the same two $Dy_2Ti_2O_7$ samples. The intrinsic susceptibility $\chi_{int}$ and $D_{int}$ are obtained with the factors $N = 0.131 \times 4\pi$ for the $^{162}$Dy sample and $N = 0.216 \times 4\pi$ for the $^{nat}$Dy. All quantities were measured at T = 900 mK.

We initially suspected that the observed effect might be related to demagnetization, which shifts the measured timescale. We performed demagnetization corrections using $N$ factors estimated from Aharoni's method, with $N = 0.131 \times 4\pi$ for the $^{162}$Dy sample (as previously used), and $N = 0.216 \times 4\pi$ for the $^{nat}$Dy. The $^{nat}$Dy sample is a parallelepiped measuring $3.55 \times 2.21 \times 1.77$ mm$^3$ and was measured along its long axis corresponding to the [001] direction (previously studied as sample 3 of Ref. [59]).

Figure 3.31 compares both the measured and intrinsic noise spectra and ac susceptibility curves at 900 mK. The shift in $\tau$ between the two samples is still clearly present even after demagnetization correction. In the high frequency limit, where demagnetization effects are weak, the $D(f)$ curves still show a clear separation between the timescales of the two compounds. The $^{nat}$Dy sample possesses a higher $N$ factor along with a longer

$\tau$ than the $^{162}$Dy sample, so the demagnetization correction actually reinforces the shift between the two characteristic times. From this check it is clear that the difference between the two different timescales for the two compounds cannot be simply explained through a demagnetization phenomenon.

By examining the temperature dependence between 4.2 K and 0.6 K of $\chi''$ and the noise spectra of the two different $Dy_2Ti_2O_7$ samples (Figure 3.32), the two timescales remain separated, and no crossing is observed. This result is expected, as the interaction energies should be the same in both compounds: the nuclear spin does not affect the dipolar or exchange interaction strength. Given that the effective interactions are identical, the divergence of the time $\tau$ at low temperature is also expected to be similar.

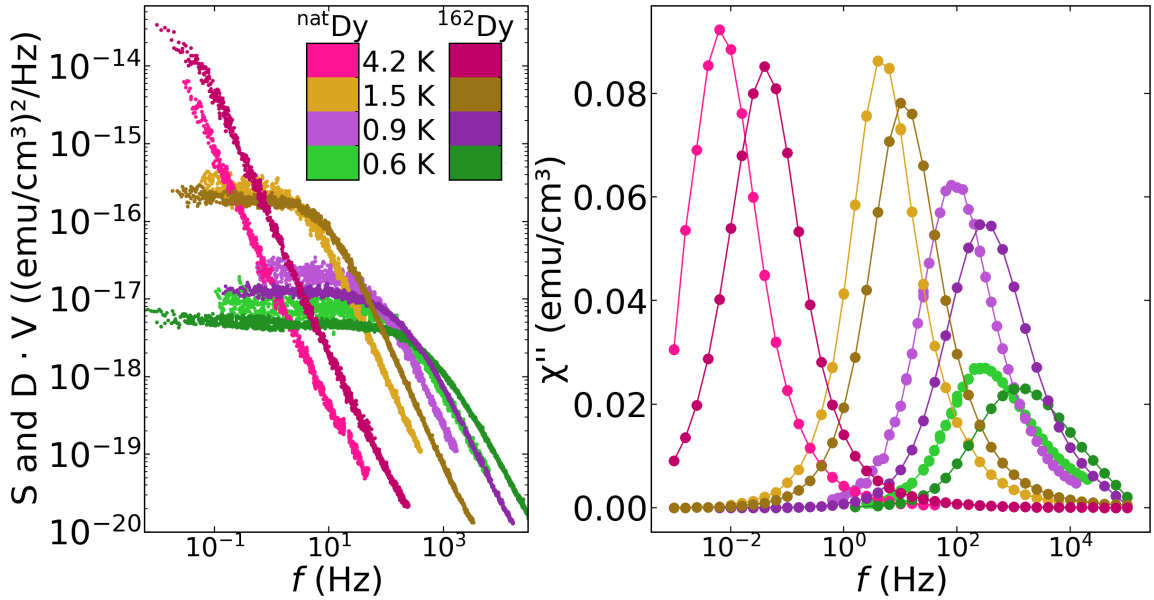


Figure 3.32: Left panel: Measured noise spectra $S_{mes}(f) \cdot V$ for four temperatures for the $^{162}Dy_2Ti_2O_7$ (dark colors) and $^{nat}Dy_2Ti_2O_7$ (clear colors) samples. Right panel: Measured out-of-phase susceptibility $\chi''_{mes}$ for the same four temperatures as left panel for the $^{162}Dy_2Ti_2O_7$ and $^{nat}Dy_2Ti_2O_7$ samples.

From this temperature dependence we have extracted the empirical parameters $\tau$ and $\alpha$ from the fitting of the noise curves for the $^{nat}$Dy sample and have compared them to the $^{162}$Dy parameters. The exact same protocol and fitting model is used for the $^{nat}$Dy sample. Figure 3.33(a) displays these two parameters with respect to temperature for the two samples. Apart from the $\tau_0$ obtained in the plateau regime, we see that the overall temperature behavior of $\tau$ and $\alpha$ is the same in the two compounds. The $^{nat}$Dy $\alpha$ shows a peak around 800 mK as well, and drops below that temperature. The similarity between the $\alpha$ values confirms that the correlations between the monopoles are not drastically changed in between the two compounds.

Comparing $\tau$ values from different isotopic $Dy_2Ti_2O_7$ samples reported in the literature, we find that $\tau_0$ can vary by more than an order of magnitude. Figure 3.33(b) presents several $\tau(T)$ datasets from the literature [43, 49, 55, 121], as well as results from internal communication (with Sean Giblin) and our own measurements. They are shown

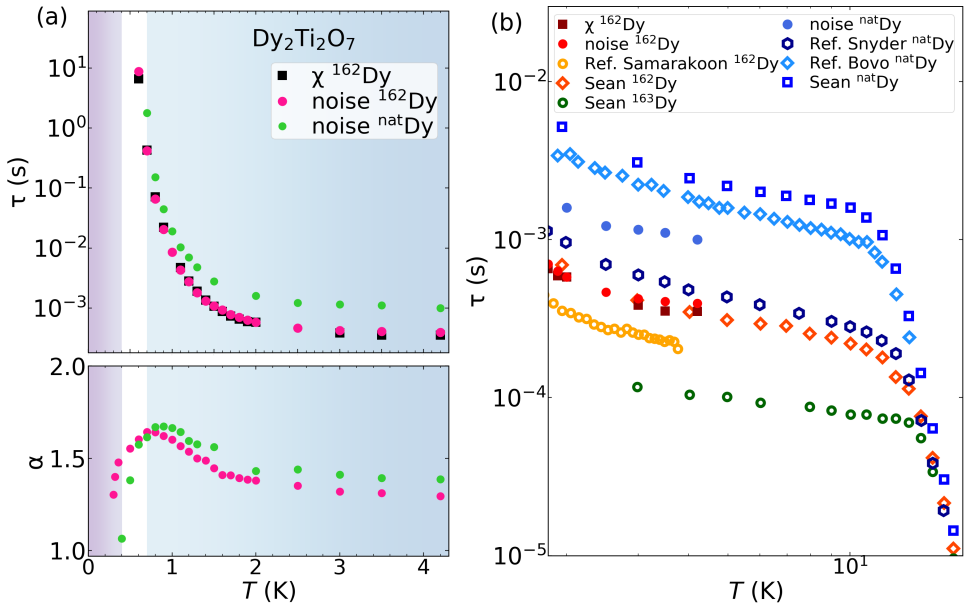


Figure 3.33: (a) Relaxation time $\tau$ (top panel) and exponent $\alpha$ (bottom panel) in $Dy_2Ti_2O_7$ for the $^{162}Dy_2Ti_2O_7$ and $^{nat}Dy_2Ti_2O_7$ samples, obtained from the fits of $\chi(f)$ with Equation 3.3 and of the noise data using Equation 3.5. Below 600 mK, it is not possible to fit the noise and ac susceptibility due to the absence of shoulder in the noise and of maxima in $\chi''$. The $\alpha$ parameter can nevertheless be obtained from the slope of the noise. The shaded backgrounds indicate the three temperature regimes: (i) equilibrium (blue), (ii) local equilibrium (white) and (iii) out of equilibrium (purple). (b) Relaxation time $\tau$ vs $T$ in $Dy_2Ti_2O_7$ for our two samples together with the $\tau$ obtained from Refs. [43, 49, 55, 121] and from Sean Giblin's data (private communication). The colors differentiate the three types of isotopes: $^{162}$Dy in orange/red, $^{163}$Dy in green and $^{nat}$Dy in blue.

on a logarithmic scale around the plateau region. A trend seems to emerge: $^{nat}$Dy samples (blue) display $\tau_0$ values higher than those of $^{162}$Dy (orange), while the lowest value is found for $^{163}$Dy (green). If hyperfine interactions were to enhance the dynamics we would have expected a different order of $\tau_0$ values with: $^{162}$Dy > $^{nat}$Dy > $^{163}$Dy. This indicates that there is no clear correlations between the $\tau_0$ and the presence or absence of nuclear spins in Dy. Moreover, the different measurements of $^{nat}$Dy yields very different results in $\tau_0$, so it is hard to confidently attribute the differences solely to isotopic effects.

Comparing directly the $\tau_0$ between all those measurements is difficult as other parameters seem to play a role. Among them there are the demagnetization effects or the methods used to extract the $\tau$, that we mentioned earlier in this manuscript. Here, we compare the dynamics above 2 K, in the plateau regime where demagnetization effects are small, so they cannot explain the observed differences. It was also discussed that sample differences in oxygen stoichiometry in $Dy_2Ti_2O_7$ can change the magnetic dynamic properties [126] of the spin ice state. Indeed, some ac susceptibility measurements were performed on as-grown and oxygen annealed samples between 500 mK and 1 K [127], and they could show that the dynamics was enhanced for the oxygen for these temperatures. However, this measurement was performed when the dynamics is strongly slowing down

and it is difficult to extrapolate this acceleration to the plateau region to deduce the $\tau_0$. Due to those effects, without dynamical measurements with more controlled samples of different isotopes, we cannot conclude on the effect of the isotope in this temperature range.

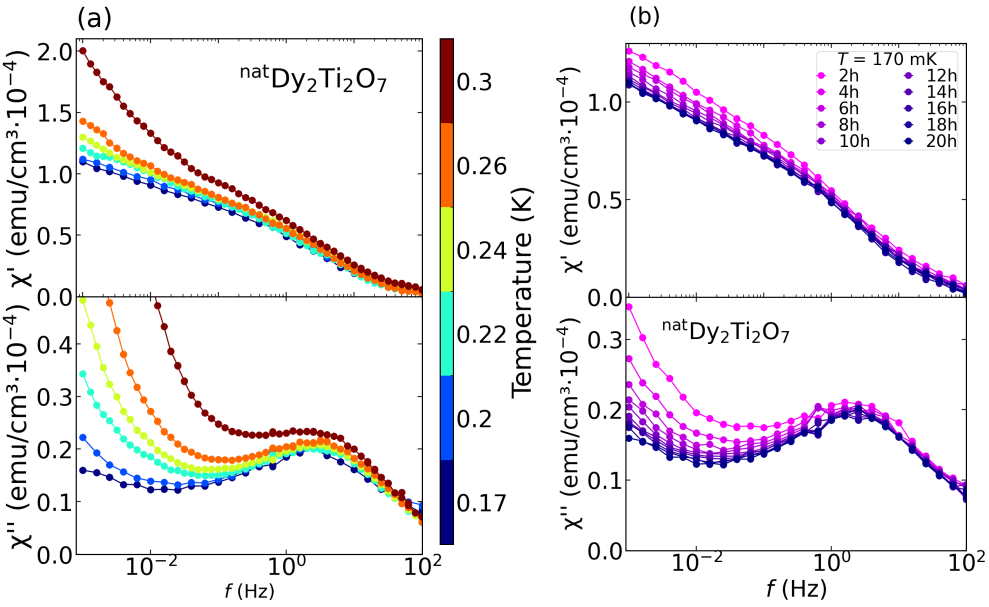


Figure 3.34: (a) ac susceptibility $\chi'$ (top panel) and $\chi''$ (bottom panel) vs $f$ for different temperatures below 300 mK in $^{nat}Dy_2Ti_2O_7$. (b) ac susceptibility measured after different waiting times at 200 mK for $^{nat}Dy_2Ti_2O_7$ at 170 mK after waiting 30 sec at 800 mK.

We also examined the susceptibility response deep in the spin freezing regime for the $^{nat}$Dy sample. In this low temperature range (below 500 mK), experiments on this sample were particularly challenging both for the noise or the ac susceptibility as the sample is significantly smaller than the two other samples studied in that regime. Unfortunately, the signal over baseline ratio was insufficient to measure correctly noise spectra below 400 mK so we were not able for this sample to explore the FDR where the deviation was found in the other samples. We nevertheless succeeded in accurately measuring the ac susceptibility down to 170 mK. The FDR was tested down to 400 mK, and no deviations were observed when comparing the measured noise with the ac susceptibility in this sample as expected from the experiments on the isotopic sample.

Figure 3.34(a) shows the temperature evolution of the ac susceptibility between 300 and 170 mK for the $^{nat}Dy_2Ti_2O_7$ sample. We clearly see the intermediate frequency peak in $\chi''$, indicating the same new magnetic process previously observed in the $^{162}Dy_2Ti_2O_7$ and $Ho_2Ti_2O_7$ compounds in this temperature range (Section 3.2.2). Interestingly, this peak appears at nearly the same frequency as the one in $^{162}$Dy ($f = 3.27$ Hz for $^{nat}$Dy against $f = 4.08$ Hz for $^{nat}$Dy), which suggests that it originates from the same effect. However, the peak amplitude is reduced in $^{nat}Dy_2Ti_2O_7$ by a factor 2.8 in comparison to the $^{162}Dy_2Ti_2O_7$ process. Figure 3.34(b) shows the magnetic susceptibility of the $^{nat}Dy_2Ti_2O_7$ is also subject to aging at 170 mK. The relative intensity of the aging properties are more pronounced than in $^{162}Dy_2Ti_2O_7$, which seems logical as the intensity of

the process is reduced in $^{nat}Dy_2Ti_2O_7$.

To summarize, the equilibrium monopole dynamics of the two isotopic $Dy_2Ti_2O_7$ compounds are well separated, and these differences cannot be explained by demagnetization effects. Along with our observations, numerous measurements reported in the literature do not show a clear trend regarding the influence of isotopes on the dynamics near the plateau regime. Other factors, such as oxygen stoichiometry and sample growth protocol, are likely to influence $\tau_0$ and must be considered before drawing conclusions about isotope effects. At lower temperatures, we were able to measure the susceptibility of $^{nat}Dy_2Ti_2O_7$ deep in the freezing regime. The low-temperature magnetic process observed in other samples is also clearly present in $^{nat}Dy_2Ti_2O_7$ and appears at the same frequency of the $^{162}Dy_2Ti_2O_7$ suggesting this new magnetic process is unaffected by the nature of the Dy nuclear spin.

In $Ho_2Ti_2O_7$, Ho naturally possess a single isotope with nuclear spin $I = 7/2$, so isotopic effects could play a role on the dynamics. However, both the equilibrium dynamics (which reveal two well-separated timescales) and the freezing regime dynamics (with the intermediate peak is located at $f = 0.16$ Hz) are so distinct to the $Dy_2Ti_2O_7$ dynamics that comparison with $Dy_2Ti_2O_7$ on the role of isotopes seems tricky. Overall, we find pronounced differences in the dynamics of both the equilibrium and freezing regimes across the compounds investigated. This emphasizes that the nature of spin ice dynamics remains far from fully understood. A large number of parameters (including isotope composition, oxygen vacancies, single ion properties, local magnetic fields, monopole correlations, etc.) are relevant and must be carefully addressed in future studies. Such efforts will help disentangle this complexity and advance our understanding of spin ice dynamics.

# Chapter 4

# Instrumental development

## Contents


4.1 Magnetic shielding . . . . . 104
4.2 Motivations for a new setup . . . . . 106
4.3 Optimization of detection . . . . . 107
4.4 Design realization . . . . . 112
4.5 Dilution refrigerator performances . . . . . 114

As part of this thesis, I carried out an independent instrumental project dedicated to magnetic shielding. As seen in the previous sections, achieving a sufficiently low residual magnetic field in the sample environment is crucial for reliable noise measurements. This work, completed prior to all the experiments presented in Chapter 3, will be presented first in this Chapter (Section 4.1).

The major instrumental challenge of my PhD was the development of a new magnetometer designed to improve the sensitivity of our measurements. This project, which is a central part of my work, will be presented just after the magnetic shielding section. I will start by outlining the motivations behind its conception (Section 4.2), before detailing the technical aspects of detection optimization and design realization (Sections 4.3 and 4.4). Finally, I will discuss the performance of the dilution refrigerator that hosts the probe, along with the remaining challenges we continue to face (Section 4.5).

## 4.1 Magnetic shielding

Having a very low residual magnetic field in the sample area is crucial to be able to measure precisely the sample noise. For instance, the earth magnetic field is about 500 mG in France, where our experiments were conducted. Without shielding, that field induces a finite sample magnetization, which in spin ice is strongly enhanced at low temperature due to effective ferromagnetic interactions. As the magnetization is temperature dependent (MvsT) the sample flux becomes sensitive to temperature effects. Any small temperature fluctuations induce a drift in the noise which results in a parasitic low frequency noise.

In order to minimize this effect, we optimized the performances of the magnetic shielding. To ensure minimal external residual magnetic flux in the sample area, we use several layers of magnetic shielding. As discussed in Section 2.3.1, outside the cryostat at room temperature two $\mu$-metal shields are used, and inside the helium bath, three Cryophy® (a Ni-Fe-Mo alloy treated for low temperature performance) shields are inserted (see Figure 2.7 of Method section).

These ferromagnetic shields possess a very high magnetic permeability, granting them the ability to efficiently trap magnetic flux lines. However as they are ferromagnetic materials, they can acquire a small remanent magnetization which can create a parasitic flux. To use these shields optimally, it is necessary to check the residual field in the cryostat and demagnetize them when the field is too high.

For that purpose, each shield is wound with a copper coil which is used to apply a demagnetization procedure. This procedure consists in applying an alternating magnetic field of a few hertz, with its amplitude progressively ramped down to zero. The initial amplitude must be strong enough to saturate the shield. We found that demagnetizing the shields sequentially, from outer to inner, yields the best performances.

The effectiveness of the procedure is quantified by measuring the vertical profile of the residual magnetic field inside the cryostat. For that purpose we used a fluxgate magnetometer [128], which can operate both at room and cryogenic temperatures.

Figure 4.1(a) shows the height profile of the residual magnetic field for 4 steps throughout the demagnetization procedure. The initial field at 300 K inside the cryostat is of the order of 4 $\mu$T, already demonstrating significant suppression of the earth magnetic field.

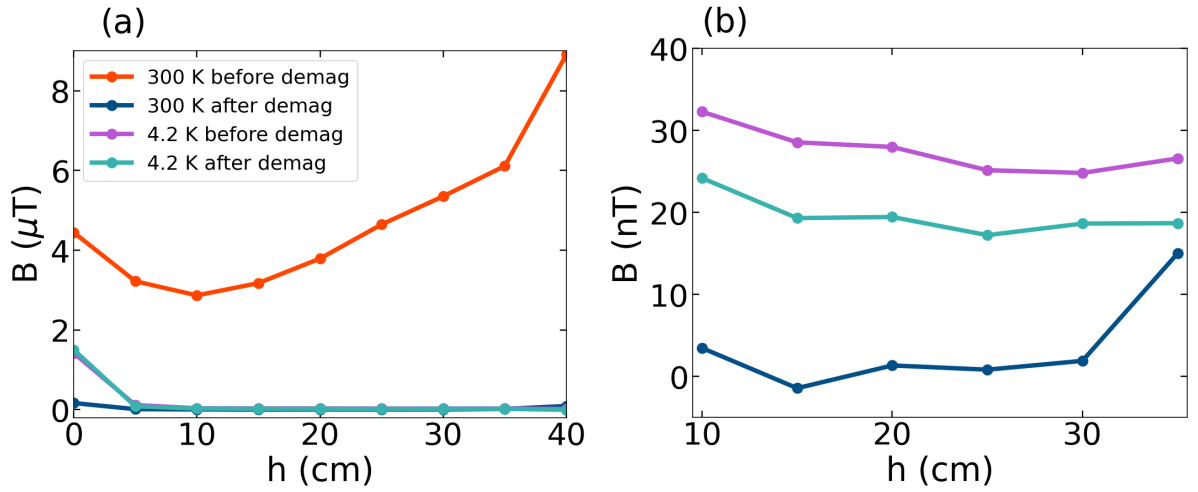


Figure 4.1: (a) Height profile of the residual magnetic field measured in the cryostat at different steps of the demagnetization procedure. The field is measured at 300 K before (orange) and after (dark blue) demagnetizing and then at 4.2 K before (purple) and after (light blue) demagnetizing a second time. (b) Zoom on the profiles obtained after a first room temperature demagnetization procedure.

After successive demagnetization of the five shields at 300 K, the residual field is considerably reduced with a value of the order of few nano-tesla (in zoom Figure 4.1(b)). Upon cooling to 4.2 K, additional residual magnetic field is acquired giving a resulting value of around 30 nT. This is puzzling, since the permeability of Cryophy® shields should in principle increase at low temperature, improving their efficiency. Nevertheless, an additional full demagnetization at 4.2 K reduced the residual field down to around 20 nT. While not as optimal as at room temperature, this remains an impressively low value. In the end, the obtained value is one order of magnitude smaller than what we had before introducing the Cryophy® shields.

Inside the dilution can, there are additional superconductive shields. In particular, a cylindrical NbTi shield is surronding the sample space. As discussed in Section 2.3.1, we exploited this shield together with the sample MvT response at our advantage to fine-tune the residual field down to 5 nT.

Finally, the signal path between the gradiometer and the SQUID is itself fully shielded. The superconducting leads are enclosed in a Pb sleeve and the SQUID has its own NbTi shield. An additional Pb sheet provides continuous shielding by connecting the sample shield to the superconducting relay box (an intermediate connector between gradiometer and SQUID leads), located near the mixing chamber. Altogether, this ensures that the detected signal originates exclusively from the sample, without contamination from the transmission wires.

## 4.2 Motivations for a new setup

The setup I used to perform the noise and susceptibility measurements (that I will call "original setup") has three main limitations which impact the quality of our measurements. First, the dilution refrigerator carrying the probe has poor cooling performance. Second, the gradiometer–SQUID distance is not optimal, reducing the sensitivity of the probe. Finally, we are limited in gradiometer geometries due to the fragility of the material used (single crystal silicon), also limiting the achievable sensitivity.

Regarding the cooling performance, it can take more than one day to cool the system down to base temperature (∼150 mK), whereas standard miniature dilution refrigerators typically reach even lower base temperatures (∼70 mK) within only a few hours. This limitation arises from the refrigerator's weak cooling power, which is difficult to improve since it would require modifying the $^3$He–$^4$He mixture circuit. Such modifications are risky, as they can introduce leaks that are difficult to repair and may result in the loss of the mixture.

As a consequence of the weak cooling power, it is difficult to perform controlled thermal quenches, which we would like to use to control the low-temperature state of our samples for out-of-equilibrium studies. Indeed, when the system is briefly heated to 0.6–1 K (for ∼30 seconds), the mixture evaporates and leaves the mixing chamber by the time of the heat pulse. Once the pulse ends, the system requires about one hour to recondense the vaporized mixture and go back to its nominal low temperature state. This slow recovery makes it impossible to tune the cooling rate in a controlled manner.

Concerning the gradiometer–SQUID geometry, because the SQUID has to be well thermalized at a fixed temperature of 4.2 K, we had to position it at the top of the calorimeter, connected to the copper 4.2 K flange, approximately 40 cm away from the gradiometer. The long leads connecting the SQUID to the gradiometer add inductance, reducing the quality factor of the detection. Moreover, the extended leads are more susceptible to mechanical vibrations and electromagnetic interferences.

The last issue concerns the single crystal silicon sample holder on which the gradiometer is mounted. This material was initially chosen as it is a good thermal conductor and has no magnetic signal, however it is very hard to machine. We realized that optimal noise detection requires several gradiometers, each fitting best the sample size but we were limited in the realization of optimal designs due to breakage of silicon. In conventional magnetometers, copper is generally used (which is easy to machine), however it produces a consequent magnetic noise because of its good electrical conductivity so it cannot be used.

To overcome these problems, I aimed to construct a new noise magnetometer using a dilution refrigerator with better cooling performance and implementing a better probe geometry. Since building a new dilution refrigerator takes time and is a complex process (typically over a year), we decided instead to repurpose an old, unused refrigerator from another group. I completely re-cabled the dilution can, tested different gradiometer geometries, designed a setup adapted to the new can, and performed cooling tests. However, I encountered many unanticipated issues with the dilution can itself, which

delayed our progress. In particular, I faced low-temperature helium leaks undetectable at room temperature that required long and difficult repairs. In the end, I managed to fix the leaks and obtained a functional dilution refrigerator. However, due to the delays, I was unable to complete a full test of the system or perform measurements with it. We therefore chose to postpone the assembly and low-temperature testing of the new setup, and instead concentrated on noise and AC susceptibility measurements with the original system.

The following sections present this instrumental work, which we hope will enable ac susceptibility and noise measurements at lower temperatures with enhanced sensitivity in the future. First, we discuss the parameters relevant for optimizing the detection and compare performance across different gradiometer geometries (Section 4.3). Next, we describe the design developed to improve sensitivity (Section 4.4). Finally, we review the cooling performance of the dilution refrigerator, its limitations, and the work needed to integrate the new setup (Section 4.5).

## 4.3 Optimization of detection

Optimizing the detection system is an important ingredient to be able to measure at lower temperatures. Indeed, as the temperature decreases, the spin ice signal shifts to very low frequencies, where the limiting factor is the $1/f$ background noise of the SQUID. By maximizing the detected flux and improving the signal-to-noise ratio, we can access temperature ranges that are otherwise masked by background contributions.

The detection system of a noise experiment consists of two main components: the gradiometer and the SQUID sensor, connected through two stages of magnetic inductive coupling. The magnetic flux from the sample first induces a current $i$ in the gradiometer (inductance $L_0$). This current then generates a flux in the SQUID input coil (inductance $L_S$), which in turn couples to the SQUID loop of inductance $l_S$. The gradiometer and SQUID input coil are connected by a twisted pair of wires with inductance $l_e$. Figure 4.2 shows a schematic of this electronic circuit.

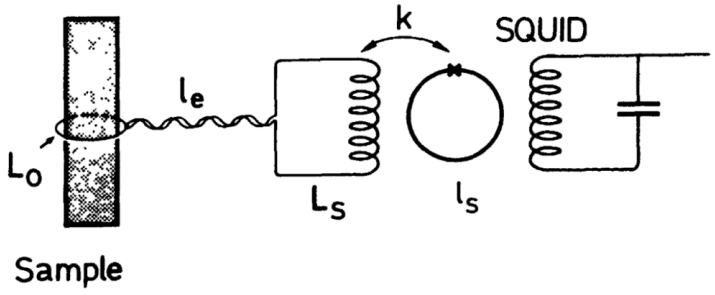


Figure 4.2: Diagram of the detection system. The gradiometer (inductance $L_0$) is connected to the SQUID input coil (inductance $L_S$) via a twisted wire with inductance $l_e$. The SQUID input coil is coupled to the SQUID loop (inductance $l_S$) with a coupling factor $k$. Figure adapted from Ref. [107].

The magnetic flux $\phi(\omega)$ collected by the gradiometer is directly proportional to the spontaneous fluctuations of the sample magnetization $M(\omega)$ [107]:

$$\bar{\phi}^2(\omega) = \bar{M}^2(\omega) 4\pi L_0 q V \tag{4.1}$$

where $V$ is the effective volume of the sample coupled to the gradiometer, $L_0$ is the gradiometer inductance, and $q$ is the filling factor (defined as the ratio of the sample cross section to the coil cross section).

For a conventional induction magnetometer, this relation summarizes the key parameters for detection: maximizing coil inductance (by adding turns), probing the largest possible sample volume, and ensuring the best filling factor.

In SQUID systems, however, two inductive stages are involved, so an additional step is needed to obtain the probed flux. The flux $\phi$ collected by the gradiometer induces a current $i$ in the wires according to $\phi = (L_0 + L_S + l_e)i$. The SQUID flux is then given by $\phi_{SQUID} = M_S \times i$, where $M_S = k\sqrt{L_S l_S}$ is the mutual inductance between the SQUID input coil and the SQUID loop, and $k$ their coupling factor. The transmission quality factor $\xi$ is therefore:

$$\xi = \frac{\phi_{SQUID}}{\phi} = \frac{M_S}{L_0 + L_S + l_e} = \frac{k\sqrt{L_S l_s}}{L_0 + L_S + l_e} \tag{4.2}$$

Combining this expression with Equation 4.1, we obtain the flux noise measured with the SQUID:

$$\bar{\phi}^2_{SQUID}(\omega) = \xi^2 \bar{\phi}^2(\omega) = \xi^2 \bar{M}^2(\omega) 4\pi L_0 q V \tag{4.3}$$

The additional quality factor $\xi$ intrinsically changes the optimization strategy compared to conventional inductive magnetometers. Since $\xi$ is inversely proportional to the gradiometer inductance $L_0$, increasing the number of coil turns no longer improves the sensitivity.

Instead, the signal is maximized when $\xi$ is maximum, which is realized by matching the sum of the inductance of the gradiometer and the leads with the inductance of the SQUID input coil with $L_0 + l_e = L_S$, giving:

$$\xi_{max} = \frac{k}{2}\sqrt{\frac{l_S}{L_S}} \tag{4.4}$$

The noise flux detected by the SQUID in the case of an ideal matching of inductance is:

$$\bar{\phi}^2_{SQUID}(\omega) = k^2 l_S \bar{M}^2(\omega) \pi \frac{L_0}{L_0 + l_e} q V \tag{4.5}$$

If the lead inductance $l_e$ is negligible compared to $L_0$, the ratio $\frac{L_0}{L_0+l_e} \approx 1$. In conventional SQUID magnetometers, where the input inductance is typically 2 $\mu H$, it is usually assumed that this condition is verified. But in our case, it is not valid. Indeed, our Magnicon two-stage SQUID [103] has a small input inductance ($L_S = 400$ nH), while the long leads ($\sim 40$ cm) give $l_e \sim 175$ nH, comparable to $L_0$ (if we obey $L_0 + l_e = L_S$). As a result, $\frac{L_0}{L_0+l_e} \approx 0.56$, reducing the detected noise signal by almost half in our case. In practice, it

is worth to increase slightly $L_0$ as there is an optimum between inductance matching and proportion of gradiometer-to-lead inductance. Nonetheless, this estimate highlights that significant improvement can be done by reducing the SQUID–gradiometer distance.

In summary, there are three main factors that strongly influence the SQUID detection: the gradiometer and leads inductances ($L_0$ and $l_e$), the effective volume of sample measured ($V$) and finally the filling factor ($q$). The three other parameters $k$, $L_S$ and $l_S$ are intrinsic to the SQUID sensor and are chosen when buying it. We could have opted for a SQUID with a larger input inductance $L_S$ to ease the inductance matching. However, the intrinsic noise of a SQUID scales with its input inductance, meaning that a higher $L_S$ would directly impact the noise detection threshold. Thus, even though imperfect matching leads to some sensitivity loss, it remains advantageous to work with a low $L_S$, as this ultimately maximizes the signal-to-noise ratio.

To experimentally study the effect of these parameters, I tested various gradiometer geometries on a $Dy_2Ti_2O_7$ sample at 4.2 K, made from superconductive NbTi wires of 0.125 mm of diameter. The sample used is the $^{nat}$Dy from Section 3.5. I tested a total of seven geometries: a single coil system, directly wound around the sample, one third order gradiometer (made of four coils) and five first order gradiometers (Figure 4.3(a)) wound around an Araldilte cylinder. All gradiometers are close to inductance matching (slightly above) and I varied the coil diameter $D$, the coil spacing $l$, the number of turns $N$, the leads lenght $d_e$ and the wire separation $s$.

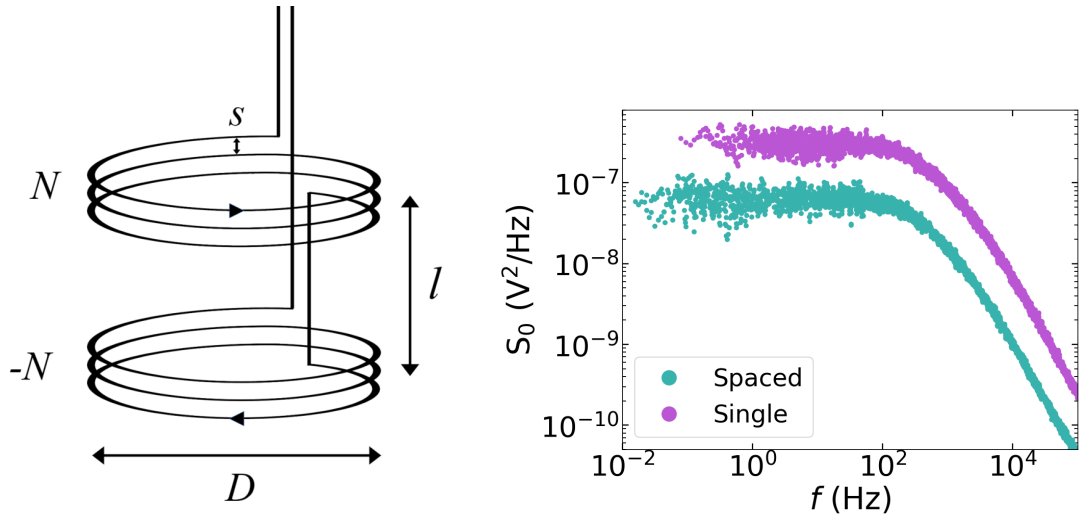


(a) (b)

Figure 4.3: (a) First order gradiometer made of two oppositely wound coils of $N$ turns, with diameter $D$, separated by a distance $l$, with leads of length $d_e$. The turns of each coil are separated by a spacing $s$. (b) Noise curves measured for a sample of $Dy_2Ti_2O_7$ at 4.2 K using the Spaced and Single geometries.

For simplicity, I assigned names to the seven geometries, summarized in Table 4.1 along with their geometric parameters. The "Si holder" corresponds to the actual sample holder used in our setup. "Small" denotes the gradiometer with the smallest $D$, while

"Spaced" has the largest coil spacing $l$. "Interm" is similar to the Spaced geometry but with a reduced $l$, and "Helico" refers to an helicoidal gradiometer characterized by a large spacing $s$. Finally the third order gradiometer and the single coil system are named "$3^{rd}$ order" and "Single" respectively. The noise spectra $S(f)$ obtained with the "Spaced" and "Coiled" geometries are shown in Figure 4.3(b) as examples. The detection quality is characterized by the magnitude of the low-frequency noise plateau $S_0$. For comparison, the ratios of $S_0$ relative to the Si holder reference geometry and $S_0$ values are also given in Table 4.1.

| | Si holder | Small | Spaced | Interm | Helico | 3rd order | Single |
|---|---|---|---|---|---|---|---|
| D (mm) | 5 | 4.3 | 5.5 | 5.5 | 5.5 | 5.5 | ∼2.2 |
| l (mm) | 4.8 | 5.5 | 9 | 7 | 14 | 7 | - |
| N | 5 | 5 | 4 | 4 | 8 | 6 | 8 |
| $d_e$ (cm) | 40 | 20 | 20 | 20 | 20 | 20 | 20 |
| s (mm) | 0.125 | 0 | 0 | 0 | 1.25 | 0 | 0 |
| $L_{\text{tot}}$ (nH) | 650 | 455 | 445 | 435 | 420 | 480 | 500 |
| $S_0$ ($V^2$/Hz) | $3\times10^{-8}$ | $1.5\times10^{-7}$ | $8\times10^{-8}$ | $5\times10^{-8}$ | $6.4\times10^{-8}$ | $5\times10^{-8}$ | $3\times10^{-7}$ |
| Ratio | 1 | 5 | 2.67 | 1.67 | 2.13 | 1.67 | 10 |

Table 4.1: Shape parameters of the different geometries: $D$ diameter, $l$ coil spacing, $N$ number of turns, $d_e$ lead distance and $s$ wire spacing. The total inductance $L_{\text{tot}} = L_0 + l_e$ is shown, obtained with formula of Ref. [129]. The measured low-frequency plateau $S_0$ values and their ratios relative to the Si holder geometry are also given. A double horizontal line separates the geometric parameters from the measured values, while a double vertical line separates the first order gradiometers from the two other types of geometries.

Looking at the first five columns, we can compare the different first order gradiometers. Si holder has the poorest performance (shown in Figure 4.4). Notably, it has the longest lead distance ($d_e \sim 40$ cm versus 20 cm for the others). Because the associated $l_e$ is very large compared to the squid inductance $L_s$, obeying the inductance matching would impose a small $L_0$, and thus a small coupling of the gradiometer with the sample. It is thus necessary to find a compromise between these two conditions. This is the reason why $L_{tot}$ was chosen larger then the optimum value. Even if perfect inductance matching were achieved, reducing $l_e$ by half would improve the measured signal magnitude by about a factor of 1.4.

This change in lead length cannot explain alone the gain in sensitivity obtained with the other geometries. This means that the other parameters we have changed also play an important role in the sensitivity. The second tendency we notice is that the Small diameter gradiometer provides the largest intensity gain, about a factor of 5 compared to the Si holder. This improvement reflects the importance of the filling factor $q$ in Equation 4.5.

Another interesting behavior is captured by the Spaced and Interm gradiometers that are identical except for their coil spacing $l$ (Interm: Figure 4.4(a), top). The comparison shows that when the coils are too close, the detected signal decreases. In a first-order gradiometer, the sample is placed inside only one of the two oppositely wound coils. If the coils are positioned too close to each other, the second (empty) coil still picks up part of

the magnetic flux generated by the sample. This induces a current opposite to that of the coil containing the sample, leading to a partial self-cancellation of the measured signal. This idea is further suppported by additional tests with the sample centered between the coils that showed a signal reduction by a factor of 2–3. This effect may also explain why, for larger samples, the signal does not scale proportionally with volume.

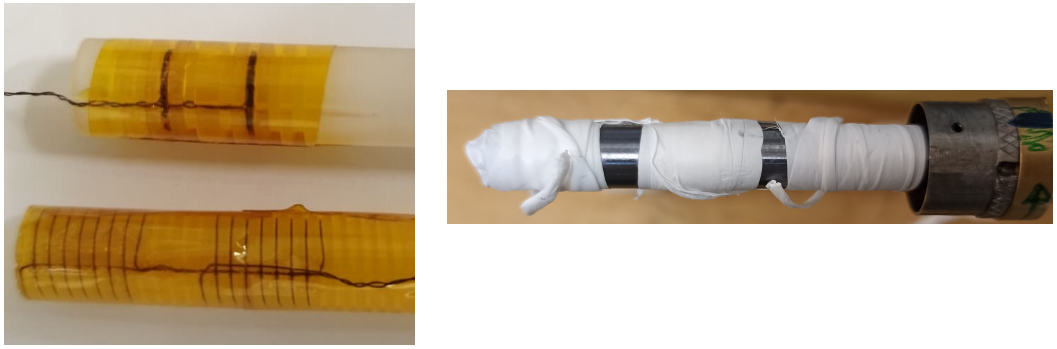

(a) (b)

Figure 4.4: (a) Photograph of two gradiometers wound on an Araldite holder: Interm (up) and Helico (down).(b) Photograph of the single crystal silicon sample holder. The Si holder gradiometer is positionned on the left under the teflon film.

Finally, we performed test on the Helico gradiometer which consists of coils with helicoidal winding with 1.25 mm spacing (Figure 4.4, right). As a result, the coils are 10 mm in length. In other geometries, since the wire diameter is small (0.0125 mm) and there is no separation between the coils, the length of the coils is less than one millimeter. The Helico gradiometer was thus designed to probe the entire sample volume within a single coil. However, it did not produce a significant signal increase compared to the Spaced configuration.

The third-order gradiometer is built from four coils (two full, $N = 6$, and two half, $N = 3$). This geometry cancels not only static external fields but also higher-order gradients. With parameters similar to the Interm gradiometer, it yielded similar intensity coupling, as expected. However, in practice it did not improve the quality of the noise (canceling of external contributions) and is way harder to fabricate. It is probable that the shielding in the sample environment is sufficiently good so that this kind of geometry is not needed.

Finally in the Single geometry, the coil is wound directly onto the sample. Since there is no compensating coil to cancel the static field, more turns can be dedicated to detecting the sample flux, and the filling factor $q$ is maximized by design. As a result, the signal strongly increases, with $S_0$ ten times larger than the Si holder and nearly five times larger than the Spaced geometry. Figure 4.3(b) illustrates this sensitivity gain. The drawback, however, is that this geometry cannot be used for ac susceptibility, since the compensating coil is essential to subtract the applied field contribution, which would otherwise saturates the SQUID signal over the sample signal.

To conclude, we have tested the parameters that were identified essential to optimize the SQUID detection: the lead inductance $l_e$, the coil spacing $l$ and most importantly the filling factor $q$. Optimizing these parameters simultaneously could improve sensitivity by up to an order of magnitude. The current Si holder geometry is clearly suboptimal.

In that geometry, the gradiometer is wound into notches machined into a single crystal silicon rod, with the sample inserted in a carved hole at its center. However, modifying the silicon rod is challenging since single crystal silicon is a extremely brittle material difficult to machine. It requires a sufficient wall thickness to avoid breakage which limits the size of the sample hole, limiting the achievable filling factor. Ideally, we would want to design interchangeable holders tailored to different sample sizes, but this requires a lot of time, money, and effort, which cannot be spared during a thesis.

It is from these observations that we wanted to change the sample environment in the new setup we were developing. Our objectives were to shorten the gradiometer-SQUID distance to minimize $l_e$, and develop a modular system allowing the gradiometer to be easily changed and adapted to each sample. The next section details the design idea and the parts that needed to be realized to upgrade the measurement setup.

## 4.4 Design realization

Let us first describe the design of the sample environment. Figure 4.5 shows a three dimensional model of the complete setup, with its different parts. On this figure, the mixing chamber is attached to the left side of the model, while the right side corresponds to the bottom of the dilution refrigerator. To understand how the sample is connected to the mixing chamber and positioned within the gradiometer, we need only to focus on the left side of the drawing.

To allow for an easy replacement of the gradiometer, we separated the thermalization of the sample to the mixing chamber from the gradiometer itself. In the original setup, the single crystal silicon sample holder both ensured thermalization and the mounting of the gradiometer.

In the new design, the cold plate is directly screwed onto the mixing chamber, with another copper piece screwed on the bottom of that plate. A silicon cylinder is inserted into this copper piece, attached and thermalized using silver paste. This constitutes the sample holder, where the sample is mounted at the bottom of the silicon cylinder using GE varnish.

The sample holder carrying the sample is placed inside a NbTi cylindrical shield, which is attached to the cold plate using three thin carbon-fiber tubes. The gradiometer and the excitation coils are mounted inside the NbTi shield, with the sample positionned inside but without making direct contact. The gradiometer holder is machined from Araldite, a material easy to work with, allowing us to machine different sizes that best fit the various samples shapes.

By simply unscrewing the three carbon-fiber tubes from the cold plate, the bottom part of the setup can be removed independently. This makes it possible to change both the sample and the gradiometer before assembling the setup for a new measurement.

In the original setup, the second issue we want to solve concerns the position of the SQUID, which is located at the top of the dilution system, next to the 4.2 K thermalization point, approximately 30–40 cm away from the gradiometer. As for the original can, the new dilution can space is limited by the calorimeter to a tube of 35 mm diameter. Since the SQUID sensor is about 56 mm long and 13 mm diameter, the only available location closer to the gradiometer is directly below it.

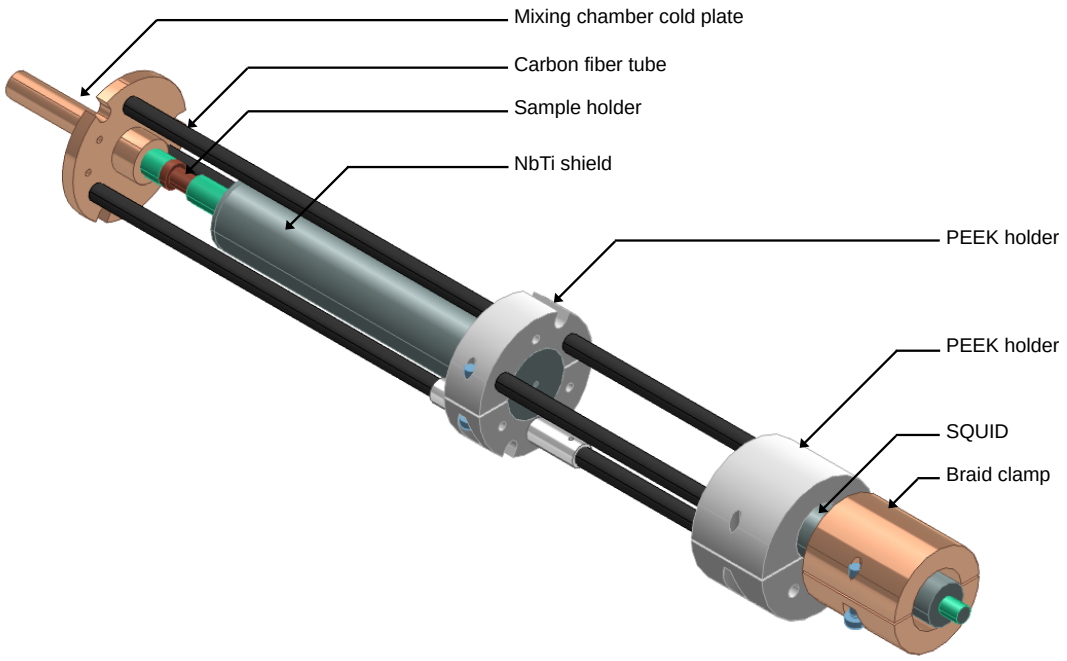


Figure 4.5: Three dimensional model of the different parts designed for the new dilution setup. The left part of the setup is attached to the mixing chamber, while the right part lies at the bottom. The Solid Edge 2023 software was used to draw the model.

We therefore decided to connect the SQUID to the bottom part of the NbTi shield using two PEEK plastic pieces and three short carbon-fiber tubes. A few centimeters of space were left to allow the connection to the SQUID Lemo connector. With this design, the distance between the gradiometer and the SQUID is reduced to about 10–15 cm, compared to the 40 cm of the original setup.

In particular, the SQUID must be kept at a highly stable temperature of 4.2 K to ensure that its operating point remains fixed throughout long measurements. To achieve this, we developed a custom calorimeter composed of a carefully chosen combination of three materials (Figure 4.6). The upper part, where the calorimeter is screwed in, is made of stainless steel: its mechanical hardness guarantees robustness against repeated screwing and unscrewing cycles. Around the sample environment, we employed glass fiber, which is both mechanically solid and perfectly non-magnetic (in contrast, stainless steel is conductive and can retain residual magnetism, leading to parasitic noise contributions). Finally, to ensure efficient SQUID thermalization, a copper clamp equipped with a thermal braid connects the SQUID to the bottom part of the calorimeter, also in copper, which is in direct contact with the liquid $^4$He bath. $^4$He leakage tests were performed on that calorimeter, and were successful.

To maintain the sample environment at the base temperature of the mixing chamber, we selected materials with poor thermal conductivity for the mechanical support of the SQUID. We chose PEEK plastic and carbon fiber tubes because both materials are known to exhibit low thermal conductivity at cryogenic temperatures [130].



Figure 4.6: Photograph of the homemade calorimeter.

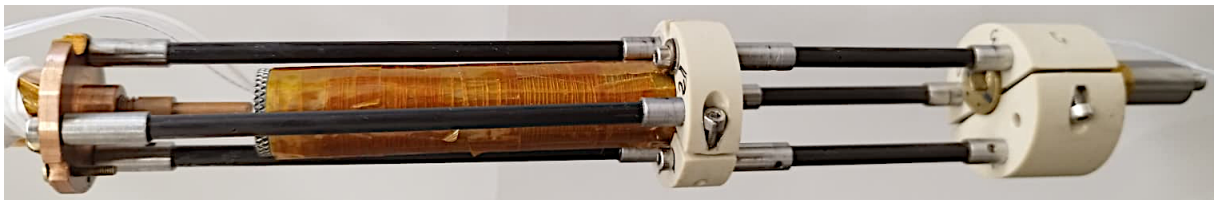

Figure 4.7: Photograph of the different fabricated parts mounted on the dilution refrigerator. Cables and wires are not connected in order to provide a clearer view of the individual parts.

I initially designed all the parts for the new setup and made a sketch using a CAD software: Solid Edge 2023. Fine tuning of the design and fabrication of the parts were carried out with the strong assistance of Anne Gerardin from the Cryogenics Group at the Néel Institute. All parts have now been manufactured, and the setup is fully assembled (see Figure 4.7). Initial tests at 4.2 K showed that a good magnetic sensitivity can be obtained with this set up. The next step is to characterize and optimize its performance at lower temperatures.

In the following section, we will first discuss the raw performance of the dilution refrigerator (without any attached setup), measured after repairing the leaks. Due to time delays, only preliminary cryogenic tests with the new setup were performed. These revealed a few issues and directions for further improvements are discussed.

## 4.5 Dilution refrigerator performances

The cooling performance of a dilution refrigerator is expected to follow the following law (see Section 2.2.2):

$$\dot{Q} \approx \dot{n}_3 T^2 + \dot{Q}_{leak} \tag{4.6}$$

Here, $Q$ is the applied power, $T$ is the temperature at the mixing chamber, $\dot{n}_3$ is the $^3$He molar circulation rate, and $\dot{Q}_{\text{leak}}$ is the power lost through thermal leaks.

To determine the cooling power, we have thus measured the increase of temperature resulting from a fixed thermal power applied to the mixing chamber via a known resistor. By observing the stabilized asymptotic temperature, we can extract the corresponding temperature $T$ for a given applied power $\dot{Q}$. Plotting Equation 4.5 then provides the relevant information about the dilution refrigerator performance.

This relation is valid only for low applied powers, before non-linear effects modify the

cooling power behavior. Typically, the linear regime is assumed to hold for $T < 100$ mK. By fitting the quadratic temperature dependence in this regime, we can extract both the heat leak power $\dot{Q}_{\text{leak}}$ and the $^3$He molar circulation rate $\dot{n}_3$.

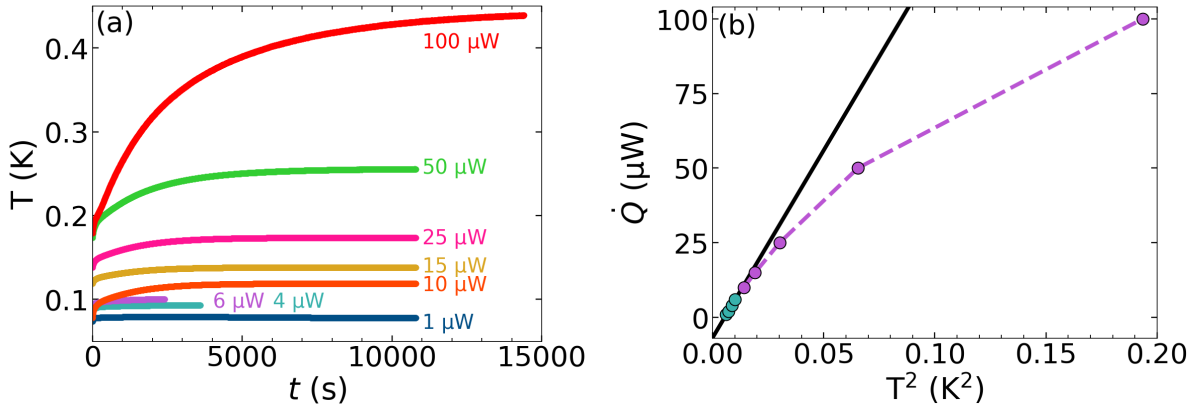


Figure 4.8: (a) Mixing chamber temperature vs time for an applied power $\dot{Q}$. (b) Power $\dot{Q}$ vs squared asymptotic temperature value. The blue dots correspond to the values in the linear working regime of the dilution while the purple points corresponds to higher power values. The black solid line corresponds to the fit in the linear regime from which we extract the dilution parameters: $\dot{Q}_{leak} \sim 7\ \mu$W and $\dot{n}_3 \sim 15\ \mu$mol/s.

The characterization of the dilution refrigerator performance was carried out with nothing attached to the mixing chamber. The base temperature obtained before applying any power was $T_{\text{min}} = 73$ mK, which is significantly higher than the expected value for standard miniature dilution refrigerators ($T_{\text{min}} \sim 50$ mK).

Figure 4.8(a) shows the relaxation curves of temperature vs time for applied powers $\dot{Q}$ ranging from 1 $\mu$W up to 100 $\mu$W. At higher powers, relaxation times increase significantly, and in particular the 100 $\mu$W curve may not be fully stabilized. For powers even higher, the behavior of the dilution becomes unstable, with temperature fluctuating over long timescales.

The extracted squared temperatures are plotted against applied power in Figure 4.8(b). A clear linear behavior is observed in the low-power regime ($T_m < 100$ mK), while deviations from linearity appear at higher powers, where the measured temperatures exceed the prediction of the ideal model.

From the linear fit, we extract $\dot{Q}_{\text{leak}} \sim 7\ \mu$W and $\dot{n}_3 \sim 15\ \mu$mol/s. The typical cooling power of miniature dilution refrigerators is about 20 $\mu$W at 100 mK, indicating that a large fraction of the available power in our system is lost in thermal leaks. From Figure 4.8(b), we see that an applied power of 6 $\mu$W heats the mixing chamber to about 100 mK, meaning that less cooling power is available at 100 mK than what is lost to leaks. The ideal cooling power at 100 mK can be estimated at $\sim 13\ \mu$W by summing the accessible and lost powers. These measurements thus demonstrate that the system exhibits both low theoretical cooling power and a high amount of heat leaks.

Improving the accessible cooling power requires reducing these leaks. Further improvements consisting of lowering the base temperature or increasing the $^3$He circulation rate would involve modifying the dilution circuit itself (like changing the heat exchang-

ers), which is risky and time consuming.

In these tests, only the bare dilution refrigerator and the wiring for thermometers and heaters were present. The wiring was designed to minimize heat conduction by using superconducting NbTi, CuNi or Phosphor bronze wires (good electrical conductivity, poor thermal conductivity). In addition, wires are thermalized at three stages before reaching the mixing chamber: to the 4.2 K bath, to the 0.8 K still, and to the heat exchangers. It is therefore unlikely that wiring alone explains the measured heat leak.

A more likely explanation is mechanical vibrations. Indeed, we observed that the central fiberglass axis, which mechanically connects the still to the mixing chamber, was poorly attached. Two hypotheses could explain the origin of the observed leak: either vibrations that generate heat and disturb the suspended mixing chamber, or a direct contact between the dilution unit and the calorimeter. This issue has not yet been corrected, but the simplest solution would likely be reinforcing the insertion point of the central axis in the still with Stycast.

We also performed quick tests with the full measurement setup (described above) attached, to evaluate its impact on base temperature. With the full setup, we could barely cool down, quickly identifying the SQUID to electronics cable as the main problem. This cable runs directly from room temperature and requires proper thermalization, otherwise, the thermal load can be enormous.

We improved 4.2 K thermalization by clamping the cable between two copper plates, but even so, the refrigerator was only able to reach around 2 K. Indeed, due to limited cooling power, proper thermalization of the cable onto the still at 800 mK is not possible. The cable, supplied by Magnicon, is made of Alloy-30 wires and a braided stainless steel sleeve. Although these materials have relatively low thermal conductivity, the cable cross-section is large and requires substantial cooling, which is not problematic in larger dilution refrigerators but is critical here. A solution could be a custom lab-made cable with superconducting wires and a reduced stainless-steel sleeve in order to greatly reduce the thermal load. That way the still could be able to thermalize properly the cable.

A second series of tests was performed with the full setup but without the SQUID cable. In this case, the base temperature was 250 mK, better but still significantly higher than expected. This likely results from the combination of limited cooling power and a thermal decoupling between the SQUID and the sample environment weaker than expected. To identify the problematic part, each component thermal leak (carbon-fiber tube, PEEK holder) could be tested separately with two thermometers and a heater. By doing so, this would allow us to replace the components responsible for excessive heat transfer to the profit of more suitable materials.

In conclusion, our measurements confirm that the dilution refrigerator's intrinsic performance is poor. By first correcting the central axis issue, a substantial gain in cooling power may be obtained. Beyond that, two critical problems must be addressed: the SQUID cable heat load and excessive heat transfer through the SQUID mounting. In the short term, replacing a few components with higher-quality materials may be sufficient. If not, a modified design in which the SQUID is attached directly to the calorimeter, independently of the dilution refrigerator (except for wiring and cabling), could provide a more robust solution.

# Chapter 5

# Impact of a magnetic metal ion in Nd-based pyrochlores

## Contents


**5.1 Symmetry analysis . . . . . 118**

5.1.1 The Nd-Nd interaction . . . . . 118

5.1.2 The *M*-*M* interaction . . . . . 119

5.1.3 The Nd-*M* interaction . . . . . 119

**5.2 Measurement and analysis of $Nd_2Ir_2O_7$ and $Nd_2Ru_2O_7$ . . . . . 125**

5.2.1 Experimental method . . . . . 125

5.2.2 Introduction to crystal electric field excitations . . . . . 126

5.2.3 $Nd_2Ir_2O_7$ . . . . . 127

5.2.4 $Nd_2Ru_2O_7$ . . . . . 136

**5.3 Discussion and conclusion . . . . . 149**

Understanding the fundamental magnetic properties of a system often requires the construction of a model that captures the microscopic origin of the spin interactions. A common route in the field of magnetism is to confront candidate models with a diverse set of experimental observables. Measurements provide meaningful observables that can be computed and compared with theory, allowing us to test, refine, and constrain models until they offer the most faithful description. This process is inherently iterative: experiments highlight discrepancies with existing models, which in turn motivates the introduction of new ingredients or entirely revised models to account for the observed physics.

We applied this methodology to investigate $Nd_2Ru_2O_7$ and $Nd_2Ir_2O_7$, and aimed at unraveling the subtle magnetic interplay between the rare earth ($Nd^{3+}$) and the metal ($M^{4+}$) ions. In the first part of this chapter, Section 5.1 introduces a symmetry analysis we carried out to identify the most general form of the Nd-M Hamiltonian consistent with the specific symmetry properties of the $Nd^{3+}$ low energy DO doublet in the pyrochlore lattice.

Section 5.2 then turns to experimental results, combining literature data with our own measurements on both compounds. We compare these findings to our model through spin wave calculations and the computation of magnetic observables. The parameters are refined and confronted directly against our experimental results. The full analysis, ranging from measurements to theoretical interpretation, is first developed for $Nd_2Ir_2O_7$ and then applied to $Nd_2Ru_2O_7$. We conclude by a comparative discussion between the two compounds, as well as with other Nd-based pyrochlores.

This approach, combining experiments experiment and modeling, provides new insights into the microscopic mechanisms at play in these compounds.

## 5.1 Symmetry analysis

In $Nd_2Ir_2O_7$ and $Nd_2Ru_2O_7$, the magnetic lattice is composed of two distinct sublattices, each of which can interact with itself and with the other. This gives rise to three distinct types of nearest-neighbor interactions: the Nd–Nd interaction, the $M$–$M$ interaction (with $M$ = Ir, Ru), and the cross-sublattice Nd-$M$ interaction. The first two interactions have already been determined and tested in previous works using symmetry analysis. In what follows, we briefly review these known results before turning to our own symmetry analysis of the Nd-$M$ interaction, which was never investigated to our knowledge but is necessary to understand the physics of both compounds.

### 5.1.1 The Nd-Nd interaction

The Nd-Nd interaction was thoroughly discussed in Section 1.4, where we compared the corresponding model with experimental results from the parent compound $Nd_2Zr_2O_7$. The dipolar–octupolar (DO) nature of the $Nd^{3+}$ ground-state wavefunction is well captured by an effective pseudo-spin-1/2 description, subject to a distinct set of symmetry transformation rules. The relevant Hamiltonian describing these pseudo-spins is the XYZ DO Hamiltonian, which was obtained from a symmetry analysis [76]:

$$\mathscr{H}_{\mathrm{DO}}^{\mathrm{XYZ}} = \sum_{\langle ij \rangle} \left[ J_x \tau_i^x \tau_j^x + J_y \tau_i^y \tau_j^y + J_z \tau_i^z \tau_j^z + J_{xz} \left( \tau_i^x \tau_j^z + \tau_i^z \tau_j^x \right) \right] \tag{5.1}$$

This Hamiltonian is written with a set of four couplings $J_i$ ($i = x, y, z, xz$) defined in a local frame defined by the $z$-local axis of the pyrochlore structure [83]. Throughout this Chapter, we will refer to this model as $\mathscr{H}_{\text{Nd-Nd}}$. Additional details on its derivation and physical interpretation can be found in Section 1.4.

### 5.1.2 The *M*-*M* interaction

For the magnetic metal ions $M^{4+}$, we do not know their single-ion anisotropy. We therefore adopt the most general symmetry-allowed description: an effective spin-1/2. The nearest-neighbor Hamiltonian consistent with the local symmetries of the pyrochlore lattice takes the form [131, 132]:

$$\begin{aligned} \mathscr{H}_{M-M} = \sum_{\langle ij \rangle} \Big\{ & \mathscr{J}_{zz} S_i^z S_j^z - \mathscr{J}_{\pm} \left( S_i^+ S_j^- + S_i^- S_j^+ \right) \\ & + \mathscr{J}_{\pm\pm} \left( \gamma_{ij} S_i^+ S_j^+ + \gamma_{ij}^* S_i^- S_j^- \right) \\ & + \mathscr{J}_{z\pm} \left[ S_i^z \left( \xi_{ij} S_j^+ + \xi_{ij}^* S_j^- \right) + i \leftrightarrow j \right] \Big\} \end{aligned} \tag{5.2}$$

where $S_i^\mu$ are pseudo-spin components expressed in a local spin coordinate frame of the pyrochlore lattice. The bond-dependent matrices $\gamma_{ij}$ and $\xi_{ij}$, with $\gamma_{ij} = -\xi_{ij}^*$, are given by:

$$\gamma_{ij} = \begin{pmatrix} 0 & 1 & \omega & \omega^2 \\ 1 & 0 & \omega^2 & \omega \\ \omega & \omega^2 & 0 & 1 \\ \omega^2 & \omega & 1 & 0 \end{pmatrix}, \qquad \omega = e^{2i\pi/3} \tag{5.3}$$

This symmetry analysis reduces the full parameter space to four independent exchange couplings, together with two bond-dependent terms. Importantly, the presence of these bond-dependent matrices reflects the fact that each site in the primitive cell has a distinct local $z$-axis, such that the symmetry of the exchange varies with bond orientation.

This result highlights an interesting property of the DO-XYZ model: it contains no bond-dependent terms. The new set of symmetry transformation rules associated to the DO pseudo-spin preserves invariance of the exchange across different bonds, simplifying greatly the model.

### 5.1.3 The Nd-*M* interaction

The Nd-*M* inter-sublattice interaction has never been investigated to our knowledge using a symmetry analysis up to now. To interpret our data within a model that faithfully captures the interplay between $Nd^{3+}$ and the magnetic $M^{4+}$ ions, we carried out such an analysis. The procedure follows the same methodology as for the Nd–Nd and *M*–*M* interactions discussed above, and was conducted with the help of Julien Robert, who has

already done this type of analysis for other systems. A recent paper was very helpful for understanding and applying this approach, as it is very didactic despite being applied to the kagome model [133].

Each magnetic sublattice (Nd and $M$) can be minimally described by a set of four spins, corresponding to the four sites of a single tetrahedron (see Appendix 5.3 for details on site positions and local bases). These two tetrahedra (one for the Nd sublattice and one for the $M$ sublattice) are embedded within a rhombohedral primitive cell (Figure 5.1 left), from which the full fcc pyrochlore cubic cell can be reconstructed (Figure 5.1 right).

The interaction Hamiltonian describing the coupling between the two sublattices can be expressed in terms of a $12 \times 12$ exchange matrix $\hat{\mathscr{K}}_{\mathrm{Nd}-M}$:

$$\mathscr{H}_{\mathrm{Nd}-M} = \boldsymbol{\tau} \begin{pmatrix} 0 & \hat{K}_{52} & \hat{K}_{53} & \hat{K}_{54} \\ \hat{K}_{61} & 0 & \hat{K}_{63} & \hat{K}_{64} \\ \hat{K}_{71} & \hat{K}_{72} & 0 & \hat{K}_{74} \\ \hat{K}_{81} & \hat{K}_{82} & \hat{K}_{83} & 0 \end{pmatrix} \mathbf{S} = \boldsymbol{\tau} \hat{\mathscr{K}}_{\mathrm{Nd}-M} \mathbf{S} \tag{5.4}$$

Here, $\mathbf{S}$ and $\boldsymbol{\tau}$ are 12-component vectors containing the pseudo-spin components of the four $M^{4+}$ ions and the four $\mathrm{Nd}^{3+}$ ions, respectively:

$$\begin{aligned} \mathbf{S} &= (S_1^x, S_1^y, S_1^z, S_2^x, S_2^y, S_2^z, S_3^x, S_3^y, S_3^z, S_4^x, S_4^y, S_4^z) \\ \boldsymbol{\tau} &= (\tau_5^x, \tau_5^y, \tau_5^z, \tau_6^x, \tau_6^y, \tau_6^z, \tau_7^x, \tau_7^y, \tau_7^z, \tau_8^x, \tau_8^y, \tau_8^z) \end{aligned} \tag{5.5}$$

Here we present only the coupling matrix of the Nd-$M$ interaction as $\hat{\mathscr{K}}_{\mathrm{Nd}-M} = \hat{\mathscr{K}}^t_{M-\mathrm{Nd}}$. The diagonal terms of this bond coupling matrix are zeros, since they correspond to second-neighbor interactions, which are not included in the present analysis. Before imposing any symmetry constraints from the pyrochlore lattice, the Hamiltonian therefore contains a total of $12 \times 9 = 108$ coupling parameters (12 bonds describes by $3 \times 3$ matrices). The central idea of this type of symmetry analysis is to identify which of these couplings are left invariant under the symmetry group of the lattice, thus greatly reducing the number of parameters.

The pyrochlore lattice belongs to the $Fd\bar{3}m$ (No. 227) space group, which contains 192 distinct symmetry operators. These can be generated from a smaller subset of elementary operators. For $Fd\bar{3}m$, the $\mathrm{D}_{3d}$ site symmetry is generated from: the primitive translations of the fcc lattice $\boldsymbol{T}_{ai}$, the inversion symmetry $\mathscr{I}$, the time reversal symmetry $\mathscr{T}$, the 3-fold rotation $\boldsymbol{C}_{3,1}$ along the [111] crystallographic axis, and the mirror reflection $\boldsymbol{M}_{x\bar{y}}$ [134].

The pseudo-spins of the metal ions, $S_i^\mu$ ($i = 1,2,3,4$; $\mu = x,y,z$), are treated like "usual" pseudo-spins. They transform as conventional axial vectors (like magnetic dipoles). By contrast, it was shown that the Nd pseudo-spins $\tau_i^\mu$ ($i = 5,6,7,8$ and $\mu = x,y,z$) do not transforms similarly due to their DO character. Instead it was shown that the appropriate symmetry transformations for these pseudo-spins are the following [76]:

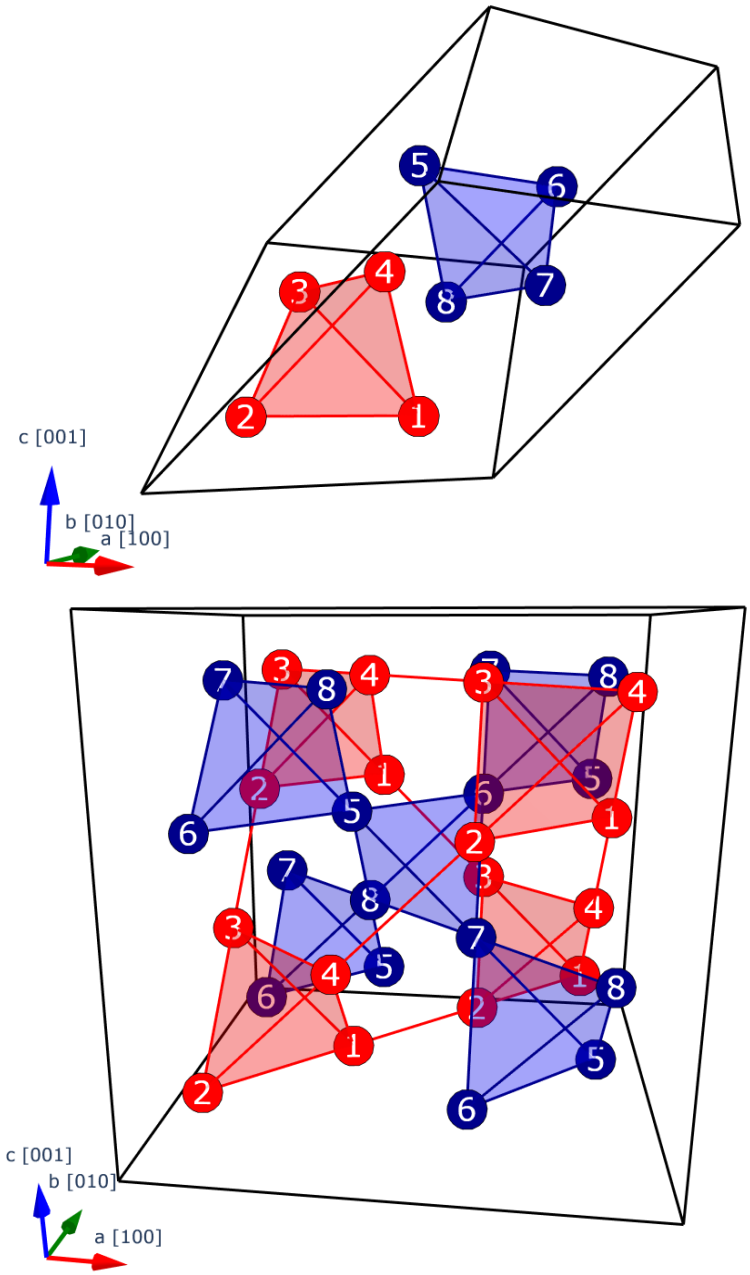


Figure 5.1: Rhombohedral primitivie cell (left) and fcc pyrochlore cubic cell (right) with Ru atoms (red) and Nd atoms (blue).

$$
\begin{aligned}
T_{ai} &: \tau_i^\mu \to \tau_{i+ai}^\mu \\
\mathscr{I} &: \tau_i^\mu \to \tau_{\mathscr{I}i}^\mu \\
C_{3,1} &: \tau_i^\mu \to \tau_{C_{3,1}i}^\mu \\
M_{x\bar{y}} &: \tau_i^{x,z} \to -\tau_{M_{x\bar{y}}i}^{x,z} \\
M_{x\bar{y}} &: \tau_i^{y} \to \tau_{M_{x\bar{y}}i}^{y} \\
\mathscr{T} &: \tau_i^\mu \to -\tau_i^\mu
\end{aligned}
\tag{5.6}
$$

There are two notable differences compared to dipolar pseudo-spin: $\tau_i^y$ remains invariant under all space-group operations, and $\tau_i^\mu$ components are unchanged under $C_{3,1}$ rotation. It is these two properties that explain why $\mathscr{H}_{\text{Nd-Nd}}$ is not bond-dependent even in the multiaxial environment of the pyrochlore lattice.

With these rules, the action of each of the 48 space group operations on the M and Nd sites can be encoded in the form of symmetry operations $\Gamma_X$ ($X = M$, Nd) acting in our $12 \times 12$ basis. As an example, we illustrate below the explicit form corresponding to the $C_{3,1}$ operator.

$$
\Gamma_M(C_{3,1}) = \begin{pmatrix}
0 & 0 & 0 & 0 & 0 & 0 & -\frac{1}{2} & -\frac{\sqrt{3}}{2} & 0 & 0 & 0 & 0 \\
0 & 0 & 0 & 0 & 0 & 0 & \frac{\sqrt{3}}{2} & -\frac{1}{2} & 0 & 0 & 0 & 0 \\
0 & 0 & 0 & 0 & 0 & 0 & 0 & 0 & 1 & 0 & 0 & 0 \\
0 & 0 & 0 & -\frac{1}{2} & -\frac{\sqrt{3}}{2} & 0 & 0 & 0 & 0 & 0 & 0 & 0 \\
0 & 0 & 0 & \frac{\sqrt{3}}{2} & -\frac{1}{2} & 0 & 0 & 0 & 0 & 0 & 0 & 0 \\
0 & 0 & 0 & 0 & 0 & 1 & 0 & 0 & 0 & 0 & 0 & 0 \\
0 & 0 & 0 & 0 & 0 & 0 & 0 & 0 & 0 & -\frac{1}{2} & -\frac{\sqrt{3}}{2} & 0 \\
0 & 0 & 0 & 0 & 0 & 0 & 0 & 0 & 0 & \frac{\sqrt{3}}{2} & -\frac{1}{2} & 0 \\
0 & 0 & 0 & 0 & 0 & 0 & 0 & 0 & 0 & 0 & 0 & 1 \\
-\frac{1}{2} & -\frac{\sqrt{3}}{2} & 0 & 0 & 0 & 0 & 0 & 0 & 0 & 0 & 0 & 0 \\
\frac{\sqrt{3}}{2} & -\frac{1}{2} & 0 & 0 & 0 & 0 & 0 & 0 & 0 & 0 & 0 & 0 \\
0 & 0 & 1 & 0 & 0 & 0 & 0 & 0 & 0 & 0 & 0 & 0
\end{pmatrix}
\tag{5.7}
$$

$$
\Gamma_{\text{Nd}}(C_{3,1}) = \begin{pmatrix}
0 & 0 & 0 & 0 & 0 & 0 & 1 & 0 & 0 & 0 & 0 & 0 \\
0 & 0 & 0 & 0 & 0 & 0 & 0 & 1 & 0 & 0 & 0 & 0 \\
0 & 0 & 0 & 0 & 0 & 0 & 0 & 0 & 1 & 0 & 0 & 0 \\
0 & 0 & 0 & 1 & 0 & 0 & 0 & 0 & 0 & 0 & 0 & 0 \\
0 & 0 & 0 & 0 & 1 & 0 & 0 & 0 & 0 & 0 & 0 & 0 \\
0 & 0 & 0 & 0 & 0 & 1 & 0 & 0 & 0 & 0 & 0 & 0 \\
0 & 0 & 0 & 0 & 0 & 0 & 0 & 0 & 0 & 1 & 0 & 0 \\
0 & 0 & 0 & 0 & 0 & 0 & 0 & 0 & 0 & 0 & 1 & 0 \\
0 & 0 & 0 & 0 & 0 & 0 & 0 & 0 & 0 & 0 & 0 & 1 \\
1 & 0 & 0 & 0 & 0 & 0 & 0 & 0 & 0 & 0 & 0 & 0 \\
0 & 1 & 0 & 0 & 0 & 0 & 0 & 0 & 0 & 0 & 0 & 0 \\
0 & 0 & 1 & 0 & 0 & 0 & 0 & 0 & 0 & 0 & 0 & 0
\end{pmatrix}
$$

We see that due to the DO transformation rules of Nd, the operator $\Gamma_{\text{Nd}}(C_{3,1})$ acts

trivially (identity), while $\Gamma_M(C_{3,1})$ rotates the $M$ pseudo-spin basis as expected for dipoles. To test the invariance under the $C_{3,1}$ symmetry we solve:

$$\Gamma_{\mathrm{Nd}}(C_{3,1})\hat{\mathscr{K}}_{\mathrm{Nd}-M}\Gamma_M^t(C_{3,1}) = \hat{\mathscr{K}}_{\mathrm{Nd}-M} \tag{5.8}$$

Repeating this procedure for all 48 space group operations reduces the initial 108 parameters down to only five, contained within 3 different bond couplings:

$$\hat{\mathscr{K}}_{\mathrm{Nd}-M} = \begin{pmatrix} 0 & \hat{K}_1 & \hat{K}_2 & \hat{K}_3 \\ \hat{K}_1 & 0 & \hat{K}_3 & \hat{K}_2 \\ \hat{K}_2 & \hat{K}_3 & 0 & \hat{K}_1 \\ \hat{K}_3 & \hat{K}_2 & \hat{K}_1 & 0 \end{pmatrix} \tag{5.9}$$

Here $\hat{K}_1$, $\hat{K}_2$ and $\hat{K}_3$ are the three resulting bond matrices, which take the following form:

$$\hat{K}_1 = \begin{pmatrix} K_{xx} & 0 & K_{xz} \\ 0 & K_{yy} & 0 \\ K_{zx} & 0 & K_{zz} \end{pmatrix} \hat{K}_2 = \begin{pmatrix} \frac{-K_{xx}}{2} & \frac{\sqrt{3}K_{xx}}{2} & K_{xz} \\ \frac{-\sqrt{3}K_{yy}}{2} & \frac{-K_{yy}}{2} & 0 \\ \frac{-K_{zx}}{2} & \frac{\sqrt{3}K_{zx}}{2} & K_{zz} \end{pmatrix} \hat{K}_3 = \begin{pmatrix} \frac{-K_{xx}}{2} & \frac{-\sqrt{3}K_{xx}}{2} & K_{xz} \\ \frac{\sqrt{3}K_{yy}}{2} & \frac{-K_{yy}}{2} & 0 \\ \frac{-K_{zx}}{2} & \frac{-\sqrt{3}K_{zx}}{2} & K_{zz} \end{pmatrix} \tag{5.10}$$

Compared to the four-parameters Hamiltonian of the Nd-Nd (Equation 5.1) and the $M$-$M$ (5.1.2) interactions, the Nd-$M$ interaction contains five distinct parameters. This additional parameter originates from the lower symmetry of the inter-sublattice, which allows in particular $K_{xz} \neq K_{zx}$.

The Nd-$M$ interaction shows the appearance of bond-dependent terms enforced by the dipolar $M$ pseudo-spin. Out of the nine components, three ($xz$, $yz = 0$, and $zz$) remain invariant while the others six acquire bond dependence. The bond-dependence becomes more evident when transforming from the $(x,y,z)$ basis to the $(+,-,z)$ basis. In this new frame, the $\hat{K}_1$, $\hat{K}_2$ and $\hat{K}_3$ bond matrices write:

$$\hat{K}_1 = \begin{pmatrix} K_{\pm\pm} & K_{\pm} & K_{\pm z} \\ K_{\pm} & K_{\pm\pm} & K_{\pm z} \\ K_{z\pm} & K_{z\pm} & K_{zz} \end{pmatrix} \hat{K}_2 = \begin{pmatrix} \omega^2 K_{\pm\pm} & \omega K_{\pm} & K_{\pm z} \\ \omega^2 K_{\pm} & \omega K_{\pm\pm} & K_{\pm z} \\ \omega^2 K_{z\pm} & \omega K_{z\pm} & K_{zz} \end{pmatrix} \hat{K}_3 = \begin{pmatrix} \omega K_{\pm\pm} & \omega^2 K_{\pm} & K_{\pm z} \\ \omega K_{\pm} & \omega^2 K_{\pm\pm} & K_{\pm z} \\ \omega K_{z\pm} & \omega^2 K_{z\pm} & K_{zz} \end{pmatrix} \tag{5.11}$$

where $\omega = e^{2i\pi/3}$ is the same phase parameter observed in the M-M interaction, which appears from the $C_3$ rotations.

Looking at one single $M$ site, the six nearest-neighbor $Nd^{3+}$ ions lie in the same kagome plane (forming a hexagonal arrangement). Figure 5.2 illustrates the case of an $M_1$ site (viewed from above its local $z$-axis), showing its connections to three distinct type of Nd neighbors ($Nd_6$, $Nd_7$ and $Nd_8$). The different bonds are shown in black with the associated matrix coupling $\hat{K}_i$ $(i = 1,2,3)$.

Summing over the six nearest-neighbor bonds leads to a convenient Hamiltonian, which in the local $(x,y,z)$ basis gives:

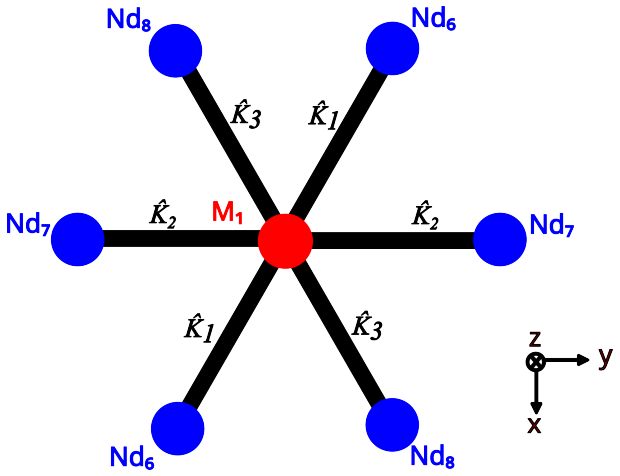


Figure 5.2: Example a site 1 of the metal sublattice (red) and its six first neighbors Nd atoms (blue). The bonds are shown in black.

$$\begin{aligned}\mathscr{H}_{\mathrm{Nd}_i-M} = \sum_{i=1}^{6}[&(\tau_i^x S^z K_{xz} + \tau_i^z S^z K_{zz}) \\ &+\tau_i^x (a_i S^x + b_i S^y) K_{xx} \\ &+\tau_i^y (-b_i S^x + a_i S^y) K_{yy} \\ &+\tau_i^z (a_i S^x + b_i S^y) K_{zx}] \\ \text{where} \quad (a_i)_{i=1}^6 &= \left(1, -\tfrac{1}{2}, -\tfrac{1}{2}, 1, -\tfrac{1}{2}, -\tfrac{1}{2}\right) \\ \text{and} \quad (b_i)_{i=1}^6 &= \left(0, \frac{-\sqrt{3}}{2}, \frac{-\sqrt{3}}{2}, 0, \frac{\sqrt{3}}{2}, \frac{\sqrt{3}}{2}\right)\end{aligned} \tag{5.12}$$

with $a_i$ and $b_i$ the bond dependent parameters expressed in the $(x,y,z)$ basis. Alternatively, we can also derive the Hamiltonian for the $(+,-,z)$ basis:

$$\begin{aligned}\mathscr{H}_{\mathrm{Nd}_i-M} = \sum_{i=1}^{6}[&(\tau_i^+ + \tau_i^-) S^z K_{\pm z} + \tau_i^z S^z K_{zz}) \\ &+(\tau_i^- \alpha_i S^+ + \tau_i^+ \alpha_i^* S^-) K_{\pm} \\ &+(\tau_i^- \alpha_i S^- + \tau_i^+ \alpha_i^* S^+) K_{\pm\pm} \\ &+(\tau_i^z (\alpha_i S^- + \alpha_i^* S^-)) K_{z\pm}] \\ \text{where} \quad (\alpha_i)_{i=1}^6 &= \left(1, \omega, \omega^2, 1, \omega, \omega^2\right)\end{aligned} \tag{5.13}$$

where $\alpha_i$ are the bond parameters for the $(+,-,z)$ basis.

To conclude, we have performed the symmetry analysis of the Nd-Nd interaction for the pyrochlore compounds, where $M$ describes a dipolar pseudo-spin and Nd a DO pseudo-spin. This analysis is valid for any type of DO pseudo-spin, meaning Ce-based compounds with magnetic metallic ion site could be studied with this same interaction.

We can now build a complete Hamiltonian, which includes the separate Hamiltonians of the $M$ and Nd sublattices, plus this new term which couples the two sublattices:

$$\mathscr{H} = \mathscr{H}_{\text{Nd-Nd}} + \mathscr{H}_{M-M} + \mathscr{H}_{\text{Nd}-M} \tag{5.14}$$

In total, this Hamiltonian involves thirteen distincts parameters: four for Nd–Nd, four for ***M***–***M***, and five for ***M***–Nd. This large parameter space provides the most general model for analyzing experimental data in our two compounds $Nd_2Ir_2O_7$ and $Nd_2Ru_2O_7$. Sylvain Petit implemented this Hamiltonian in his homemade spin wave mean-field software [135], which we used to analyze our measurements. In the next section, for $Nd_2Ir_2O_7$ and then for $Nd_2Ru_2O_7$ we discuss our experimental measurements and apply our new Hamiltonian to interpret their magnetic excitations.

## 5.2 Measurement and analysis of $Nd_2Ir_2O_7$ and $Nd_2Ru_2O_7$

### 5.2.1 Experimental method

Measurements were performed on $Nd_2Ir_2O_7$ and $Nd_2Ru_2O_7$ powder samples which were synthesized at Néel Institute by Elise Pachoud and Abdellali Hadj-Azzem. On $Nd_2Ir_2O_7$, several studies from other groups already exist on single crystals, that we will use in our analysis [93, 136]. The obtained single crystals for these compounds are nevertheless very small and not suitable for inelastic neutron scattering experiments. For $Nd_2Ru_2O_7$, single crystal growth was recently reported, but involves specific equipment which is not available in our lab [137, 138]. We have thus performed all the study on polycrystalline powder samples.

$Nd_2Ir_2O_7$ properties had already been reported in the literature before the start of my PhD thesis. It includes the CEF excitations [139], magnetization on single crystals [93], Raman scattering [136], powder neutron diffraction and low energy inelastic neutron scattering [94]. Nevertheless the temperature dependent properties had not been studied thoroughly, and some debate existed about the magnitude of the ordered moment. In particular no Hamiltonian had been proposed which reconciles all the observations. For this reason, the team at Néel had performed neutron diffraction on the whole temperature range (50 mK - 150 K) before my arrival, and I performed detailed inelastic neutron scattering at low energy. From these results, we could perform a detailed spin wave analysis using our new model. On the contrary, $Nd_2Ru_2O_7$ had been less measured, so I have performed magnetization measurements, neutron diffraction and inelastic neutron scattering to determine the CEF and the low energy magnetic excitations over the full temperature range of interests. These results are not fully modeled yet, but I will show the first analysis. Unfinished analysis and prospective will be discussed for both compounds.

This section is divided into four parts. We will first introduce in more details the CEF properties of the $Nd^{3+}$ ion (subsection 5.2.2). Then for each compound, starting with $Nd_2Ir_2O_7$ (subsection 5.2.3) and finishing with $Nd_2Ru_2O_7$ (subsection 5.2.4): we will begin with the CEF measurements from which we obtain insights on the exotic single-ion physics found in these DO rare-earth system. Then we discuss the low temperature magnetic ordering, unveiled by neutron diffraction experiments. Afterwards, we present the bulk magnetic properties, especially the magnetization with respect to temperature and magnetic field. And to end, we interest ourselves to the spin wave excitations associated to the DO AIAO order, comparing them to our model using spin wave analysis. To con-

clude, a last part (Section 5.3) will be dedicated to a comparison of the properties of these two compounds with the ones of other members of the Nd-based family, emphasizing on what could be done in future investigations.

### 5.2.2 Introduction to crystal electric field excitations

As introduced in Section 1.2, the single-ion properties are determined from the total angular moment $J$, which is 9/2 for the $Nd^{3+}$ ion. The corresponding ground state multiplet is thus $(2J+1) = 10$-fold degenerate and composed from $m_J$ states ranging from $-9/2$ up to 9/2.

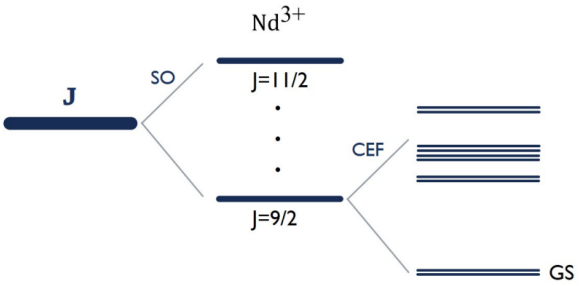


Figure 5.3: Splitting of the $Nd^{3+}$ single ion state by spin–orbit coupling and by the CEF in the pyrochlore structure. Figure from Ref. [8].

The CEF further lifts the $(2J+1)$ degeneracy and the final scheme of states is constituted by a ladder of energy levels (Figure 5.3). These levels (named CEF levels) and specifically the ground state level will dictate the magnetic properties of the single-ion.

The effect of the local CEF on the ground-state multiplet of angular momentum $J$ can be expressed in terms of the Stevens Hamiltonian:

$$\mathscr{H}_{\mathrm{CEF}} = \sum_{n,m} S_n^m \hat{O}_n^m \tag{5.15}$$

where $\hat{O}_n^m$ are Stevens operators (polynomials of $J_x$, $J_y$, $J_z$ components of the angular momentum) and $S_n^m$ are Stevens coefficients. This representation is particularly convenient, but it is strictly valid only if the ion can be treated as a pure $J$-multiplet.

In practice, mixing between multiplets can occur when the first excited multiplet is close in energy to the ground one. For $Nd^{3+}$, the first excited multiplet corresponds to $J = 11/2$, which lies above the ground $J = 9/2$ multiplet. When taking the first excited level into account, a more general formalism must be used (the Wybourne formalism), where the CEF Hamiltonian is expressed in a basis including all multiplets.

In this re-expression instead of $S_n^m$ Stevens parameters, Wybourne $B_m^n$ coefficients are employed. In the literature the $B_m^n$ notation is often used for both Stevens and Wybourne paramereters, although the two types of parameters are different. The $\hat{O}_n^m$ operators also follow the same notation but are different operators.

As a result, one should take care when comparing Stevens and Wybourne parameters across the literature. Since it is only when considering the ground multiplet, that they are related through multiplicative factors $\lambda_{nm}$ and numerical coefficient $\theta_n$ following:

$$S_n^m = \lambda_{nm}\theta_n B_m^n \tag{5.16}$$

In pyrochlore materials, the rare-earth ion sits at a site with local $D_{3d}$ symmetry. This constrains the allowed CEF terms: only six survive ($B_2^0, B_4^0, B_4^3, B_6^0, B_6^3, B_6^6$), while all others vanish [21]. The effective Hamiltonian reduces to:

$$\mathscr{H}_{\text{CEF}} = B_2^0\hat{O}_2^0 + B_4^0\hat{O}_4^0 + B_4^3\hat{O}_4^3 + B_6^0\hat{O}_6^0 + B_6^3\hat{O}_6^3 + B_6^6\hat{O}_6^6 \tag{5.17}$$

The values of these coefficients are directly related to the nature of the doublet ground state (for example non-Kramers, DO) as discussed in Ref. [26]. In the case of $Nd^{3+}$ in the pyrochlore environment, the corresponding low-energy wavefunction takes the following general form:

| | $-\frac{9}{2}$ | $-\frac{7}{2}$ | $-\frac{5}{2}$ | $-\frac{3}{2}$ | $-\frac{1}{2}$ | $+\frac{1}{2}$ | $+\frac{3}{2}$ | $+\frac{5}{2}$ | $+\frac{7}{2}$ | $+\frac{9}{2}$ |
|---|---|---|---|---|---|---|---|---|---|---|
| $\lvert\uparrow\rangle$ | $a$ | 0 | 0 | $b$ | 0 | 0 | $c$ | 0 | 0 | $d$ |
| $\lvert\downarrow\rangle$ | $-d$ | 0 | 0 | $c$ | 0 | 0 | $-b$ | 0 | 0 | $a$ |

(5.18)

This wavefunction involves only $|m_J = \pm 9/2\rangle$ and $|m_J = \pm 3/2\rangle$ components. Within this restricted subspace, some octupole operators (e.g. $O_3^{\pm 3}$) acquire finite matrix elements, enabling effective to the moments octupolar degrees of freedom in addition to the usual dipolar ones. They act as third order operators that can couple components like $|\pm 3/2\rangle$ or $|-9/2\rangle$ with $|-3/2\rangle$ for instance. It is precisely this wavefunction structure that underlies the peculiar DO character of $Nd^{3+}$. Similar properties are found in $Ce^{3+}$, because its ground doublet is built from $|\pm 3/2\rangle$ (which similarly can be coupled by octupolar operators).

The CEF parameters can be determined experimentally by measuring the CEF excitations, i.e. transitions between the ground doublet and higher-lying levels. In neutron scattering experiments, these appear as dispersionless (flat) modes with intensity decreasing as a function of momentum transfer $Q$. In the following, we will use such measurements on $Nd_2Ir_2O_7$ and $Nd_2Ru_2O_7$ to determine the details of their ground state wavefunction and to quantify the associated magnetic moments.

### 5.2.3 $Nd_2Ir_2O_7$

#### CEF levels measurements

Figure 5.4 shows constant $Q$-cuts up to 50 meV of inelastic neutron scattering (INS) measurements, performed by Watahiki et al. [139]. Such cuts highlight the local, dispersionless CEF excitations. A first excited level is observed at 26 meV, followed by two overlapping level at 41 meV. Very similar CEF excitations have also been reported in the parent compound $Nd_2Zr_2O_7$ at nearby energies [82].

The refined CEF parameters and ground state doublet wavefunction of $Nd_2Ir_2O_7$ are shown in Table 5.1. They use the Stevens formalism taking into account only the $J = 9/2$ lowest-energy multiplet. The extracted parameters are very close to those of $Nd_2Zr_2O_7$, confirming that the single-ion ground state of $Nd^{3+}$ is similar in $Nd_2Ir_2O_7$.

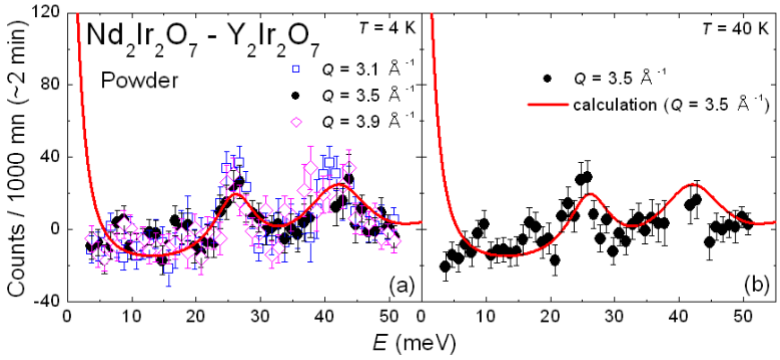


Figure 5.4: Constant $Q$-cut of powder sample $Nd_2Ir_2O_7$ at 4 and 40 K. CEF levels are fitted using the Stevens formalism. Figure from Ref. [139].

| $S_{20}$ | $S_{40}$ | $S_{43}$ | $S_{60}$ | $S_{63}$ | $S_{66}$ | $g_\parallel$ | $g_\perp$ |
|---|---|---|---|---|---|---|---|
| $-0.28$ | $-0.96\cdot10^{-1}$ | 0.34 | $-0.44\cdot10^{-3}$ | $0.18\cdot10^{-2}$ | $-0.46\cdot10^{-2}$ | 4.74 | 0 |

| $J_z$ | $-9/2$ | $-7/2$ | $-5/2$ | $-3/2$ | $\pm1/2$ | $3/2$ | $5/2$ | $7/2$ | $9/2$ |
|---|---|---|---|---|---|---|---|---|---|
| $\|\uparrow\rangle$ | $-0.057$ | 0 | 0 | $-0.286$ | 0 | $-0.489$ | 0 | 0 | $-0.822$ |
| $\|\downarrow\rangle$ | $-0.822$ | 0 | 0 | 0.489 | 0 | $-0.286$ | 0 | 0 | 0.057 |

Table 5.1: Stevens coefficients (in K), $g$ factors, and ground state wave functions of $Nd^{3+}$ in $Nd_2Ir_2O_7$ from inelastic neutron scattering analysis [139].

The ground-state doublet is composed exclusively of $|\pm9/2\rangle$ and $|\pm3/2\rangle$ components, confirming the DO character of the doublet. The $g$-factors further reveal an Ising anisotropy with $g_\parallel = 4.74$ and $g_\perp = 0$, corresponding to a magnetic moment of 2.37 $\mu_B$ aligned along the local $\langle111\rangle$ axis. Moreover, since the first excited CEF level lies at ~25 meV (~290 K), the ground state is well isolated. This validates the effective pseudo-spin-1/2 description as an excellent approximation for the $Nd^{3+}$ ions in $Nd_2Ir_2O_7$.

**Neutron diffraction and magnetic ordering**

Most pyrochlore iridates (Nd, Sm, Eu, Gd, Tb, Dy and Ho) undergo a metal-insulator (MI) transition, which is associated to the magnetic ordering of the Ir sublattice in an AIAO ground state [140, 141]. In the case of $Nd_2Ir_2O_7$, investigation of the magnetic ordering was done using neutron diffraction experiments above and below the temperature of the MI transition ($T_{MI} = 33$ K).

From neutron diffraction, Tomiyasu et al. [94], proposed that the Nd $^{3+}$ moments order in an AIAO configuration. As shown in Figure 5.5(a), the temperature dependence of the sum of (222) and (113) peak intensities (characteristic of AIAO order in pyrochlores) indicates that the Nd moments begin to order around 15 K and fully order around 3 K. Unfortunately, due to a lack of statistics, they were not able to unambiguously resolve the ordering of the Ir moments, as they are smaller than the Nd ones and also order AIAO.

Later on, Guo et al. [22, 142] were able to resolve the Ir moments contribution with measurement of powder neutron diffraction data with better statistics. With their mea-

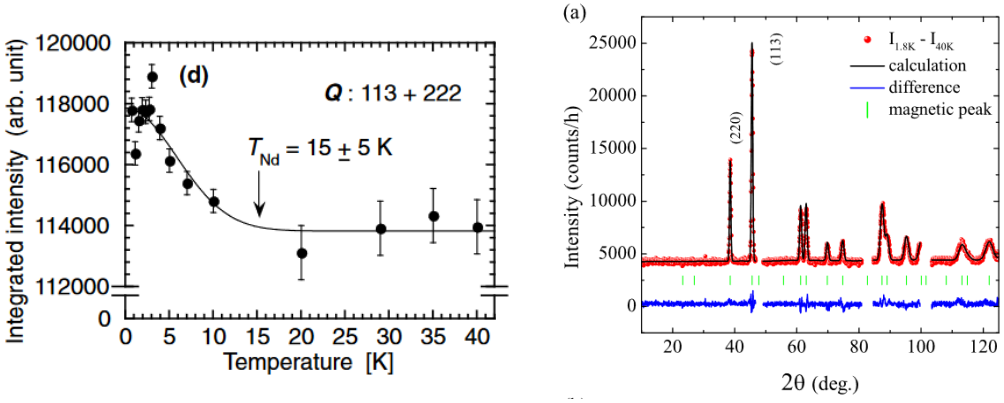


(a) (b)

Figure 5.5: (a) Temperature dependence of the sum of the integrated intensities of the (113) and (222) Bragg peaks, in powder $Nd_2Ir_2O_7$. Figure from Ref. [94] (b) Difference between powder diffractograms measured at 1.8 K and 40 K in $Nd_2Ir_2O_7$. Figure from Ref. [22].

surements (Figure 5.5(b)), the quality of the refinement of the magnetic structure at 15 K and 8 K is considerably increased when considering AIAO orderings for both Nd and Ir. They estimate ordered moments of 1.27 $\mu_B$ for Nd and 0.34 $\mu_B$ for Ir at 1.8 K. From CEF calculations, we know that the total Nd moment is about 2.35 $\mu_B$. The persistence of a reduced Nd moment confirms the DO character of the AIAO Nd ordering.

In pyrochlore iridates, it has been shown that the AIAO ordering of the Ir sublattice acts as local staggered molecular field along the $\langle 111 \rangle$ directions (Figure 5.6(b)), which in turn favors an AIAO ordering on the rare-earth sublattice [23, 143]. Within this molecular field approach, one would expect in $Nd_2Ir_2O_7$ that the Nd moments should align strictly along their local $z$ axis and recover their full moment. Instead, the persistence of a reduced moment even at the lowest temperatures reveals that the coupling between Ir and Nd cannot be described by a simple molecular field effect along the local $z$ directions.

Nonetheless, from these first studies, it is clear that Ir favors Nd ordering, which occurs at a higher temperature than expected. Indeed, these $Nd_2Ir_2O_7$ studies estimate the ordering around 15 K, whereas in other Nd-based pyrochlores with a non magnetic metal ion, the ordering is found at only a few hundred millikelvins.

To investigate the Ir effect further, we measured the temperature dependence of the Nd ordered moment. Powder neutron diffraction diffractograms were measured between 70 mK and 80 K on the LLB-G41 diffractometer and analyzed using Rietveld refinements. The refined Nd moment (using FullProf software) is shown in Fig.5.6(a) between 70 mK and 30 K and agrees with Tomiyasu measurements [94]. Below 15 K, the Nd ordered moment emerges and increases until it saturates at about 3 K. The behavior of the Nd moment, with a non vanishing tail at higher temperatures is typical of an externally induced moment, confirming that Nd ordering is induced by the Ir sublattice ordering. This temperature dependence of the Nd magnetic moment will be used to test and constrain our new model.

In conclusion, in $Nd_2Ir_2O_7$ both sublattices order in an AIAO state, but the ordered

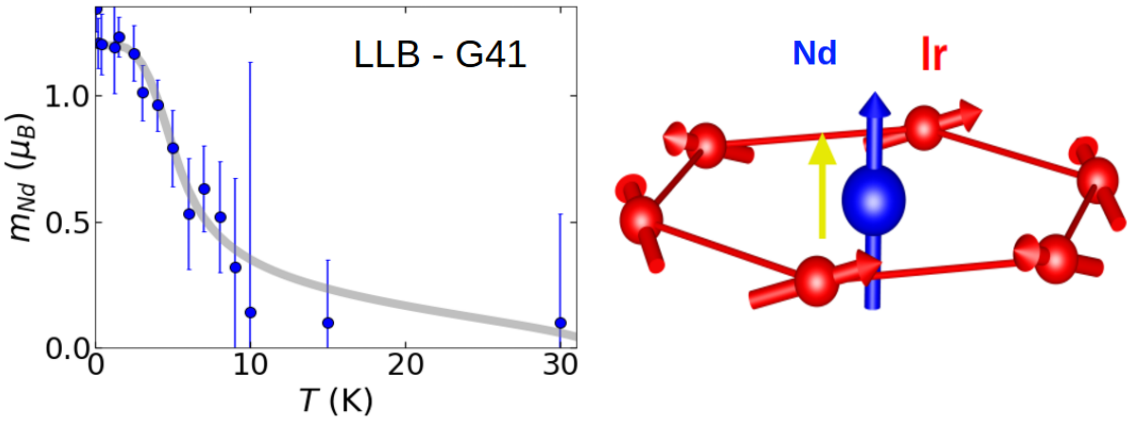


(a) (b)

Figure 5.6: (a) Temperature dependence of the refined ordered moment from powder diffraction measurements in $Nd_2Ir_2O_7$. The grey line is a guide for the eye. (b) Schematic of the six first-neighbor Ir moments surrounding an Nd moment. The molecular field produced from Ir moments is shown in yellow.

Nd moment remains reduced due to its DO nature. The Ir order clearly induces Nd ordering at an anomalously high temperature compared to Nd-based pyrochlores with a non magnetic metal ion, yet the coupling mechanism goes beyond a simple molecular field picture. The "true" couplings between the Nd and Ir sublattices, as formulated in our symmetry analysis, have to be taken into account to describe the observed properties.

**Bulk magnetometry**

The magnetic properties of $Nd_2Ir_2O_7$ were further investigated through magnetization and susceptibility measurements on single crystals [93]. Figure 5.7(c) shows the temperature dependence of the ZFC-FC susceptibility. A clear splitting between the ZFC and FC curves appears near $T_{MI}$ (see inset), coinciding with the $Ir^{4+}$ AIAO ordering. The Ir magnetization being very small, this ZFC-FC signal is associated to the Nd magnetization induced by the Ir ordering. No distinct anomaly associated with an independent Nd ordering is observed down to 2 K.

Figure 5.7(a) displays the MvsH measurement at 2 K, revealing a saturation at about 1.2 $\mu_B$/Nd, consistent with CEF calculations. The differences between the magnetization at saturation between the [001], [111] and [110] crystallographic directions are consistent with a local Ising anisotropy on the pyrochlore lattice. Along the [111] direction, an anomaly occurs at a critical field $\mu_0 H_c \sim 3.6$ T, displaying a hysteretic behavior. This feature is linked to field-induced transitions of the Nd sublattice.

Considering just one tetrahedron, when the system is saturated with a large enough negative field, the spins adopt a 1-out/3-in configuration. As the field is increased toward zero, the "out" spin turns progressively leading the tetrahedron to the all-in configuration, consistent with the AIAO ground state. Upon further increasing the field, three spins flip simultaneously, producing a sudden transition to the 3-out/1-in configuration. This transition generates a sharp peak in the derivative $dM/dH$, as seen in Figure 5.7(b).

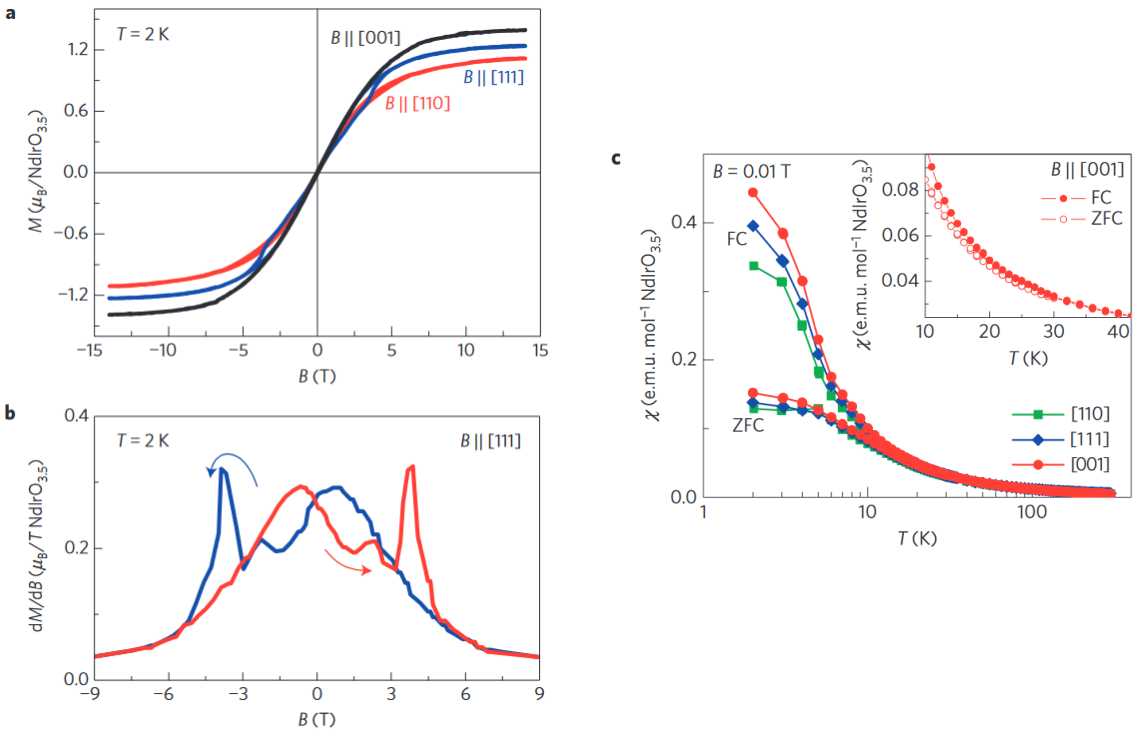


Figure 5.7: (a) Magnetization versus field at 2 K along the [001], [111], and [110] directions. (b) Derivative $dM/dH$ versus field along the [111] direction at 2 K both from initial negative and positive saturation. (c) Susceptibility versus temperature along the [001], [111], and [110] directions. Inset: Zoom on the ZFC-FC splitting region. Figures from Ref. [93].

When the field is swept in the opposite direction with initial saturation of the moments with a large enough positive field, the same process occurs in reverse order: the system begins in the 3-out/1-in state, evolves into the all-out state, and then abruptly flips to the 1-out/3-in configuration at the critical field $\mu_0 H_c \sim -3.6$ T.

A similar phenomenon has been observed in other Nd-based pyrochlores such as $Nd_2Zr_2O_7$, though the critical field is much smaller ($\mu_0 H_c \sim 0.1$T)[80, 90, 144, 145]. The much larger value of $\mu_0 H_c$ in $Nd_2Ir_2O_7$ reflects the higher energy scale of the interactions, consistent with the strong coupling introduced by the $Ir^{4+}$ sublattice.

### Spin wave measurements

The excitations characteristic of Nd-based pyrochlores arising from dynamic fragmentation consists of two main contributions: a divergence-free flat mode gapped at an energy $\Delta_{\text{flat}}$, and divergence-full dispersive branches sitting on top of the flat mode (see Section 1.4).

Measurements of INS spectra were performed on the TOF spectrometer IN5@ILL, with the temperature dependence of the excitations investigated below the transition $T_{MI}$ down to 2 K. An additional set of INS measurements was carried out on SHARP-CRG@ILL down to 50 mK, which revealed no significant change compared to the 2 K

data. In the following, only the IN5@ILL data are presented, as they are of better quality.

Figure 5.8 displays three INS spectra: one in the fully ordered state (2 K), one at an intermediate temperature (10 K) where the inelastic signal is fading, and one at high temperature (40 K) where the Nd moments exhibit paramagnetic behavior. In the low-temperature spectrum, the flat mode is clearly observed at $\Delta_{\text{flat}} = 1.24$ meV, together with a broad feature around 1.5-2 $\text{Å}^{-1}$ corresponding to the dispersive excitations. The excitations are not as well defined as those observed in $Nd_2Zr_2O_7$ materials, as they are averaged over $Q$ due to powder sample measurements. Additionally, the strong neutron absorption of Ir resulted in a small intensity of the signal.

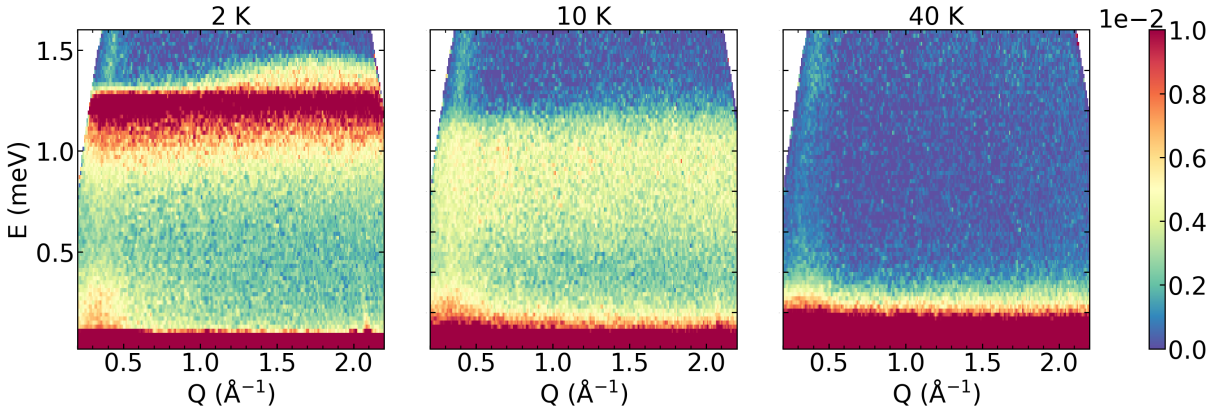


Figure 5.8: Intensity of INS spectra depending on the energy $E$ (in meV) and the momentum transfer $Q$ (in $\text{Å}^{-1}$) measured at 2 K, 10 K and 40 K with an incident beam wavelength of 4.4 Å and an energy resolution of 20 $\mu$eV on powder $Nd_2Ir_2O_7$.

A total of twelve temperatures were measured between 1.7 K and 40 K. $Q$-cuts integrated over 1.5-2 $\text{Å}^{-1}$ (Figure 5.9(a)), show the full temperature dependence of the excitations. The flat mode is well resolved, decreasing in energy and loosing in intensity with increasing temperature. The dispersive branches appear in the cuts as a small shoulder around 1.4 meV. Figures 5.9(b)-(c) show the temperature dependence of the flat mode energy $\Delta_{flat}$ and its intensity, clearly indicating that the excitations persist up to 25 K. The temperature dependence of those two quantities resembles the one of the refined ordered moment obtained from the diffraction patterns. At 30 K and 40 K, the cuts show that the excitations have disappeared completely, explaining why no information on the flat mode can be extracted above 25 K.

The observed temperature dependence is also consistent with previous measurements by Tomiyasu et al. [94]. These results further confirm that the phenomenology of $Nd_2Ir_2O_7$ cannot be described by a molecular field model alone. The excitations observed can only occur if the Nd moments still possess a DO character: they must have an ordered component along the local $x$ axis so that a part of the fluctuations are projected along the local $z$ direction.

In the following, using both the temperature dependence of the ordered moment $m_{\text{ord}}$ and the spin wave spectra, we will determine the parameters of the model found in Section 5.1. This analysis will provide valuable insight into the coupling parameters responsible for the induced ordering observed on the Nd sublattice due to the Ir sublattice.

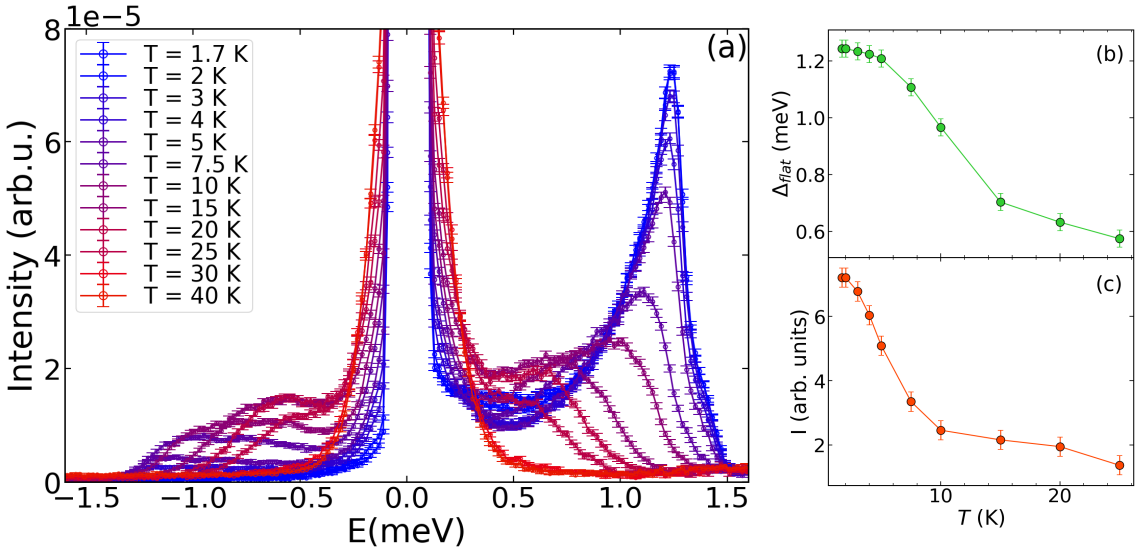


Figure 5.9: (a) Constant $Q$-cuts of INS spectra integrated between 1.5 Å$^{-1}$ and 2 Å$^{-1}$ with an incident wavelength of 4.4 Å at various temperature between 1.7 K and 40 K. (b)-(c) Temperature dependence of the energy gap $\Delta_{flat}$ and the intensity $I$ of the flat band excitation.

**Analysis using the model Hamiltonian**

The complete model describing the Nd–Nd, Nd–Ir, and Ir–Ir interactions contains a total of thirteen parameters. This is a large number of parameters, which we want to constrain to avoid overfitting. For the Ir–Ir interaction, the Ir sublattice in $Nd_2Ir_2O_7$ stabilizes an AIAO ground state configuration at 33 K. To reproduce this ground state and the corresponding Néel temperature, a single parameter is sufficient: $\mathscr{J}_{zz} = -21$ K, with all other parameters set to zero. Unfortunately, our measurements do not allow independent access to the microscopic parameters of this interaction, so fine-tuning is not possible. Nonetheless, we are primarily interested on the effect of Ir on the Nd, which to a first approximation should be well described by this single parameter.

Reproducing the gap $\Delta_{flat}$ at an energy of about 1.25 meV, strongly constrains one parameter of the Nd-Ir interaction: it requires $K_{xz} \approx 4$ K. Other parameters such as $K_{xx}$, $K_{yy}$, $K_{zx}$ from Nd-Ir or $J_y$ from Nd-Nd are set to zero as they have negligible effect on the measured observables. After this first step, the parameter space is reduced to only five parameters: $J_x$, $J_z$, $J_{xz}$, $K_{xz}$ and $K_{zz}$.

To refine these five coupling parameters, we use two experimental results that can be simulated using the spin wave software: the temperature dependence of the ordered moment $m_{\mathrm{ord}}(T)$ and the spin wave excitation spectra. For $m_{\mathrm{ord}}(T)$, we define a cost function $\chi$ as the least-square difference between the experimental and calculated temperature series:

$$\chi = \sum_{T_i} (m_{ord,exp}(T_i) - m_{ord,calc}(T_i))^2 \tag{5.19}$$

For the spin waves, calculating the INS spectra as a function of both energy and $Q$ is

computationally expensive. Thus, defining a cost function as for $m_{ord}(T)$ would require too much computation time. At $Q = (220), (113)$, two characteristic energies can be deduced from the excitation spectrum: the gap and the top of the dispersion branches $e_2$. In the powder spectrum, it corresponds to $Q \approx 1.9$ Å$^{-1}$. We can thus optimize the parameters to match the two observed energies: $(\Delta_{\text{flat}}, e_2) = (1.24, 1.45)$ meV.

Using the cost function and extracting $(\Delta_{\text{flat}}, e_2)$, we systematically explore our reduced parameter space. The parameters are varied two at a time, while the other three remain fixed. This allows the construction of 2D maps of the cost function and the corresponding values of the gap and maximum of the dispersion, from which the most promising regions of parameter space can be identified. The parameters are varied in steps of 0.2 K over a wide range, from $-4$ K to 4 K.

Figure 5.10(a) illustrates how far a particular set of parameters can deviate from the measured $m_{\text{ord}}(T)$. The set of parameters used here was chosen randomly for illustration purposes: $(J_x = 0.6$ K$, J_{xz} = 3$ K$, J_z = -1.6$ K$, K_{xz} = 4$ K$, K_{zz} = 0.4$ K$)$. This position is indicated by the black star symbol in Figure 5.11. Figure 5.10(b) shows the calculated intensity as a function of energy along $Q = (220)$ for the same set. Two peaks are visible, corresponding to the gap and the maximum of the dispersion, at energies that do not fit the experiment: $(\Delta_{\text{flat}}, e_2) = (1.4, 1.6)$ meV.

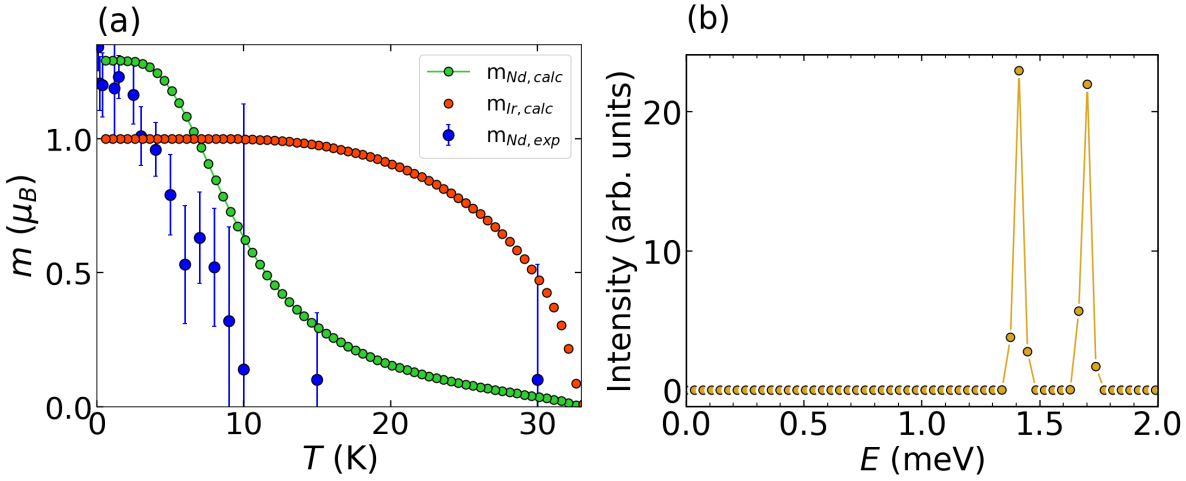


Figure 5.10: (a) Temperature dependence of the ordered moment $m_{\text{ord}}(T)$: measured (blue) and calculated (green) using a randomly chosen parameter set. The ordered moment of the $Ir^{4+}$ is also shown in orange. (b) Calculated INS intensity as a function of energy for $Q = (220)$ for the same parameter set. Two peaks are visible corresponding to the gap $\Delta_{\text{flat}}$ and the top of the dispersion $e_2$.

Figure 5.11(a), shows the results obtained by varying $J_x$ and $J_{zx}$ of the Nd-Nd interaction, with $J_z = -1.6$ K, $K_{xz} = 4$ K, and $K_{zz} = 0.4$ K. The map displays the calculated $\chi$, with the two black lines indicating isovalues of the two energies: 1.24 meV for $(\Delta_{\text{flat}}$ and 1.45 meV for $e_2$. In that calculation, $J_z = -1.6$ K, $K_{xz} = 4$ K and $K_{zz} = 0.4$ K were already refined using the same procedure. The optimal set of parameters is found for the lowest $\chi$ values in the region where the two iso-values intersect.

In other tests, the gap and dispersive excitation values may not cross over a sufficiently

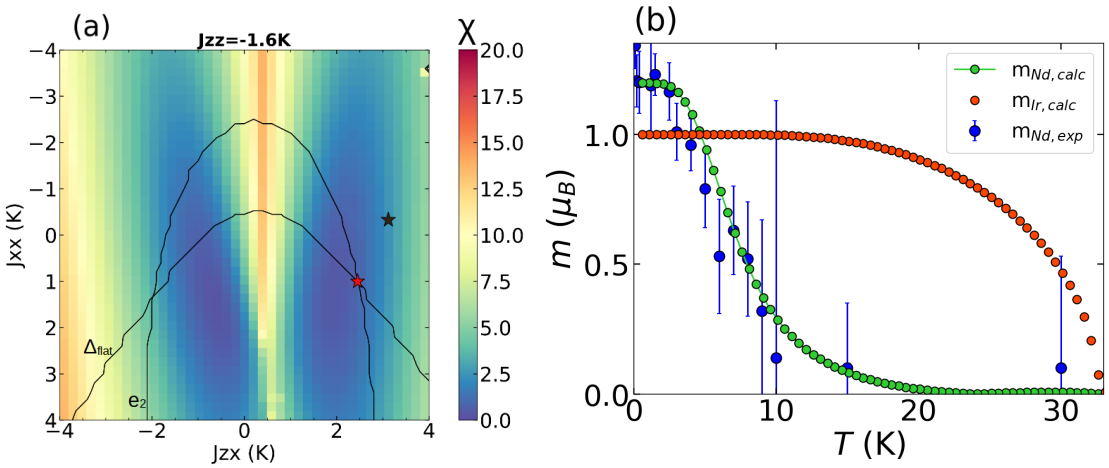


Figure 5.11: (a) 2D map of the cost function $\chi$ for varying $J_x$ and $J_{xz}$, with black lines corresponding to iso-values of $\Delta_{\text{flat}}$ and $e_2$. (b) Calculated temperature dependence of the ordered moment $m_{\text{ord}}(T)$ using the optimized parameter set compared to the measured one.

low $\chi$ region. In the case of Figure 5.11(a), the crossing occurs within a favorable $\chi$ region, indicated by the red star. After, some fine-tuning around that point, the parameter set ($J_x = 0.8$ K, $J_{xz} = 2.4$ K, $J_z = -1.36$ K, $K_{xz} = 4$ K, $K_{zz} = 0.4$ K), is the most optimal set found within the large parameter space we have explored.

Figure 5.11(b) shows the direct comparison of the measured and calculated $m_{ord}(T)$ for the optimized parameter set, demonstrating very good agreement. We also computed INS spectra using this set of parameters for three temperatures (2 K, 10 K and 20 K), as shown in Figure 5.12. The calculated spin wave spectra are also in good agreement with the measurements. The temperature dependence is well captured, with the spectra at 2 and 10 K displaying similar energies for the flat mode. At 10 K and 20 K, the dispersive excitations have totally vanished. At 20 K, however, the model slightly overestimates the energy of the gap compared to our measurements.

The methodology applied here successfully identified a parameter set that reproduces our neutron measurements. However, this set of parameters does not reproduce the measured critical field $H_c$ from Ref. [93], although the good range is obtained: it gives $\mu_0 H_c \approx 4.5$ T instead of the experimental value of 3.6 T. The critical field is closely linked to the Nd–Ir $K_{xz}$ term. Reducing the calculated $H_c$ requires decreasing $K_{xz}$, which unfortunately also reduces the gap value. Increasing $K_{zz}$ can partially compensate for the gap reduction, but this impacts negatively the agreement with $m_{\text{ord}}(T)$. However, it is hard in calculations to reproduce the metastability effects that can be observed in hysteretic magnetization. This may explain why $H_c$ is overestimated compared to experiments. Further investigations are necessary to compare more accurately our model to the experimental $H_c$.

As mentioned earlier, the Ir–Ir interaction was parametrized only to reproduce the correct ground state and transition temperature. We are currently investigating how a more precise determination of the Ir–Ir parameters could impact the properties of the Nd sublattice. Recently, a refined set of Ir–Ir interaction parameters was obtained from

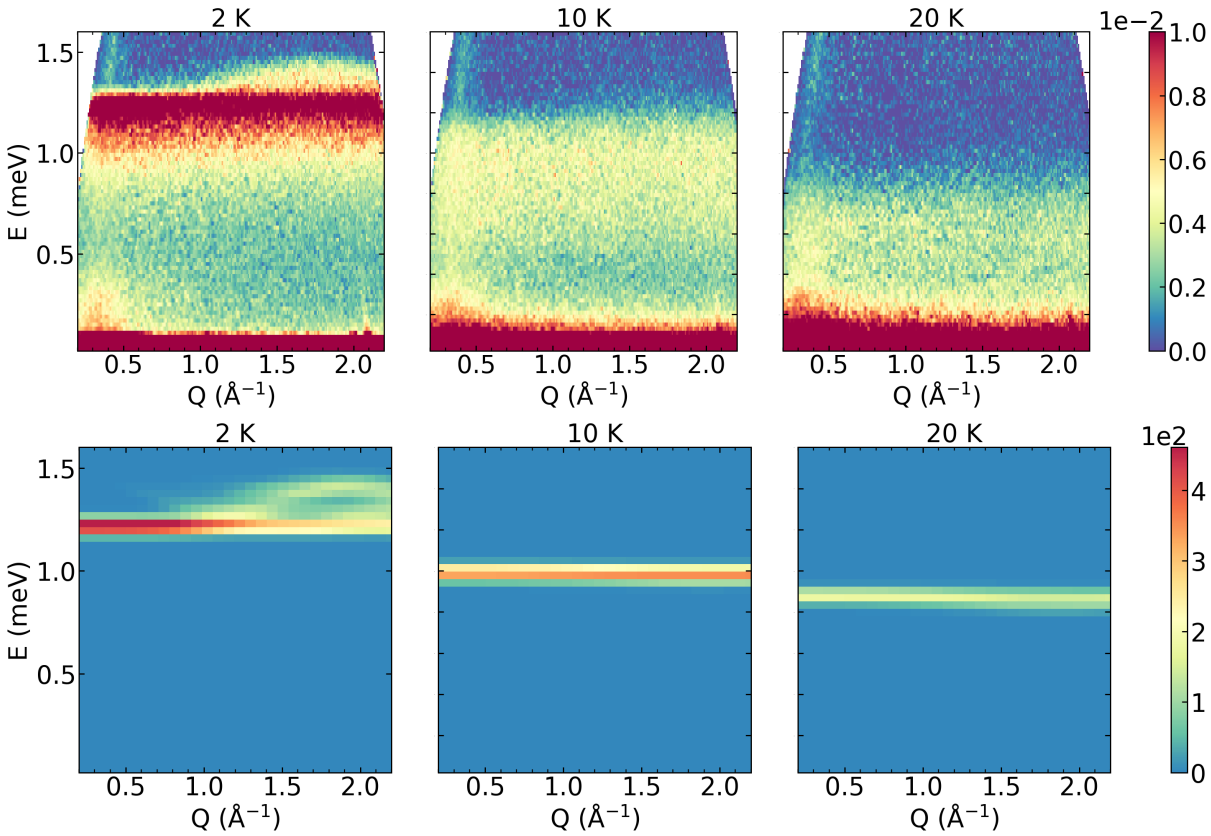


Figure 5.12: Top: Measured INS spectra of powder $Nd_2Ir_2O_7$ at 2 K, 10 K, and 20 K. Bottom: Calculated INS spectra using the optimized parameter set for the same temperatures.

Raman spectroscopy measurements [136]. Using these parameters as a starting point could help further improve the description of our measurements within our symmetry-based model.

### 5.2.4 $Nd_2Ru_2O_7$

#### CEF levels measurements

Inelastic neutron scattering (INS) spectra of powder $Nd_2Ru_2O_7$ were measured on the TOF spectrometer: PANTHER@ILL (Section 2.1.5). Additional measurements with an empty sample holder were also performed in order to correct the spectra for background contributions. All spectra presented here are therefore background corrected.

A first set of measurements with incident neutron energy $E_i = 50$ meV was performed at three temperatures: 3 K, 160 K and 300 K. The left panel of Figure 5.13 displays the spectrum at lowest temperature: 3 K. Two flats modes, indicative of CEF levels, are observed around 25 meV and 41 meV, and are characterized by vanishing intensities at large $Q$, consistent with the magnetic form factor. Two additional modes at 9 meV and 18 meV are also visible, whose intensities increase at large $Q$, which we identify as phonons (lattice excitations).

Both phonon modes and CEF excitations were also reported in the parent compounds $Nd_2Zr_2O_7$ and $Nd_2Ir_2O_7$ at comparable energies [82, 139]. The second CEF mode, located around 41 meV in $Nd_2Ru_2O_7$, was found to consist of two doublets with neighboring energies in $Nd_2Zr_2O_7$ and $Nd_2Ir_2O_7$. In Figure 5.13, the second mode in $Nd_2Ru_2O_7$ appears broader both in the cuts and in the map, suggesting that it may likewise correspond to two nearly degenerate doublets. Already from this first set of measurements, it appears that the magnetic properties of the $Nd^{3+}$ ion in $Nd_2Ru_2O_7$ are very similar to those observed in other Nd-based compounds.

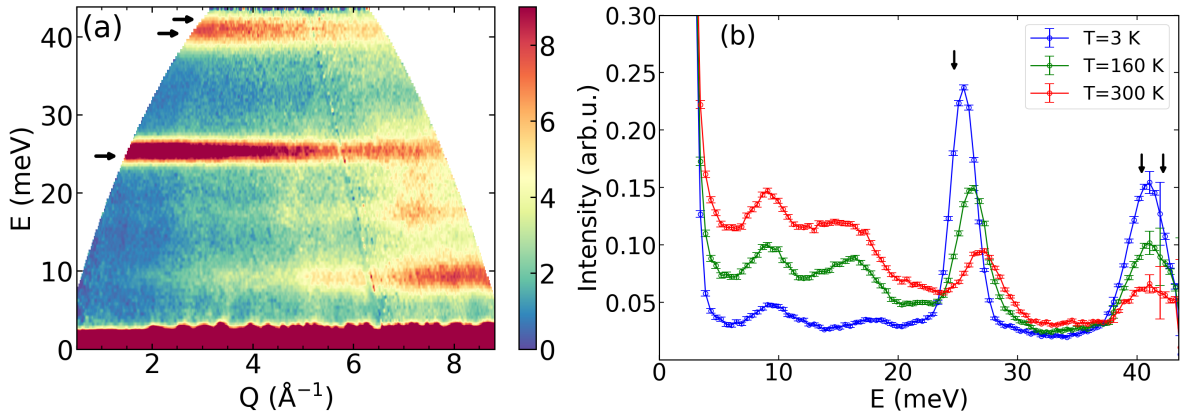


Figure 5.13: (a) INS spectra depending on the energy $E$ (in meV) and the momentum transfer $Q$ (in Å$^{-1}$) measured at 3 K with an incident beam energy of 50 meV. The map obtained after subtraction of a background map. (b) Constant-$Q$ cuts of the spectra, integrated between 2.5 Å$^{-1}$ and 3.5 Å$^{-1}$, showing data at 3 K (blue), 160 K (green), and 300 K (red).

The refinement of the Wybourne coefficients of $\mathscr{H}_{\text{CEF}}$ was carried out by Sylvain Petit using his dedicated software. The first excited $J = 11/2$ multiplet was taken into account along with the ground state multiplet $J = 9/2$. The refinement employed the positions and intensities of the three measured CEF levels, together with the low-temperature saturated moment of 2.36 $\mu_B$ (deduced from magnetization versus field, see Section 5.2.4). The resulting CEF levels energies are 24.7, 40.4, 42.2, and 117.1 meV. The first three excitations are highlighted by black arrows in Figures 5.13.

Interestingly, a fourth higher-energy CEF level was predicted at 117.1 meV, which we initially missed. By carefully examining the spectrum taken with a higher incident energy, $E_i = 130$ meV, at 3 K (Figures 5.14), we observe in a constant-$Q$ cut (integrated over 5-7 Å$^{-1}$) a weak intensity peak precisely at 117 meV. In the INS spectra (Figure 5.14), this level is barely visible, yet its $Q$-dependence decreases at higher $Q$, confirming its magnetic origin. In addition, two higher-energy flat phonon modes are detected around 50 meV and 70 meV with this incident energy.

The Wybourne coefficients are listed in Table 5.2 together with the components of the wavefunction of the ground state doublet. It is worth noting that the scale of the Wybourne coefficients differs from that of the Stevens coefficients in $Nd_2Ir_2O_7$. This illustrates the point made in Section 5.2.2, namely that one need to be careful when comparing different sets of CEF parameters.

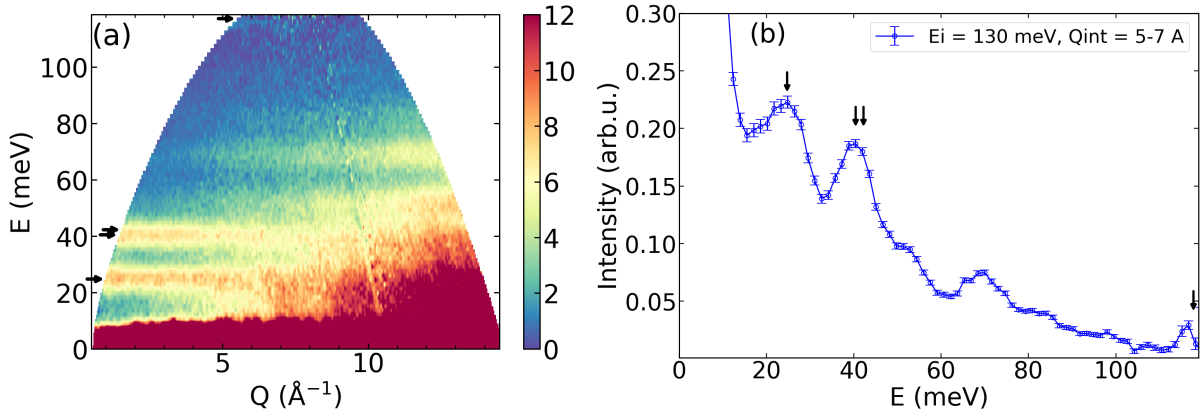


Figure 5.14: (a) INS spectra depending on the energy $E$ (in meV) and the momentum transfer $Q$ (in Å$^{-1}$) measured at 3 K with an incident beam energy of 130 meV. The map is subtracted by a background map. (b) Constant-$Q$ cut of the 3 K spectrum, integrated between 5 Å$^{-1}$ and 7 Å$^{-1}$.

| $B_{20}$ | $B_{40}$ | $B_{43}$ | $B_{60}$ | $B_{63}$ | $B_{66}$ | $g_\parallel$ | $g_\perp$ |
|---|---|---|---|---|---|---|---|
| 61.5 | 408.9 | 106.4 | 166.6 | −122.5 | 173.9 | 4.72 | 0 |

| $J_z$ | $-9/2$ | $-7/2$ | $-5/2$ | $-3/2$ | $\pm 1/2$ | $3/2$ | $5/2$ | $7/2$ | $9/2$ |
|---|---|---|---|---|---|---|---|---|---|
| $\lvert\uparrow\rangle$ | 0.794 | 0 | 0 | 0.446 | 0 | 0.139 | 0 | 0 | 0.362 |
| $\lvert\downarrow\rangle$ | −0.362 | 0 | 0 | 0.139 | 0 | −0.446 | 0 | 0 | 0.794 |

| $J_z$ | $-11/2$ | $-9/2$ | $-7/2$ | $-5/2$ | $-3/2$ | $\pm 1/2$ | $3/2$ | $5/2$ | $7/2$ | $9/2$ | $11/2$ |
|---|---|---|---|---|---|---|---|---|---|---|---|
| $\lvert\uparrow\rangle$ | 0 | 0.009 | 0 | 0 | 0.037 | 0 | 0.041 | 0 | 0 | 0.130 | 0 |
| $\lvert\downarrow\rangle$ | 0 | −0.130 | 0 | 0 | 0.041 | 0 | −0.037 | 0 | 0 | 0.009 | 0 |

Table 5.2: Wybourne coefficients (in K), $g$ factors, and ground state wave functions of $Nd^{3+}$ in $Nd_2Ru_2O_7$ from our inelastic neutron scattering analysis.

The $Nd_2Ru_2O_7$ wavefunction consists of a mixture of only two components: $|\pm 9/2\rangle$ and $|\pm 3/2\rangle$, as in $Nd_2Ir_2O_7$. As shown previously, such a wavefunction is characteristic of a DO ground state doublet. Moreover, the first excited CEF level at 24.7 meV lies at a similar energy as the one in $Nd_2Ir_2O_7$ and also indicates that the ground-state doublet is well separated from higher energy state. It is therefore possible to describe the ground-state doublet in $Nd_2Ru_2O_7$ accurately using an effective pseudo-spin-1/2.

### Neutron diffraction and magnetic ordering

Similarly to pyrochlore iridates, in most ruthenates the Ru sublattice also orders magnetically, with transition temperatures ranging from 75 K up to 160 K [25]. Within this family, $Nd_2Ru_2O_7$ exhibits the second-highest Ru ordering temperature, with $T_N \approx$ 147 K.

Neutron diffraction measurements revealed that, contrary to $Nd_2Ir_2O_7$, the $Ru^{4+}$ ions order in a local easy-plane antiferromagnetic structure called $\Gamma_5$ (Figure 5.15) [146]. This

magnetic structure is constituted of two states $\Psi_2$ and $\Psi_3$, and the magnettic structure can be any linear combination of $\Psi_2$ et $\Psi_3$, since powder neutron diffraction cannot dissociate the two components.

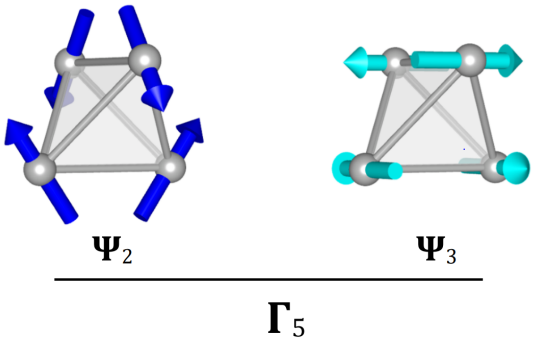


Figure 5.15: $\Gamma_5$ easy plane antiferromagnetic order composed of two states: $\Psi_2$ and $\Psi_3$. Figure from Ref. [147].

The $\Gamma_5$ order is evidenced by the (111) and (220) reflections, characteristic of that order, which increase in intensity below the ordering temperature. By contrast, the absence of an intensity increase at the (111) reflection, combined with increasing intensity at the (220) and (113) reflections, instead indicate an AIAO order. Figure 5.16(a) shows the temperature dependence of the peak intensity at the (111) and (220) positions from Ito et al. [146], confirming the onset of $\Gamma_5$ order around 147 K.

The ordering of the Nd sublattice in $Nd_2Ru_2O_7$ occurs at 1.8 K, much lower than the ordering temperature of the Ru sublattice. Ku et al. [92] performed neutron diffraction at 0.4 K and 8 K revealing that the Nd moments adopt an AIAO configuration in this compound. The refined ordered moment at 0.4 K is 1.46 $\mu_B$, again indicative of a reduced moment.

Figure 5.16(b) illustrates the arrangement of the six nearest-neighbor Ru spins in a $\Gamma_5$ order around a Nd spin aligned along the local $z$-axis. The molecular field produced by the Ru moments on the Nd site is shown in yellow and is purely perpendicular to the local $z$-axis. As a result, since for Nd moments $g_\perp = 0$, considering such a molecular field has no effect on the Nd spins. Thus within that molecular field picture no direct effect from the Ru sublattice is expected.

Nonetheless, motivated by our findings in $Nd_2Ir_2O_7$ we followed the full temperature dependence of the Nd moments using powder diffraction measurements in order to investigate if Nd-Ru couplings do exist. In $Nd_2Ru_2O_7$, it is easier to measure the Ru and Nd moments independently, since the Ru moment is larger, less absorbent than Ir, and some of its magnetic reflections appear at positions distinct from those of Nd. This allowed us to determine the temperature dependence of the Ru sublattice as well. The experiment was performed at D1B-CRG@ILL, from 200 K down to 40 mK (base temperature), using an incident beam with wavelength $\lambda = 2.527$ Å. The sample was place in a dilution insert. It was cooled down 1.6 K using pumped $^4$He of an orange cryostat and exchange gas, and further cooled down to 40 mK using the dilytion refrigerator.

Copper contributions from the experimental setup were taken into account to separate

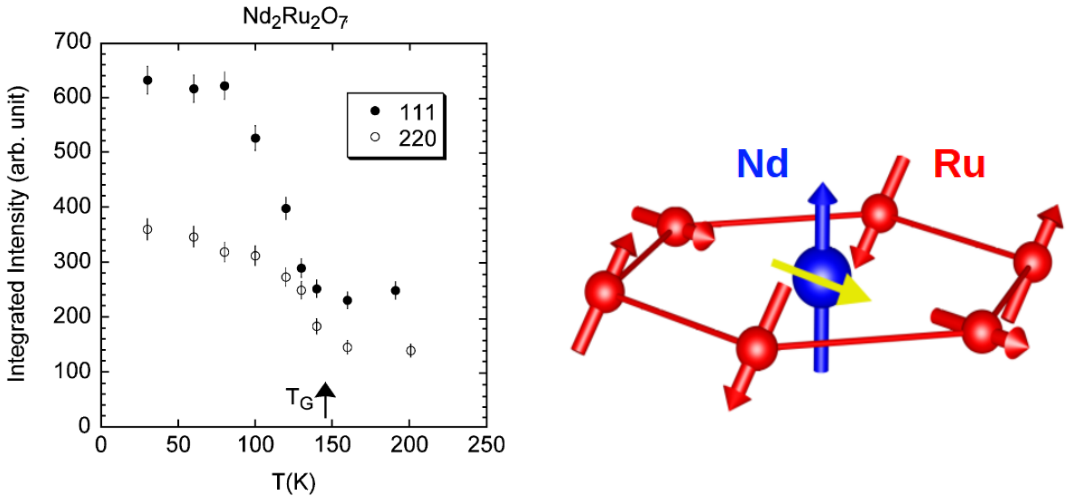


(a) (b)

Figure 5.16: (a) Temperature dependence of the integrated intensity of the (111) and (220) Bragg peaks, characteristic of Ru ordering. (b) Schematic of the six first-neighbor Ru moments surrounding a Nd moment. The molecular field produced from Ru moments is shown in yellow.

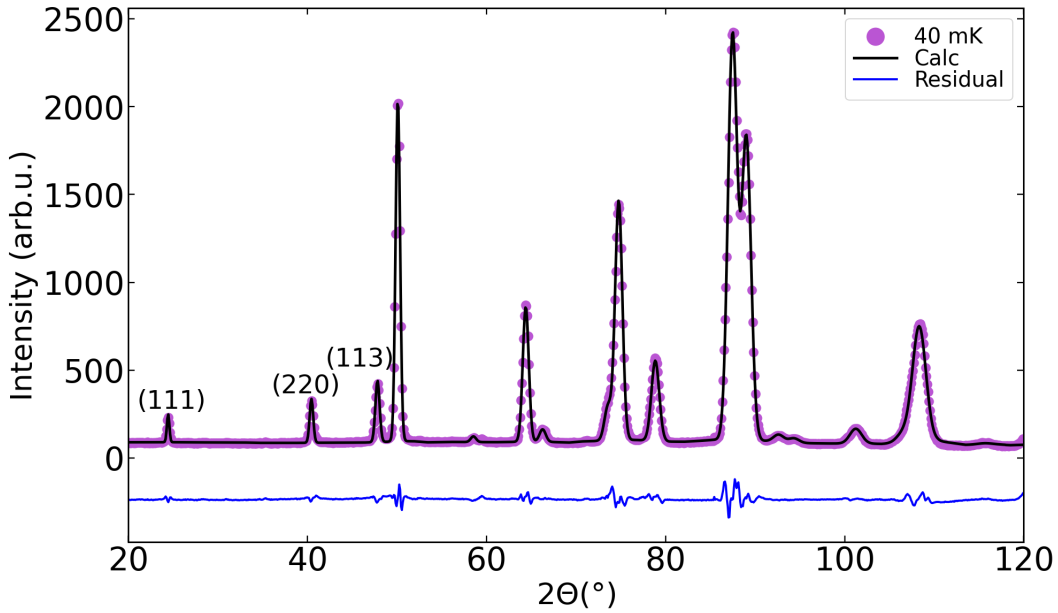


Figure 5.17: Refined diffractogram at the lowest temperature of 40 mK, over the full measured 2Θ range.

nuclear phases, which were refined at 200 K together with the nuclear structure. The refinement of the diffractograms was performed using the Rietveld method implemented in the FullProf software suite. The intermediate temperature range (170–10 K) was

refined by adding a $\Gamma_5$ magnetic phase for the Ru moments, along with the background and nuclear phases. Finally, the low-temperature range (10 K–40 mK) was refined by including the AIAO magnetic phase to extract the Nd ordered moment.

Figure 5.17 shows the refined 40 mK diffractogram over the full $2\Theta$ range accessible in the experiment. The Rietveld refinement is in good agreement with the expected pyrochlore nuclear structure, the magnetic $\Gamma_5$ phase for Ru, and the AIAO phase for Nd. The refined lattice parameter of 10.35 Å for $Nd_2Ru_2O_7$ is consistent with values reported for other compounds in the same family. The (111) and (220) reflections characteristic of the Ru order, as well as the (220) and (113) reflections characteristic of the Nd order, are highlighted in the figure.

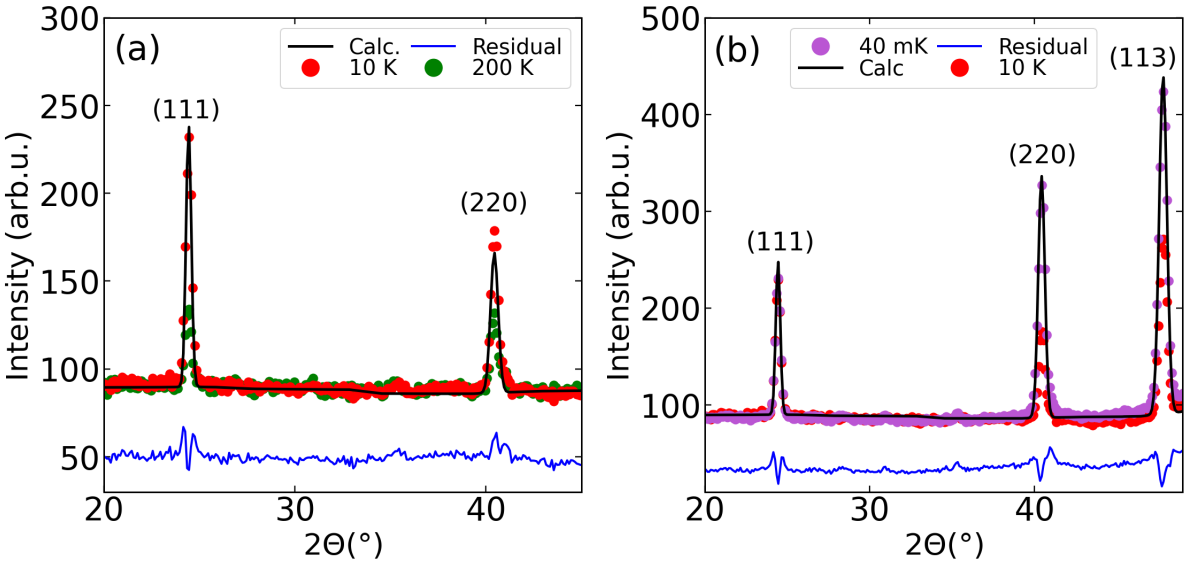


Figure 5.18: (a) Refined 10 K diffractogram (red) compared to the 200 K diffractogram (green), zoomed in the low $2\Theta$ region with the (111) and (220) reflections. (b) Refined 40 mK diffractogram (purple) compared to the 10 K diffractogram (red), zoomed in the low $2\Theta$ region with the (111) and (220) and (113) reflections.

We can take a closer look at the low $2\Theta$ region where these Bragg peaks characteristic of the magnetic orderings develop. Figure 5.18(a) shows the peaks associated to the Ru magnetic ordering above and below the order, where a clear gain in intensity is observed. Similarly, for Nd, Figure 5.18(b) displays the (111), (220), and (113) reflections at 10 K and 40 mK. As expected, the (111) reflection does not gain intensity, while the (220) and (113) peaks associated with the AIAO order increase in intensity.

The temperature dependence of both magnetic moments is shown in Figure 5.19. The Ru moments start to order at about 150 K and saturate at a value of 1 $\mu_B$ at 80 K. The Nd moments order below 1.8 K, reaching 1.65 $\mu_B$ at 40 mK. Once again, the ordered Nd moment is reduced compared to the expected value of about 2.4 $\mu_B$. The DO character of the Nd order is thus still present in $Nd_2Ru_2O_7$, even though the refined value of 1.65 $\mu_B$ is the largest within the family (typically around 1.2 $\mu_B$) [80].

Interestingly, the temperature dependence of the Nd moment also appears to be induced by the Ru moment in $Nd_2Ru_2O_7$. The increase of the moment below the transition

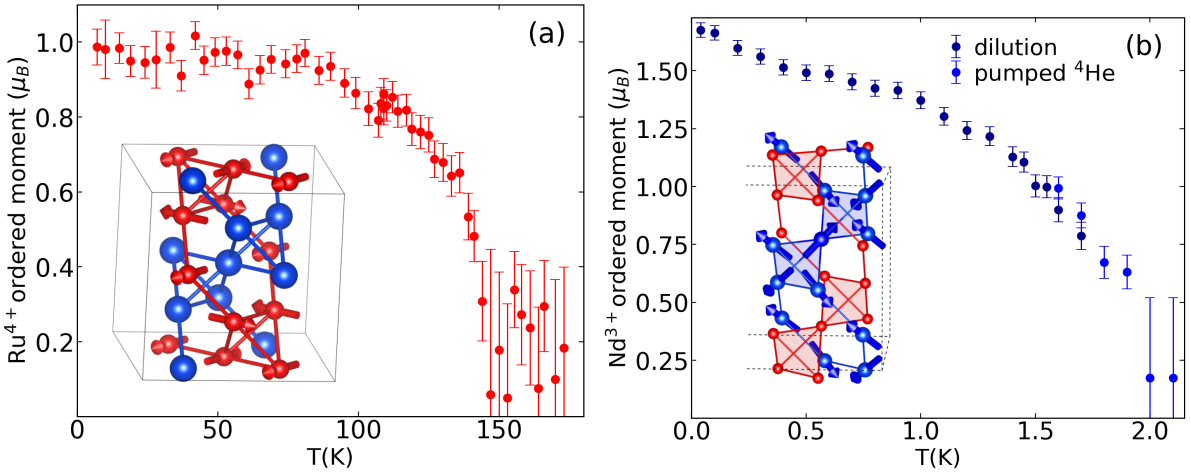


Figure 5.19: Temperature dependence of the refined Ru (a) and Nd (b) ordered moment from powder diffraction measurements in $Nd_2Ru_2O_7$. The $\Gamma_5$ order of Ru the and AIAO order of Nd are also shown in (a) and (b), respectively.

is not as sharp as in conventional magnetic ordering (as observed for Ru). Moreover, the ordering temperature is relatively high (at 1.8 K). Except for $Nd_2Ir_2O_7$, where the two sublattices are clearly coupled, $Nd_2Ru_2O_7$ is the first member of the family to display ordering above 1 K. These two observations suggest that a weak coupling between the Nd and Ru sublattices must exist.

Additionally, a small reinforcement of the Nd moment appears below 500 mK, whose origin remains unclear. Our inelastic scattering data obtained on IN5@ILL (presented later in Section 5.2.3) show that the integrated intensity of the (220) Bragg peak exhibits a similar reinforcement, confirming that this effect is not an experimental artifact. Even though this kink is not fully understood, it suggests that the dipolar component of the Nd moment is favored at the expense of the octupolar component below 500 mK.

**Bulk magnetometry**

Magnetization measurements were performed to fully characterize the $Nd_2Ru_2O_7$ state. A first set of measurements was conducted using a MPMS magnetometer to access the high and intermediate temperature ranges (1.8-300 K). For the low temperature range (100 mK-4.2 K), a second set of measurements was performed using a homemade extraction dilution magnetometer (see Section 2.6).

MvsT measured in a ZFC-FC protocol on the MPMS (Figure 5.20(b)) shows a clear bifurcation around 147 K, indicating the ordering of the $Ru^{4+}$ moments. This result is consistent with the transition observed in neutron diffraction. MvsH measurements up to 7 T (Figure 5.20(a)) were performed between 300 K and 1.8 K and show a saturation of the Nd moments of approximately 1.18 $\mu_B$ at 1.8 K. In this system, the energy scale of the interactions between the $Ru^{4+}$ ions is so large that even applied fields of 7 T hardly tilt their moments. Furthermore, the Ru moments are smaller, so their contribution to the magnetization in this temperature and field range can be be considered as negligible.

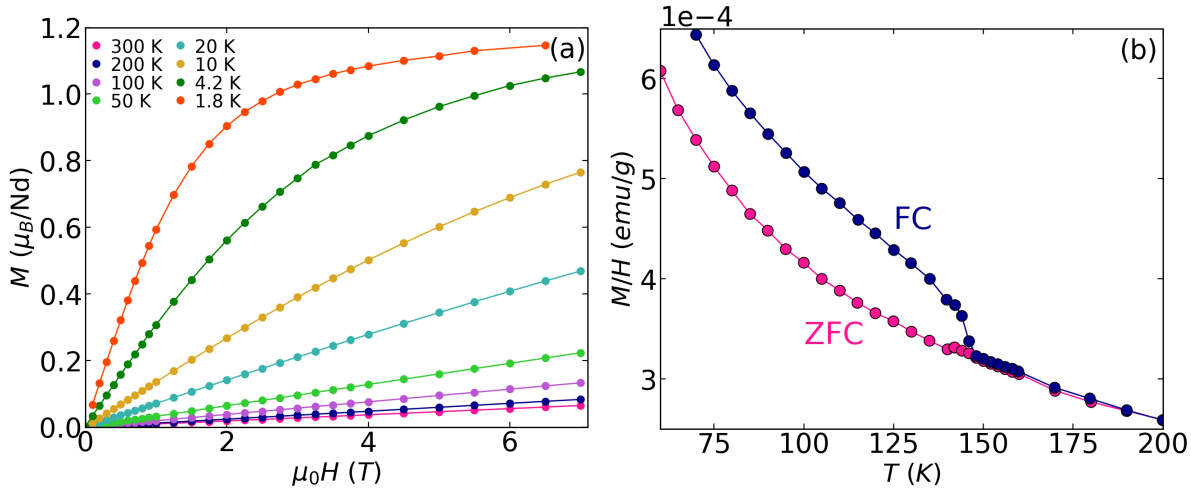


Figure 5.20: (a) $M$ versus $\mu_0 H$ measured between 1.8 K and 300 K up to 7 T in $Nd_2Ru_2O_7$ using a MPMS. (b) $M/H$ versus $T$ measured at low field (100 Oe) in a ZFC-FC procedure around the Ru ordering transition.

For a powder pyrochlore sample with Ising moments along the $\langle 111 \rangle$ directions, the saturation value is expected to be half of the total magnetic moment. Therefore, the observed saturation of 1.18 $\mu_B$/Nd is consistent with the expected $Nd^{3+}$ moment of approximately 2.4 $\mu_B$. The value of 2.36 $\mu_B$ determined for the $Nd^{3+}$ ion was used earlier in the refinement of the CEF parameters, along with the measured CEF levels (see Section 5.2.2).

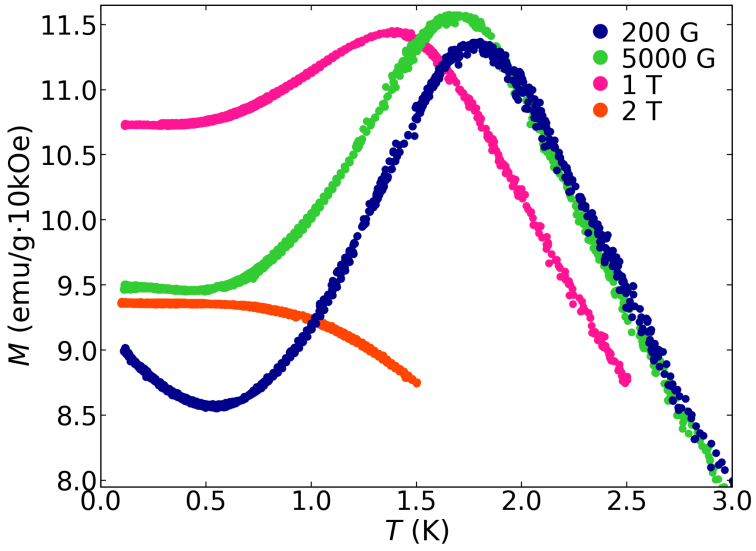


Figure 5.21: $M/H$ versus temperature for $Nd_2Ru_2O_7$ at four different fields between 200 G (0.02 T) and 2 T around the Nd transition.

The MvsT ZFC-FC measurements were also performed at low temperature around the expected $Nd^{3+}$ transition under various applied fields (Figure 5.21). They show a broad

maximum at 1.8 K, consistent with the onset of the Nd ordred moment determined from neutron diffraction. At low temperature, the ZFC-FC curves display almost no splitting, even under a small applied field of 200 Oe. The maximum in $M/H$ shifts to lower temperatures with increasing applied field and disappears below 2 T.

The shape of the MvsT curve is indicative of antiferromagnetic correlations, but the maximum is very broad, which is not expected for an antiferromagnetic transition. Ac susceptibility measurements around the transition did not reveal any feature in the imaginary part $\chi''(T)$. It contrasts with other Nd-pyrochlore compounds where the transition is well defined and shows a sharp peak $\chi''(T)$ [80]. Such a broad feature could suggest a distribution of transition temperatures arising from impurities. However, impurity effects are typically sample dependent, whereas Ku et al. [92] reported a similar broad anomaly in the specific heat at the same temperature, pointing instead to an intrinsic origin.

The absence of a well defined magnetic transition is probably due to the presence of the Ru. It is possible that due to the interactions between the Nd and Ru sublattices, the transition is transformed into a crossover, so that the observe behavior resembles a field induced phenomenon. Further studies have to be performed to understand the origin of this crossover.

MvsH measurements at low temperature were performed (Figure 5.22(a)) both above and below the broad bump at 1.8 K. The saturation at the lowest temperature of 120 mK is 1.18 $\mu_B$/Nd, consistent with the value measured at 1.8 K using the MPMS. Interestingly, the curves show a clear inflection at about 1 T when going below 1.8 K.

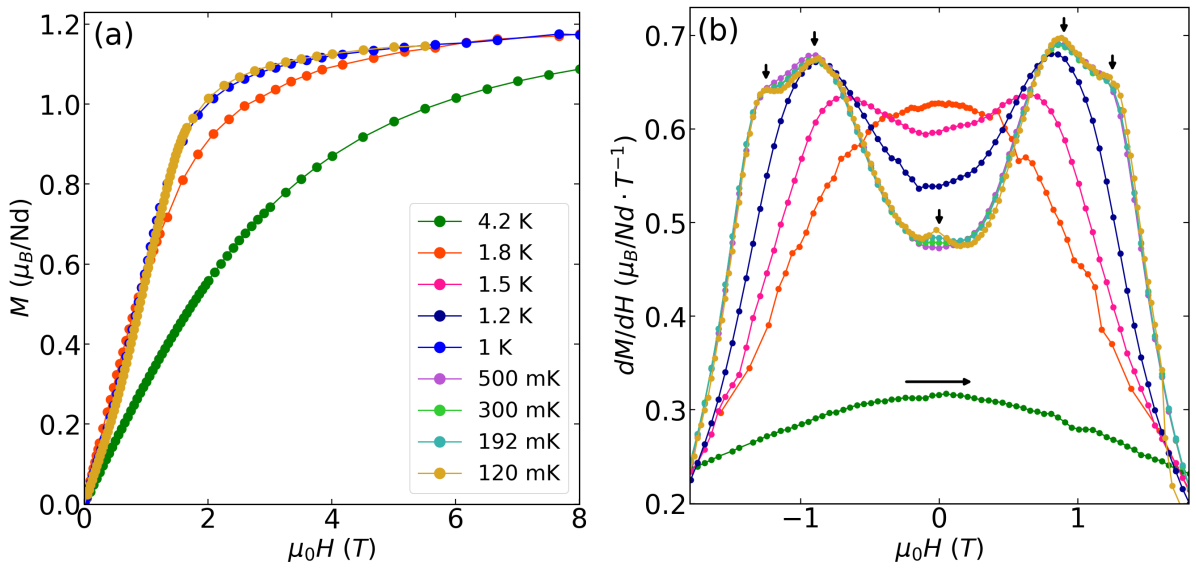


Figure 5.22: (a) $M$ versus $\mu_0 H$ measured between 120 mK and 4.2 K up to 8 T in $Nd_2Ru_2O_7$. (b) Derivative $dM/dH$ with respect to field in $Nd_2Ru_2O_7$ between 120 mK and 4.2 K. The horizontal arrow indicates that the field is ramped from negative to positive field.

Figure 5.22(b) shows the derivative of the MvsH curves (between -1.7 T and 1.7 T) obtained when sweeping the field from negative to positive values. An inflection point first appears at 1.5 K, below the Nd ordering, and evolves into two distinct inflection

points (two local maxima in the derivative) at temperatures below 1 K. These features are not perfectly symmetric with respect to positive and negative fields: there is a slight imbalance in intensity, with a stronger response for positive fields. However, their field positions of the maxima remain symmetric.

These effects arise from field-induced phase transitions between the AIAO, the 3-in/1-out, and 1-in/3-out configurations, similar to what we discussed for $Nd_2Ir_2O_7$. Unlike $Nd_2Ir_2O_7$, the measurements here were performed on a powder sample, which averages over all crystallographic directions. As a result, the cusps in the derivative are less sharp, producing two broad inflection points (instead of a single sharp feature along the [111] direction).

Additionally, another small feature appears in the derivative $dM/dH$ around 0 T between 500 mK and 120 mK. A bump grows around 0 T, which ends into a small peak at 120 mK. This feature could be indicative of a change in the magnetic properties $Nd_2Ru_2O_7$ due to competing interactions at temperatures well below the induced ordering. It may be linked to the reinforcement of the ordered Nd moment observed in neutron diffraction around 500 mK. While these phenomena occur in the same temperature range, it is not yet clear whether they are directly connected or what microscopic mechanism could be at play.

A speculative idea is that the ordering of the Nd moments are primarily induced by Nd-Ru couplings below 1.8 K, and that at sufficiently low temperature (about 500 mK), Nd–Nd interactions become relevant, partially tilting the moments back along the local $z$ axis. Given that Nd–Nd interactions in Nd-based compounds typically occur on the scale of hundreds of mK, the observed 500 mK features are consistent with this energy scale. While still speculative, these observations suggest intriguing low-temperature behavior that merits further investigation.

**Spin wave measurements**

INS spectra were measured on the TOF spectrometer IN5@ILL. A complete temperature dependence of these excitations was made, from room temperature down to dilution temperatures (50 mK). Figure 5.23 displays three INS spectra, one when the moment is fully ordered (50 mK), one around the transition (1.8 K) where the inelastic signal is fading, and one at higher temperature (10 K) when the Nd exhibits a paramagnetic behavior. In the low temperature spectra, we observe the flat mode located around 300 $\mu$eV, with the two dispersive excitations on top, previously observed in the dipolar-octupolar ordered state of Nd pyrochlores.

Compared to $Nd_2Ir_2O_7$, $Nd_2Ru_2O_7$ is less absorbent so despite measurements carried out on a powder sample, the magnetic excitations are very well defined. A total of thirteen temperatures were measured between 50 mK and 10 K. $Q$-cuts integrating over 1.45-1.75 $\mathrm{\AA}^{-1}$ (Figure 5.24(a)), show the full temperature dependence of the excitations. The flat mode and the dispersive branches appears at low temperature. When increasing the temperature, the gap decreases and the excitations intensity decreases. The dispersive branches of Figure 5.23 are seen in the cuts as two peaks: one at 0.4 meV and the other at 0.5 meV (which corresponds to the top of the branches).

In $Nd_2Ir_2O_7$ we directly extracted the energy of the flat mode by looking at the position of the peak. Here in $Nd_2Ru_2O_7$, there are three well defined peaks so data were

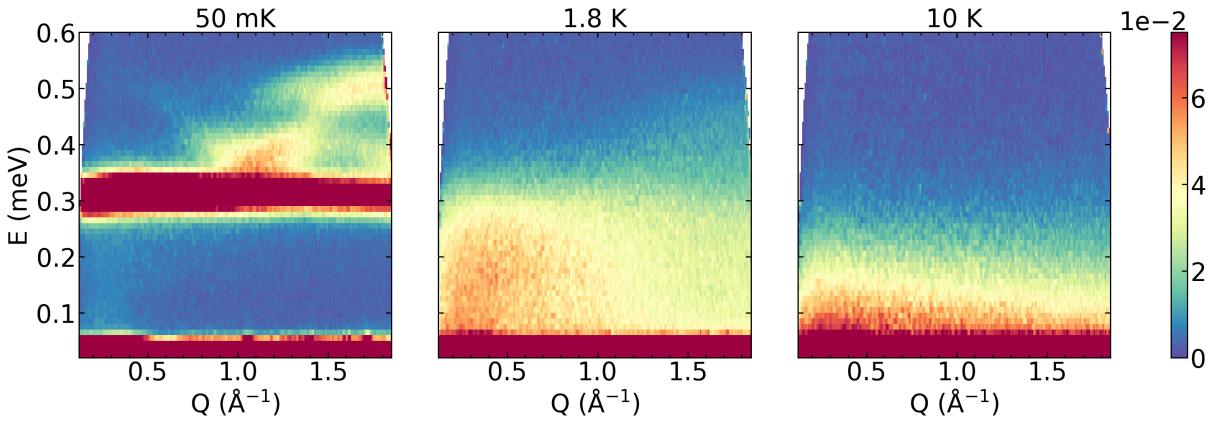


Figure 5.23: Intensity of INS spectra depending on the energy $E$ (in meV) and the momentum transfer $Q$ (in Å$^{-1}$) measured at 50 mK, 1.8 K and 10 K with an incident beam energy of 6 Å on powder $Nd_2Ir_2O_7$.

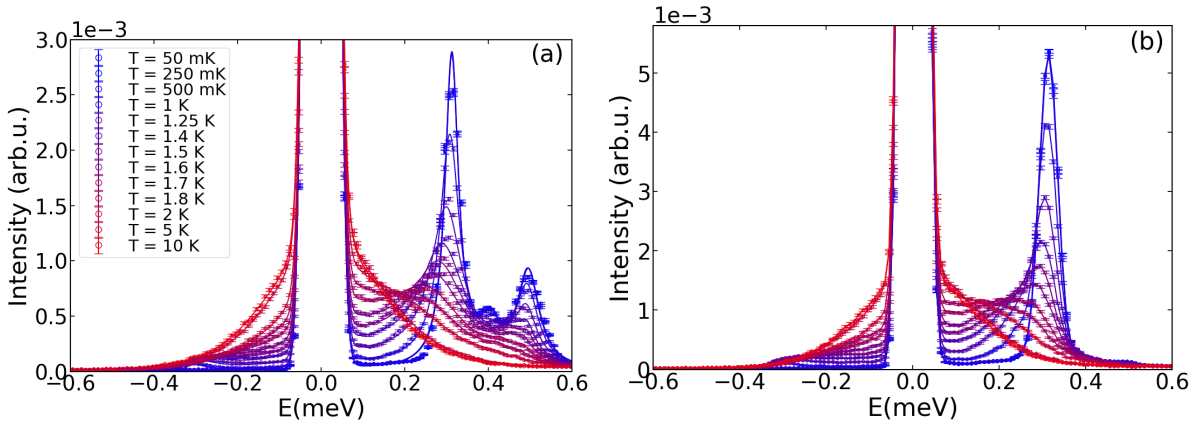


Figure 5.24: (a) Constant $Q$-cuts of INS spectra integrated between 1.45 Å$^{-1}$ and 1.75 Å$^{-1}$ with an incident wavelength of 6 Å at various temperature between 50 mK and 10 K. Lines are fits using the Equation 5.2.4 as a model. (b) Constant $Q$-cuts of INS spectra integrated between 0.4 Å$^{-1}$ and 0.7 Å$^{-1}$ with only the flat band. Lines are guides to the eye.

fitted in order to extract the temperature dependence of these characteristic energies using the following model:

$$S(E) = b + I_c(E) + F(E,T) \times \left[S_0(E) + S_1(E) + S_2(E) + S_3(E)\right] \tag{5.20}$$

Here $b$ is a flat background, $I_c(E)$ is a Gaussian function centered at zero energy to account for the elastic Bragg and incoherent scattering. $F(E,T) = 1 + n(E,T)$ is the detailed balance factor to reproduce positive and negative energies (with $n = (\exp(E/k_BT) - 1)^{-1}$ the Bose-Einstein distribution). The four $S_i(E)$ are Lorentzian profiles centered at finite energy, which represent the flat band, the two dispersive branches and the quasi-elastic

signal.

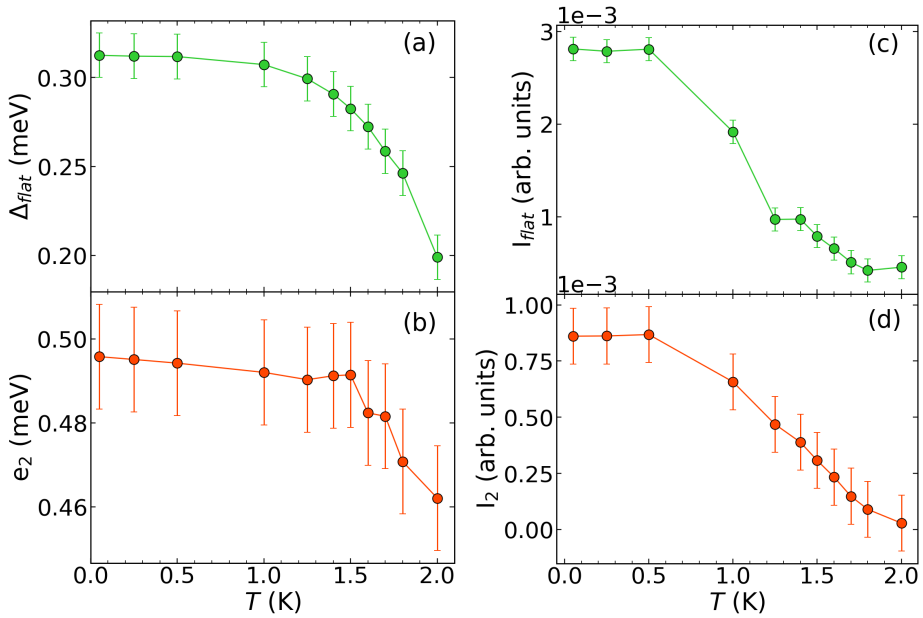


Figure 5.25: (a)-(c) Temperature dependence of the energy gap $\Delta_{flat}$ and the intensity $I_{flat}$ of the flat band excitation (green). (b)-(d) Temperature dependence of the maximum of the dispersion $e_2$ and its intensity $I_2$ (orange). Lines are guides to the eye.

Figures 5.25(a)-(b) shows the energy of the flat band and the top of the second dispersive branch vs temperature. The corresponding intensities are shown in (c) and (d). The temperature dependence of the two energies is similar and decreases sharply close to the crossover temperature, while the intensities on the other hand decrease more smoothly. Above 2 K the flat mode and the dispersive excitations cannot be resolved as they are masked by the quasi-elastic signal.

**Analysis**

The analysis of spin wave excitations in $Nd_2Ru_2O_7$ is not achieved yet. We began with an initial test considering only the Nd–Nd interactions to check whether they could account for the observed excitations without taking into account the Ru role. Unlike in $Nd_2Ir_2O_7$, the role of Ru is less obvious here, as the Nd ordering occurs at a much lower temperature. Indeed, the Ru sublattice exhibits a $\Gamma_5$ order, which lies perpendicular to the local $z$ axis of the $Nd^{3+}$ AIAO order, making any Ru–Nd interplay less evident.

In $Nd_2Ru_2O_7$, the excitations are better resolved in energy, making it possible to deduced three characteristics energies from the excitations spectrum. Similarly to $Nd_2Ir_2O_7$, we obtain the gap $\Delta_{flat}$ and the top of the dispersive $e_2$ located at $Q = (220), (113)$ but in addition we can extract $e_1$ the dispersion at the Brillion zone boundaries $Q = (110), (112), (221)$. Thanks to these characteristic energies it is possible to estimate the Nd–Nd coupling parameters, with the following set of equations [83, 148]:

$$\begin{aligned}\Delta_{flat} &= \sqrt{\left(3|\tilde{J}_z| - \tilde{J}_x\right)\left(3|\tilde{J}_z| - \tilde{J}_y\right)},\\ e_1 &= \sqrt{\left(3|\tilde{J}_z| + \tilde{J}_x\right)\left(3|\tilde{J}_z| + \tilde{J}_y\right)},\\ e_2 &= 3\sqrt{\left(|\tilde{J}_z| + \tilde{J}_x\right)\left(|\tilde{J}_z| + \tilde{J}_y\right)}.\end{aligned} \tag{5.21}$$

Using the values obtained from the spectra at the lowest temperature (($\Delta_{flat}$, $e_1$, $e_2$)=(0.31, 0.41, 0.51) meV), we obtain the following set of Nd-Nd interaction parameters: $(\tilde{J}_x, \tilde{J}_y, \tilde{J}_z) = (0.58, 0.58, -1.39)$ K with an ordered moment of $1.6\mu_B$. It gives $(J_x, J_y, J_z, J_{xz})$=$(-0.51, 0.58, -0.295, 0.98)$ K, using the transformation between the $\tilde{J}$ and $J$ parameters is detailed in Section 1.4. The calculated spin wave spectrum based on these parameters is shown in Figure 5.26, together with the measured spectrum at 50 mK. The agreement is very good, even without including any Nd–Ru interactions.

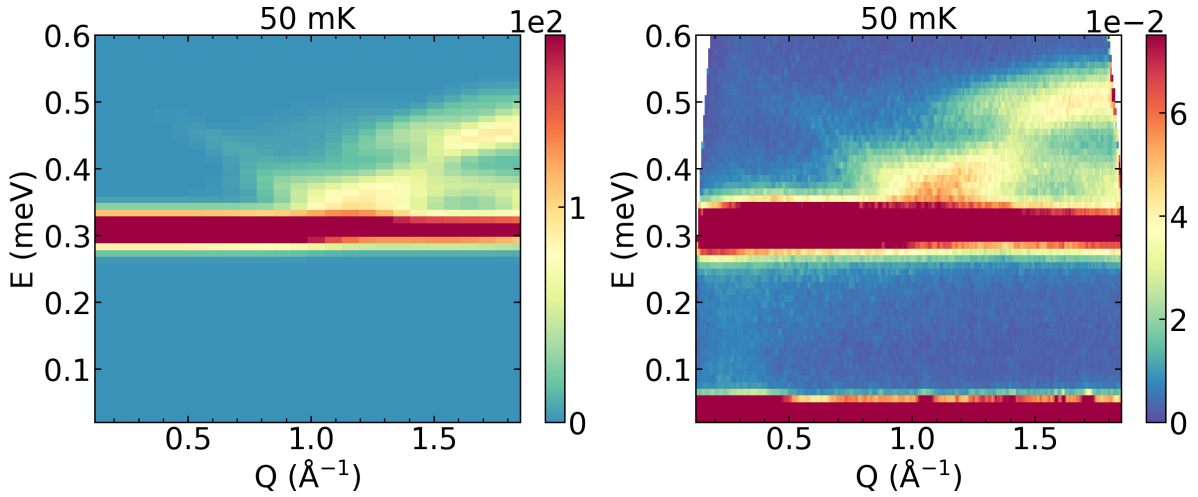


Figure 5.26: Intensity of INS spectra calculated (left) and measured (right) at 50 mK for $Nd_2Ru_2O_7$. Calculations were performed only taking into the Nd-Nd interaction with the set of parameters: ($J_x$, $J_y$, $J_z$, $J_{xz}$)=$(-0.51, 0.58, -0.295, 0.98)$ K.

A comparison between the calculated and measured ordered moments (Figure 5.27(a)) confirms that this first test captures the main features of the neutron data, though some discrepancies remain. Specifically, the calculations cannot explain the small reinforcement observed below 500 mK. Notably, in this parameter set, $J_y$ is relatively large compared to other Nd-based compounds, where it is usually close to zero (as in $Nd_2Ir_2O_7$). It is possible that $J_y$ should actually be small in $Nd_2Ru_2O_7$ as well, but that it mimics the influence of the Ru lattice when considering the Nd-Nd Hamiltonian only. A natural next step is to explicitly include the Nd-Ru interactions while reducing $J_y$, to verify whether this interpretation holds.

From experiments, it is clear that the Nd–Ru interplay must play a role, particularly in explaining the broad transitions observed in our MvsT and in the specific heat measurements [92]. When including the Nd–Ru interaction, we adopt the same strategy used for $Nd_2Ir_2O_7$. Since the Ru sublattice orders with a $\Gamma_5$ symmetry (easy-plane ordering),

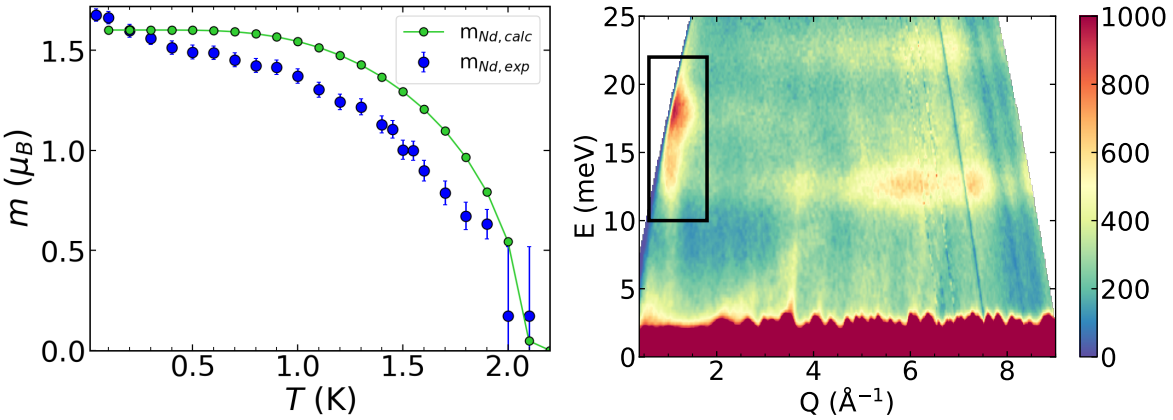


Figure 5.27: Left: Calculated (green) and measured (blue) ordered moment $m_{ord}(T)$ of Nd between 0 and 2 K. Calculations were performed only taking into the Nd-Nd interaction with the set of parameters: ($J_x$, $J_y$, $J_z$, $J_{xz}$)=$(-0.51, 0.58, -0.295, 0.98)$ K. Right: Intensity of INS spectrum measured in powder $Y_2Ru_2O_7$ at 2 K at PANTHER@ILL.

we set $\mathscr{J}_{\pm} = 51$ K for the Ru–Ru interactions, which reproduces the transition temperature of 147 K. From our preliminary tests, only the $K_{zz}$ and $K_{xz}$ components of the Nd–Ru coupling appear to have a meaningful effect. We have not yet converged to a definitive set of parameters, so further results including the new Nd-Ru interaction for $Nd_2Ru_2O_7$ cannot be shown.

Recently, while preparing this manuscript, Nathan Bujault (a PhD student in the group) performed measurements at PANTHER@ILL on $Y_2Ru_2O_7$. Since $Y^{3+}$ is non-magnetic, this allowed direct observation of the Ru spin waves in the pyrochlore structure. The signal appears at small $Q$ values (Figure 5.27 (right), around 1 $Å^{-1}$ at 2 K).

These new spin wave data will enable independent refinement of the Ru–Ru interaction parameters. It is a piece of information we currently lack for $Nd_2Ir_2O_7$, which has been found to be limiting. This will be highly valuable for refining the full Hamiltonian of $Nd_2Ru_2O_7$. More generally, such measurements will provide critical information to determine the coupling parameters in other pyrochlore ruthenates that we may investigate in the future.

## 5.3 Discussion and conclusion

The objective of this chapter was to understand how additional couplings arising from the magnetic metal sublattice can impact the established physics of the Nd sublattice. To this end, we determined a general Hamiltonian for the inter-sublattice coupling between Nd and $M$ ($M$ = Ir, Ru) using symmetry analysis. The peculiarity of this interaction is that it couples dipolar (Ir, Ru) and DO (Nd) ions. Symmetry constraints reveal that a total of 5 coupling parameters constitute the interaction, with allowed coupling between the dipolar components of the metal moments and the octupolar components of the Nd moments.

To estimate these coupling terms, we carried out extensive measurements of the

$Nd_2Ir_2O_7$ and $Nd_2Ru_2O_7$ compounds. The metal ions order into two distinct magnetic structures: AIAO in $Nd_2Ir_2O_7$ and easy plane antiferromagnetic $\Gamma_5$ in $Nd_2Ru_2O_7$, occurring at very different temperature scales (33 K and 147 K, respectively).

Nonetheless, in both compounds the $Nd^{3+}$ sublattice exhibits an AIAO ordering with a reduced ordered moment, reminiscent of the DO AIAO order in $Nd_2Zr_2O_7$. The reduced ordered moment values are 1.17 $\mu_B$ for $Nd_2Ir_2O_7$ and 1.65 $\mu_B$ for $Nd_2Ru_2O_7$. The measured temperature dependence of these Nd ordered moments suggests that the $Nd^{3+}$ ions experience inter-sublattice couplings. Due to the AIAO Ir ordering, these couplings are stronger in $Nd_2Ir_2O_7$, inducing the $Nd^{3+}$ order at the onset of Ir ordering. Inter-sublattice couplings are also definitely present in $Nd_2Ru_2O_7$, as further confirmed by thermodynamic measurements, including magnetization and specific heat [92].

Importantly, the usual molecular field approach applied to iridate systems is not valid here. Such an effective coupling would fully realign the Nd moments along the local $z$ direction in the Ir case, which is incompatible with the reduced ordered moments observed experimentally. In the case of $Nd_2Ru_2O_7$, a molecular field approach would also fails since the Ru molecular field is perpendicular to the Nd moments.

Through the analysis of spin wave measurements, we used our new model to numerically optimize the inter-sublattice couplings. This approach was successful in $Nd_2Ir_2O_7$, yielding a set of parameters that reproduce experiments well. A large inter-sublattice coupling $K_{xz}$ of 4 K is required, further demonstrating the strong influence of Ir moments. This key interaction couples the local $z$ component of the dipolar Ir moment to the local $x$ octupolar component of the Nd DO moment, demonstrating that dipolar $\boldsymbol{M}$ and octupolar Nd components are interacting. Ongoing investigations are being carried out, as the model does not yet reproduce the critical field measured in single crystal studies [93]. We expect that improvements can be made by incorporating more accurate Ir–Ir coupling parameters. A first step would be to used parameters already determined in the literature using other techniques [136].

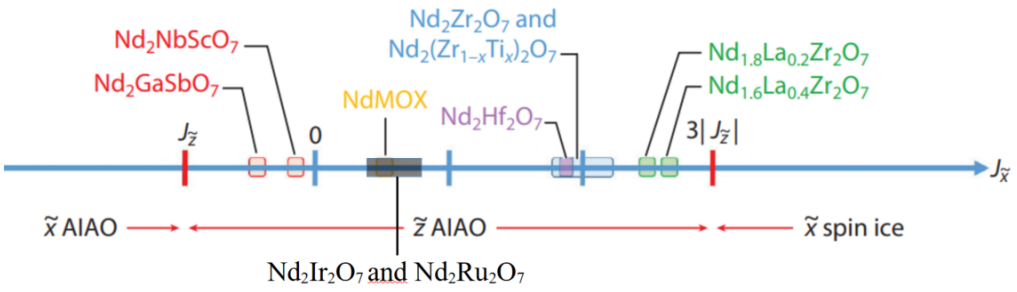


Figure 5.28: Phase diagram of the XYZ dipole-octupole model for $\tilde{J}_z < 0$ and $\tilde{J}_y = 0$, that describes well Nd-based pyrochlores. The positions of our two compounds, $Nd_2Ir_2O_7$ and $Nd_2Ru_2O_7$, together with several Nd-based compounds are included. Figure adapted from Ref. [80].

For $Nd_2Ru_2O_7$, we were able to reproduce inelastic scattering neutron measurements quantitatively using only Nd–Nd interactions.The Nd-Nd Hamiltonian nevertheless cannot reproduces other experimental observations. Work is in progress to determine a set of parameters that includes Nd–Ru interactions. Thanks to new measurements of the

Ru–Ru spin waves in $Y_2Ru_2O_7$, we will be able to independently estimate the Ru–Ru interaction parameters, enabling a complete modeling of the Hamiltonian. In the future, low-temperature magnetization measurements on $Nd_2Ru_2O_7$ single crystals could be interesting to better characterize field-induced effects which can help the determination of the coupling parameters.

Using our best parameter sets for $Nd_2Ir_2O_7$ and $Nd_2Ru_2O_7$, we can estimate their positions on the phase diagram of Nd-based compounds. For $Nd_2Ir_2O_7$, the set ($J_x = 0.8$ K, $J_{xz} = 2.4$ K, $J_z = -1.36$ K, $K_{xz} = 4$ K, $K_{zz} = 0.4$ K) leads to $\tilde{J}_x = 2.35$ K and $\tilde{J}_z = -2.91$ K. For $Nd_2Ru_2O_7$, using only the Nd–Nd interaction we find ($J_x = -0.51$ K, $J_y = 0.58$ K, $J_z = -0.295$ K, $J_{xz} = 0.98$ K), giving $\tilde{J}_x = 0.58$ K and $\tilde{J}_z = -1.39$ K. The ratios $\tilde{J}_x/|\tilde{J}_z|$ are estimated as 0.8 and 0.4 for $Nd_2Ir_2O_7$ and $Nd_2Ru_2O_7$, respectively. As shown in Figure 5.28, both compounds are located near NdMox (with ratio 0.53), deep in the region of the DO AIAO order.

In the Nd-based pyrochlore family, it has been observed that substituting on the metallic Zr site of the parent compound $Nd_2Zr_2O_7$ leads to a decrease in the lattice parameter. The ratio $\tilde{J}_x/|\tilde{J}_z|$ follows this trend, decreasing as the lattice parameter becomes smaller. The NdMox compounds have a lattice parameter $a = 10.56$ Å, while $Nd_2Ir_2O_7$ and $Nd_2Ru_2O_7$ exhibit smaller values of 10.37 Å and 10.35 Å, respectively. These values are closer to those reported for the compound with the lowest $\tilde{J}_x/|\tilde{J}_z|$ found: $Nd_2GaSbO_7$ [149]. This suggests that coupling with the metal site $M$ may reduce $\tilde{J}_x/|\tilde{J}_z|$ in a manner similar to structural disorder on the $M$ site, but without requiring any actual disorder.

# General conclusion

During this thesis, we investigated the dynamic excitations of two families of pyrochlore compounds. In the spin-ice systems $Dy_2Ti_2O_7$ and $Ho_2Ti_2O_7$, we focused on the slow dynamics of magnetic monopoles, while in $Nd_2Ru_2O_7$ and $Nd_2Ir_2O_7$ we studied the dipolar-octupolar Nd spin waves under the influence of magnetic metal moments. Measurements were performed using a wide range of experimental techniques, each adapted to the specific system in order to reveal the properties of these excitations.

In particular, instrumental investigations were carried out for improving our sensitive noise magnetometer technique, employed to probe the fluctuation dissipation relation (FDR) at very low temperatures. This work included optimizing detection through improvements in magnetic shielding and tests on gradiometer geometries. A new noise magnetometer apparatus, designed from scratch to incorporate these improvements, was developed. Although implementation was delayed due to leak issues, all parts were fabricated, and an initial series of cryogenic tests was performed. These tests revealed limitations in the current cooling power of the apparatus, arising from the central axis mounting and heat conduction along the SQUID cable. Both issues can be corrected, and further development on this new noise magnetometer is ongoing which will enable measurements at lower temperatures with enhanced sensitivity.

Nonetheless, our original noise magnetometer allowed us to investigate quantitatively the FDR, unraveling the properties of the dynamical processes in classical spin ice. Using this technique we evidenced three characteristic dynamical regions: (i) the high temperature region, where the system is trivially in equilibrium, and the FDR is obeyed; (ii) the intermediate region, where ergodicity breaking is observed in the magnetization, but where we find that the FDR remains obeyed indicating that local equilibrium is preserved; (iii) the low temperature region, where the FDR is violated at low frequency, typically below 0.1 Hz, indicating that the system enters an out-of-equilibrium state. In the low temperature regime, we also observe new low intensity relaxation processes that exhibits aging properties. They are emergent short timescale processes appearing in the temperature range where deviations of the FDR are reported and may corresponds to monopoles confined in short loops, while long timescales may correspond to the monopole deconfinement time.

Finally, as we measured different isotopic $Dy_2Ti_2O_7$ samples, we considered the potential influence of rare-earth isotopes on spin ice dynamics. From our observations, along with the numerous measurements reported in the literature we did not identified a clear trend regarding the influence of isotopes on the monopole dynamics. It is due to the

large number of parameters (including isotope composition, oxygen vacancies, single ion properties, local magnetic fields, monopole correlations, etc.) that are relevant and disentangling these contributions can be tricky. Overall, we found pronounced differences in the dynamics of both the equilibrium and freezing regimes across the compounds investigated and the literature. This emphasizes the richness of the classical spin ice monopoles dynamics, and many effects still needs to be addressed both experimentally and theoretically.

The second part of the thesis was devoted to the two Nd-based compounds $Nd_2Ru_2O_7$ and $Nd_2Ir_2O_7$ and unraveling the subtle magnetic interplay between the rare earth ($Nd^{3+}$) and the metal ($\boldsymbol{M}^{4+}$) ions. We performed a symmetry analysis which identified the most general form of the Nd-$\boldsymbol{M}$ Hamiltonian consistent with the symmetry properties of the $Nd^{3+}$ low energy DO doublet in the pyrochlore lattice. This model successfully described our $Nd_2Ir_2O_7$ results, using spin wave and ordered moment calculations. In this compound, we have found that couplings between the magnetic metal $z$ dipolar component and the Nd $x$ octupolar component are essential to describe the characteristic energies of the spin wave excitations. In $Nd_2Ru_2O_7$, the spin waves can be described by a pure Nd-Nd interaction, suggesting the role of these DO inter-sublattice couplings is not as straighforward. However, bulk probes (magnetization and specific heat [92]) show a broad anomaly at the onset of Nd ordering, suggesting a temperature crossover rather than a sharp phase transition. This phenomenology points toward induced ordering, as it was observed in $Nd_2Ir_2O_7$. Work is still under development on this project to further refine the models. This study also opens perspectives beyond Nd-based pyrochlores. Indeed, if Ce-based pyrochlores, which are proposed to stabilize quantum spin liquid states, could be synthesized with magnetic metal ions in the future, novel phases may be discovered, and our Hamiltonian could be applied to explore their properties.

# Appendix

**Atomic positions and local bases**

The coordinate system used for the eight atomic positions contained within the rhombohedral cell is given by:

$$\begin{aligned} \mathrm{Ru}_1 &= \frac{a}{4}(1,1,0) \quad & \mathrm{Nd}_5 &= \frac{a}{4}(1,1,2) \\ \mathrm{Ru}_2 &= \frac{a}{4}(0,0,0) \quad & \mathrm{Nd}_6 &= \frac{a}{4}(2,2,2) \\ \mathrm{Ru}_3 &= \frac{a}{4}(0,1,1) \quad & \mathrm{Nd}_7 &= \frac{a}{4}(2,1,1) \\ \mathrm{Ru}_4 &= \frac{a}{4}(1,0,1) \quad & \mathrm{Nd}_8 &= \frac{a}{4}(1,2,1) \end{aligned} \tag{5.22}$$

where $a$ is the lattice parameter of the pyrochlore fcc cell, with the origin defined at coordinates $\frac{a}{8}(-1,-1,-1)$.

The corresponding vectors that constitute the local bases $(\hat{a}_i, \hat{b}_i, \hat{e}_i)$ of each moment are:

$$\begin{aligned} \hat{a}_1 = \hat{a}_5 &= \frac{1}{\sqrt{6}}(-1,-1,-2) \quad & \hat{e}_1 = \hat{e}_5 &= \frac{1}{\sqrt{3}}(1,1,-1) \\ \hat{a}_2 = \hat{a}_6 &= \frac{1}{\sqrt{6}}(1,1,-2) \quad & \hat{e}_2 = \hat{e}_6 &= \frac{1}{\sqrt{3}}(-1,-1,-1) \\ \hat{a}_3 = \hat{a}_7 &= \frac{1}{\sqrt{6}}(1,-1,2) \quad & \hat{e}_3 = \hat{e}_7 &= \frac{1}{\sqrt{3}}(-1,1,1) \\ \hat{a}_4 = \hat{a}_8 &= \frac{1}{\sqrt{6}}(-1,1,2) \quad & \hat{e}_4 = \hat{e}_8 &= \frac{1}{\sqrt{3}}(1,-1,1) \end{aligned} \tag{5.23}$$

where $\hat{b}_i = \hat{e}_i \times \hat{a}_i$.

# Bibliography


[1] G. H. Wannier, "Antiferromagnetism. The triangular Ising net", *Phys. Rev.* **79**, 357–364 (1950).

[2] P. W. Anderson, "Ordering and Antiferromagnetism in Ferrites", *Phys. Rev.* **102**, 1008–1013 (1956).

[3] G. Toulouse, "Theory of the frustration effect in spin glasses. I." *Commun. Phys*, **2**, 115–119 (1977).

[4] J. Villain, "Two-level systems in a spin-glass model I. General formalism and two-dimensional model", *J. Phys. C: Sol. State Phys.* **10**, 4793–4803 (1977).

[5] J. Vannimenus and G. Toulouse, "Theory of the frustration effect II. Ising spins on a square lattice", *J. Phys. C: Sol. State Phys.* **10**, L537–L542 (1977).

[6] D. Loison and P. Simon, "Monte Carlo analysis of the phase transitions in the two-dimensional J1-J2 XY model", *Phys. Rev. B*, **61**, 6114–6125 (2000).

[7] A. Kitaev, "Anyons in an exactly solved model and beyond", *Ann. Phys.* **321**, 2–111 (2006).

[8] M. Léger. "Fragmentation quantique dans les systèmes magnétiques frustrés". PhD thesis. Université Grenoble Alpes, 2020.

[9] L. Pauling, "The Structure and Entropy of Ice and of Other Crystals with Some Randomness of Atomic Arrangement", *J. Amer. Chem. Soc.* **57**, 2680–2684 (1935).

[10] M. J. Harris, S. T. Bramwell, D. F. McMorrow, T. Zeiske, and K. W. Godfrey, "Geometrical Frustration in the Ferromagnetic Pyrochlore $Ho_2Ti_2O_7$", *Phys. Rev. Lett.* **79**, 2554–2557 (1997).

[11] R. Moessner, "Relief and generation of frustration in pyrochlore magnets by single-ion anisotropy", *Phys. Rev. B.* **57**, R5587–R5589 (1998).

[12] S. T. Bramwell and M. J. Harris, "Frustration in Ising-type spin models on the pyrochlore lattice", *J. Phys. Condens. Matter*, **10**, L215–L220 (1998).

[13] R. Valentin. "Dynamique hors équilibre des monopôles magnétiques dans la glace de spin". fr. PhD thesis. ENS Lyon, 2018.

[14] A. P. Ramirez, A. Hayashi, R. J. Cava, R. Siddharthan, and B. S. Shastry, "Zero-point entropy in 'spin ice'", *Nature*, **399**, 333–335 (1999).

[15] S. V. Isakov, K. Gregor, R. Moessner, and S. L. Sondhi, "Dipolar Spin Correlations in Classical Pyrochlore Magnets", *Phys. Rev. Lett.* **93**, 167204 (2004).

[16] C. L. Henley, "Power-law spin correlations in pyrochlore antiferromagnets", *Phys. Rev. B*, **71**, 014424 (2005).

[17] C. L Henley, "The "Coulomb Phase" in frustrated systems", *Ann. Rev. Condens. Matter Phys.* **1**, 179–210 (2010).

[18] T. Fennell, P. P. Deen, A. R. Wildes, K. Schmalzl, D. Prabhakaran, A. T. Boothroyd, R. J. Aldus, D. F. McMorrow, and S. T. Bramwell, "Magnetic Coulomb Phase in the Spin Ice $Ho_2Ti_2O_7$", *Science*, **326**, 415–417 (2009).

[19] I. A. Ryzhkin, "Magnetic relaxation in rare-earth oxide pyrochlores", *J. Exp. Theor. Phys.* **101**, 481–486 (2005).

[20] C. Castelnovo, R. Moessner, and S. L. Sondhi, "Magnetic monopoles in spin ice", *Nature*, **451**, 42–45 (2008).

[21] J. S. Gardner, M. J. P. Gingras, and J. E. Greedan, "Magnetic pyrochlore oxides", *Rev. Mod. Phys.* **82**, 53–107 (2010).

[22] H. Guo, C. Ritter, and A. C. Komarek, "Direct determination of the spin structure of $Nd_2Ir_2O_7$ by means of neutron diffraction", *Phys. Rev. B*, **94**, 161102 (2016).

[23] V. Cathelin, E. Lefrançois, J. Robert, P. C. Guruciaga, C. Paulsen, D. Prabhakaran, P. Lejay, F. Damay, J. Ollivier, B. Fåk, L. C. Chapon, R. Ballou, V. Simonet, P. C. W. Holdsworth, and E. Lhotel, "Fragmented monopole crystal, dimer entropy, and Coulomb interactions in $Dy_2Ir_2O_7$", *Phys. Rev. R.* **2** (2020).

[24] E. Lefrançois, V. Simonet, R. Ballou, E. Lhotel, A. Hadj-Azzem, S. Kodjikian, P. Lejay, P. Manuel, D. Khalyavin, and L. C. Chapon, "Anisotropy-Tuned Magnetic Order in Pyrochlore Iridates", *Phys. Rev. Lett.* **114**, 247202 (2015).

[25] M. Ito, Y. Yasui, M. Kanada, H. Harashina, S. Yoshii, K. Murata, M. Sato, H. Okumura, and K. Kakurai, "Nature of spin freezing transition of geometrically frustrated pyrochlore system $R_2Ru_2O_7$ (R=rare earth elements and Y)", *J. Phys. Chem. Sol.* **62**, 337–341 (2001).

[26] J. G. Rau and M. J. P. Gingras, "Frustrated Quantum Rare-Earth Pyrochlores", *Ann. Rev. Condens. Matter Phys.* **10**, 357–386 (2019).

[27] F. Hund, "Zur deutung verwickelter spektren, insbesondere der elemente scandium bis nickel", *Zeitschrift für Physik*, **33**, 345–371 (1925).

[28] K. Matsuhira, Y. Hinatsu, K. Tenya, H. Amitsuka, and T. Sakakibara, "Low-temperature magnetic properties of pyrochlore stannates", *J. Phys. Soc. Jap.* **71**, 1576–1582 (2002).

[29] M. Udagawa and L. Jaubert. *Spin Ice*. Springer Series in Solid-State Sciences. 2021.

[30] R. Siddharthan, B. S. Shastry, A. P. Ramirez, A. Hayashi, R. J. Cava, and S. Rosenkranz, "Ising Pyrochlore Magnets: Low-Temperature Properties, "Ice Rules" and Beyond", *Phys. Rev. Lett.* **83**, 1854–1857 (1999).

[31] B. C. Den Hertog and M. J. P. Gingras, "Dipolar Interactions and Origin of Spin Ice in Ising Pyrochlore Magnets", *Phys. Rev. Lett.* **84**, 3430–3433 (2000).

[32] Roger G Melko and Michel J P Gingras, "Monte Carlo studies of the dipolar spin ice model", *J. Phys.: Condens. Matter*, **16**, R1277 (2004).

[33] S. T. Bramwell, M. J. Harris, B. C. Den Hertog, M. J. P. Gingras, J. S. Gardner, D. F. McMorrow, A. R. Wildes, A. L. Cornelius, J. D. M. Champion, R. G. Melko, and T. Fennell, "Spin Correlations in $Ho_2Ti_2O_7$: A Dipolar Spin Ice System", *Phys. Rev. Lett.* **87** (2001).

[34] M. J. P. Gingras and B. C. den Hertog, "Origin of spin-ice behavior in Ising pyrochlore magnets with long-range dipole interactions: an insight from mean-field theory", *Canadian J. Phys.* **79**, 1339–1351 (2001).

[35] S. V. Isakov, R. Moessner, and S. L. Sondhi, "Why spin ice obeys the ice rules", *Phys. Rev. Lett.* **95**, 217201 (2005).

[36] R. G. Melko, B. C. Den Hertog, and M. J. P. Gingras, "Long-Range Order at Low Temperatures in Dipolar Spin Ice", *Phys. Rev. Lett.* **87**, 067203 (2001).

[37] D. Pomaranski, L. R. Yaraskavitch, S. Meng, K. A. Ross, H. M. L. Noad, H. A. Dabkowska, B. D. Gaulin, and J. B. Kycia, "Absence of Pauling's residual entropy in thermally equilibrated $Dy_2Ti_2O_7$", *Nature Phys.* **9**, 353–356 (2013).

[38] S. R. Giblin, M. Twengström, L. Bovo, M. Ruminy, M. Bartkowiak, P. Manuel, J. C. Andresen, D. Prabhakaran, G. Balakrishnan, E. Pomjakushina, C. Paulsen, E. Lhotel, L. Keller, M. Frontzek, S. C. Capelli, O Zaharko, P. A. McClarty, S. T. Bramwell, P Henelius, and T Fennell, "Pauling Entropy, Metastability, and Equilibrium in $Dy_2Ti_2O_7$ Spin Ice", *Phys. Rev. Lett.* **121**, 067202 (2018).

[39] Anjana M. Samarakoon, André Sokolowski, Bastian Klemke, Ralf Feyerherm, Michael Meissner, R. A. Borzi, Feng Ye, Qiang Zhang, Zhiling Dun, Haidong Zhou, T. Egami, Jonathan N. Hallén, Ludovic Jaubert, Claudio Castelnovo, Roderich Moessner, S. A. Grigera, and D. Alan Tennant, "Structural magnetic glassiness in the spin ice $Dy_2Ti_2O_7$", *Phys. Rev. Research*, **4**, 033159 (2022).

[40] T. Yavors'kii, T. Fennell, M. J. P. Gingras, and S. T. Bramwell, "$Dy_2Ti_2O_7$ Spin Ice: A Test Case for Emergent Clusters in a Frustrated Magnet", *Phys. Rev. Lett.* **101**, 037204 (2008).

[41] K. Matsuhira, Y. Hinatsu, and T. Sakakibara, "Novel dynamical magnetic properties in the spin ice compound $Dy_2Ti_2O_7$", *J. Phys. Conden. Matter*, **13**, L737–L746 (2001).

[42] J. Snyder, J. S. Slusky, R. J. Cava, and P. Schiffer, "How 'spin ice' freezes", *Nature*, **413**, 48–51 (2001).

[43] J. Snyder, B.G. Ueland, J.S. Slusky, H. Karunadasa, R.J. Cava, and P. Schiffer, "Low-temperature spin freezing in the $Dy_2Ti_2O_7$ spin ice", *Phys. Rev. B*, **69**, 064414 (2004).

[44] G. Ehlers, A. L. Cornelius, M. Orendac, M. Kajnakov, T. Fennell, S. T. Bramwell, and J. S. Gardner, "Dynamical crossover in hot spin ice", *J. Phys. Condens. Matter*, **15**, L9–L15 (2003).

[45] G. Ehlers, A. L. Cornelius, T. Fennell, M. Koza, S. T. Bramwell, and J. S. Gardner, "Evidence for two distinct spin relaxation mechanisms in hot spin ice $Ho_2Ti_2O_7$", *J. Phys. Condens. Matter*, **16**, S635–S642 (2004).

[46] C. Sangregorio, T. Ohm, C. Paulsen, R. Sessoli, and D. Gatteschi, "Quantum Tunneling of the Magnetization in an Iron Cluster Nanomagnet", *Phys. Rev. Lett.* **78**, 4645–4648 (1997).

[47] L. D. C. Jaubert and P. C. W. Holdsworth, "Signature of magnetic monopole and Dirac string dynamics in spin ice", *Nature Phys.* **5**, 258–261 (2009).

[48] L. D. C. Jaubert and P. C. W. Holdsworth, "Magnetic monopole dynamics in spin ice", *J. Phys. Condens. Matter*, **23**, 164222 (2011).

[49] K. Matsuhira, C. Paulsen, E. Lhotel, C. Sekine, Z. Hiroi, and S. Takagi, "Spin Dynamics at Very Low Temperature in Spin Ice $Dy_2Ti_2O_7$", *J. Phys. Soc. Jap.* **80**, 123711 (2011).

[50] J. A. Quilliam, L. R. Yaraskavitch, H. A. Dabkowska, B. D. Gaulin, and J. B. Kycia, "Dynamics of the magnetic susceptibility deep in the Coulomb phase of the dipolar spin ice material $Ho_2Ti_2O_7$", *Phys. Rev. B*, **83**, 094424 (2011).

[51] C. V. Topping and S. J. Blundell, "AC susceptibility as a probe of low-frequency magnetic dynamics", *J. Phy. Condens. Matter*, **31**, 013001 (2019).

[52] Bruno. Tomasello, C. Castelnovo, R. Moessner, and J. Quintanilla, "Single-ion anisotropy and magnetic field response in the spin-ice materials $Ho_2Ti_2O_7$ and $Dy_2Ti_2O_7$", *Phys. Rev. B*, **92**, 155120 (2015).

[53] Bruno Tomasello, Claudio Castelnovo, Roderich Moessner, and Jorge Quintanilla, "Correlated Quantum Tunneling of Monopoles in Spin Ice", *Phys. Rev. Lett.* **123**, 067204 (2019).

[54] G. Sala, C. Castelnovo, R. Moessner, S. L. Sondhi, K. Kitagawa, M. Takigawa, R. Higashinaka, and Y. Maeno, "Magnetic Coulomb Fields of Monopoles in Spin Ice and Their Signatures in the Internal Field Distribution", *Phys. Rev. Lett.* **108**, 217203 (2012).

[55] Anjana M. Samarakoon, S. A. Grigera, D. Alan Tennant, Alexander Kirste, Bastian Klemke, Peter Strehlow, Michael Meissner, Jonathan N. Hallén, Ludovic Jaubert, Claudio Castelnovo, and Roderich Moessner, "Anomalous magnetic noise in an imperfectly flat landscape in the topological magnet $Dy_2Ti_2O_7$", *Proc. Natl. Acad. Sci. U.S.A.* **119**, e2117453119 (2022).

[56] Jonathan N. Hallén, Santiago A. Grigera, D. Alan Tennant, Claudio Castelnovo, and Roderich Moessner, "Dynamical fractal and anomalous noise in a clean magnetic crystal", *Science*, **378**, 1218 (2022).

[57] Yishu Wang, T. Reeder, Y. Karaki, J. Kindervater, T. Halloran, N. Maliszewskyj, Yiming Qiu, J. A. Rodriguez, S. Gladchenko, S. M. Koohpayeh, S. Nakatsuji, and C. Broholm, "Monopolar and dipolar relaxation in spin ice $Ho_2Ti_2O_7$", *Sci. Adv.* **7**, eabg0908 (2021).

[58] C. Castelnovo, R. Moessner, and S. L. Sondhi, "Thermal Quenches in Spin Ice", *Phys. Rev. Lett.* **104**, 107201 (2010).

[59] C. Paulsen, M. J. Jackson, E. Lhotel, B. Canals, D. Prabhakaran, K. Matsuhira, S.R. Giblin, and S.T. Bramwell, "Far-from-equilibrium monopole dynamics in spin ice", *Nature Phys.* **10**, 135 (2014).

[60] C. Paulsen, S. R. Giblin, E. Lhotel, D. Prabhakaran, G. Balakrishnan, K. Matsuhira, and S. T. Bramwell, "Experimental signature of the attractive Coulomb force between positive and negative magnetic monopoles in spin ice", *Nature Phys.* **12**, 661–666 (2016).

[61] S. T. Bramwell, S. R. Giblin, S. Calder, R. Aldus, D. Prabhakaran, and T. Fennell, "Measurement of the charge and current of magnetic monopoles in spin ice", *Nature*, **461**, 956–959 (2009).

[62] V. Kaiser, S. T. Bramwell, P. C. W. Holdsworth, and R. Moessner, "ac Wien Effect in Spin Ice, Manifest in Nonlinear, Nonequilibrium Susceptibility", *Phys. Rev. Lett.* **115** (2015).

[63] M. Ocio, H. Bouchiat, and P. Monod, "Observation of 1/f magnetic fluctuations in a spin glass", *J. Phys. Lettres*, **46**, 647–652 (1985).

[64] M. Ocio, J. Hammann, Ph. Refregier, and E. Vincent, "Experimental investigation on the spin glass dynamics in $CdIn_{0.3}Cr_{1.7}S_4$ from noise measurements", *Physica B*, **150**, 353–360 (1988).

[65] Ritika Dusad, Franziska K. K. Kirschner, Jesse C. Hoke, Benjamin R. Roberts, Anna Eyal, Felix Flicker, Graeme M. Luke, Stephen J. Blundell, and J. C. Séamus Davis, "Magnetic monopole noise", *Nature*, **571**, 234 (2019).

[66] Leticia F Cugliandolo, "The effective temperature", *J. Phys. A: Math. Theor.* **44**, 483001 (2011).

[67] T. S. Grigera and N. E. Israeloff, "Observation of Fluctuation-Dissipation-Theorem Violations in a Structural Glass", *Phys. Rev. Lett.* **83**, 5038–5041 (1999).

[68] L. Bellon, S. Ciliberto, and C. Laroche, "Violation of the fluctuation-dissipation relation during the formation of a colloidal glass", *Euro. Lett.* **53**, 511–517 (2001).

[69] S. Joubaud, B. Percier, A. Petrosyan, and S. Ciliberto, "Aging and Effective Temperatures Near a Critical Point", *Phys. Rev. Lett.* **102** (2009).

[70] D. Hérisson and M. Ocio, "Fluctuation-Dissipation Ratio of a Spin Glass in the Aging Regime", *Phys. Rev. Lett.* **88** (2002).

[71] V. Raban, L. Berthier, and P. C. W. Holdsworth, "Violation of the fluctuation-dissipation theorem and effective temperatures in spin ice", *Phys. Rev. B*, **105**, 134431 (2022).

[72] V. Cathelin. "Les glaces de spins : monopoles magnétiques, relation fluctuation-dissipation et fragmentation". PhD thesis. Université Grenoble Alpes, 2020.

[73] P. W. Anderson, "Resonating valence bonds: A new kind of insulator?", *Mat. Res. Bulletin*, **8**, 153–160 (1973).

[74] M. Hermele, M. P. A. Fisher, and L. Balents, "Pyrochlore photons: The U(1) spin liquid in a S = 1/2 three-dimensional frustrated magnet", *Phys. Rev. B*, **69**, 064404 (2004).

[75] M. J. P. Gingras and P. A. McClarty, "Quantum spin ice: a search for gapless quantum spin liquids in pyrochlore magnets", *Rep. Prog. Phys.* **77**, 056501 (2014).

[76] Y.-P. Huang, G. Chen, and M. Hermele, "Quantum Spin Ices and Topological Phases from Dipolar-Octupolar Doublets on the Pyrochlore Lattice", *Phys. Rev. Lett.* **112**, 167203 (2014).

[77] J. G. Rau and M. J. P. Gingras, "Magnitude of quantum effects in classical spin ices", *Phys. Rev. B*, **92**, 144417 (2015).

[78] O. Benton, "Ground-state phase diagram of dipolar-octupolar pyrochlores", *Phys. Rev. B*, **102** (2020).

[79] E. M. Smith, E. Lhotel, S. Petit, and B. D. Gaulin, "Experimental Insights into Quantum Spin Ice Physics in Dipole–Octupole Pyrochlore Magnets", *Ann. Rev. of Condens. Matt. Phys.* **16**, 387–415 (2025).

[80] M. Léger, F. Vayer, M. Ciomaga Hatnean, F. Damay, C. Decorse, D. Berardan, B. Fåk, J. M. Zanotti, Q. Berrod, J. Ollivier, J. P. Embs, T. Fennell, D. Sheptyakov, S. Petit, and E. Lhotel, "Impact of disorder in Nd-based pyrochlore magnets", *Phys. Rev. B*, **109**, 224416 (2024).

[81] E. Lhotel, S. Petit, S. Guitteny, O. Florea, M. Ciomaga Hatnean, C. Colin, E. Ressouche, M. R. Lees, and G. Balakrishnan, "Fluctuations and All-in–All-out ordering in dipole-octupole $Nd_2Zr_2O_7$", *Phys. Rev. Lett.* **115**, 197202 (2015).

[82] J. Xu, V. K. Anand, A. K. Bera, M. Frontzek, D. L. Abernathy, N. Casati, K. Siemensmeyer, and B. Lake, "Magnetic structure and crystal-field states of the pyrochlore antiferromagnet $Nd_2Zr_2O_7$", *Phys. Rev. B*, **92** (2015).

[83] O. Benton, "Quantum origins of moment fragmentation in $Nd_2Zr_2O_7$", *Phys. Rev. B*, **94**, 104430 (2016).

[84] R. Sibille, N. Gauthier, E. Lhotel, V. Porée, V. Pomjakushin, R. A. Ewings, T. G. Perring, J. Ollivier, A. Wildes, C. Ritter, T. C. Hansen, D. A. Keen, G. J. Nilsen, L. Keller, S. Petit, and T. Fennell, "A quantum liquid of magnetic octupoles on the pyrochlore lattice", *Nature Phys.* **16**, 546–552 (2020).

[85] S. Petit, E. Lhotel, B. Canals, M. Ciomaga Hatnean, J. Ollivier, H. Mutka, E. Ressouche, A.R. Wildes, M. R. Lees, and G. Balakrishnan, "Observation of magnetic fragmentation in spin ice", *Nature Phys.* **12**, 746–750 (2016).

[86] M. Ciomaga Hatnean, M. R. Lees, O. A. Petrenko, D. S. Keeble, G. Balakrishnan, M. J. Gutmann, V. V. Klekovkina, and B. Z. Malkin, "Structural and magnetic investigations of single-crystalline neodymium zirconate pyrochlore $Nd_2Zr_2O_7$", *Phys. Rev. B*, **91** (2015).

[87] M. E. Brooks-Bartlett, S. T. Banks, L. D. C. Jaubert, A. Harman-Clarke, and P. C. W. Holdsworth, "Magnetic-Moment Fragmentation and Monopole Crystallization", *Phys. Rev. X*, **4** (2014).

[88] H. Yan, R. Pohle, and N. Shannon, "Half moons are pinch points with dispersion", *Phys. Rev. B*, **98** (2018).

[89] J. Xu, O. Benton, A. T. M. N. Islam, T. Guidi, G. Ehlers, and B. Lake, "Order out of a Coulomb Phase and Higgs Transition: Frustrated Transverse Interactions of $Nd_2Zr_2O_7$", *Phys. Rev. Lett.* **124**, 097203 (2020).

[90] M. Léger, E. Lhotel, M. Ciomaga Hatnean, J. Ollivier, A. R. Wildes, S. Raymond, E. Ressouche, G. Balakrishnan, and S. Petit, "Spin Dynamics and Unconventional Coulomb Phase in $Nd_2Zr_2O_7$", *Phys. Rev. Lett.* **126**, 247201 (2021).

[91] F. Museur, J. Robert, F. Morineau, V. Simonet, E. Pachoud, A. Hadj-Azzem, C. Colin, P. Manuel, J. R. Stewart, P. C. W. Holdsworth, and E. Lhotel. *Ferromagnetic fragmented ground state in the pyrochlore $Ho_2Ru_2O_7$*. en. Nov. 2024.

[92] S. T. Ku, D. Kumar, M. R. Lees, W. T. Lee, R. Aldus, A. Studer, P. Imperia, S. Asai, T. Masuda, S. W. Chen, J. M. Chen, and L. J. Chang, "Low temperature magnetic properties of $Nd_2Ru_2O_7$", *J. Phys. Condens. Matter*, **30**, 155601 (2018).

[93] Z. Tian, Y. Kohama, T. Tomita, H. Ishizuka, T. H. Hsieh, J. J. Ishikawa, K. Kindo, L. Balents, and S. Nakatsuji, "Field-induced quantum metal–insulator transition in the pyrochlore iridate $Nd_2Ir_2O_7$", *Nature Phys.* **12**, 134–138 (2016).

[94] K. Tomiyasu, K. Matsuhira, K. Iwasa, M. Watahiki, S. Takagi, M. Wakeshima, Y. Hinatsu, M. Yokoyama, K. Ohoyama, and K. Yamada, "Emergence of Magnetic Long-range Order in Frustrated Pyrochlore $Nd_2Ir_2O_7$ with Metal–Insulator Transition", *J. Phys. Soc. Jap.* **81**, 034709 (2012).

[95] A. T. Boothroyd. *Principles of Neutron Scattering from Condensed Matter*. July 2020.

[96] E. Lefrançois. "Synthèse de composés à base d'oxydes d'iridium à forte intrcation spin-orbite". PhD thesis. Université Grenoble Alpes, 2016.

[97] *NIST Center for Neutron Research*. https://www.ncnr.nist.gov/resources/n-lengths/.

[98] *ILL instrument list*. https://www.ill.eu/for-ill-users/instruments/instruments-list.

[99] G. K. White and P. J. Meeson. *Experimental Techniques in Low-Temperature Physics*. Feb. 2002.

[100] *Wikipedia: Dilution refrigerator*. https://en.wikipedia.org/wiki/Dilution_refrigerator.

[101] C. Paulsen, "DC magnetic measurements", *Servicio de Publicaciones de la Universidad de Zaragoza* (2001).

[102] *Hyperphysics*. http://hyperphysics.phy-astr.gsu.edu/hbase/Solids/Squid.html.

[103] *Magnicon SQUID*. http://www.magnicon.com/.

[104] *Encyclopedia Magnetica*. https://www.e-magnetica.pl/doku.php/wiki/about_encyclopedia_magnetica.

[105] L. F. Cugliandolo. "Course 7: Dynamics of Glassy Systems". In: *Slow Relaxations and nonequilibrium dynamics in condensed matter*. Ed. by Jean-Louis Barrat, Mikhail Feigelman, Jorge Kurchan, and Jean Dalibard. 2003, 367–521.

[106] R. Kubo, "The fluctuation-dissipation theorem", *Rep. Prog. Phys.* **29**, 255 (1966).

[107] P. Refregier and M. Ocio, "Measurement of spontaneous magnetic fluctuations", *Rev. Phys. App.* **22**, 367–374 (1987).

[108] F. Morineau, V. Cathelin, P. C. W. Holdsworth, S. R. Giblin, G. Balakhrishnan, K. Matsuhira, C. Paulsen, and E. Lhotel, "Satisfaction and Violation of the Fluctuation-Dissipation Relation in Spin Ice Materials", *Phys. Rev. Lett.* **134**, 096702 (2025).

[109] T. Fennell, O. A. Petrenko, B. Fåk, S. T. Bramwell, M. Enjalran, T. Yavors'kii, M. J. P. Gingras, R. G. Melko, and G. Balakrishnan, "Neutron scattering investigation of the spin ice state in $Dy_2Ti_2O_7$", *Phys. Rev. B*, **70**, 134408 (2004).

[110] P. J. W. Debye. *Polar molecules*. 1929.

[111] S. Havriliak and S. Negami, "A complex plane representation of dielectric and mechanical relaxation processes in some polymers", *Polymer*, **8**, 161–210 (1967).

[112] A. V. Klyuev, M. I. Ryzhkin, and A. V. Yakimov, "Statistics of Fluctuations of Magnetic Monopole Concentration in Spin Ice", *Fluctuation and Noise Letters*, **16**, 1750035 (2017).

[113] K. Matsuhira, Y. Hinatsu, K. Tenya, and T. Sakakibara, "Low temperature magnetic properties of frustrated pyrochlore ferromagnets $Ho_2Sn_2O_7$ and $Ho_2Ti_2O_7$", *J. Phys.: Condens. Matter*, **12**, L649–L656 (2000).

[114] Leticia F. Cugliandolo, Jorge Kurchan, and Luca Peliti, "Energy flow, partial equilibration, and effective temperatures in systems with slow dynamics", *Phys. Rev. E*, **55**, 3898 (1997).

[115] P. C. Hohenberg and B. I. Shraiman, "Chaotic behavior of an extended system", *Physica D: Nonlinear Phenomena*, **37**, 109–115 (1989).

[116] M. Twengström, L. Bovo, M. J. P. Gingras, S. T. Bramwell, and P. Henelius, "Microscopic aspects of magnetic lattice demagnetizing factors", *Phys. Rev. Mat.* **1**, 044406 (2017).

[117] J. A. Osborn, "Demagnetizing Factors of the General Ellipsoid", *Phys. Rev.* **67**, 351–357 (1945).

[118] A. Aharoni, "Demagnetizing factors for rectangular ferromagnetic prisms", *J. of App. Phys*, **83**, 3432–3434 (1998).

[119] D. Billington, E. Riordan, C. Cafolla-Ward, J. Wilson, E. Lhotel, C. Paulsen, D. Prabhakaran, S. T. Bramwell, F. Flicker, and S. R. Giblin. *Power spectrum of magnetic relaxation in spin ice: anomalous diffusion in a Coulomb fluid*. en. Dec. 2024.

[120] M. Twengström, L. Bovo, O. A. Petrenko, S. T. Bramwell, and P.Henelius, "$LiHoF_4$ : Cuboidal demagnetizing factor in an Ising ferromagnet", *Phys. Rev. B*, **102**, 144426 (2020).

[121] L. Bovo, L. D. C. Jaubert, P. C. W. Holdsworth, and S. T. Bramwell, "Crystal shape-dependent magnetic susceptibility and Curie law crossover in the spin ices $Dy_2Ti_2O_7$ and $Ho_2Ti_2O_7$", *J. Phys.: Condens. Matter*, **25**, 386002 (2013).

[122] R. L. Kronig, "On the Theory of Dispersion of X-Rays", *J. Opt. Soc. Amer.* **12**, 547 (1926).

[123] D. M. Roessler, "Kramers-Kronig analysis of reflection data", *Brit. J. App. Phys.* (1965).

[124] S. T. Bramwell, "Sample-shape dependence of magnetic noise", *Phys. Rev. B*, **111** (2025).

[125] C. Paulsen, S.R. Giblin, E. Lhotel, D. Prabhakaran, K. Matsuhira, G. Balakrishnan, and S.T. Bramwell, "Nuclear spin assisted quantum tunnelling of magnetic monopoles in spin ice", *Nature Comm.* **10**, 1509 (2019).

[126] G. Sala, M. J. Gutmann, D. Prabhakaran, D. Pomaranski, C. Mitchelitis, J. B. Kycia, D. G. Porter, C. Castelnovo, and J. P. Goff, "Vacancy defects and monopole dynamics in oxygen-deficient pyrochlores", *Nature Mat.* **13**, 488–493 (2014).

[127] D. Pomaranski. *Precision Low Temperature Calorimetry and Susceptibility of Magnetic Pyrochlores*. en.

[128] Bartington Instruments. *Single Axis Fluxgate Magnetometer*. bartington-fluxgate.

[129] F.W. Grover. *Inductance calculations working formulas and tables*. 1962.

[130] M. C. Runyan and W. C. Jones, "Thermal conductivity of thermally-isolating polymeric and composite structural support materials between 0.3 and 4 K", *Cryogenics*, **48**, 448–454 (2008).

[131] S. Onoda and Y. Tanaka, "Quantum fluctuations in the effective pseudospin-1/2 model for magnetic pyrochlore oxides", *Phys. Rev. B*, **83**, 094411 (2011).

[132] K. A. Ross, L. Savary, B. D. Gaulin, and L. Balents, "Quantum Excitations in Quantum Spin Ice", *Phys. Rev. X*, **1**, 021002 (2011).

[133] K. Essafi, O. Benton, and L. D. C. Jaubert, "Generic nearest-neighbor kagome model: XYZ and Dzyaloshinskii-Moriya couplings with comparison to the pyrochlore-lattice case", *Phys. Rev. B*, **96**, 205126 (2017).

[134] *Bilbao Crystallographic server*. https://www.cryst.ehu.es/.

[135] S. Petit, "Numerical simulations and magnetism", *Ecole them. SFN*, **12**, 105–121 (2011).

[136] Y. Xu, Y. Yang, J. Teyssier, T. Ohtsuki, Y. Qiu, S. Nakatsuji, D. Van Der Marel, N. B. Perkins, and N. Drichko, "Ramification of complex magnetism in $Nd_2Ir_2O_7$ observed by Raman scattering spectroscopy", *npj Quant. Mat.* **10**, 88 (2025).

[137] B. K. Patel, M. T. K. Kolambage, C. D. McMillen, and J. W. Kolis, "Hydrothermal synthesis of lanthanide ruthenate single crystals", *Journal of Crystal Growth*, **602**, 126979 (2023).

[138] D. Wulferding, J. Kim, M. K. Kim, Y. Yang, J. H. Lee, D. Song, D. Oh, H.-S. Kim, L. E Chern, Y. B. Kim, M. Noh, H. Choi, S. Choi, N. B. Perkins, C. Kim, and S. R. Park, "Collective magnetic Higgs excitation in a pyrochlore ruthenate", *npj Quant. Mat.* **8**, 40 (2023).

[139] M. Watahiki, K. Tomiyasu, K. Matsuhira, K. Iwasa, M. Yokoyama, S. Takagi, M. Wakeshima, and Y. Hinatsu, "Crystalline electric field study in the pyrochlore $Nd_2Ir_2O_7$ with metal-insulator transition", *J. Phys. Conf. Series*, **320**, 012080 (2011).

[140] D. Yanagishima and Y. Maeno, "Metal-nonmetal changeover in pyrochlore iridates", *J. Phys. Soc. Jap.* **70**, 2880–2883 (2001).

[141] K. Matsuhira, M. Wakeshima, R. Nakanishi, T. Yamada, A. Nakamura, W. Kawano, S. Takagi, and Y. Hinatsu, "Metal-insulator transition in pyrochlore iridates $Ln_2Ir_2O_7$ (Ln= Nd, Sm, and Eu)", *J. Phys. Soc. Jap.* **76**, 043706 (2007).

[142] H. Guo, K. Matsuhira, I. Kawasaki, M. Wakeshima, Y. Hinatsu, I. Watanabe, and Z. Xu, "Magnetic order in the pyrochlore iridate $Nd_2Ir_2O_7$ probed by muon spin relaxation", *Phys. Rev. B*, **88**, 060411 (2013).

[143] E. Lefrançois, V. Cathelin, E. Lhotel, J. Robert, P. Lejay, C. Colin, B. Canals, F. Damay, J. Ollivier, B. Fåk, L. C. Chapon, R. Ballou, and V. Simonet, "Fragmentation in spin ice from magnetic charge injection", *Nature Comm.* **8** (2017).

[144] L. Opherden, J. Hornung, T. Herrmannsdörfer, J. Xu, A. T. M. N. Islam, B. Lake, and J. Wosnitza, "Evolution of antiferromagnetic domains in the all-in-all-out ordered pyrochlore $Nd_2Zr_2O_7$", *Phys. Rev. B*, **95**, 184418 (2017).

[145] E. Lhotel, S. Petit, M. Ciomaga Hatnean, J. Ollivier, H. Mutka, E. Ressouche, M. R. Lees, and G. Balakrishnan, "Evidence for dynamic kagome ice", *Nature Comm.* **9**, 3786 (2018).

[146] M. Ito, Y. Yasui, M. Kanada, H. Harashina, S. Yoshii, K. Murata, M. Sato, H. Okumura, and K. Kakurai, "Neutron Diffraction Study of Pyrochlore Compound $R_2Ru_2O_7$ (R=Y, Nd) above and below the Spin Freezing Temperature", *J. Phys. Soc. Jap.* **69**, 888–894 (2000).

[147] F. Museur. "Fragmentation in frustrated pyrochlore magnets: theory and experiment". PhD thesis. Université Grenoble Alpes, 2023.

[148] J. Xu, O. Benton, V. K. Anand, A. T. M. N. Islam, T. Guidib, G. Ehlers, E. Feng, Y. Su, A. Sakai, P. Gegenwart, and B. Lake, "Anisotropic exchange Hamiltonian, magnetic phase diagram, and domain inversion of $Nd_2Zr_2O_7$", *Phys. Rev. B*, **99**, 144420 (2019).

[149] S. J. Gomez, P. M. Sarte, M. Zelensky, A. M. Hallas, B. A. Gonzalez, K. H. Hong, E. J. Pace, S. Calder, M. B. Stone, Y. Su, E. Feng, M. D. Le, C. Stock, J. P. Attfield, S. D. Wilson, C. R. Wiebe, and A. A. Aczel, "Absence of moment fragmentation in the mixed B-site pyrochlore $Nd_2GaSbO_7$", *Phys. Rev. B*, **103**, 214419 (2021).

**Résumé** : Le magnétisme frustré est le domaine d'étude des systèmes magnétiques dans lesquels les interactions entre moments magnétiques (spins) ne peuvent pas être satisfaites simultanément, en raison de la géométrie du réseau cristallin ou de la compétition entre interactions. Cette frustration empêche l'établissement d'un ordre magnétique conventionnel à basse température et favorise l'émergence d'états exotiques tels que les glaces de spins ou les liquides de spins quantiques. Parmi les réseaux géométriquement frustrés, le réseau pyrochlore, composé de tétraèdres connectés par leurs sommets, héberge un grand nombre d'états fondamentaux originaux. Expérimentalement, ce réseau est réalisé dans des oxydes de terres rares de formule générale $R_2M_2$O7, où $R^{3+}$ est un ion terre rare et $M4+$ un ion métallique. Dans cette thèse, nous nous intéressons à deux cas : celui de l'état glace de spins avec $R$=Ho, Dy et celui des états dipolaires-octupolaires avec $R$=Nd.

Dans l'état glace de spins, les interactions effectives ferromagnétiques imposent une contrainte locale, appelée règle de la glace, qui génère un état corrélé macroscopiquement dégénéré. Lorsque l'énergie thermique est suffisante, la règle de la glace peut localement être brisée, générant des excitations fractionnalisées : les monopoles magnétiques. Ces charges magnétiques peuvent se propager presque librement à travers le réseau, interagissant entre elles par interaction coulombienne. Leur dynamique complexe a été intensivement étudiée dans $Dy_2Ti_2O_7$ et dans une moindre mesure dans $Ho_2Ti_2O_7$ et reste encore aujourd'hui mal comprise. A très basse température, il a été observé que la dynamique ralentit très fortement résultant en un gel dans les mesures d'aimantation suggérant un état hors équilibre. La première partie de cette thèse s'intéresse à la dynamique fortement corrélée des monopoles jusqu'à très basse température (150 mK) et à la nature de cet état hors-équilibre en sondant le théorème fluctuation-dissipation. Elle se base sur la conception et l'optimisation d'une expérience cryogénique permettant de mesurer simultanément la susceptibilité alternative et le bruit magnétique associé aux monopoles. Trois régimes de température et de fréquence ont pu être mis en évidence: un régime d'équilibre, un régime où l'équilibre local est préservé, et un régime hors-équilibre où des déviations à la relation fluctuation-dissipation sont observées. Cette expérience a aussi permis de démontrer et quantifier le rôle des effets de champ démagnétisant sur les mesures de bruit magnétique.

Dans la seconde partie, cette thèse étudie les composés pyrochlores dipolaires-octupolaires $Nd_2Ru_2O_7$ et $Nd_2Ir_2O_7$. Dans ces systèmes, les effets de champ cristallin confèrent à l'ion de terre rare des propriétés de symétries inhabituelles générant des composantes magnétiques à la fois dipolaires et octupolaires et qui peuvent se coupler mutuellement. Ces couplages agissent comme une perturbation quantique permettant de réaliser de nouvelles phases magnétiques. Dans la famille des pyrochlores à base de Nd, un ordre "all-in/all-out" mixte dipolaire-octupolaire est observé. L'objectif de cette étude est de comprendre l'effet d'un ion métallique magnétique ($M$=Ir, Ru) sur cet état. Pour cela, des mesures de diffusion neutronique et d'aimantation à basse température ont été réalisées et analysées en déterminant les termes d'interaction Nd-M autorisés par symétrie. Les paramètres du Hamiltonien ont alors pu être estimés en optimisant numériquement les paramètres du modèle par confrontation avec l'expérience.

**Abstract:** Frustrated magnetism focus in magnetic system in which the interactions between magnetic moments (spins) cannot be simultaneously satisfied, due to the geometry of the lattice or competition of interactions. This frustration prevents from the stabilization of conventional magnetic order at low temperature and favors the emergence of exotic states such as spin ices or quantum spin liquids. Among geometrically frustrated lattices, the pyrochlore lattice, composed of corner-sharing tetrahedra, hosts a large number of original ground states. Experimentally, this lattice is realized in rare-earth oxides with the general formula $R_2M_2$O7, where $R^{3+}$ is a rare-earth ion and $M^{4+}$ a metallic ion. In this thesis, we focus on two cases: the spin ice state with $R$ = Ho, Dy and the dipolar-octupolar states with $R$ = Nd.

In the spin ice state, effective ferromagnetic interactions impose a local constraint, called the ice rule, which generates a macroscopically degenerate correlated state. When thermal energy is large enough, the ice rule can be broken locally, generating fractionalized excitations: the magnetic monopoles. These magnetic charges can propagate almost freely through the lattice, interacting with each other via Coulomb interactions. Their complex dynamics have been extensively studied in $Dy_2Ti_2O_7$ and, to a lesser extent, in $Ho_2Ti_2O_7$, and remain poorly understood. At very low temperature, it has been observed that the dynamics slow down drastically, resulting in a freezing in magnetization measurements, suggesting an out-of-equilibrium state. The first part of this thesis focuses on the strongly correlated dynamics of monopoles down to very low temperature (150 mK) and on the nature of this out-of-equilibrium state by probing the fluctuation-dissipation theorem. It relies on the design and optimization of a cryogenic experiment allowing the simultaneous measurement of the ac susceptibility and the magnetic noise associated to the monopoles. Three regimes of temperature and frequency have been identified: an equilibrium regime, a regime where local equilibrium is preserved, and an out-of-equilibrium regime where deviations from the fluctuation-dissipation relation are observed. This experiment also made it possible to demonstrate and quantify the role of demagnetizing field effects on magnetic noise measurements.

In the second part, this thesis studies the dipolar-octupolar pyrochlore compounds $Nd_2Ru_2O_7$ and $Nd_2Ir_2O_7$. In these systems, crystal electric field effects confer unusual symmetry properties to the rare-earth ion, generating both dipolar and octupolar magnetic components which can couple to each other. These couplings act as a quantum perturbation allowing the realization of new magnetic phases. In the family of Nd-based pyrochlores, a mixed dipolar-octupolar all-in/all-out order is observed. The objective of this study is to understand the effect of a magnetic metallic ion ($M$ = Ir, Ru) on this state. For this purpose, neutron scattering and low-temperature magnetization measurements were carried out and analyzed by determining the symmetry-allowed Nd-M interaction terms. The parameters of the Hamiltonian were then estimated by numerically optimizing the model parameters in comparison with the experimental data.